TWO-DIMENSIONAL BISMUTH-BASED LAYERED SUPERCELL FOR MULTIFERROISM

A Dissertation

by

LEIGANG LI

Submitted to the Office of Graduate and Professional Studies
Texas A&M University
in partial fulfillment of the requirements for the degree of

DOCTOR OF PHILOSOPHY

Chair of Committee,	Haiyan Wang
Co-Chair of Committee,	Xiaofeng Qian
Committee Members,	Hong Liang
	Xinghang Zhang
Head of Department,	Ibrahim Karaman

May 2017

Major Subject: Materials Science and Engineering

ABSTRACT

Room-temperature multiferroics, possessing ferroelectricity and ferromagnetism simultaneously in one phase, hold great promise in miniaturized devices including sensors, actuators, transducers, and multi-state memories. However, single-phase multiferroics are scarce because of the drastically different orbital requirements for ferroelectricity (requiring empty d-orbital) and ferromagnetism (coming from partially filled d-orbitals). Combining two cations possessing ferroelectric and ferromagnetic ordering respectively into one phase is one of the effective routes towards creating single-phase multiferroic materials, such as the Bi-based perovskites $BiFeO_3$ and Bi_2FeMnO_6. For Bi-based perovskites, the ferroelectricity comes from the high stereochemical activity of the lone-pair electrons of the Bi^{3+} cation and the B-site cation provides the magnetism. $Bi_3Fe_2Mn_2O_{10+\delta}$ supercell (BFMO322 SC) is a layered structure with enhanced ferroelectricity and magnetism compared to the conventional pseudocubic Bi_2FeMnO_6 phase. BFMO322 SC has been fabricated on $LaAlO_3$ (001) substrate and can also be fabricated on CeO_2 buffer layer.

In this dissertation, the influence of CeO_2 thickness to the growth and magnetic property of BFMO322 SC has been first investigated. The result shows that a CeO_2 buffer layer as thin as 6.7 nm is sufficient to trigger the growth of BFMO322 SC and the sample exhibits the best magnetic properties with both highest magnetization and anisotropy. The growth of BFMO322 SC with high phase purity and superior magnetic properties on CeO_2

with a thickness of 6.7 nm is attributed to the lattice match between Ce-Ce and Bi-Bi bond as well as the smooth surface of CeO_2 buffer layer.

Next, the influence of Fe/Mn molar ratio to the growth and magnetic property of Bi-based layered supercell structure has been studied by both experimental and theoretical methods. It was found that that Mn is more important than Fe in facilitating the growth of Bi-based layered supercell structures. With more Fe than Mn in the structure, the layered supercell structure cannot be formed. The three-dimensional distribution of Young's modulus of the Bi-based layered supercell structures is calculated based on density functional theory. The theoretical calculation indicates that the strain energy is too high to keep the layered supercell structure if there is more Fe than Mn. In particular, the layered supercell structure with Bi_2O_x slabs can also be obtained on CeO_2 buffer layer and $SrTiO_3$ (001) for single-perovskite $BiMnO_3$ under well controlled growth conditions.

Then tunable layered supercell (SC) structures have been designed and achieved in both $BiMnO_3$ and Bi_2NiMnO_6 thin films. More specifically, both supercells with two layer BiO_x-slabs (2-Bi SC) and three layer structure BiO_x-slabs (3-Bi SC) have been achieved on both $LaAlO_3$ (001) and $SrTiO_3$ (001) under deposition parameter tuning. The novel layered supercell structures consist of alternative layered stacking of Bi_2O_x (or Bi_3O_x) slabs and Mn-O (or Ni-Mn-O) octahedra layers along out-of-plane direction, respectively. Both the $BiMnO_3$ and Bi_2NiMnO_6 layered supercell structures exhibit robust multiferroic response at room temperature and tunable ferromagnetic and optical properties attributed to the variable SC structures.

Finally, a new layered supercell structure with Bi_3O_x slabs has been designed and fabricated from the new material system Bi_2AlMnO_6 (BAMO). The new BAMO layered supercell structure is self-assembly grown by alternative layered stacking of three-layer-thick Bi-based slabs $[Bi_3O_{3+\delta}]$ and one-layer-thick $[MO_2]_\infty$ layer (M = Al/Mn). It can be fabricated on single-crystal substrates $SrTiO_3$ (001) and $LaAlO_3$ (001), with or without CeO_2 (001) and $La_{0.7}Sr_{0.3}MnO_3$ (001) buffer layers. Robust room-temperature multiferroic responses have been observed for the new BAMO misfit (incommensurate) layered structure with non-magnetic cations Al^{3+} and magnetic cations Mn^{3+}.

The Bi-based layered supercell structures present great composition flexibility and hold great significance towards the design and creation of new two-dimensional layered materials with a wide range of potential functionalities, such as single-phase multiferroic materials, thermoelectrics, and layered materials with tunable band gaps.

DEDICATION

to all my families

ACKNOWLEDGMENTS

I would like to sincerely thank my research supervisor, Dr. Haiyan Wang, for all her patient and great guidance during my Ph.D. study at Texas A&M University. First, I want to express my appreciation to Dr. Wang for giving me the chance to study in her group. I treasure this great opportunity. The thing that inspires me the most during my study is that she always keeps positive, happy, and enthusiastic to both life and research. Dr. Wang tries her best to provide us the state-of-the-art experimental tools which ensures high-quality research. I want to thank Dr. Wang's encouragement as well as her great support which helps me discover many interesting things in research. I benefited a lot from Dr. Wang's strong network in research community. I am also impressed by Dr. Wang's broad knowledge in both materials science and experimental skills. I also appreciate Dr. Wang's great support and guidance to my personal life. I feel I am very lucky to pursue my Ph.D. study in Dr. Wang's group.

I would like to acknowledge all my thesis committee members, Dr. Xiaofeng Qian, Dr. Hong Liang, and Dr. Xinghang Zhang for their great help and attention to my research. I am thankful for their great efforts to my preliminary exam and final defense.

I want to thank my former and present group members, Dr. Aiping Chen, Dr. Qing Su, Dr. Wenrui Zhang, Dr. Fauzia Khatkhatay, Dr. Clement Jacob, Dr. Liang Jiao, Dr. Jie Jian, Dr. Jijie Huang, Meng Fan, Han Wang, Xuejing Wang, Xingyao Gao, Bruce Zhang, and Zhimin Qi for their camaraderie and collaboration.

I also want to acknowledge the faculty and staff at the Microscopy and Imaging Center as well as the Materials Characterization Facility at Texas A&M for their help and advice with equipment training.

Finally, I would like to thank all my families for their great support during all my Ph.D. study. Without their encouragement and support, I could not reach this far.

CONTRIBUTORS AND FUNDING SOURCES

Contributors

Funding Sources

NOMENCLATURE

PVD	Physical Vapor Deposition
CVD	Chemical Vapor Deposition
MBE	Molecular Beam Epitaxy
PLD	Pulsed Laser Deposition
DC	Direct Current
RF	Radio Frequency
APCVD	Atmospheric Pressure CVD
LPCVD	Low-Pressure CVD
PECVD	Plasma-Enhanced CVD
ALCVD	Atomic Layer CVD
MOCVD	Metal-Organic CVD
P_s	Saturation Polarization
P_r	Remanent Polarization
E_c	Electric Coercive Field
E_s	Electric Switching Field
T_C	Curie Temperature
CMR	Colossal Magnetoresistance
T	Tesla
^{o}C	Degree Centigrade
K	Kelvin

t	Goldschmidt Tolerance Factor
GK	Goodenough-Kanamori
μ_B	Bohr Magneton
PFM	Piezoelectric Force Microscopy
XRD	X-ray Diffraction
Oe	Oersted
T_N	Antiferromagnetic Neel Temperature
emu/cc	Magnetic Moment/Cubic Centimeter
kOe	Kilo-Oersted
SQUID	Superconducting Quantum Interference Device
XMCD	X-ray Magnetic Circular Dichroism
f.u.	Formula Unit
TEM	Transmission Electron Microscope
GPA	Geometric Phase Analysis
BF	Bright-Field
DF	Dark-Field
STEM	Scanning Transmission Electron Microscopy
ADF	Annular Dark-Field
HAADF	High-Angle Annular Dark-Field
EDS	Energy-Dispersive X-ray Spectroscopy
VSM	Vibrating Sample Magnetometer
PPMS	Physical Properties Measurement System

M	Magnetization
T	Temperature
FC	Field Cooling
ZFC	Zero-Field Cooling
PED	Precession Electron Diffraction
ABF	Annular Bright-Field
AFM	Atomic Force Microscopy
XPS	X-ray Photoelectron Spectroscopy
PEDT	Precession Electron Diffraction Tomography
SSG	Super-Space Groups

TABLE OF CONTENTS

LIST OF FIGURES

LIST OF TABLES

CHAPTER I

INTRODUCTION

Complex oxide materials have been extensively studied because of their various crystal structures, multifunctionalities and potential device applications. In this chapter, functional metal oxides will be reviewed first in section 1.1, including crystal structures of oxides and oxide thin film growth. Then in section 1.2 the functionalities of oxide thin films including ferroelectricity, magnetism and multiferroism are introduced. In section 1.3, several well-known multiferroic materials are briefly reviewed. In section 1.4, two-dimensional materials including non-oxide based and oxide-based two-dimensional materials will be reviewed and finally the research motivation for this work is introduced.

1.1 Functional metal oxide thin films

1.1.1 Overview of functional metal oxides

Metal oxides, especially transition metal oxides, represent a large family of materials that cover a wide range of crystal structures and functionalities. Metal oxides have found various applications and have played an incredible role in modern technology. Oxides with high ferroelectric response and dielectric constant such as $BaTiO_3$ and $Pb(Zr,Ti)O_3$ have been used for tranducers, capacitors, sensors, thermistors, etc.[1, 2] Superconductors (e.g. $YBa_2Cu_3O_7$ and FeSe) have been extensively studied and the proposed applications include superconducting cables, superconducting transformers, and superconducting filters.[3, 4] The Li-based metal oxides (e.g. $LiCoO_2$ and $LiMn_2O_4$) with

layered structures have been commercialized and used as cathode materials in Li-ion batteries.[5, 6] Single phase multiferroic materials including $BiFeO_3$ and $BiMnO_3$ have been extensively studied for the application of data storage.[7]

Compared to their bulk forms, metal oxides in thin film form have remarkably different crystalline quality and physical properties. With the development of high-quality thin film growth techniques and characterization capabilities, the field of functional metal oxides has experienced unprecedented development in terms of discovering new materials, understanding of fundamental physics, and controlling of physical properties.[8] The increasing needs for miniature devices with small volume and low energy consumption have also stimulated the study of functional metal oxide thin films.

1.1.2 Crystal structures of functional metal oxides

As mentioned above, metal oxides have been extensively studied with a wide range of crystal structures and fascinating properties. To understand metal oxides especially their physical properties, one should have solid knowledge of the crystal structures of various oxides. Metal oxides are ionically bonded and can be categorized to binary and ternary oxides as shown in Table 1.1. Binary oxides cover a series of crystal structures including rock salt, fluorite, wurtzite, rutile and corundum (Figure 1.1). The ternary systems include perovskite, spinel, ilmenite, Ruddlesden-Popper, and layered-perovskite (Figure 1.2).

Table 1.1 The classification of metal oxides.

Systems	Crystal structures	Representative oxides
Binary oxides	Rock salt	MgO, TiO, VO, MnO, NiO
	Wurtzite	ZnO, BeO
	Fluorite	CeO_2, ZrO_2, HfO_2, ThO_2
	Rutile	TiO_2, MoO_2, RuO_2
	Corundum	Al_2O_3, V_2O_3, Cr_2O_3
Ternary oxides	Perovskite	$CaTiO_3$, $BiFeO_3$, $SrRuO_3$
	Spinel	$CoFe_2O_4$, $NiFe_2O_4$, $MgAl_2O_4$
	Ilmenite	$FeTiO_3$, $MnTiO_3$, $LiNbO_3$
	Layered perovskite	$YBa_2Cu_3O_7$
	Ruddlesden-Popper	$SrRuO_3$, Sr_2RuO_4, $Sr_3Ru_2O_7$
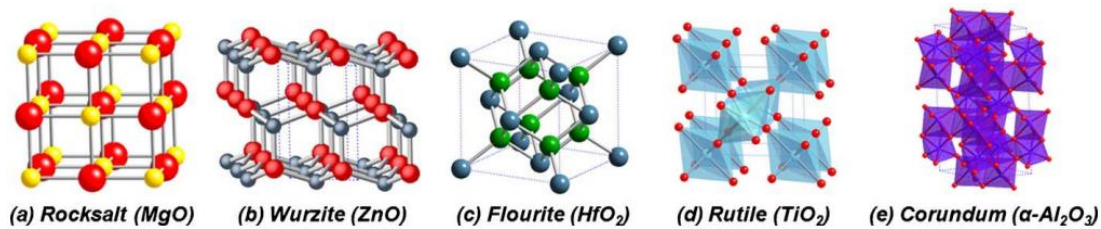
Figure 1.1 Common binary oxide crystal structures including (a) rocksalt, (b) wurzite, (c) fluorite, (d) rutile, and (e) corundum.[8]
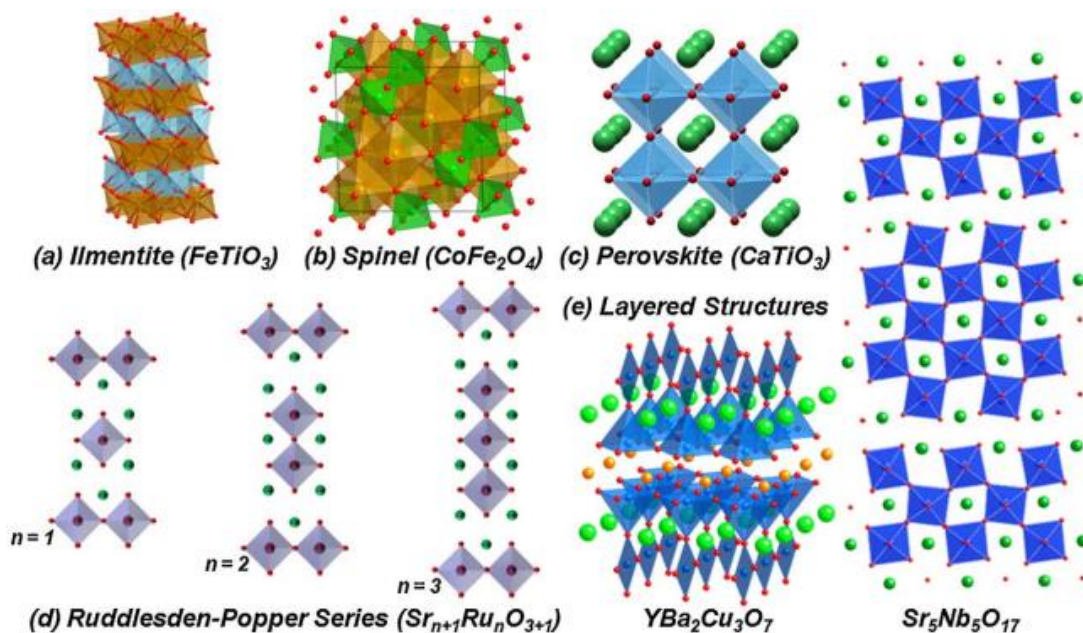
Figure 1.2 Common ternary oxide crystal structures including (a) ilmentite, (b) spinel, (c) perovskite, and derivatives of the perovskite such as (d) the Ruddlesden-Popper series, and (e) layered perovskites.[8]

Among the binary and ternary material systems, metal oxides with perovskite and perovskite-related structures have gained increasing research interest with a variety of attracting physical properties including ferroelectricity, ferromagnetism, superconductivity, and multiferroicity. Perovskites are ABO_3-type cubic or pseudocubic materials which was named after the prototype $CaTiO_3$. Perovskites are composed of

corner-sharing octahedral with the *A*-site cation coordinated by 12 oxygen ions and the *B*-site cation by 6 oxygen ions. The ionic radius of *A*-site cation is larger than that of the *B*-site cation and the overall charge of A and B is +6. The structure can easily accommodate a wide range of valence states on both *A*- and *B*-site and includes three categories: $A^{+1}B^{+5}O_3$, $A^{+2}B^{+4}O_3$, and $A^{+3}B^{+3}O_3$. The perovskite structure acts as the parent phase for a wide range of structures such as the Ruddlesden-Popper series.

1.1.3 Growth of metal oxide thin films

1.1.3.1 Thin film growth techniques

Basically, thin film growth techniques can be classified into two categories: physical vapor deposition (PVD) and chemical vapor deposition (CVD). There are also methods that combine both physical and chemical reactions. Table 1.2 shows the summary and comparison of different thin film growth techniques demonstrated for oxide growth.

Both physical vapor deposition (PVD) and chemical vapor deposition (CVD) are performed under vacuum for thin film growth. PVD is a process of using physical sources (e.g. heating and sputtering) to produce plasma to deposit thin films on an object. PVD mainly includes molecular beam epitaxy (MBE), pulsed laser deposition (PLD), magnetron sputtering (direct current (DC) and radio frequency (RF)), thermal evaporation and electron-beam evaporation. PVD techniques need relatively simple experimental set-up and can provide precise thin film stoichiometry for complex oxide thin films. Moreover, almost all materials, including metal oxide thin films, metal nitride thin films, and metals, can be grown by PVD with high quality. However, the disadvantages of PVD

such as high cost, limited surface coverage and low productivity limit its practical applications.

CVD is a chemical process which is used to obtain high quality thin film materials, especially in semiconductor industry. For typical CVD, the wafer is exposed to volatile precursors which react/decompose on the substrate surface to produce the desired materials. CVD includes atmospheric pressure CVD (APCVD), low-pressure CVD (LPCVD), plasma-enhanced CVD (PECVD), atomic layer CVD (ALCVD), and metal-organic CVD (MOCVD). CVD has the advantages of high surface coverage, high throughput, easily varied stoichiometry, and reasonable cost. But it suffers from the safety issue.

Besides the pure physical and chemical deposition techniques under vacuum, other non-vacuum thin film deposition techniques have also been developed. These techniques include liquid phase epitaxy and solution-based techniques (sol-gel and polymer assisted deposition). These non-vacuum techniques are more cost-effective and widely used in large-scale industrial applications.

Table 1.2 Comparison of different categories of thin film deposition techniques.

Category	Sub-category	Main characteristics	Advantages	Disadvantages
PVD	MBE	low-energy atomic beams of each component generated by heater/e-beam evaporators	high film quality, in-situ diagnosis, no contaminations, no exhaustion gas	high cost, low throughput

Table 1.2 Continued.

Category	Sub-category	Main characteristics	Advantages	Disadvantages
	PLD	high-power laser beam focused on the target surface to produce plasma	simple deposition technique, can deposit nearly all metals and ceramic materials, reproduction of target stoichiometry	high cost due to laser system, low surface coverage, formation of particulates
	Magnetron sputtering	magnetic field to confine electrons near the target to sustain plasma	precise target-film stoichiometry, low-temperature processing, high film quality	substrate heating during sputtering, radiation damage
	E-beam evaporation	high-energy beam from an electron gun to boil a target material	can deposit both metals and ceramic materials, less contamination	poor film uniformity and density, high cost
CVD	LPCVD	lowering the total pressure of the gas stream increases the diffusion and extends the reaction to higher temperature	high deposition rate at reduced pressure, high production rate, less auto doping, low cost, less particulates formation	shadowing and less uniform surface coverage

Table 1.2 Continued.

Category	Sub-category	Main characteristics	Advantages	Disadvantages
	PECVD	plasma source to supply additional energy and reduce the reaction temperature	reduced deposition temperature, enhanced deposition rate at low temperature, better surface coverage for non-planar structures	Nonstoichiometric composition of films, incorporation of byproducts into films
	ALCVD	two complementary precursors alternatively introduced into the reaction chamber	extremely precise control of film thickness and uniformity	high cost, low throughput
	MOCVD	a CVD method based on metal-organic precursors	high film quality, high throughput, large area production	requiring high temperature, not for all materials
Other deposition techniques	Liquid phase epitaxy	top seeded solution growth method with a substrate introduced vertically	high film quality, high deposition rate	ultrahigh temperature needed, hard to deposit thin films
	Solution-based deposition	transition of a system from liquid phase to solid phase	simple, low cost	poor surface roughness and coverage

Among the above thin film growth techniques, PLD has gained ever increasing attention in the past several decades for oxide thin film growth. PLD is a relatively simple thin film growth technique and offers many advantages as discussed in the following Chapter 2. The microstructures and physical properties of the thin films can be easily tuned by controlling the substrate temperature, oxygen partial pressure in the chamber, laser beam frequency and energy density.

1.1.3.2 Epitaxy theory for thin film growth

The term "epitaxy" comes from the Greek roots "epi" (meaning "above") and "taxis" (meaning "in ordered manner"). In the area of thin film study, epitaxy refers to the extended single-crystal film growth on top of a crystalline substrate. There are two types of epitaxy: *homoepitaxy* and *heteroepitaxy*.[9] *Homoepitaxy* means that the thin film material is the same as the substrate material while *heteroepitaxy* refers that the thin film material is different from the substrate material. For *homoepitaxy* or if the lattice constants of film and substrate are the same or nearly identical, there will be no strained interfacial bonds due to the perfectly matched lattice. Such film-substrate structures are called *lattice-matched epitaxial* structures as shown in Figure 1.3(a). Usually the lattice parameters for thin films and substrates are different and thus the films can grow on the substrates either coherently (called *coherently strained lattice-mismatched heteroepitaxy*) or incoherently (*relaxed lattice-mismatched heteroepitaxy*) as shown in Figure 1.3(b) and (c).
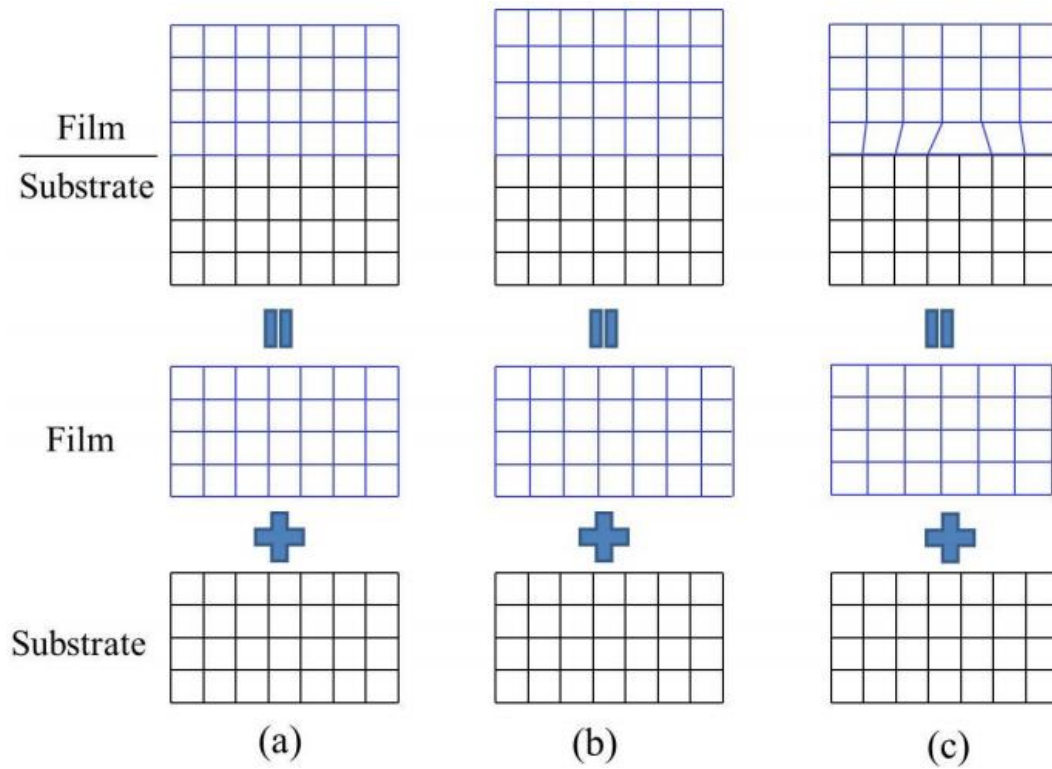
Figure 1.3 Schematic illustration of (a) lattice-matched epitaxy, (b) coherently strained lattice-mismatched heteroepitaxy, and (c) relaxed lattice-mismatched heteroepitaxy.[9]

Strain plays an important role in controlling the microstructures and tuning the physical properties of the thin films. For the heteroepitaxial structures, lattice mismatch between the films and the substrates will cause the films to be in compression or in tension. Thus there will be a lattice parameter change from the equilibrium values and therefore the physical properties will be influenced. For a heteroepitaxial structure, the lattice mismatch strain f is evaluated by,

$$f = 2 \times (a_f - a_s)/(a_f + a_s) \quad (1\text{-}1)$$

where a_f and a_s are the unstrained lattice parameters of film and substrate, respectively.

When the misfit strain f is < 7%, coherently strained lattice-mismatched heteroepitaxy is preferred while if f is larger than 7%, relaxed lattice-mismatched heteroepitaxy occurs. For the strained heteroepitaxial structures, the atoms of the films are constrained to the substrate interatomic spacing in the plane of the interface. Due to the lattice misfit, elastic strain energy is stored in the structures. The elastic strain energy increases linearly with the increase of the film thickness. When the elastic strain energy is large enough after a "critical thickness", the strain energy at the interface will be relaxed via the formation of misfit dislocations.

If the lattice mismatch is very large (> 10%), the films can't grow coherently at the initial stages. In this situation, domain matching epitaxy will be possible for the epitaxial growth of thin films. For domain matching epitaxy, although the initial mismatch is very large, the strain can be relaxed by matching of m planes of the film with n planes of the substrate. The matching of integral multiples of lattice planes usually leaves a residual strain f_r given by the following equation,

$$f_r = (ma_f - na_s)/na_s \quad (1\text{-}2)$$

where $n = m + 1$, n and m are simple integers.

One such example of domain matching epitaxy is the epitaxial growth of TiN on Si (100). The mismatch strain is as large as ~24.6% based on the strained lattice-mismatched epitaxy. However, by the domain matching epitaxy the residual strain can be reduced to be ~4.4%. TiN will grow epitaxially on Si (100) by 3/4 domain matching.[10] Other examples of domain matching epitaxy include AlN/Si (100) with 4/5 matching,

ZnO/α-Al$_2$O$_3$ (0001) with 6/7 matching, and SrTO$_3$/MgO (001) with 14/13 matching (Figure 1.4).[11, 12]
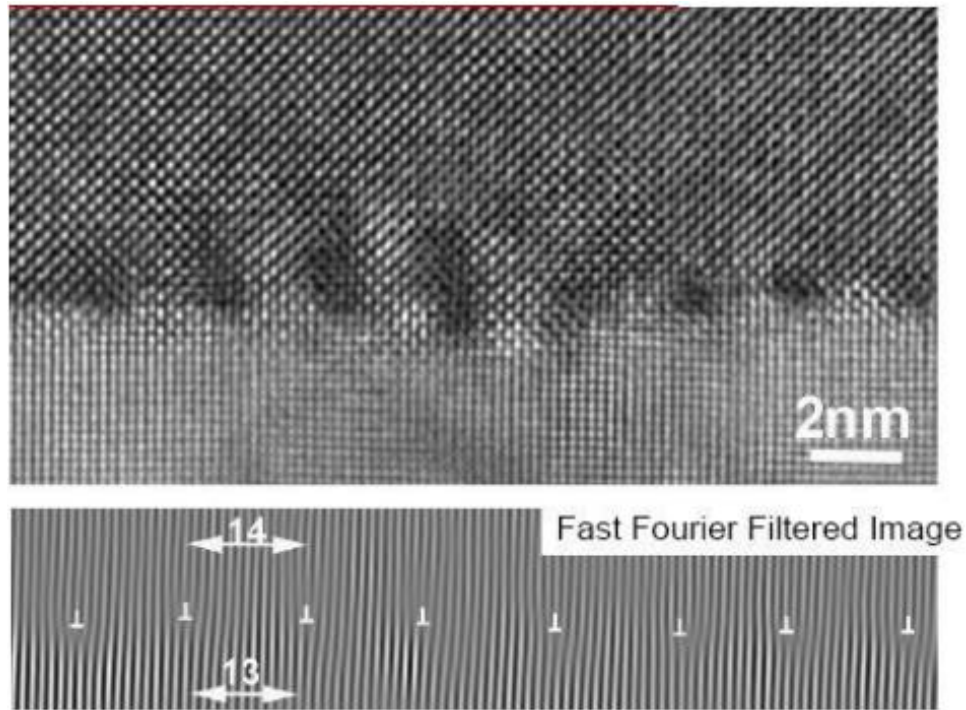
Figure 1.4 HRTEM and fast Fourier filtered images of domain matching epitaxy of SrTiO$_3$ thin film grown on MgO substrate with a 14/13 matching.[12]

1.1.3.3 Thin film growth modes

There are three major thin film growth modes: (1) Frank-Van der Merwe or layer-by-layer growth, (2) Volmer-Weber or island growth, and (3) Stranski-Krastanov growth. It was reported by Bauer that relative surface energies play an important role in determining which growth mode occurs at the thermodynamic equilibrium.[13] When the extension of the smallest nucleus occurs in two dimensions and results in the formation of planar sheets, the layer-by-layer growth dominates the film growth. For this growth mode,

the atoms are more strongly bonded to the substrates but not to each other. Usually semiconductors and oxides grown by this mode. When the atoms deposited onto the substrate are more strongly bonded to each than to the substrate, Volmer-Weber or island growth occurs. This island growth mode usually happens when the film and substrate are dissimilar materials. This is often the case when metals or semiconductors are grown on oxide substrates. Stranski-Krastanov growth mode is a combination of layer-by-layer and island growth. For this growth mode, one or more monolayers are formed first and then island growth will dominate the film growth because the layer-by-layer growth becomes energetically unfavorable.

1.2 Functionalities of oxide thin films

Functional oxide thin films represent a large family of materials with varieties of crystal structures and abundant physical properties. Oxide thin films have received ever increasing attention both from scientific and technological points of view. Various interesting physical phenomenon have been discovered in functional oxide thin films including ferroelectricity, ferromagnetism, and multiferroicity.

1.2.1 Ferroelectricity

Ferroelectricity is a physical property of the materials that have noncentrosymmetric crystal structures and spontaneous electric polarizations which can be reversed by applying an external electric field. The ferroelectric polarization only

occurs in noncentrosymmetric materials which lack a center of symmetry leading to the shift in the relative positions of anions and cations and thus formation of electrical dipoles.

The ferroelectric response of a material is characterized by the ferroelectric hysteresis loop as shown in Figure 1.5.[14] For a typical ferroelectric hysteresis loop, several important parameters are considered when evaluating a ferroelectric material. P_s is the saturation polarization which refers to the total dipole moment per unit volume of a poled ferroelectric material. Its value does not increase with the increase of the electric field. P_r refers to the remanent polarization retained in the ferroelectrics when the electric field is removed. E_c is the coercive field which is required to reverse the polarization to zero. E_s means the switching field required for the complete reversal of polarization.
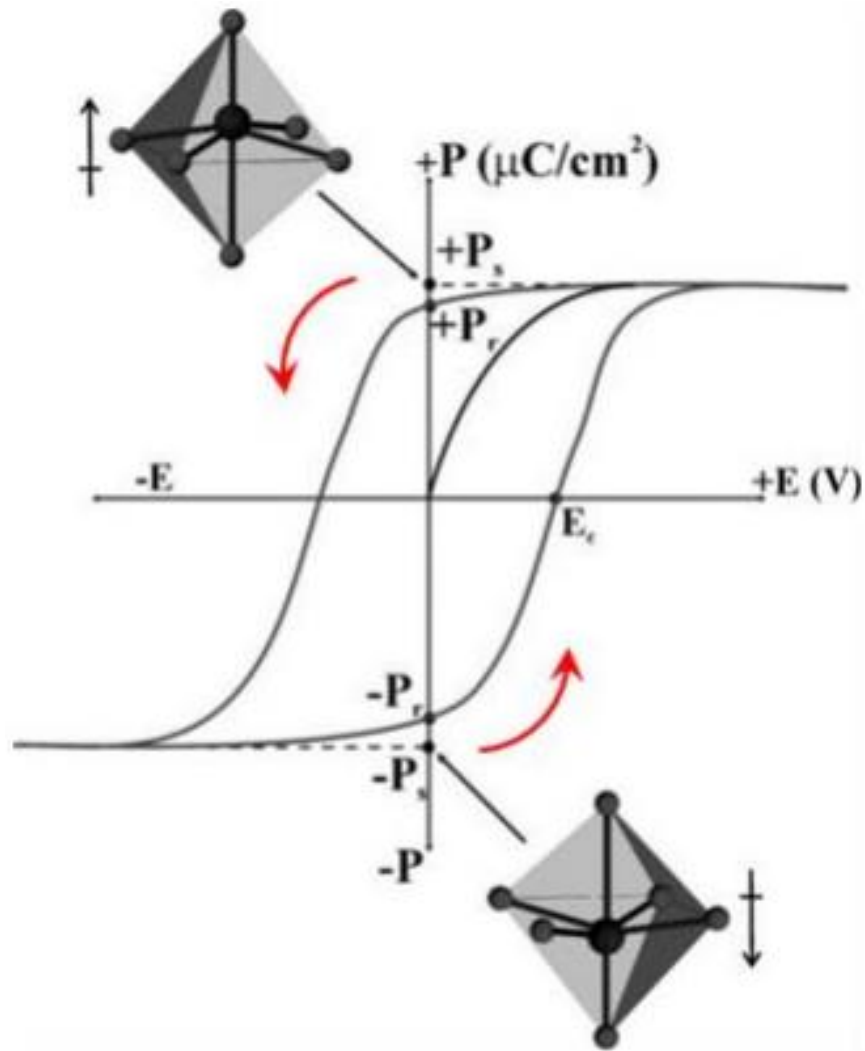
Figure 1.5 Ferroelectric polarization-electric field hysteresis loop corresponding to two lattice distortions, polarization up and polarization down.[14]

For a ferroelectric material, its dipoles are randomly oriented in the virgin state and the net polarization is zero. With the application of an external electric field, the dipoles are forced to orient in a parallel manner to each other. However, this happens only under a certain temperature which is called Curie temperature (T_C). Above the Curie temperature, the electric polarization will disappear because the thermal motion will

cancel the individual electron spins. Across the Curie temperature, a phase transformation

occurs and above the Curie temperature the crystal structure will be centrosymmetric (also

called paraelectric phase) while below the Curie temperature it is ferroelectric phase. The

ferroelectric phase always has a lower symmetry than the paraelectric phase as shown by

the case of $BaTiO_3$ (Figure 1.6). $BaTiO_3$ transforms from the centrosymmetric cubic phase

to the low symmetric tetragonal phase at around 120 °C.
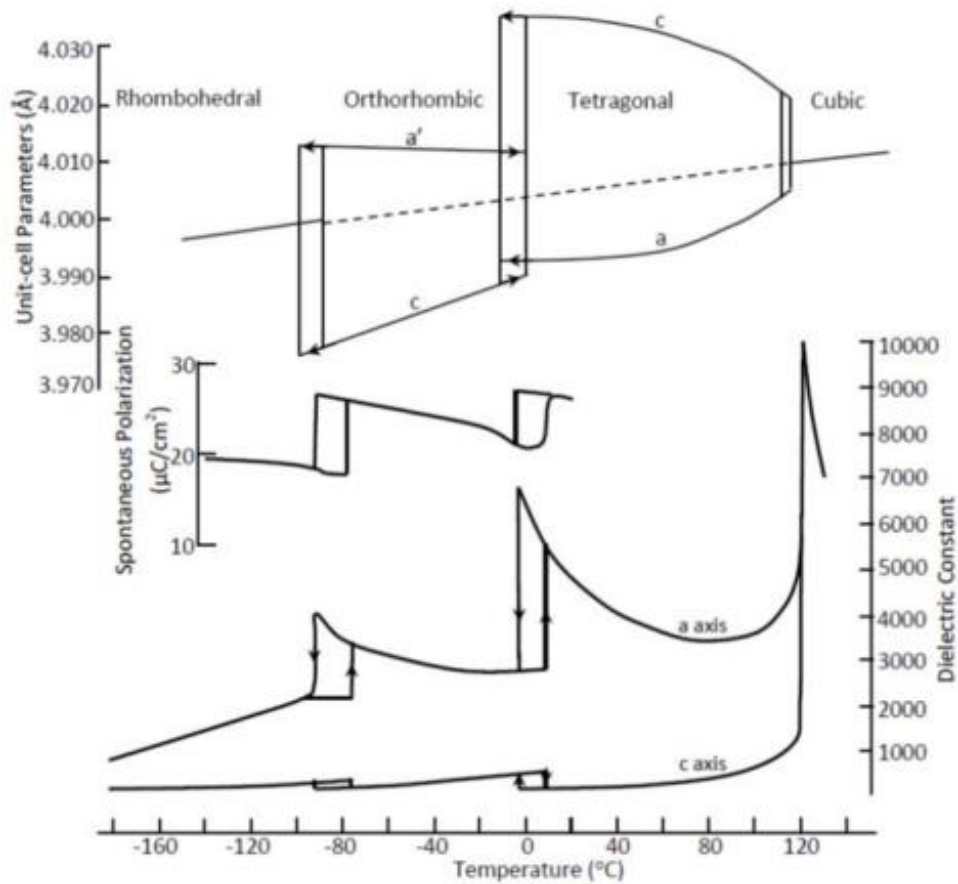
Figure 1.6 Temperature-dependent unit cell dimensions, spontaneous polarization, and dielectric constant of $BaTiO_3$.[15]

Among all the ferroelectric materials, $PbZr_xTi_{1-x}O_3$ was once extensively studied because of its good thermal stability, strong electrochemical coupling, easy poling and sintering.[16, 17] However, more attentions have been drawn to other alternative ferroelectric materials which do not contain the toxic Pb with the increase of environmental consciousness. $BaTiO_3$ is the first perovskite that was discovered to possess ferroelectricity and the first ceramic that was implanted in a piezoelectric transducer.[18] $BaTiO_3$ is very stable but its applications are severely limited by the low T_C of around 120 ^{o}C. Dopants called T_C shifters like $SrTiO_3$, $PbTiO_3$, and $CaZrO_3$ are incorporated to increase or decrease the T_C. Stoichiometry is very critical in controlling the ferroelectric response of $BaTiO_3$ because the composition directly determines the unit cell structure and therefore the physical and chemical properties. It was reported that the laser fluence and oxygen partial pressure could both influence the Ba/Ti ratio in the $BaTiO_3$ thin films and therefore the ferroelectric properties (Figure 1.7).[19, 20, 21] Another ferroelectric material that is extensively studied is $BiFeO_3$ with a theoretical ferroelectric polarization value of more than 100 $\mu C/cm^2$ and a high T_C value of 830 ^{o}C. $BiFeO_3$ will be discussed in more detail in the following section.
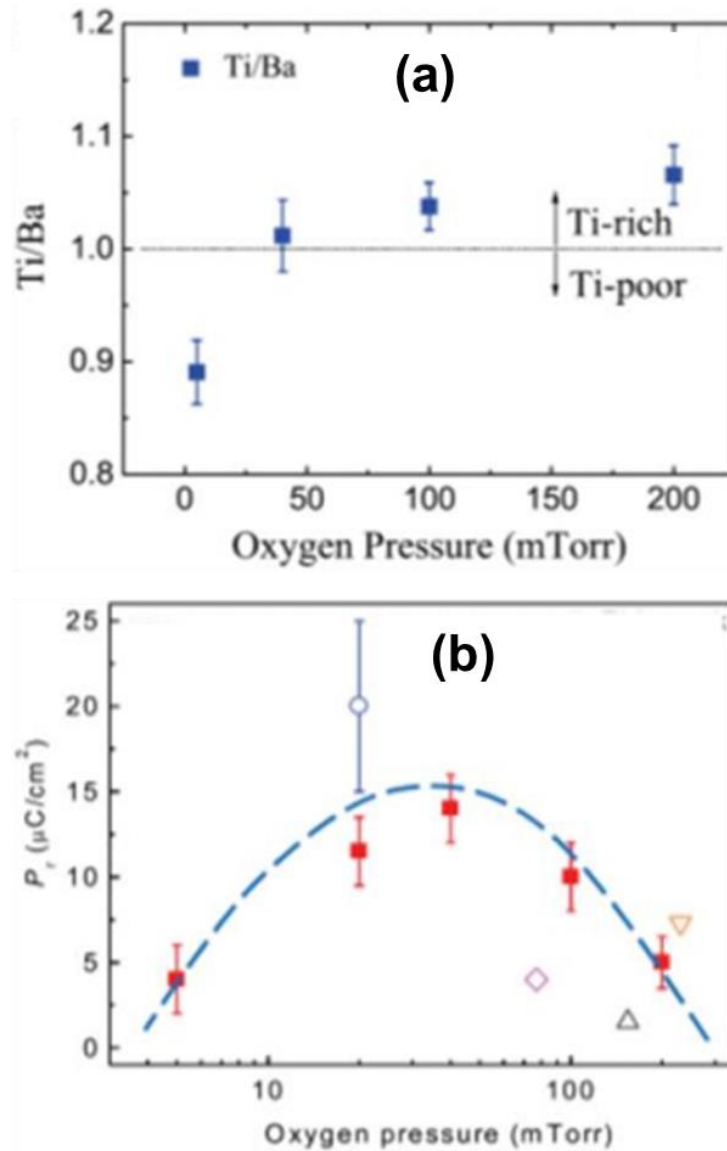
Figure 1.7 Oxygen pressure dependent (a) Ti/Ba ratio and (b) Pr in BaTiO$_3$ films.[21]

1.2.2 Magnetism

1.2.2.1 Overview of magnetism

Magnetism is a physical property of a material that responds to an applied magnetic field at atomic or subatomic level. There are several kinds of magnetism depending on the orbital and spin motions of electrons and how the electrons interact with

each other.[22] With different spin alignments of the electrons, the main magnetic interactions include ferromagnetism, antiferromagnetism, ferrimagnetism, paramagnetism, superparamagnetism, and diamagnetism. For a ferromagnet, spontaneous net magnetization exists even in the absence of an external magnetic field because of the long range and parallel alignment of the atomic magnetic moments. For the ferromagnetic materials, they don't exhibit net magnetization above the Curie temperature with the atomic moments randomly oriented resulting a paramagnetic phase. For superparamagnetism, it refers to a magnetism existing in small ferromagnetic or ferromagnetic nanoparticles where the magnetization can flip the direction. The net magnetization will be measured to be zero if the time used to measure the magnetization is much longer than the time between two flips (called *Neel relaxation time*). This small nanoparticle can still be magnetized by applying a magnetic field but the magnetic susceptibility is much larger than that of paramagnets. Antiferromagnetism means that the atomic moments are aligned antiparallel. For ferrimagnetism, the spins are also aligned antiparallel, but the net magnetism is not zero because one subset of dipoles is larger than the other. Diamagnetism is a material property belonging to all materials and can be neglected if the materials show some forms of magnetism such as ferromagnetism and paramagnetism. Diamagnetic materials are usually those nonmagnetic materials including water, wood, most organic compounds, some plastics and many metals such as copper, gold, and bismuth. The magnetic susceptibility for diamagnetic materials is negative. The schematic in Figure 1.8 shows the spin alignment for different magnetism.[23]
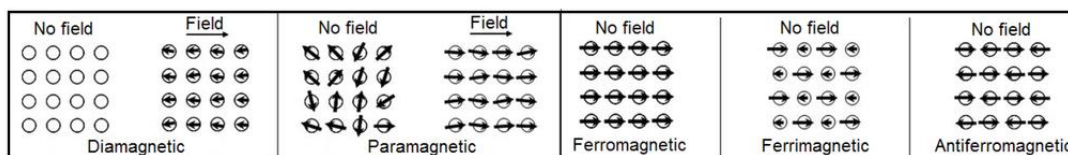
Figure 1.8 Schematic diagram showing the spin alignment for different magnetism.[23]

Several fundamental coupling mechanisms have been developed to explain how indirect exchange which is mediated through nonmagnetic ions like oxygen to give rise the effects in the oxide materials. The three main magnetic coupling model include superexchange, double exchange, and RKKY coupling as shown in Figure 1.9. Superexchange is a magnetic coupling getting its name from the fact that it extends the short-range exchange to long-range interaction which was formally developed in 1950.[24] Superexchange can well describe how antiferromagnetism occur in some ionic compounds where $3d$ and $2p$ orbitals of transition metals and oxygen/fluorine atoms interact to each other. The superexchange coupling can well describe the antiferromagnetism in $LaMnO_3$. One electron from the $2p$ orbital of oxygen is donated to the $3d$ orbital of neighboring Mn and the spins of the two nearest neighboring Mn are antiparallel leading to antiferromagnetism of $LaMnO_3$ as shown by Figure 1.9(a). Double exchange was proposed to describe the magneto-conductive properties of the mixed valence compounds (Sr or Ca doped $LaMnO_3$ on the A site). For the case of $La_{0.7}Sr_{0.3}MnO_3$ containing Mn^{3+} and Mn^{4+} the O^{2-} ion has full p-orbitals (Figure 1.9(b)). The electron on the Mn-sites jump back and forth through the oxygen and the electron is thus delocalized over the entire M-O-M group. This model can describe the ferromagnetic alignment and conductive mechanism of $La_{0.7}Sr_{0.3}MnO_3$. RKKY is used to explain the coupling in dilute magnetic

semiconductors where the magnetic ions are too far to interact with each other directly (Figure 1.9(c)). This model describes that a local moment can induce a spin polarization which oscillates in sign as a function of distance and this spin information can be carried over relatively long distances.
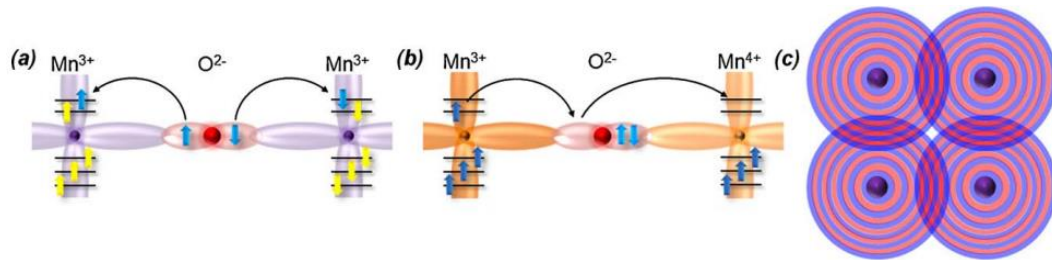
Figure 1.9 Schematic diagram showing the magnetic couplings in oxides. (a) superexchange, (b) double exchange, and (c) RKKY coupling.[8]

1.2.2.2 Magnetic ferrites

Several types of magnetic oxides have been investigated both for fundamental study and technological applications. Here two types of magnetic materials will be discussed: ferrites and manganites. Ferrites refers to the Fe-containing oxides including spinels (AFe_2O_4), garnets (AFe_5O_{12}), hexaferrites ($AFe_{12}O_{19}$), and orthoferrites ($RFeO_3$, R is one or more of the rare-earth elements). Ferrites have been used as transformer cores, microwave magnetic devices, magneto-optic data storage materials, and flux guides and sensors. Among these ferrites, spinel ferrites have been extensively investigated to create high quality thin films to enable better understanding of structure-property relationship. Ferrites have also been widely studied to create vertically aligned nanocomposites for

multiferroism.[25, 26] In this section, the epitaxial thin films of Fe_3O_4, $NiFe_2O_4$, and $CoFe_2O_4$ will be briefly reviewed.

Fe_3O_4 is an old magnetic material and has been used in the compass for navigation several thousand years ago. Band structure calculations show that the majority of the spin electrons are semiconducting and minority spins metallic.[27] Fe_3O_4 has a high Curie temperature of ~858 K and undergoes a first-order metal-insulator transition from cubic to monoclinic phase with an increase in resistivity and decrease in magnetic moment.[28, 29] It is still under debate on the fundamental mechanism of the transition. Epitaxial Fe_3O_4 thin films have been grown on MgO (001) by various techniques such as pulsed laser deposition with a temperature range of 200 and 500 ºC, yield bulk-like properties.[30, 31, 32] $NiFe_2O_4$ exhibits an insulating state because of the sizeable gap in the majority spins and a smaller one in the minority spins. Epitaxial $NiFe_2O_4$ thin films have been fabricated on various substrates including c-plane sapphire and $SrTiO_3$ (001) by pulsed laser deposition.[33, 34] Anomalous magnetic behavior including diminished magnetization has been observed for these epitaxial $NiFe_2O_4$ thin films.[35] During the study of ultrathin films of $NiFe_2O_4$ grown on $SrTiO_3$ (001) indicates an anomalous distribution of Fe and Ni cations among the A and B sites and distinctly different magnetic and electronic behaviors including enhanced magnetic moments by 250% and metallic character were observed. For $CoFe_2O_4$, the thin film form has quite different properties from its bulk form and the magnetic properties are significantly influenced by the microstructure. Various substrates including MgO (100) and $MgAl_2O_4$ (110) have been used to create $CoFe_2O_4$ films free of antiphase boundaries which allows the study of the correlation of cation distribution and

22

lattice distortion to the anomalous magnetic behavior.[36, 37] As mentioned above, the ferrimagnetic $CoFe_2O_4$ has been combined with other oxides to create the vertically aligned nanocomposites for multiferroism recently.[25, 26]

1.2.2.3 Magnetic manganites

In the past two decades, colossal magnetoresistance (CMR) materials such as doped manganites are especially attractive because of their strong couplings between lattice, charge, spin and orbital degrees of freedom. These manganese-based oxides with perovskite structure shows half-metallic characteristics and CMR response which make these manganites especially intriguing both for fundamental physics study and development of novel electronic devices.

The discovery of CMR effect in $La_{0.67}Ca_{0.33}MnO_3$ thin film has aroused the rejuvenation of research interest in manganite materials. In 1994, Jin et al. reported the thousandfold change in resistivity in the magnetoresistive $La_{0.67}Ca_{0.33}MnO_3$ thin film,[38] which is three orders of magnitude larger than that in giant magnetoresistance materials (Figure 1.10). Strain was then believed to play an important role in controlling the physical properties of the manganite thin films. The CMR effect was attributed to the mixed Mn^{3+}-Mn^{4+} valence state in $La_{0.67}Ca_{0.33}MnO_3$ thin film. The CMR in $La_{0.67}Ca_{0.33}MnO_3$ thin film requires a large magnetic field which limits its application. Recently, another magnetic transport effect called low-field (< 0.1 T) magnetoresistance has been reported for $La_{0.7}Sr_{0.3}MnO_3$ thin films. Grain boundary was considered to play a predominant role. Chen et al. reported the enhanced low-field magnetoresistance in vertically aligned

nanocomposites created from the combination of $La_{0.7}Sr_{0.3}MnO_3$ and other insulating oxides such as ZnO and CeO_2.[39, 40, 41, 42, 43]
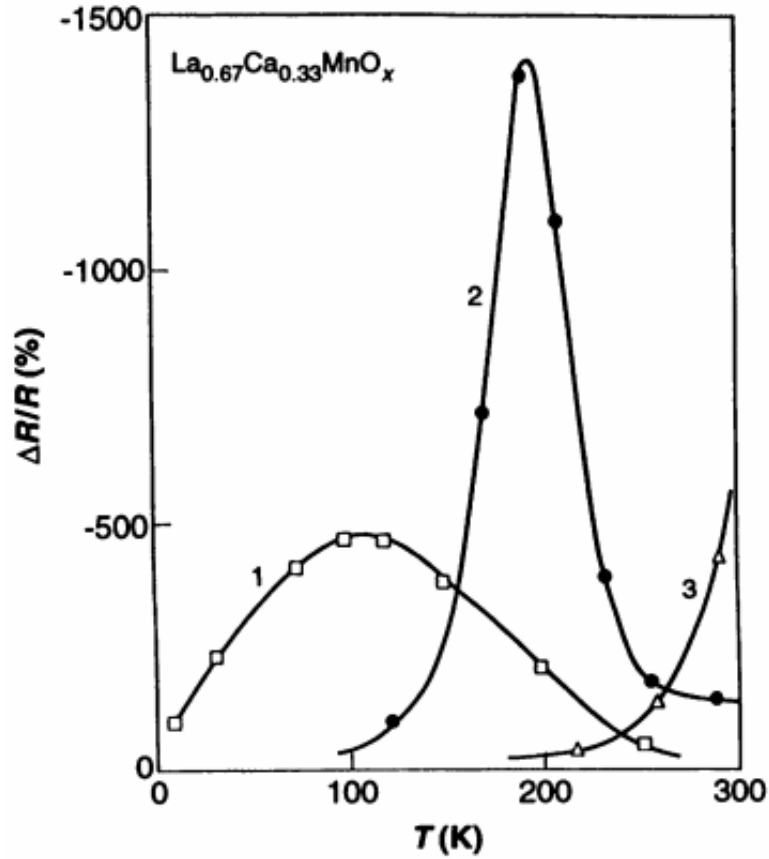
Figure 1.10 Magnetoresistance ratio (ΔR/RH) versus temperature curves for the La-Ca-Mn-O films treated under different conditions: curve 1, as deposited; curve 2, annealing at 700 ^{o}C in O_2 for 30 min; curve 3, annealing at 900 ^{o}C in O_2 for 3 hours.[38]

1.2.3 Multiferroism

1.2.3.1 Overview of multiferroism

Multiferroics refers to a class of materials where at least two primary ferroic orderings coexist in a single material.[44, 45, 46] There are four primary ferroic orderings including ferromagnetism, ferroelectricity, ferroelasticity, and ferrotoroidicity.

24

Nowadays, the definition of multiferroics has been expanded and non-primary ferroic orderings are also included such as antiferromagnetism and ferrimagnetism. Ferromagnetism is a phenomenon that a material shows spontaneous magnetization which can be switched by an applied magnetic field. Ferroelectricity is a material property that a material have spontaneous electric polarization and its direction can be reversed by applying an external electric field. Ferroelasticity refers to that a material may have strain due to the externally applied stress. Ferrotoroidicity means a phase transition to spontaneous long-range order of microscopic magnetic toroidal moments but ferrotoroidicity is still under debate because no clear evidence has yet been presented. Among the four primary ferroic orderings, ferroelectricity and ferromagnetism could be coupled to produce the magnetoelectric effect and has received a lot of attention both from the fundamental physics and technological point of view.[45, 47] Hereafter, multiferroicity refers specifically to the coexistence of (ferro)magnetism and ferroelectricity as shown by the schematic in Figure 1.11. The magnetoelectric effect was first proposed by Curie in 1894 and confirmed by the work on Cr_2O_3 in 1960s.[48] Taking the advantages of magnetoelectric materials, a wide range of devices with different applications have been proposed, including devices for magnetoelectric data storage and switching, optical diodes, spin-wave generation, amplification, and frequency conversion.
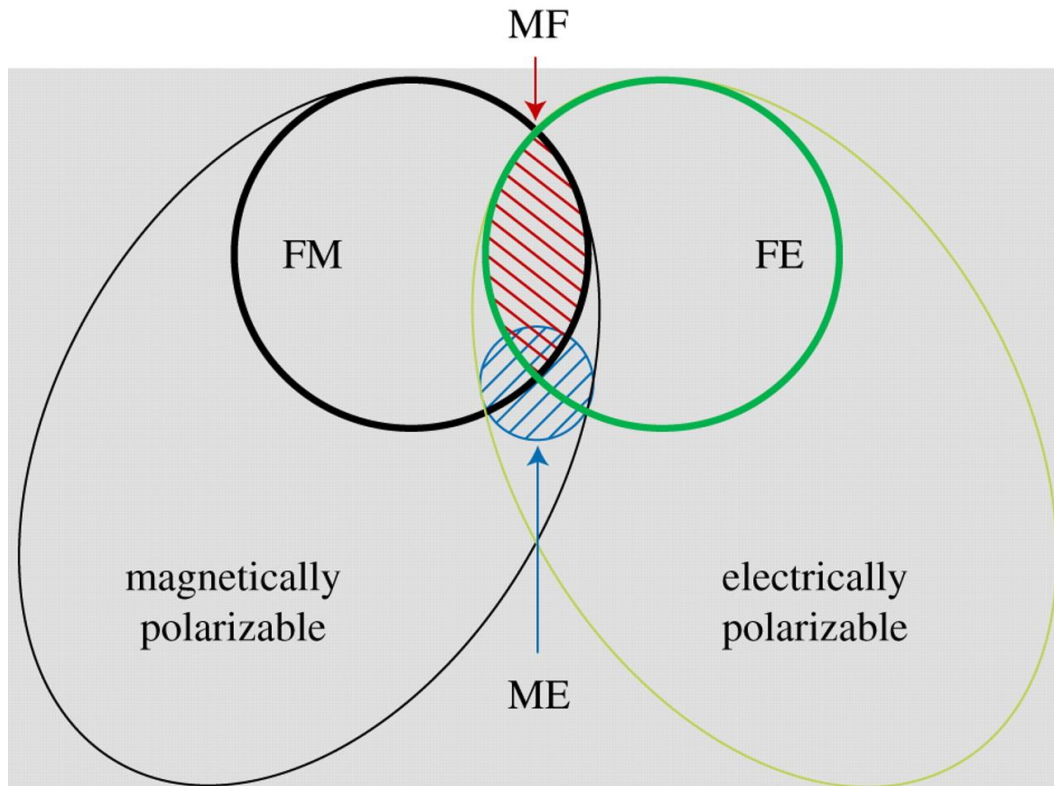
Figure 1.11 A schematic showing the relationship between ferroelectricity, magnetism, and multiferroism.[49]

1.2.3.2 Pathways to multiferroism

Multiferroic materials exhibit great potentials in ferroelectric random access memory, magnetic data storage, multiple state memories, etc. $Ni_3Bi_7O_{13}I$ is believed to be the earliest multiferroic material which was reported in 1960s.[50] With the development of high-quality thin film growth techniques and extensive research on multiferroic materials, different kinds of multiferroics have been discovered or created. From the fundamental mechanism and geometry, the thin film multiferroic materials can be classified into three categories: single-phase epitaxial thin films, horizontal multilayered heterostructures, and vertically aligned heterostructures as shown in Figure 1.12.
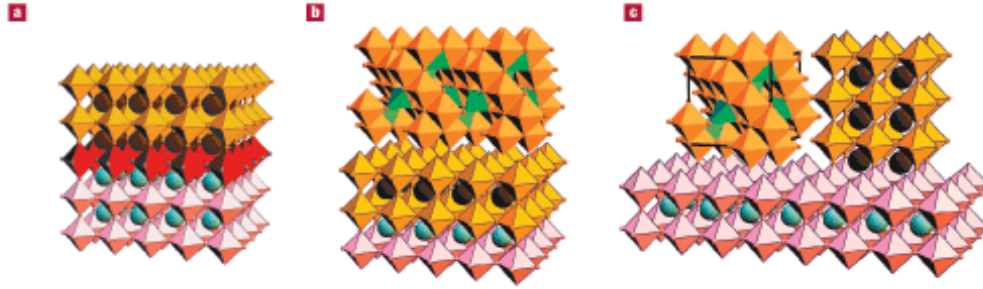
Figure 1.12 Schematic diagrams showing the three types of multiferroic materials: (a) single-phase epitaxial thin films, (b) horizontal multilayered heterostructures, and (c) vertically aligned heterostructures.[44]

Horizontal multilayered multiferroic heterostructures is created by atomic level layering to engineer specific magnetic ordering and the compositional ordering leads to polarizations. The multilayered heterostructures include $CaTiO_3/BaTiO_3/SrTiO_3$, Co-doped TiO_2/PZT, $Fe/BaTiO_3$, etc.[51, 52, 53] Vertically aligned heterostructures for multiferroism have been fabricated by nanostructured columnar growth of oxide-oxide by careful selection considering lattice matching, immiscibility and different elastic modulus. $BaTiO_3:CoFe_2O_4$ is one of the typical vertically aligned heterostructures created by the alternating columnar growth of $BaTiO_3$ and $CoFe_2O_4$.[25, 26, 54] This kind of heterostructure with large interface/volume ratio removes the clamping effect from the substrate and could allow better strain induced couplings. Many other vertically aligned nanostructures have been created for the creation of multiferroics including $BiFeO_3-CoFe_2O_4$,[55] and $BaTiO_3-NiFe_2O_4$.[56]

Compared to the heterostructures mentioned above, single-phase multiferroic thin films are more intriguing with rich physical phenomena behind and could allow the fundamental mechanism study. The single-phase multiferroics can be classified into four

groups based on the mechanism of creating ferroelectricity. The first group is the lone-pair multiferroics which usually have the perovskite structure of the form ABO_3, such as $BiFeO_3$,[7] $BiMnO_3$,[57] and $PbVO_3$.[58] The ferroelectricity comes from the stereochemical activity of the lone pair on the *A*-site cation while the smaller B-site cation provides the magnetism. $BiFeO_3$ and $BiMnO_3$ are two of the most important lone-pair multiferroic materials and will be discussed in detail in the following sections.

The second group is the geometrically driven ferroelectricity which is compatible with the coexistence of magnetism. $YMnO_3$[59, 60] and $BaMF_4$ (M = Fe, Co, Ni)[61, 62] belong to this group. $YMnO_3$ is the earliest hexagonal manganite which was investigated for multiferroism (Figure 1.13). The long range dipole-dipole interactions and oxygen rotations lead to the ferroelectricity and antiferromagnetism. The first epitaxial films of $YMnO_3$ with hexagonal structure was grown by magnetron sputtering on MgO (111) and ZnO (0001)/sapphire (0001).[63] Later on, it was found that metastable, non-ferroelectric $YMnO_3$ thin films with orthorhombic structure can be obtained on appropriate substrates such as $SrTiO_3$ (001) and $NdGaO_3$ (101) owing to the epitaxial strain.[59] This is the first evidence that strain can be utilized to tune the crystal structure of $YMnO_3$ between hexagonal and orthorhombic phases.
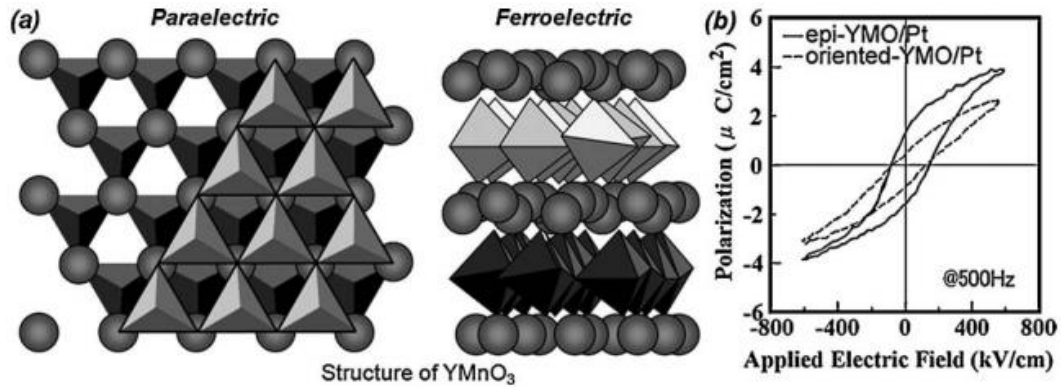
Figure 1.13 (a) Crystal structures of $YMnO_3$ with paraelectric and ferroelectric phases. (b) polarization-electric field hysteresis of the epitaxial-$YMnO_3$/Pt and the oriented-$YMnO_3$/Pt.[64]

Third, certain non-centrosymmetric charge-ordering can also lead to ferroelectricity in some magnetic materials, like $LuFe_2O_4$.[65, 66] $LuFe_2O_4$ belongs to the family of RFe_2O_4 (R is rare-earth elements) and the crystal structure consists of alternating stacking of triangular lattices of rare-earth elements, iron and oxygen as shown in Figure 1.14. The mixed-valence $LuFe_2O_4$ consists of the same amount of Fe^{2+} and Fe^{3+} at the same site in the triangular lattice. $LuFe_2O_4$ is believed to be a charge-frustrated system of triangular lattices. The postulated charge structure allows the presence of a local electrical polarization indicating the possibility of ferroelectricity. Also, the magnetic ordering around 250 K gives a small net moment. Finally, a new mechanism for inducing ferroelectricity was identified in $TbMnO_3$,[67] and $TbMn_2O_5$,[68] where the ferroelectricity is resulted from a symmetry-lowering magnetic ground state that lacks inversion symmetry.
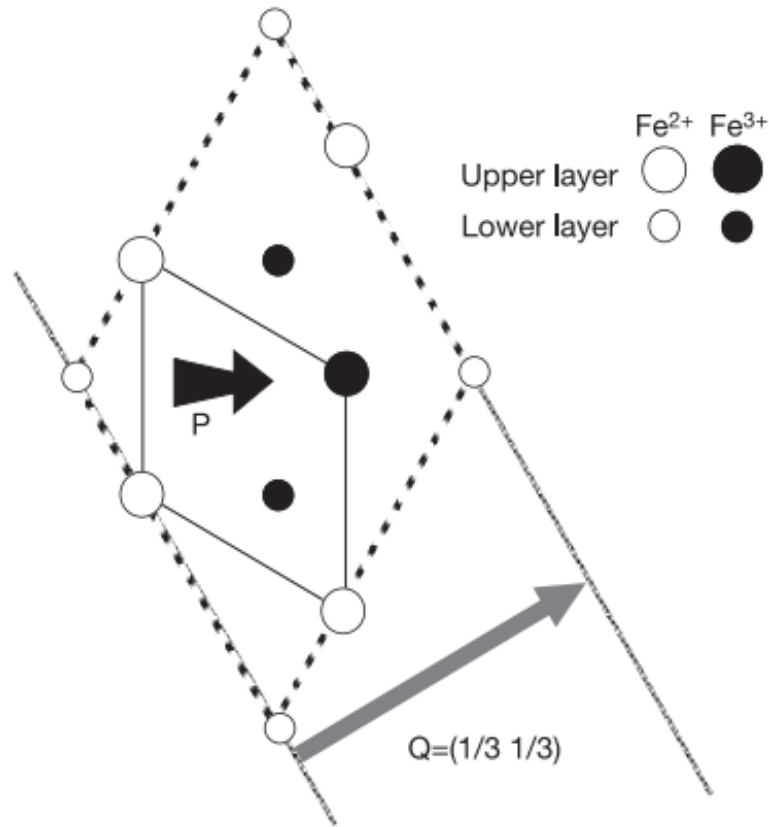
Figure 1.14 The charge-ordering model for RFe_2O_4 showing the double iron layer.[66]

1.3 Bismuth-based perovskites for multiferroism

1.3.1 Overview of perovskites

Despite the existence of the above mentioned single-phase multiferroics, single-phase multiferroics are still scarce owing to the drastically different orbital requirements for ferroelectricity (requiring empty d-orbital) and ferromagnetism (coming from partially filled d-orbitals) as mentioned above. Even for the current single-phase multiferroic materials, they suffer from different kinds of disadvantages which prevents the practical applications. For instance, although $BiFeO_3$ shows a polarization as high as 100 $\mu C/cm^2$, its room temperature magnetization coming from the canting spin is very weak and the

strong antiferromagnetism is not convenient for practical applications. However, Bi-based perovskites with the Bi $6s^2$ lone pair giving rise to ferroelectricity and magnetic cations provide people important clues of designing new multiferroic materials. In the following several sections, several important Bi-based perovskites including Bi-based single-perovskites and double-perovskites will be reviewed which may provide people some hints to design new materials for multifunctionalities.

In this section, the perovskite structures are reviewed first. The perovskites are a group of materials named after calcium titanium oxide ($CaTiO_3$), known as perovskite structure. The perovskite structure can be represented by the chemical formula ABO_3 where A and B are cations. The ideal cubic-symmetry perovskite structure has B cations in 6-fold coordination and A cations in 12-fold coordination. B cations are surrounded by 6 first-neighbor oxygen anions forming BO_6 octahedron and A cations are surrounded by 12 oxygen anions forming cuboctahedron. The perovskite structure can be viewed as alternating stacking of BO_2 and AO atomic planes along any of the orthogonal directions.

The stability of perovskite structure can be evaluated by the Goldschmidt tolerance factor t which is defined as below.

$$t = \frac{r_A + r_O}{\sqrt{2}(r_B + r_O)} \quad (1\text{-}3)$$

where r_A, r_B, and r_O are the ionic radius of cation A, cation B, and oxygen anion, respectively. The tolerance factor t can directly affect the crystal structure of the perovskites. When $t = 1$, the perovskites has ideal cubic structure and $SrTiO_3$ is one typical example ($r_A = 1.44$ Å, $r_B = 0.605$ Å, and $r_O = 1.40$ Å). When t deviates from 1, it will lead to structure distortion which is compensated by the rotation of BO_6 octahedron. To keep

a cubic perovskite structure the tolerance factor is usually in the range of $0.9 < t < 1.0$. When $t < 1$, it means that A cation has smaller ionic radius than cation B. Typically, orthorhombic or rhombohedral structures are formed to achieve a close packaging of the ions with the BO_6 octahedron tilted. One example is the orthorhombic $GdFeO_3$ with a tolerance factor of 0.81. When $t > 1$, it means that the A cation is much larger than B cation and it is not possible to accommodate A cation in the cubic perovskite. In this case, different hexagonal polymorphs become stable.

For bismuth-based perovskites, the ferroelectricity comes from the stereochemically active Bi^{3+} $6s^2$ lone pair electrons which always locates at the A-site. Bi^{3+} has an electron configuration of $[Xe]4f^{14}5d^{10}6s^26p^0$ with two outer $6s$ orbital electrons called lone pairs. The two outer electrons do not participate in chemical bonds and are nearly spherically distributed. Due to the Coulombian electrostatic repulsion, the lone pairs shift away the centrosymmetric position when surrounded by the oxygen anions. A lobe-like distribution of the electrons is then formed. Thus the lone pairs form an electric dipole which breaks the spatial inversion symmetry and becomes the driving force for the ferroelectric response in all Bi-based compounds.

For the B-site magnetic cations, they are interrupted by the oxygen anions and the magnetic interactions are mediated by the adjacent oxygen ions through the superexchange interaction. Pauli's exclusion principle states that two electrons in the same orbital must possess antiparallel spins and Hund's rule states that the d orbital electrons minimize their energy in a parallel spin alignment. The magnetic nature depends largely on the filling of e_g orbitals according to Goodenough-Kanamori's (GK) rules. Figure 1.15

demonstrates several the magnetic interactions giving rise to antiferromagnetism or ferromagnetism depending on the e_g orbital filling. These magnetic interactions are for the simplest scenario where the B-O-B bond angle is 180°. Different B-O-B bond angles, distorted perovskites, and rotation of oxygen octahedron may lead to different magnetic interactions. Usually $BiBO_3$ perovskites ($BiMnO_3$ is an exception) are antiferromagnetic caused by the same oxidation states, i.e. have the same e_g orbital filling. For double perovskites it is possible to achieve ferromagnetism by appropriately choosing B (empty e_g orbitals) and B' (half-filled e_g orbitals). Even if antiferromagnetic interaction dominates in a double perovskite, ferrimagnetism is likely to occur because each cation possesses different magnetic moments producing a net magnetization.
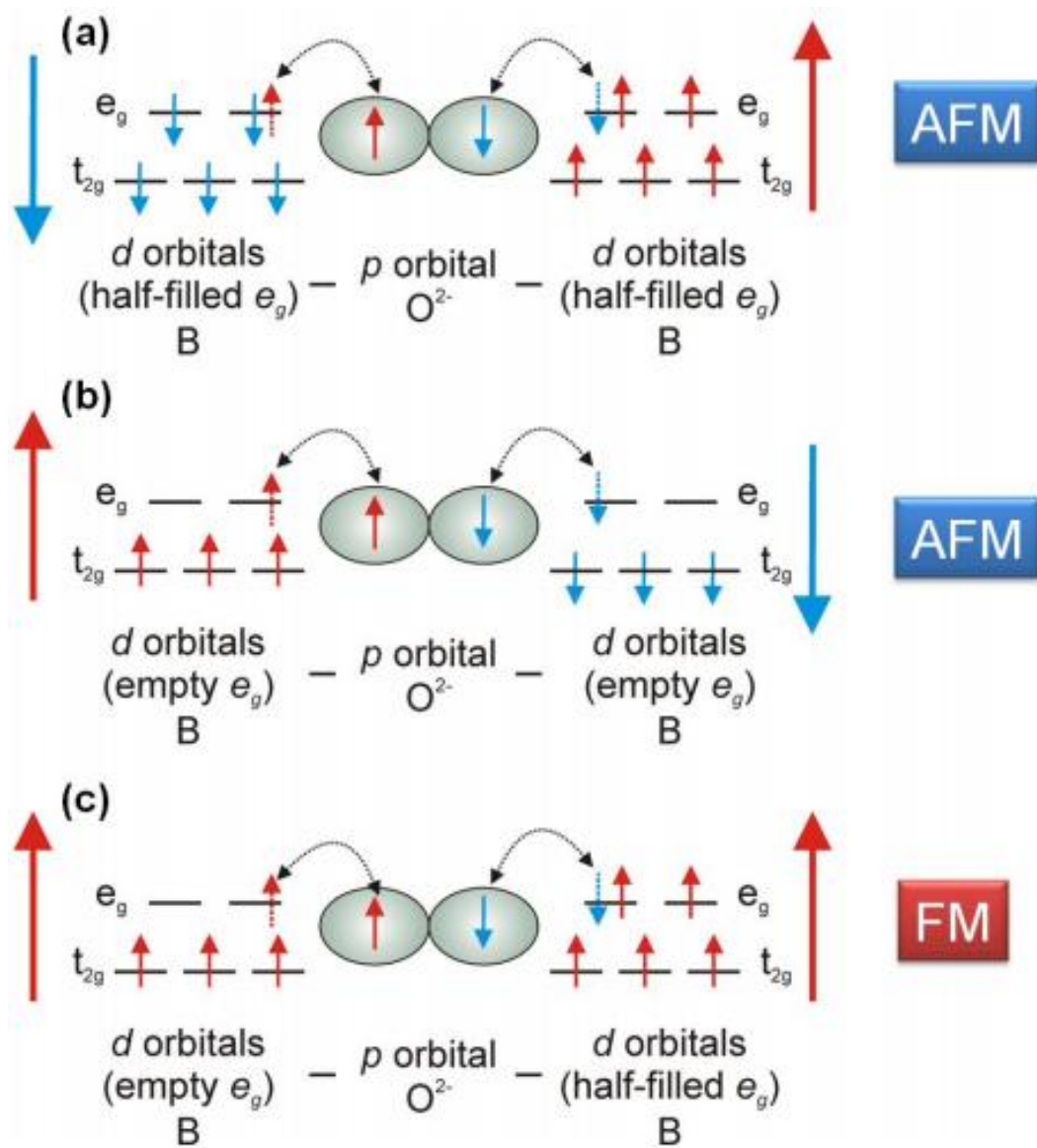
Figure 1.15 A schematic showing the superexchange interaction in ABO_3 perovskite with 180° B-O-B bond angle. The magnetic interaction can be either antiferromagnetic (a, b) or ferromagnetic (c) depending on the occupation of e_g orbitals.[69]

1.3.2 BiFeO₃

1.3.2.1 Overview of BiFeO₃

BiFeO₃ (BFO) has received the most attention as a famous single-phase multiferroic material since its discovery. BFO was first produced in the late 1950s and many efforts were spent to understand its fundamental crystal structure and physical properties since then. Bulk BFO at room temperature has a rhombohedral structure belonging to the space group of $R3c$ while thin film BFO shows a monoclinic crystal structure.[8] Studies show that BFO is a G-type antiferromagnet (Figure 1.16) with a Néel temperature of ~673 K. Owing to the spin canting of the antiferromagnetic moments, BFO also shows weak ferromagnetism at room temperature (~0.05 μ_B per unit cell). The Curie temperature for the ferroelectricity is ~1100 K and theoretical calculations indicate a polarization value of 90-100 μC/cm^2 which is consistent with the experimental measurement.[7] The details of the physical properties will be discussed in the following sections.
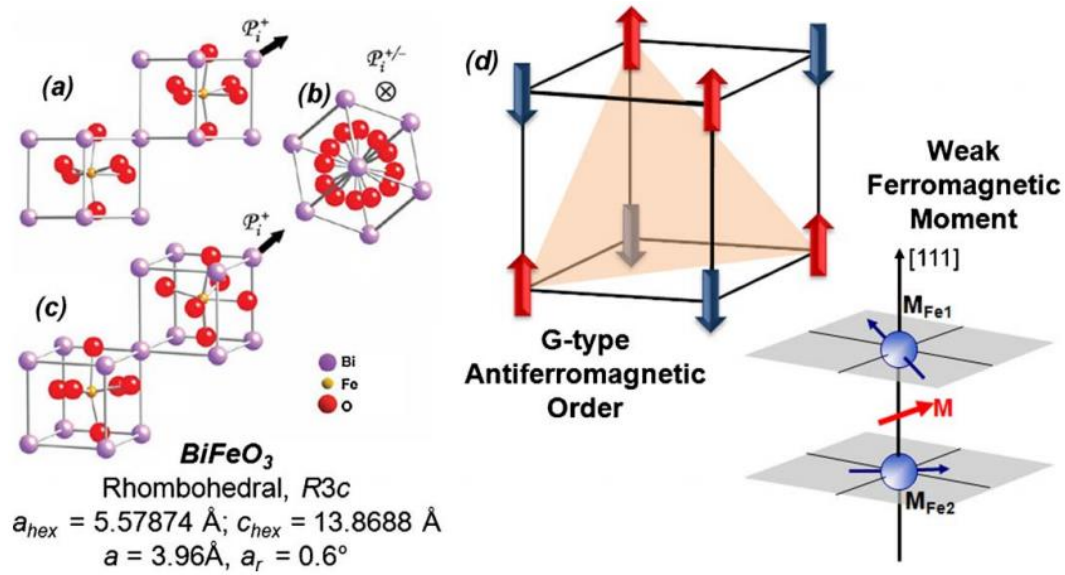
Figure 1.16 Crystal structure of $BiFeO_3$ from different orientations: (a) pseudocubic-[110], (b) pseudocubic-[111], and (c) a general three dimensional view of the structure. (d) The magnetic structure of $BiFeO_3$.[70]

1.3.2.2 Ferroelectricity in BiFeO₃

Much efforts have been made to elucidate the structural and physical properties of BFO throughout the 1960s and 1970s, including the ferroelectric nature. There was once doubt about whether BFO is a ferroelectric material until the ferroelectric measurements for BFO at 77 K was made in 1970.[71] A polarization value of ~6.1 $\mu C/cm^2$ was observed for BFO along the <111> direction which was consistent with the rhombohedral polar space group $R3c$. This finding was further confirmed in 1980 by the characterization of ferroelectric/ferroelastic monodomain single crystal samples of BFO. Later on, the chemical etching experiments proved that the ferroelectric/ferroelastic phase was stable between 4 and ~1103 K.[72] The ferroelectric polarization of BFO is achieved by the displacement of Bi ions relative to the FeO_6 octahedra. Theoretical calculations

demonstrate a polarization value of 90-100 μC/cm^2 and a paper in 2003 has aroused the rejuvenation of research interest in BFO.[7] Since the report of high ferroelectric polarization in 2003, much efforts have been made to investigate BFO to explore its fundamental physics and potential applications.

Domain structure in ferroelectrics is the result of minimizing elastic and electrostatic energy and plays an important role in influencing the physical properties of the ferroelectric materials. Much advances have been made in controlling the ferroelectric domain structures through the use of thin film epitaxy. Phase field simulations have shown that strain affects the polarization variants and can be used to predict the domain structure of BFO thin films.[73] These theoretical studies show that the domain structure of BFO can be controlled by selecting proper film orientations (by selecting the substrate types) and strain constraints. Chu et al. have done a lot work to control the domain structure of BFO by selecting proper substrates which confirms the theoretical prediction. In 2006, Chu et al. created one-dimensional nanoscale arrays of domain walls in BFO thin films taking advantage of the close lattice matching of $BiFeO_3$, $SrRuO_3$, $DyScO_3$ and the anisotropic in-plane lattice parameters of $DyScO_3$.[74] The buffer layer of $SrRuO_3$ plays an important role in determining the final domain structures of the BFO thin films which results in ferroelectric domain structure with 4-polarization and 2-polarization variants. The stripe-like domain structures of BFO predicted by phase field simulations were confirmed by experiment (Figure 1.17). These BFO thin films have shown excellent ferroelectric response with room temperature remanent polarization of ~65 μC/cm^2.[75] Later on in 2007,

the same authors showed the ability of controlling the domain structures of BFO thin films

by selecting the substrate orientations of $SrTiO_3$ ((001), (110), and (111)).[76]
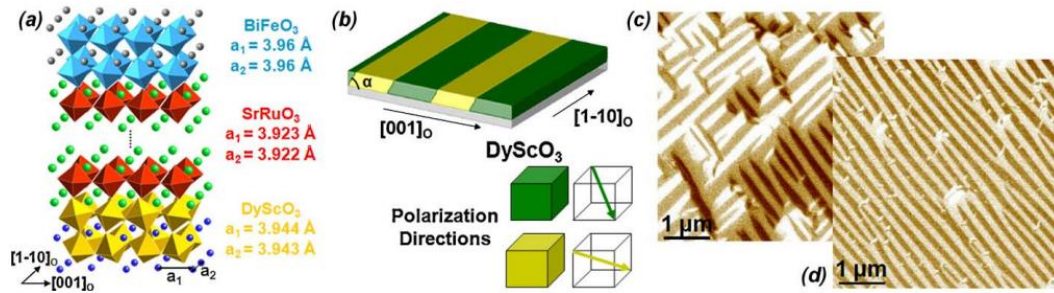
Figure 1.17 (a) Schematic diagrams showing the heterostructures of $BiFeO_3/SrRuO_3/DyScO_3$. (b) Domain structure of BFO thin film predicted by phase field simulations. The in-plane PFM images of domain structures in BFO thin films showing (c) 4-polarization variants (left), and 2-polarization variants (right).[74]

A problem with BFO as a ferroelectric material is that the leakage current is large

which is caused by defects and non-stoichiometric compositions. Element doping (both at

A-site and B-site) has been used to reduce the leakage current in order to improve the

ferroelectricity and piezoelectricity of BFO. Doing of Ti^{4+} and Cr has been proved to

increase the resistivity and doping Ni^{2+} can decrease the resistivity.[77] Different from the

aforementioned doping, Yang et al. observed large physical property change by doping

Ca in BFO.[78] An electronic conductor-insulator transition in Ca-doped BFO was observed

by controlling of band-filling. A new pseudo-tetragonal phase is formed around a Ca

concentration of 1/8 (Figure 1.18(a)). Upon the application of an electric field the doped

BFO can become conductive and this effect can be reversibly controlled by

applying/removing the electric field as shown by Figure 1.18(b) and (c). This modulation

of conduction is attributed to the naturally produced oxygen vacancies acting as donor impurities to compensate Ca acceptors and to maintain the highly stable Fe^{3+} valence state.
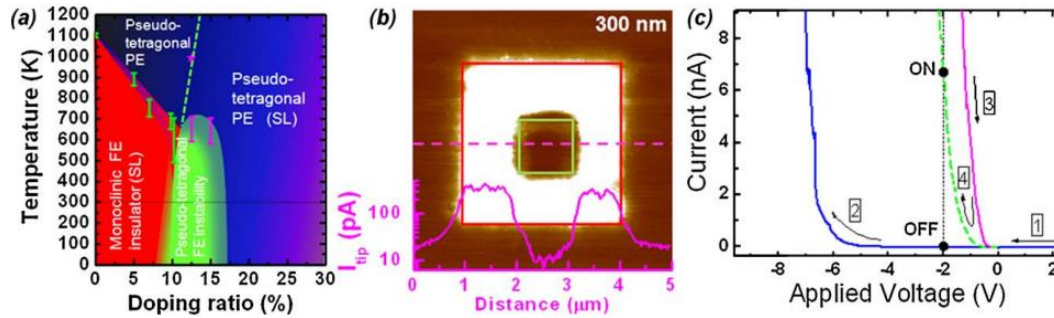
Figure 1.18 (a) A pseudo-phase diagram demonstrating the structural and property evolution of Ca-doped $BiFeO_3$. (b) Conducting-atomic force microscopy image showing an electrically poled and re-poled area of the doped $BiFeO_3$ film. (c) Illustration of the process of creating a multi-state memory.[8, 78]

1.3.2.3 Multiferroism and magnetoelectric coupling in BiFeO₃

As aforementioned, BFO is a G-type antiferromagnet with weak ferromagnetism caused by the spin canting of the antiferromagnetic moments.[79] The paper in 2003 spawned a hailstorm of research into BFO thin film which showed enhanced electric polarization and ferromagnetism (Figure 1.19).[7] Although there is still debate about its ferromagnetism, BFO has been extensively studied for its multiferroism and magnetoelectric effect.
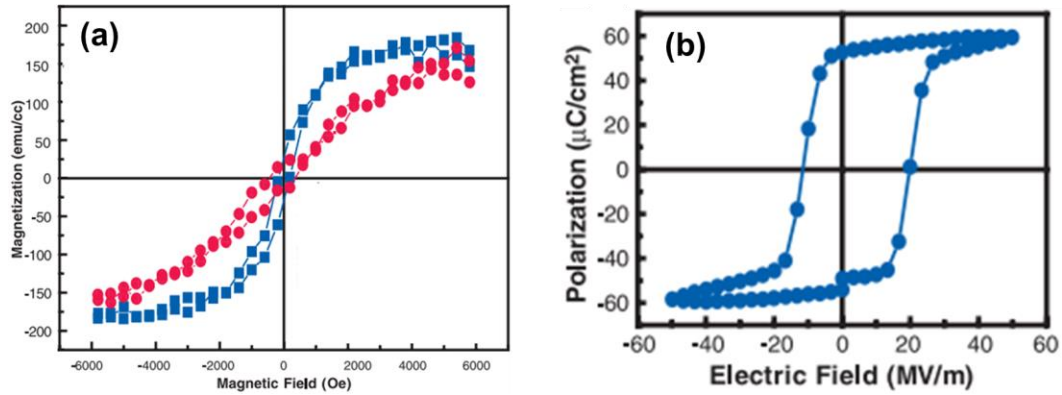
Figure 1.19 (a) Magnetic hysteresis loops of a 70 nm BFO thin film (blue: in-plane, red: out-of-plane). (b) Ferroelectric hysteresis loop of BFO thin film.[7]

Magnetoelectric effect refers to the coupling between ferroelectric and magnetic orders where the electric polarization can be induced by applying an external magnetic field or the magnetization can be induced by applying an electric field. The magnetoelectric coupling in BFO was already anticipated and the first direct evidence was reported by Zhao et al. in 2006.[45] The authors observed the direct changes of the antiferromagnetic domain structure in BFO by applying an electric field. The X-ray photoemission electron microscopy images in Figure 1.20(a) and (b) clearly show the antiferromagnetic domain changes before and after poling, respectively. The piezoelectric force microscopy images in Figure 1.20(c) and (d) together with the superposition of in-plane PFM scans shown in (c) and (d) demonstrate the ferroelectric domain changes.
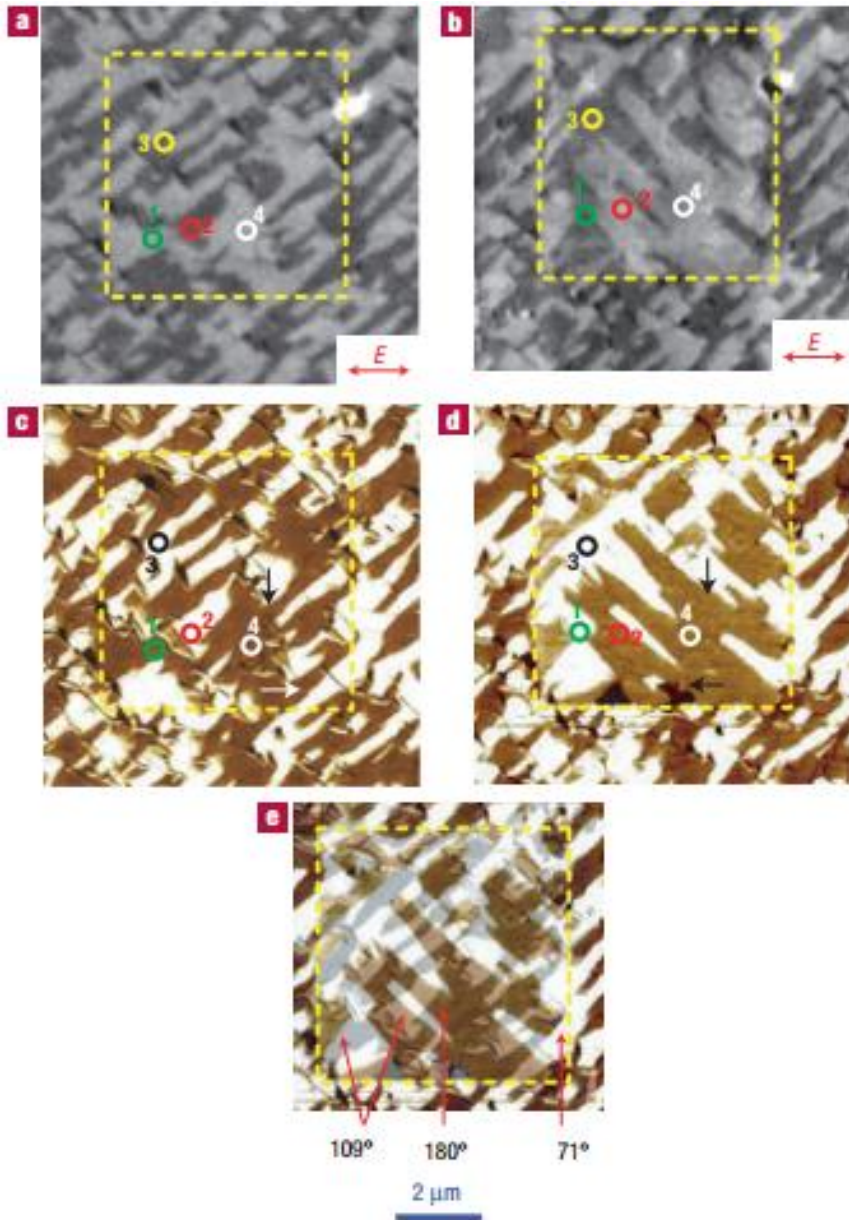
Figure 1.20 X-ray photoemission electron microscopy images before (a) and after (b) poling. In-plane piezoelectric force microscopy (PFM) images before (c) and after (d) poling. (e) A superposition of in-plane PFM scans shown in (c) and (d) used to identify the different switching mechanisms that appear with different colors and are labeled in the figure.[45]

1.3.3 BiMnO₃

1.3.3.1 Overview of BiMnO₃

BiMnO₃ (BMO) is also one of the most promising multiferroics. The crystal structure of bulk BMO at room temperature is noncentrosymmetric monoclinic with space group of *C2*. The lattice parameter is a = 9.5323 Å, b = 5.6064 Å, c = 9.8535 Å, β = 110.667°.[80] To gain more insight into the physics of BMO, it is helpful to view it as a pseudo-perovskite structure and the lattice parameter is a = 3.950 Å, b = 3.995 Å, c = 3.919 Å, α = 90.7°, β = 90.9°, γ = 91.0°. BMO undergoes several phase transitions in a wide temperature range (Table 1.3).

Table 1.3 Crystal structure information and phase transitions of BiMnO₃.[81]

Temperature	Crystal structure information
> ~770 K	Centrosymmetric structure, *Pbnm* orthorhombic
< ~770 K	Non-centrosymmetric structure, monoclinic *C2* a_m = ~9.58 Å, b_m = ~5.58 Å, c_m = ~9.75 Å, and β = ~108°
< ~450 K	Non-centrosymmetric structure, monoclinic *C2* a_m = ~9.532 Å, b_m = ~5.605 Å, c_m = ~9.854 Å, and β = ~110.7°
< ~105 K	Spins of Mn^{3+} ions ordered ferromagnetically

BMO is not stable at atmospheric pressure and the synthesis of bulk BMO requires high pressure (~6 GPa) and high temperature (~1100 K).[82] Strain, exposed by the substrate could be used to replace the high pressure requirement to stabilize the BMO in thin film

form.[82, 83, 84, 85] The first growth of BMO in thin film form was by pulsed laser deposition on $SrTiO_3$ (001) single crystal substrate.[82] The growth of pure BMO in thin film form is very difficult due to the volatility of Bi and the easy formation of impure phases like Bi_2O_3 and $Bi_{12}MnO_{20}$. The ferromagnetic transition temperature T_C of bulk BMO is 105 K and depending on the substrate, it can be as low as 50 K on $LaAlO_3$.[86] The ferromagnetic transition temperature is far below the room temperature which prevents the practical application of BMO. Similar to BFO, BMO also suffers from the high leakage current which limits the direct polarization-electric field hysteresis loop measurement. The detailed information regarding ferroelectricity, ferromagnetism, and growth of BMO thin film will be discussed in the following sections.

1.3.3.2 Ferroelectricity and ferromagnetism of BMO

Due to the stereochemical activity of Bi cations, BMO crystallizes in a highly distorted non-centrosymmetric monoclinic structure at low temperatures. The monoclinic unit cell contains 8 formula units. BMO can also be treated as a triclinic lattice ($a_t \approx c_t \approx$ 3.935 Å, $b_t \approx$ 3.989 Å, $\alpha \approx \gamma \approx$ 91.46º, $\beta \approx$ 90.96º) with one formula unit and the pseudocubic representation is usually used for BMO thin films. At high temperatures, BMO undergoes two phase transitions at ~450 K and ~770 K as shown in Table 1.3. The phase transition at ~770 K leads to a centrosymmetric structure which does not allow spontaneous polarization and 770 K is usually considered at the ferroelectric Curie temperature.

43

The magnetic behavior of BMO can be understood based on the superexchange interaction between Mn^{3+}-O-Mn^{3+}. The d^4 transition metal ion Mn^{3+} has a d-orbital electron configuration of t_{2g}^3, e_g^1 with the four electrons occupying the d-orbitals to maximize the total spin. To reduce the Coulomb electrostatic repulsion of the surrounding oxygen anions, the MnO_6 octahedron is slightly elongated (the so-called Jahn-Teller).

Based on the Goodenough-Kanamori rules, a perovskite can be either ferromagnetic or ferrimagnetic based on the superexchange coupling of Mn^{3+}-O-Mn^{3+} and the ferrimagnetism is more possible. However, an overall long-range ferromagnetism occur in BMO due to the highly distorted monoclinic structure caused by the stereochemical active Bi^3.[87] The actual Mn-O-Mn bond angle is between 140° and 160°.

1.3.3.3 Growth of BMO thin films

It is a fact that single-phase Bi-based manganite-family perovskites is difficult to be synthesized because of the multiphase formation and high volatility of bismuth.[82, 88, 89] High pressure and high temperatures are required to synthesize bulk single-phase Bi-based manganite-family perovskites such as $BiMnO_3$. Strain, exposed by the lattice mismatch between the film and single-crystal substrate, could be used to replace the high pressure requirement to achieve single-phase synthesis of Bi-based manganite-family perovskites. For example, $SrTiO_3$ (001) (a = 3.905 Å) has been chosen as the substrate to fabricate BMO thin films with pseudocubic structure (pseudocubic representation: $a_t \approx c_t \approx 3.935$ Å, $b_t \approx 3.989$ Å, $\alpha \approx \gamma \approx 91.46^o$, $\beta \approx 90.96^o$). Much efforts have been made to optimize the

growth conditions of fabricating single-phase BMO thin films by pulsed laser deposition, such as optimizing the substrate temperature, oxygen pressure, doping, etc.

Oxygen pressure can highly influence the phase formation of Bi-Mn-O thin films. In 2007, Fujino et al. studied the multiphase thin film growth of Bi-Mn-O system on SrTiO$_3$ (001) using a stoichiometric BiMnO$_3$ target. It was shown that the dominant phase can be tuned from the single phase BiMnO$_3$ to epitaxially grown ferromagnetic Mn$_3$O$_4$ by controlling the oxygen pressure (Figure 1.21).[85] A composite consisting of BiMnO$_3$ and Mn$_3$O$_4$ was obtained when the oxygen pressure was 10 mTorr.
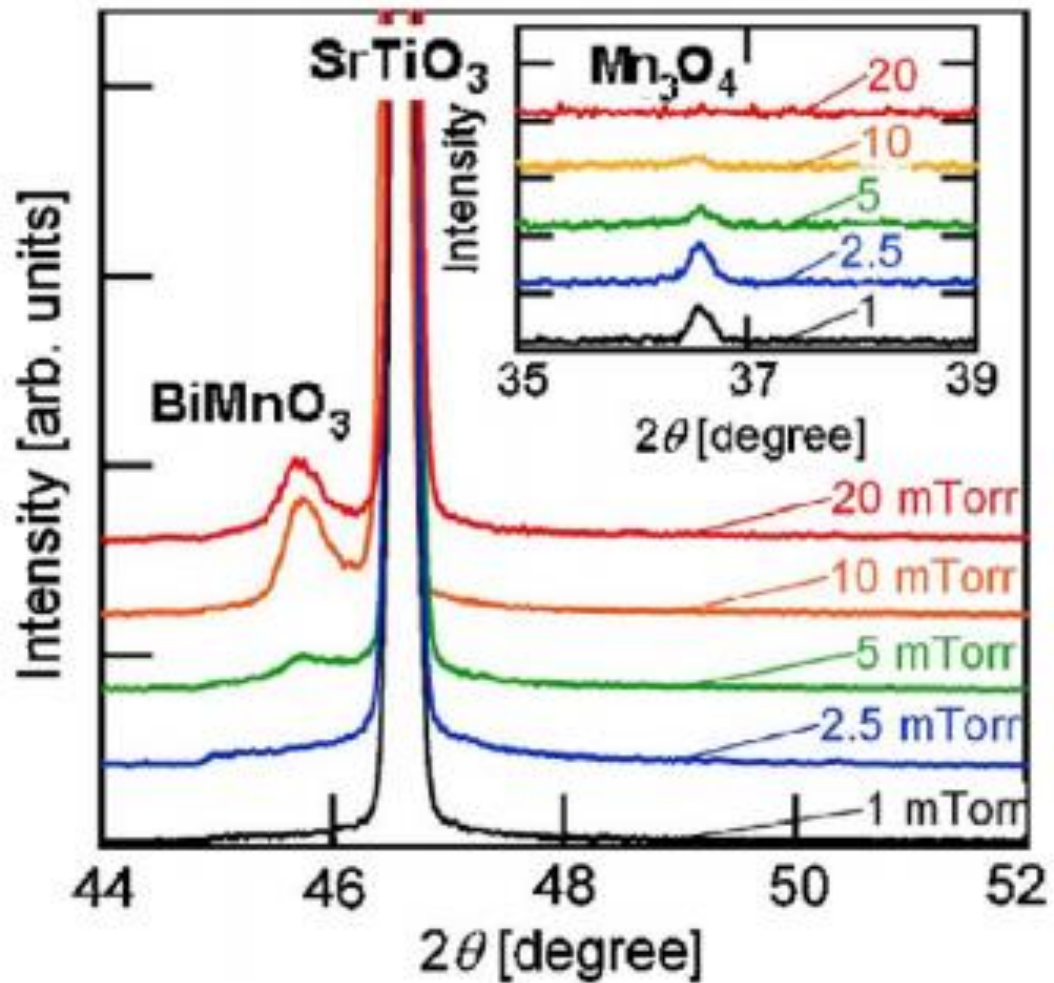
Figure 1.21 XRD θ-2θ scans of Bi-Mn-O thin films deposited on SrTiO$_3$ (001) substrates at 650 °C under an oxygen pressure range of 1 and 20 mTorr.[85]

Langenberg et al. did temperature dependence study on the growth of Bi-Mn-O thin films and showed that the BiMnO$_3$ phase can be obtained in a narrow temperature window around 630 °C with multiple impure phases formed (Bi$_2$Mn$_4$O$_{10}$, Mn$_3$O$_4$, Bi$_2$O$_3$, etc.).[90] There are several other reports regarding BMO where pure pseudocubic BMO thin films were fabricated on STO (001). Gajek et al. studied the spin filtering and tunnel junctions using the pseudocubic BMO as the multiferroic tunnel barriers and the

46

pseudocubic BMO thin films were grown on STO (001) in a narrow temperature window around 625 °C.[83, 91] Lee et al. fabricated highly epitaxial and pure pseudocubic BMO thin film on STO (001) at 500 °C using a target $Bi_{1.2}MnO_3$ to compensate the Bi loss (Figure 1.22).[92] Yang et al. obtained pure pseudocubic BMO thin film on STO (001) at an even lower temperature around 460 °C.[93]
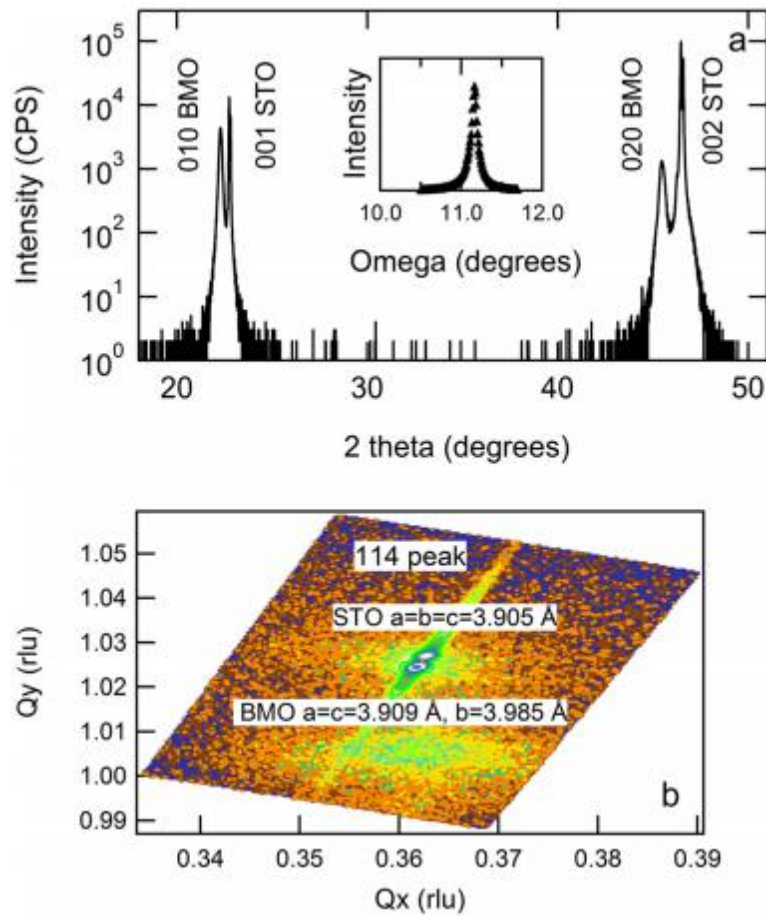
Figure 1.22 (a) XRD θ-2θ pattern for the $BiMnO_3$ thin film grown on $SrTiO_3$ (001). Inset shows the rocking curve for a (010) $BiMnO_3$ peak. (b) X-ray reciprocal space mapping around the $SrTiO_3$ (114) plane shows well-developed peaks for $BiMnO_3$ in the lower region and two strong substrate peaks in the upper region.[92]

Substituting Bi^{3+} by a cation with smaller ionic radius has also been used to stabilize the BMO phase to achieve the highly pure growth. La^{3+} (ionic radius 1.22 Å) has been doped into BMO to substitute Bi^{3+} (ionic radius 1.24 Å) to make the growth of BMO easier because the smaller La^{3+} exerts a chemical pressure strain to the unit cell of BMO to stabilize the phase.[88, 91, 94, 95, 96] As a rare single-phase multiferroics, BMO is intriguing but its low ferromagnetic transition temperature of 105 K has limited its practical applications at room temperature. For BMO thin films, the Curie temperature T_C is even lower than that of bulk BMO. The physical properties of BMO thin films highly depend on the substrates. Son et al. reported a ferromagnetic transition temperature of 50 K for the pseudocubic BMO thin film grown on $LaAlO_3$ (001) (lattice mismatch -4.3%).[86] Luca et al. reported a T_C value of 100 K for ultrathin BMO thin films grown on STO (001) (lattice mismatch -1.0%) which is slightly lower than that of bulk BMO.[97]

Although the smaller La^{3+} lowers the structural distortion, it also causes a slight reduction of the Jahn-Teller distortion leading to weaker ferromagnetic properties (T_C ~ 90 K). Choi et al. studied the doped growth and multiferroic properties of $Bi_{1-x}Sm_xMnO_3$ (BSMO).[98] It was found that the dopant Sm^{3+} can facilitate the pure phase growth of BMO as shown in Figure 1.23. Similar to the dopant of La^{3+}, the much smaller Sm^{3+} (1.13 Å compared to Bi^{3+} 1.22 Å) also exerts a chemical pressure to the unit cell causing a reduced unit cell volume to achieve the stabilized growth of BMO. Besides, both the ferroelectric and ferromagnetic responses are improved with the doping of Sm^{3+}. Compared to the pure BMO, BSMO shows a much higher d_{33} value of 10 pm/V than that of $Bi_{0.9}La_{0.1}MnO_3$ (2 pm/V). The ferromagnetic transition temperature of BSMO was measured to be around

140 K, 40 K higher than that of pure BMO thin films (Figure 1.23). The enhancement of

the multiferroic properties is ascribed to the fact that the out-of-plane Mn-O-Mn

ferromagnetic bonds were reduced which enhanced the out-of-plane ferromagnetic

coupling. At the meantime, the in-plane Mn-O-Mn antiferromagnetic bonds were not

reduced and hence the in-plane antiferromagnetic coupling was not enhanced. These two

aspects lead to an enhanced ferromagnetic response of the BSMO thin film.
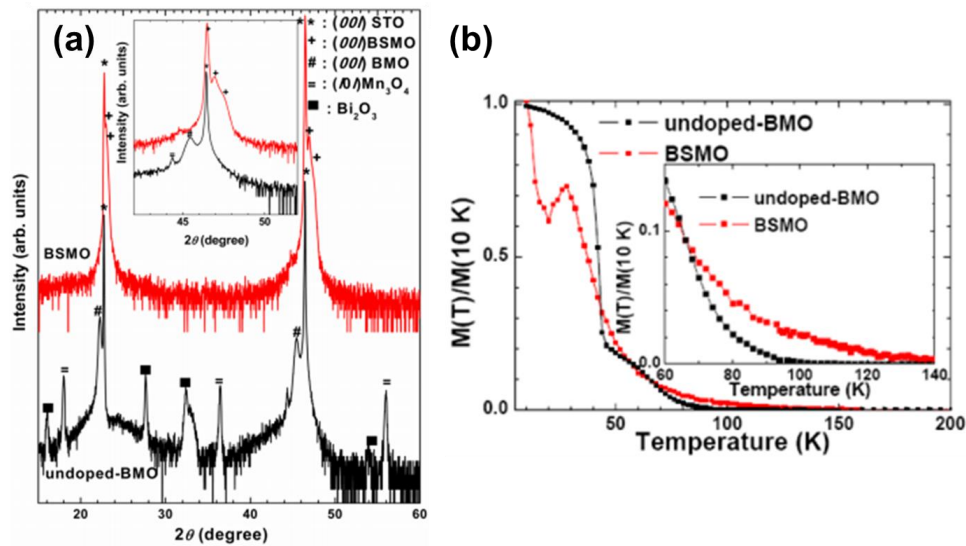
Figure 1.23 (a) XRD θ-2θ scans of undoped-BMO and BSMO films. (b) Normalized magnetization-temperature curve of undoped-BMO and BSMO thin films under a magnetic field of 200 Oe.[98]

Besides the above mentioned single-perovskites BFO and BMO, there are also

several other potential multiferroic candidates. $BiCrO_3$ was predicted to be

antiferromagnetic and antiferroelectric in 2002 and later on in 2006 thin film of $BiCrO_3$

was prepared on single substrates, which was shown to be antiferromagnetic (T_N: 120-140

K) with weak ferromagnetism. $BiCoO_3$ was predicted to show a giant polarization of 150

49

μC/cm^2 but the efforts on the preparation of thin film BiCoO$_3$ was not successful.[99] High-quality epitaxial BiAlO$_3$ thin film was deposited on LaAlO$_3$ (001) and exhibited a remanent polarization of about 29 μC/cm^2.[100]

Bi-based double-perovskites also attract people's attention besides the single perovskites mainly because of the above room-temperature ferromagnetic transition as well as the desirable ferroelectricity. Two of the extensively studied double perovskites are Bi$_2$FeMnO$_6$ and Bi$_2$NiMnO$_6$.

1.3.4 Bi$_2$FeMnO$_6$

As stated above, BFO shows a polarization value as large as 90 μC/cm^2 but its drawbacks, for example, the weak magnetic moment caused by the cycloidally modulated G-type antiferromagnetic structure with a large period of 62 nm, limit its practical applications. The problem for BMO lies in its low ferromagnetic Curie temperature (50-105 K). To enhance the magnetic moment of BFO, various transition metal elements have been doped into BFO including Mn. Pálová et al. theoretically predicted that it may be possible to achieve the co-existent of ferromagnetism and ferroelectricity by Mn doping.[101] Azuma et al. studied the magnetic and structural properties of BiFe$_{1-x}$Mn$_x$O$_3$ and proved that solid solutions was formed in the entire composition range when fabricated at high pressure of several GPa.[102] In the composition range of 0.2 and 0.6, a new orthorhombic phase was formed and a tentative phase diagram was proposed as shown in Figure 1.24.
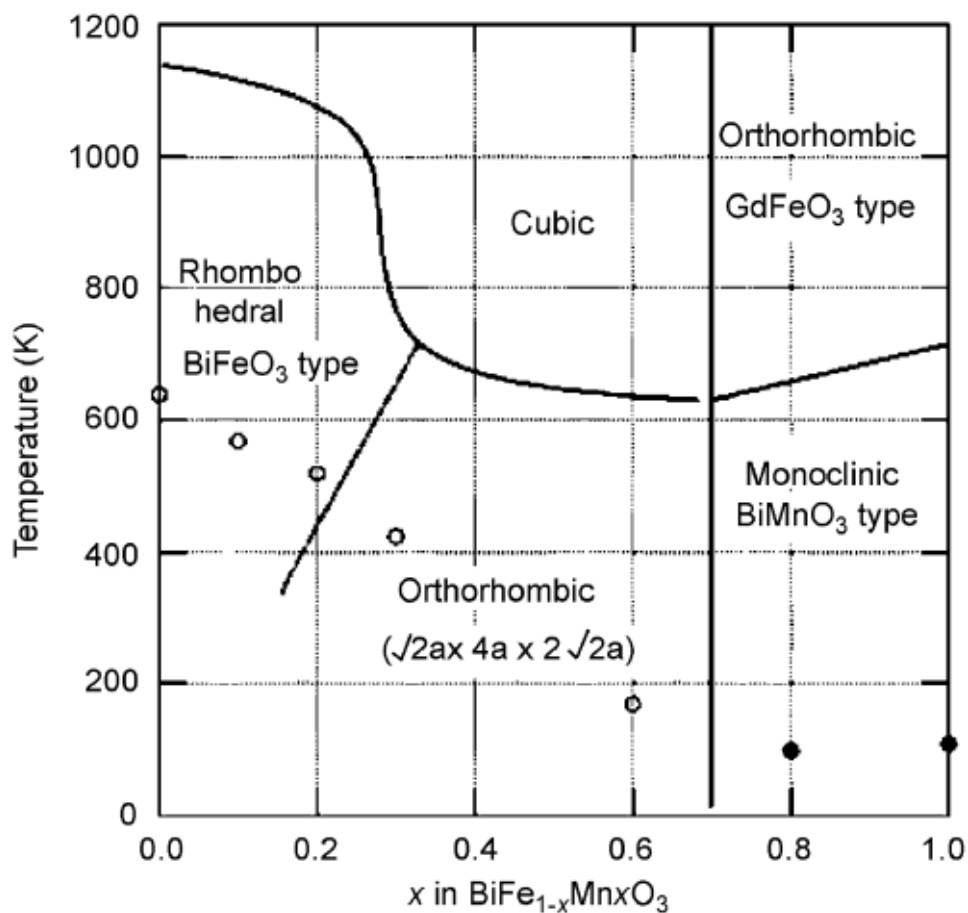
Figure 1.24 Phase diagram for $BiFe_{1-x}Mn_xO_3$. The open circles stand for the antiferromagnetic T_N and the closed ones are for ferromagnetic T_C.[102]

Among the whole $BiFe_{1-x}Mn_xO_3$ system, $BiFe_{0.5}Mn_{0.5}O_3$, which can be viewed as Bi_2FeMnO_6 (BFMO), has been especially and extensively studied as one of the famous bismuth-based double-perovskites ($Bi_2BB'O_6$, B and B' are transition metal cations). Both bulk and thin film of BFMO have been studied for its multiferroic response. Rana et al. reported a magnetization value of 10 emu/cc at 10 K for bulk BFMO.[103] In fact, there is controversy regarding the magnetic response of BFMO. Different researchers have obtained drastically different magnetization values for the double perovskite BFMO. For

many of the literatures, weak magnetizations for BFMO were demonstrated.[102, 103, 104, 105,] [106, 107, 108, 109, 110, 111, 112, 113, 114] In 2008 Bi et al. did the oxygen pressure dependence study of the growth of BFMO on STO (001). The results showed that the Bi loss decreased with the increase of oxygen pressure and pure BFMO thin film can be obtained under 1 mTorr of oxygen (Table 1.4). But the magnetization value of BFMO thin film is only 0.8 emu/cc (under a magnetic field of 10 kOe) at room temperature (Figure 1.25(a)).[108] It was assumed that the magnetization of BFMO thin film originates from the canted antiferromagnetism at room temperature. To investigate the low-temperature magnetic ordering of BFMO, the magnetization of BFMO at 5 K was measured using a superconducting quantum interference device (SQUID) magnetometer. A magnetization value of 5.4 emu/cc at 9 kOe, corresponding to 0.03 μ_B per B-site ion, was obtained. This value is much lower than the values expected from ordered Fe and Mn ordering (4 μ_B for ferromagnetic and 0.5 μ_B for antiferromagnetic ordering of Fe^{3+} and Mn^{3+}). These results indicate that most of the B-site cations are disordered for the BFMO sample in this study. However, in 2011 Choi et al. reported a strong room-temperature magnetization value of 90 emu/cc at $H = 3$ kOe for BFMO thin film grown on STO (001) (Figure 1.25(b)).[111] The magnetic transition temperature is as high as 600 K, much higher than the value of 105 K for bulk BMO. They attributed the high magnetization value to the high level of strain induced by the epitaxial growth. The BFMO film is 30 nm thick and highly strained showing high tetragonality with high epitaxial quality and phase purity.

Table 1.4 Phases and compositions of Bi_2FeMnO_6 films grown on $SrTiO_3$ (001) substrates at 680 $^\circ$C and various oxygen partial pressures.[108]

P_{O2} (mTorr)	Phases	Bi/(Fe + Mn) (at. %)	Fe/Mn (at. %)
0.8	Bi_2FeMnO_6, γ-Fe_2O_3, Mn_3O_4	0.94	0.91
1	Bi_2FeMnO_6	1.07	0.92
3.5	Bi_2FeMnO_6, Bi_2O_3	1.10	0.91
2.5 (*in situ* annealed)	Bi_2FeMnO_6, Bi_2O_3, γ-Fe_2O_3, Mn_3O_4	0.56	0.95
7.5 (*in situ* annealed)	Bi_2FeMnO_6, Bi_2O_3, γ-Fe_2O_3, Mn_3O_4	0.65	0.94
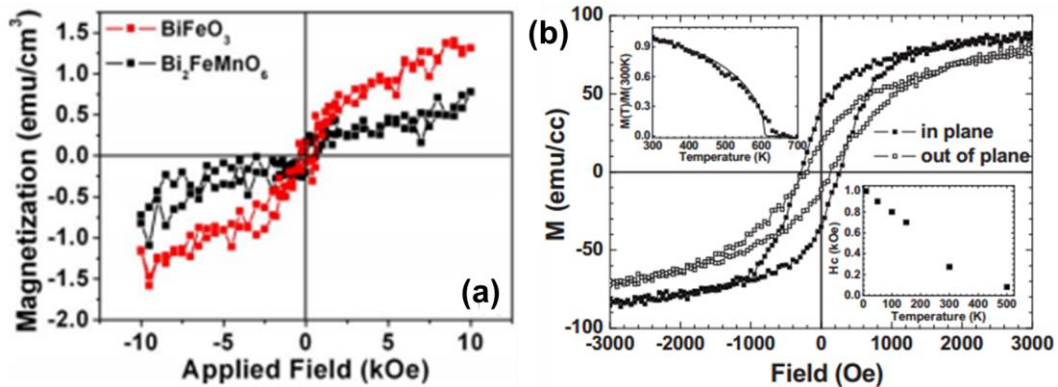
Figure 1.25 (a) Magnetic hysteresis loops of BFO and BFMO thin films along the out-of-plane direction at room temperature.[108] (b) Magnetic hysteresis loops of BFMO thin films along the in-plane and out-of-plane directions.[111]

In 2014, Choi et al. studied the influence of strain to the magnetism of BFMO thin films in more detail.[113] Highly epitaxial and pure BFMO thin films with thicknesses of 30,

60, and 120 nm were fabricated on STO (001) and with the decreasing of the film thickness, the crystallinity of the films increased (Figure 1.26(a) and (b)). Figure 1.26(c) indicated that the thinner films exhibit higher tetragonality. These results showed that the films are highly epitaxial and strained throughout the whole film thickness. The magnetic measurement results showed that films with higher tetragonality exhibited higher saturated magnetization value and higher magnetic transition temperature (Figure 1.26(d)). The maximum magnetic moment in this study is 50-60 emu/cc at 5 kOe at 300 K. This value (~0.4 μ_B/f.u.) is less than half of the theoretical value of 1.0 μ_B/f.u. for the fully ordered BFMO. This may indicate partial or full disordered Fe^{3+} and Mn^{3+}.[115, 116] X-ray magnetic circular dichroism (XMCD) could provide information regarding the spin and orbital moments of the atomic level as well we element sensitivity.[117] With the help of XMCD, the authors probed the origin of the magnetic properties and confirmed that Fe and Mn order antiferromagnetically with respect to each other. The magnetization of Fe is parallel and Mn is antiparallel to the magnetic field, producing a ferrimagnetic ordering. There is no evidence of long range ordering of Fe and Mn and hence the possible bonds are Fe^{3+}-O-Fe^{3+}, Mn^{3+}-O-Mn^{3+}, and Fe^{3+}-O-Mn^{3+}. So it is understood that the reduced magnetization of 90 emu/cc comes from the Fe^{3+}-O-Mn^{3+} ordering.
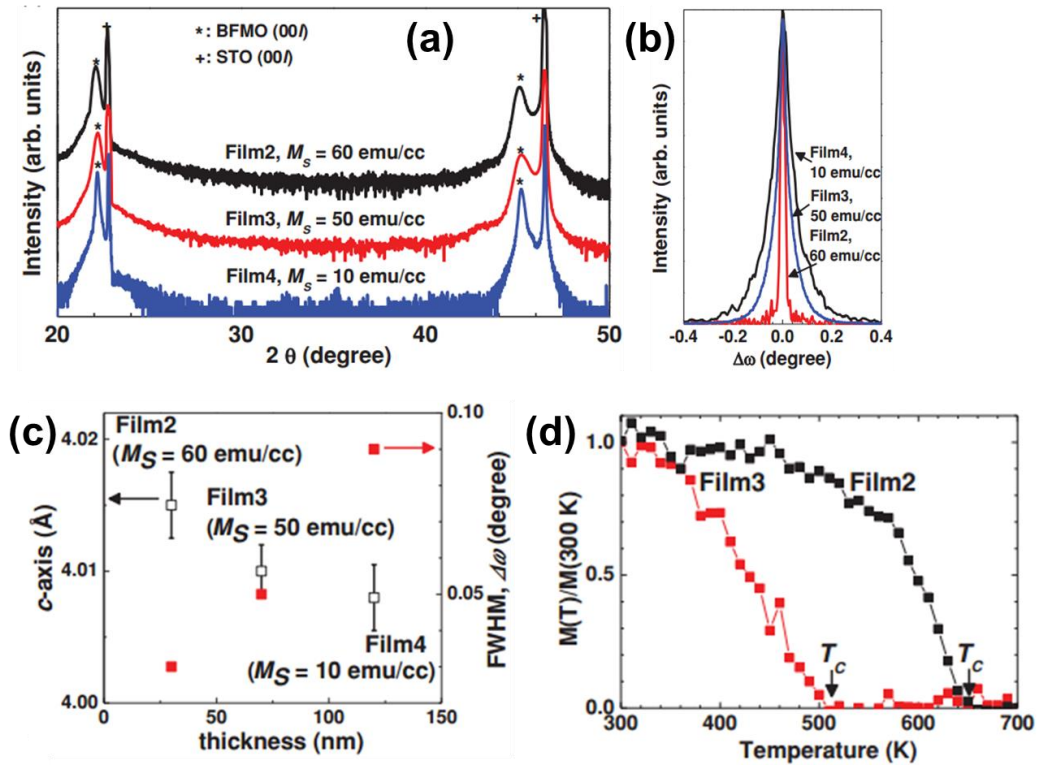
Figure 1.26 (a) XRD θ-2θ scans and (b) ω-rocking curves of BFMO thin films: Film 2 (30 nm thick), Film 3 (60 nm thick), Film 4 (120 nm thick). (c) Normalized in-plane M-T curves of Film 2 and Film 3. (d) The relationship between c-axis lattice parameter (open squares), FWHM of ω-rocking curves (red squares), and film thickness.[113]

Most of the work on BFMO thin films were focused on the magnetic properties with little work on its electric properties. Miao et al. studied the ferroelectricity and magnetism of BFMO thin films grown on $CaRuO_3$-buffered STO (001) (Figure 1.27). At 350 K, an ellipslike shape of polarization-electric field loop was obtained due to the considerable leakage current. But below 250 K, a remnant polarization value of ~23 $\mu C/cm^2$ was observed for the BFMO thin film. The magnetic measurement showed a remnant magnetization of ~1 emu/cc at 50 K. The authors stated that the weak magnetism of BFMO in this study may be attributed to the ferrimagnetic ordering of Fe and Mn at

~140 K while the magnetization above 200 K comes from the canted antiferromagnetic arranged spins between Mn ions.
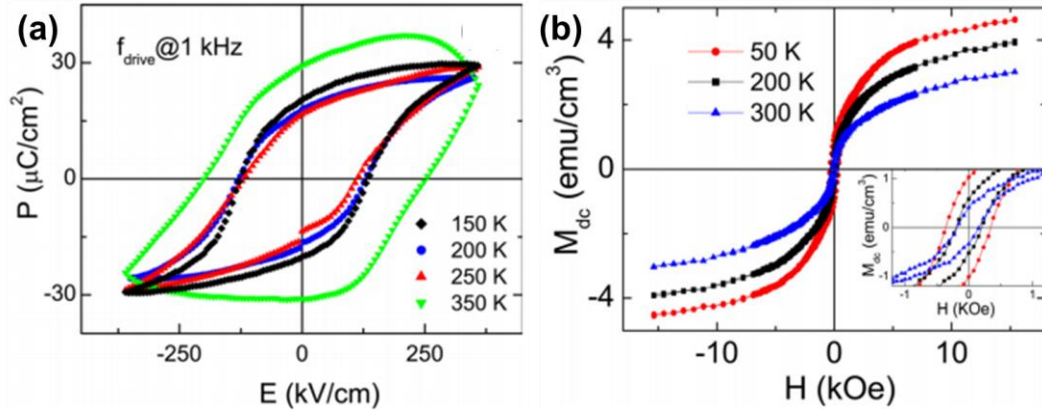
Figure 1.27 (a) Polarization-electric field loops and (b) magnetization hysteresis loops of BFMO thin films.[110]

1.3.5 Bi$_2$NiMnO$_6$

1.3.5.1 Overview of Bi$_2$NiMnO$_6$

Bi$_2$NiMnO$_6$ (BNMO) is another famous double-perovskite with the B-site cations ordered in a 3D rock-salt pattern as shown by the schematic in Figure 1.28. Similar to BMO, BNMO is also a metastable compound and the synthesis of BNMO needs high pressure (6 GPa) and high temperature (~800 $^{\circ}$C). As a multiferroic material, BNMO has also been studied either in bulk or in thin film form.[118, 119, 120, 121, 122, 123, 124, 125, 126]
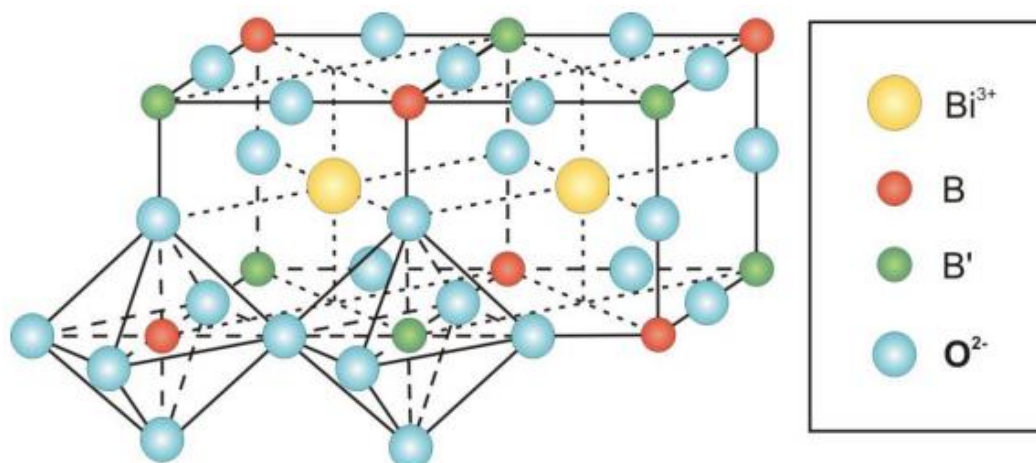
Figure 1.28 A schematic diagram showing the double-perovskite structure with long-range B-site order in a rock-salt configuration.[69]

In 2005, Azuma et al. designed and fabricated the new double perovskite BNMO under high temperature and high pressure.[127] Synchrotron X-ray powder diffraction pattern taken at room temperature shows that the BNMO has a monoclinic unit cell with the lattice parameters of $a_m = $ ~5.4041 Å, $b_m = $ ~5.5669 Å, $c_m = $ ~7.7338 Å, and $\beta = $ ~90.184°, which is quite close to the unit cell of BMO. The monoclinic $C2$ symmetry of BNMO allows spontaneous polarization and a theoretical polarization of 20 μC/cm^2 was predicted. The dielectric constant measurement shows an anomaly at 485 K which can be treated as the ferroelectric temperature (Figure 1.29(a)). At 500 K, the unit cell of BNMO was indexed as centrosymmetric monoclinic with the lattice parameters of $a_m = $ ~5.4041 Å, $b_m = $ ~5.5669 Å, $c_m = $ ~7.7338 Å, and $\beta = $ ~90.184°. The crystal structure and phase information is summarized in Table 1.5. The monoclinic supercell of BNMO is the same as that of La_2NiMnO_6 with Ni^{2+} and Mn^{4+} ordered in a rock-salt configuration.[128]
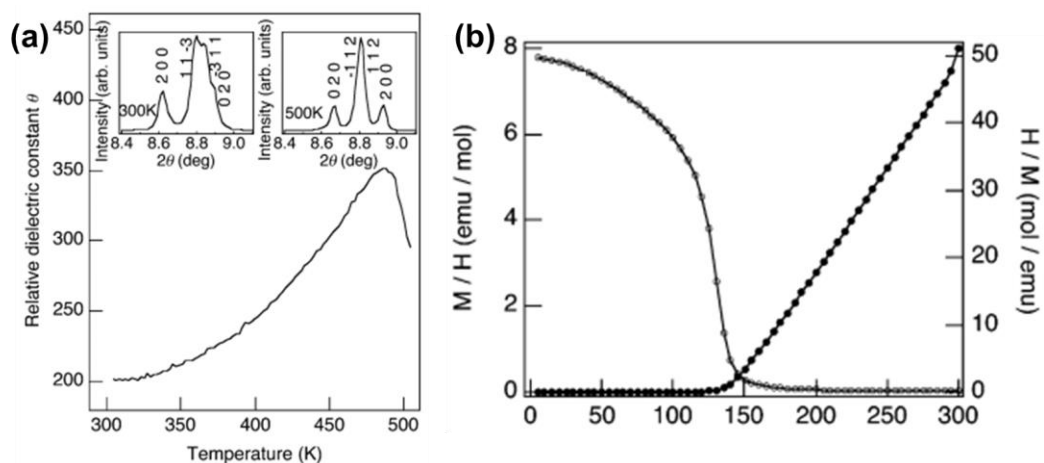
Figure 1.29 (a) Temperature dependence of relative dielectric constant and (b) temperature dependences of magnetic susceptibility and inverse susceptibility of Bi_2NiMnO_6.[127]

From the crystal structure of BNMO, the magnetic exchange path is $-Ni^{2+}-O-Mn^{4+}-O-Ni^{2+}$. Ni^{2+} possesses the e_g^2 configuration and Mn^{4+} has no e_g electron which may favor the ferromagnetic interaction between the neighboring spins. It was also shown that there is no Jahn-Teller distortion in NiO_6 and MnO_6 octahedra which also supports the Ni^{2+} ($t_{2g}^6 e_g^2$) and Mn^{4+} ($t_{2g}^6 e_g^0$) oxidation states in BNMO. The magnetic susceptibility measurement as a function of temperature shows a sharp increase in at 140 K indicating the ferromagnetic transition (Figure 1.29(b)). The saturated magnetization measured at 5 K was 4.1 μ_B at 5 T which is quite close to the theoretical value of 5 μ_B expected from the ferromagnetic coupling between Ni^{2+} (S = 1, 2 μ_B) and Mn^{4+} (S = 3/2, 3 μ_B). The smaller magnetization may come from small antisite disorder of Ni^{2+} and Mn^{4+}. The Ni-O-Ni and Mn-O-Mn interaction leads to antiferromagnetism which will reduce the saturated magnetization.

58

Table 1.5 Crystal information and phase transitions of double-perovskite Bi_2NiMnO_6.[127]

Temperature	Crystal structure information
> ~485 K	Monoclinic *P2₁/c*, centrosymmetric structure a_m = ~5.4041 Å, b_m = ~5.5669 Å, c_m = ~7.7338 Å, and β = ~90.184°
< ~485 K	Monoclinic *C2*, non-centrosymmetric structure a_m = ~9.4646 Å, b_m = ~5.4230 Å, c_m = ~9.5431 Å, and β = ~107.8°
< ~140 K	Spins of Ni^{2+} and Mn^{4+} are ferromagnetically ordered.

1.3.5.2 Thin film growth of Bi_2NiMnO_6

As mentioned above, BNMO is a multiferroic material with the ferroelectric transition temperature of 485 K and ferromagnetic transition temperature of 140 K. The high pressure requirement for the synthesis of bulk BNMO can be replaced by the epitaxial strain exposed by the substrates. Much efforts have been made to fabricate BNMO thin films. However, the high volatility of Bi and multiphase tendency of Bi-based compounds make it difficult to stabilize BNMO as pure single phase although Sakai et al. fabricated single phase BNMO thin film on STO (001) at 630 °C.[120] The growth window of the thin film deposition condition is narrow and it is difficult to optimize the growth conditions.

One strategy of stabilizing the single phase Bi-based compounds is to partially replace Bi^{3+} by La^{3+}.[88] The ionic radius of La^{3+} (1.30 Å) is a little smaller than that of Bi^{3+} (1.31 Å) which reduces the unit cell volume and exerts a chemical pressure to the unit cell to prevent the volatility of Bi.[129, 130, 131] Langenberg et al. fabricated epitaxial $(Bi_{0.9}La_{0.1})_2NiMnO_6$ (BLNMO) thin films on STO (001) and studied the influence of

temperature and oxygen pressure to the growth of BLNMO thin films as shown in Figure 1.30.[129] The results showed that the substrate temperature can influence the phase growth of BLNMO and the optimized temperature is 620 °C. The growth of BLNMO thin films is not sensitive to the oxygen pressure.
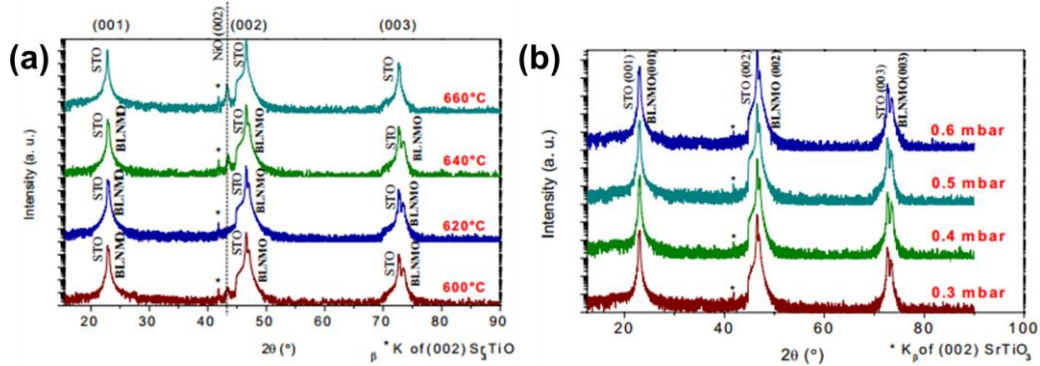
Figure 1.30 XRD θ-2θ scans of BLNMO thin films grown (a) at 0.5 mbar of O_2 at different temperatures and (b) at 620 °C at different oxygen pressures.[129]

Other double-perovskites include Bi_2FeCrO_6,[132, 133, 134] which was predicted to have a polarization of 80 $\mu C/cm^2$ and was theoretically confirmed. However, the magnetization of Bi_2FeCrO_6 is very weak for both bulk and thin film samples (0.2 μ_B/f.u.).

1.4 Two-dimensional layered materials

1.4.1 Overview of two-dimensional materials

Two-dimensional (2D) layered materials, no longer possessing the same behavior as their three-dimensional forms, has sparked special research interest because of their unique anisotropic structures and rich physics as well as the potentials of fabricating

nanoscale devices. Graphene and transition metal chalcogenides (e.g., GeS, SnSe, WS$_2$, and MoS$_2$) represent two kinds of hotly studied 2D materials nowadays with varieties of physics discovered such as quantum spin Hall effects, topological insulating transitions and ferromagnetism, which paves an avenue towards 2D devices. Besides the non-oxide 2D materials, oxide-based 2D materials have also attracted wide attention and have been the focus of condensed matter physics and material science with the underlying rich physical phenomena. For example, perovskite-related 2D materials like Aurivillius and Ruddlesden-Popper phases exhibit remarkable structural variability because of their unique ionic structural framework. And intriguing physical properties such as piezoelectricity and ionic conductivity have been reported for these kinds of perovskite-related 2D layered materials. In the following sections, the 2D non-oxide based and oxide-based layered materials will be briefly discussed.

1.4.2 Non-oxide based two-dimensional layered materials

The non-oxide based 2D materials include graphene, transition metal dichalcogenides, boron nitride (BN), magnesium diboride (MgB$_2$), etc (Figure 1.31). Graphene is a crystalline allotrope of carbon with 2D layered structures. Its carbon atoms are densely packed in hexagonal pattern. Graphene has many unique properties. Its strength is 100 times stronger than that of the strongest steel. It can conduct heat and electron very efficiently and is nearly transport. In addition, several other physical phenomena have been discovered in graphene, such as bipolar transistor effect, ballistic transport of charges, and large quantum oscillations. Graphene has been widely studied

and has potential applications in different areas such as medicine, electronics, energy, environmental, and structural materials.[135, 136, 137, 138, 139, 140, 141, 142, 143, 144] Transition metal dichalcogenides are atomically thin semiconductors with the form MX_2, where M is transition metal atoms such as Mo and W, and X represents the chalcogen atom such as S, Se, and Te.[145, 146, 147, 148, 149, 150] The M atom layer lies between two layers of X atoms. Transition metal dichalcogenides have potential applications in the areas of electronics (e.g. transistor), optics (e.g. emitters and detectors), etc. Boron nitride is a compound composed of boron and nitrogen with the formula BN. BN has three crystal structure: hexagonal, cubic and wurtzite.[151, 152, 153] Among these different forms of BN, the hexagonal BN is the most stable and soft one and can be used as lubricant and addition to cosmetic products. Magnesium diboride is an ionic compound with the formula MgB_2. MgB_2 is proved to be a superconducting material with a critical temperature of T_C of 39 K.[154]
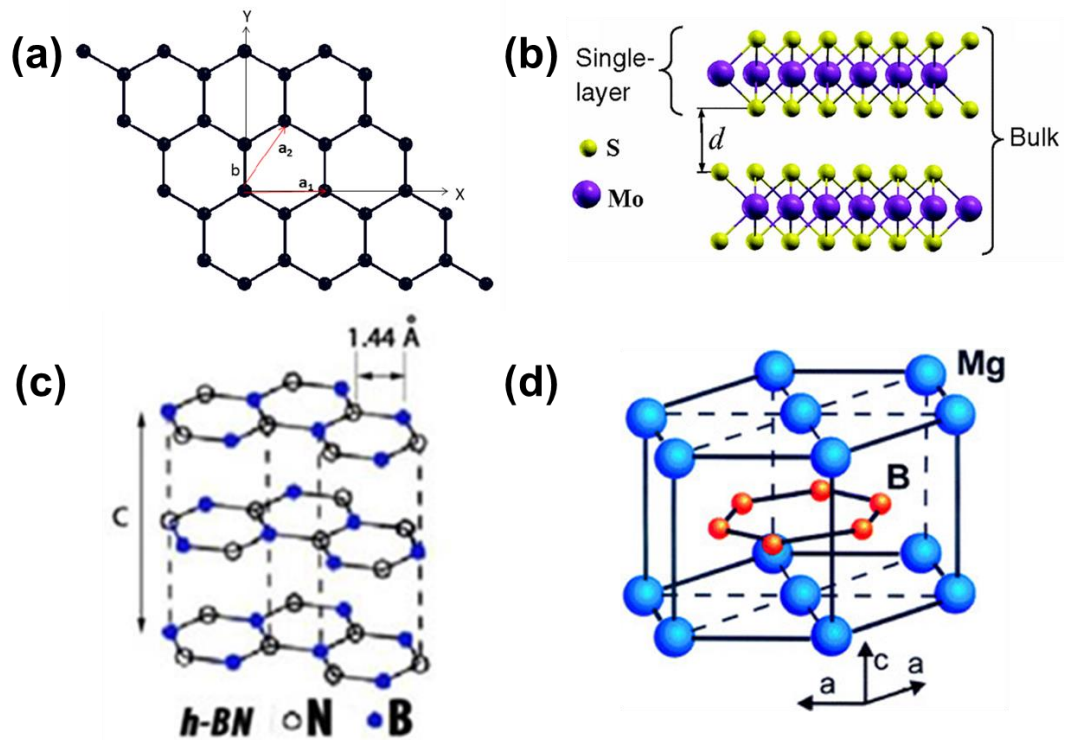
Figure 1.31 Crystal structure model of (a) graphene, (b) MoS_2, (c) BN, and (d) MB_2.[154, 155, 156, 157, 158]

1.4.3 Oxide-based two-dimensional layered materials

The oxide-based 2D materials cover a wide range of compounds which include $LiMO_2$ (M = Co, Mn, Ni), vanadium dioxide (VO_2), Ruddlesden-Popper phases, $YBa_2Cu_3O_7$, Aurivillius phases, etc (Figure 1.32). $LiMO_2$ (M = Co, Mn, Ni) is a series of compounds consist of Li^+ and MO_2^- with layered structure and these kinds of layered materials are used as cathode materials in lithium ion battery.[159] Vanadium dioxide (VO_2) has four different structures which are rutile (R phase), monoclinic (M phase), monoclinic (B phase), and tetragonal (A phase). The metastable monoclinic B phase shows layered structure and attracts interests as lithium ion battery cathode material.[160] Ruddlesden-

Popper phases are a series of materials composed of two dimensional perovskite slabs interleaved with cations. Several examples of Ruddlesden-Popper phases include Sr_2TiO_4, Ca_2MnO_4 and $SrLaAlO_4$. Yttrium barium copper oxide ($YBa_2Cu_3O_7$) is a perovskite structure consisting of layers and is a famous superconductor with high critical temperature.[3] Aurivillius phases are a form of perovskite structures which are built by alternating layers of $[Bi_2O_2]^{2+}$ and pseudo-perovskite blocks. The simplest example of Aurivillius phases is Bi_2WO_6. Aurivillius phases represent an intriguing family of layered structures with great flexibility in structure construction and provide people more capabilities to design new layered materials for desired functionalities. In the following section, the Aurivillius phases will be discussed in detail.
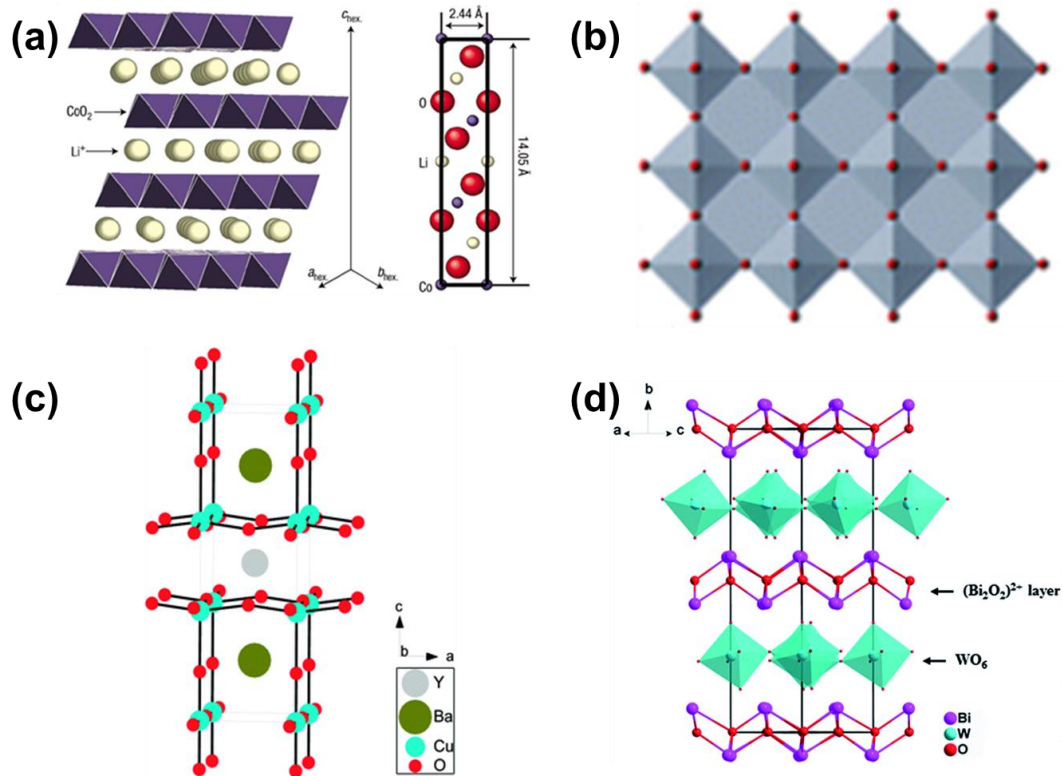
Figure 1.32 Crystal structure model of (a) $LiCoO_2$, (b) VO_2, (c) $YBa_2Cu_3O_7$, and (d) Bi_2WO_6.[161, 162, 163, 164]

1.4.3.1 Aurivillius phases

Aurivillius phases are a kind of layered materials built by alternating stacking of $[Bi_2O_2]^{2+}$ slabs and pseudo-perovskite blocks. It can be represented by the general formula $(Bi_2O_2)(A_{m-1}B_mO_{3m+1})$, where A and B are a large 12 co-ordinate cation and a small 6 co-ordinate cation, respectively. The Aurivillius phases were first described by B. Aurivillius in 1949. People first showed interest to Aurivillius phases because of their ferroelectricity arising from the Bi^{3+} $6s^2$ lone pairs. Oxide ion-conducting properties of Aurivillius phases were also discovered by Takahashi et al. in 1970s.[165] One important and intriguing feature of Aurivillius phases is the compositional flexibility of the perovskite layers where various

cations can be incorporated into A site such as Na^+, K^+, Sr^{2+}, Ca^{2+}, Bi^{3+}, Ba^{2+}, Ln^{3+}, Y^{3+}, U^{4+} and into B site such as Fe^{3+}, Ga^{3+}, Ti^{4+}, Nb^{5+}, Ta^{5+}, Cr^{3+}, W^{6+}, Mo^{6+}. In addition, the m value can be as large as 8 from the reported Aurivillius phases. Owing to the flexibility in structure construction, various Aurivillius phases have been fabricated by incorporating different cations and adjusting the m values. Table 1.6 lists some examples of the reported Aurivillius phases.[166]

Table 1.6 Examples of reported Aurivillius phases.[166]

m = 1	Bi_2WO_6, Bi_2MoO_6, Bi_2TeO_6, Bi_2NbO_5F, Bi_2TaO_5F, $Bi_2TiO_4F_2$	[167, 168, 169, 170]
m = 2	Bi_3TiNbO_9, $Bi_2PbNb_2O_9$, $Bi_2CaNb_2O_9$	[171, 172, 173]
m = 3	$Bi_4Ti_3O_{12}$, $Bi_2LaTi_3O_{12}$	[174, 175, 176, 177]
m = 4	$Bi_4BaTi_4O_{15}$, $Bi_5Ti_3GaO_{15}$, $Bi_5Ti_3FeO_{15}$	[175]
m = 5	$Bi_4Pb_2Ti_5O_{18}$, $Bi_5NaNb_4O_{18}$, $Bi_{2.5}Na_{3.5}Nb_5O_{18}$, $Bi_4Pr_2Ti_3Fe_2O_{18}$	[178]
m = 6	$Bi_4Pb_3Ti_6O_{21}$	[178]
m = 7	$Bi_4Pb_4Ti_7O_{24}$	[178]
m = 8	$Bi_9Ti_3Fe_5O_{27}$	[179]

Here we will use the first three members of the Aurivillius phases ($m = 1, 2,$ and 3) as examples to briefly discuss the crystal chemistry of the Aurivillius phases. As shown in Figure 1.33, the Aurivillius phases consist of Bi_2O_2 sheets interleaved with perovskite-like $A_{m-1}B_mO_{3m+1}$ layers. Many of the reported Aurivillius phases are ferroelectric materials caused by the displacement of Bi atoms along the *a* axis in the perovskite A sites with respect to the chains of the octahedra. All the known ferroelectric Aurivillius phases can be described on the basis of a doubled orthorhombic (pseudo-tetragonal) diagonal cell with an *Fmmm* underlying, nonpolar parent structure. The real structure of Bi_2WO_6, Bi_3TiNbO_9, and $Bi_4Ti_3O_{12}$ was determined by Newnham et al. and refined by Withers et al. as shown in Figure 1.33(d-f).[166] Compared to the prototype structure, the real structures show deformation which is directly caused by the anisotropic behavior of the lone-pair Bi^{3+} cation. Take Bi_3TiNbO_9 as an example. The strong covalent Bi-O bonds in the Aurivillius phases will cause the atomic movements. The Nb and Ti atoms are shifted along the polar *a* axis away from the center of the octahedra with the octahedral rotating about *c* axis which causes a decrease of the *a* and *b* parameters and therefore a slight orthorhombic distortion. In addition, the very short Bi(1)-O(1) bond causes the rotation of the (Nb, Ti)O_6 octahedra around *a* axis and this rotation is enhanced by Bi(2)-O(2) bond. The corresponding (Nb, Ti)-O distance increases strongly and leads to the elongation of the octahedra along *c* axis and an increase of the *c* parameter.
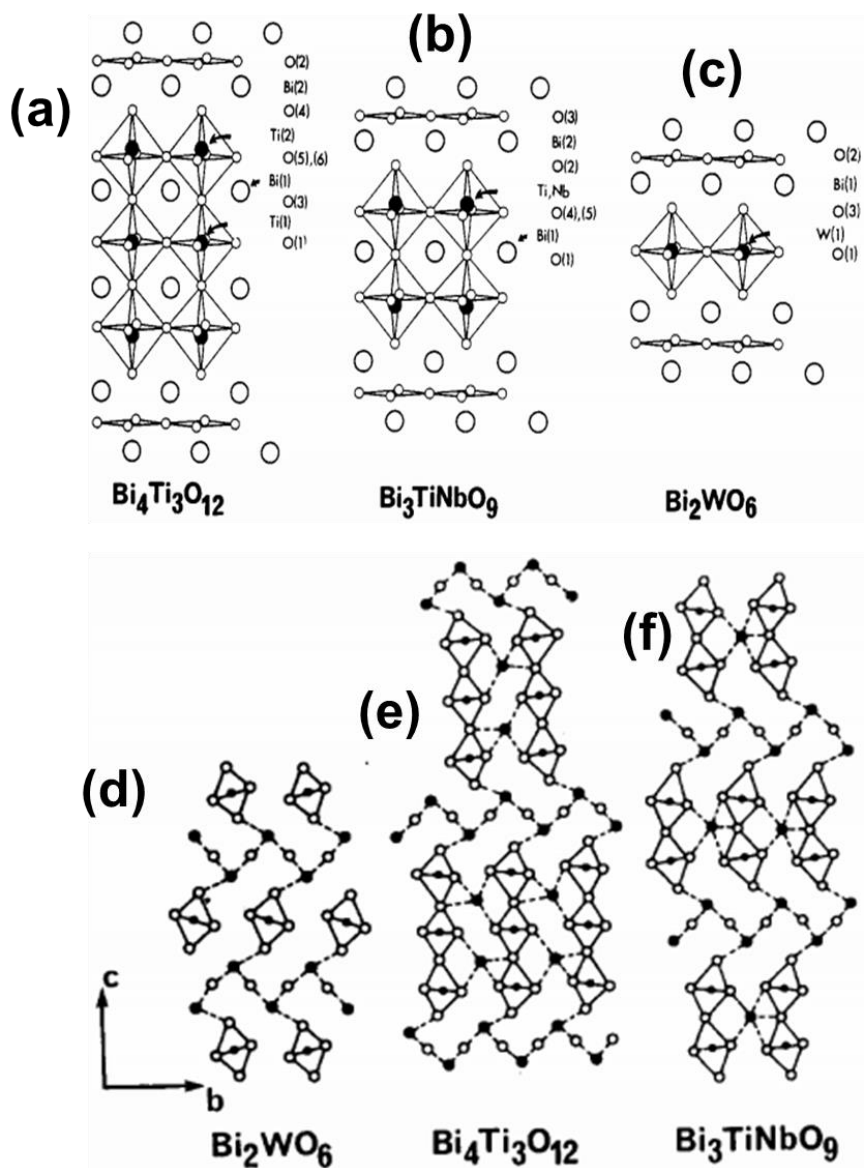
Figure 1.33 A perspective drawing of the undistorted patent structures: (a) $Bi_4Ti_3O_{12}$ (m = 3), (b) Bi_3TiNbO_9 (m = 2), and (c) Bi_2WO_6 (m = 1). (011) sections of (d) Bi_2WO_6, (e) Bi_3TiNbO_9, and (f) $Bi_4Ti_3O_{12}$ real structures. The dashed lines indicated strong Bi-O bond.[166]

For perovskites the stability can be evaluated by the tolerance factor but for the Aurivillius phases the possibilities of forming layered structures are reduced because the Bi_2O_2 layer and perovskite layer need to conform to the same lateral dimensions. By

calculation it was found that the tolerance factor window for perovskite layer is narrower than that of pure perovskites. By examining the solubility limit of various cations in A and B sites of $Bi_4Ti_3O_{12}$, Newnham et al. concluded that the lower limit of the ionic radius depends on the stability of the perovskite layer while the upper limit is determined by the mismatch between Bi_2O_2 and perovskite layers.[180] Theoretically the m values can range from 1 to ∞ (pure perovskite) but only a few systems have been investigated in order to synthesize high-order superstructures. And the results showed that the synthesized superstructures are composed of various mixtures. The results are confusing and contradictory. It appears that phases with m larger than 5 are very difficult to be synthesized and ordered.

Besides the Aurivillius phases listed in Table 1.6, many other Aurivillius phases have been synthesized in order to achieve different functionalities since the discovery of Aurivillius phases by B. Aurivillius in 1949. The Aurivillius phases have found applications as ferroelectrics, piezoelectrics, ion conductors, multiferroics, etc. Compared to $BaTiO_3$ and $Pb_{1-x}Zr_xTiO_3$, the Aurivillius phases have the following characteristics: (1) lower dielectric constants; (2) higher Curie temperature: (3) lower temperature coefficients of the resonant frequency; (4) stronger anisotropic electromechanical coupling factors; (5) a lower aging rate. With the development of high-quality thin film growth techniques, much efforts have been made to the thin film fabrication of Aurivillius phases besides ceramic Aurivillius phases. Here, several examples of Aurivillius phases in thin film form as ferroelectrics and multiferroics will be briefly introduced. As ferroelectrics, the structural origin of ferroelectricity for Aurivillius phases comes from

69

the *a* axis displacement of Bi atoms in the perovskite A sites with respect to the chains of octahedra.

Many of the Aurivillius phases are ferroelectrics including Bi_2WO_6, $Bi_4Ti_3O_{12}$, $Bi_{m+1}Ti_3Fe_{m-3}O_{3m+3}$, etc. In 2002, a paper published in *Science* by Lee et al. reported the thin film growth of La-substituted $Bi_4Ti_3O_{12}$ ($Bi_{3.25}La_{0.75}Ti_3O_{12}$, BLT) by pulsed laser deposition.[181] By optimizing the growth conditions, $Bi_{3.25}La_{0.75}Ti_3O_{12}$ thin film can be grown on yttria-stabilized zirconia-buffered Si (100) substrates using $SrRuO_3$ as the bottom electrode with nearly 99% volume fraction of phase along the *a* axis. A remanent polarization value of as high as 32 $\mu C/cm^2$ was achieved by poling the thin film entirely along the direction normal to the film plane (Figure 1.34).
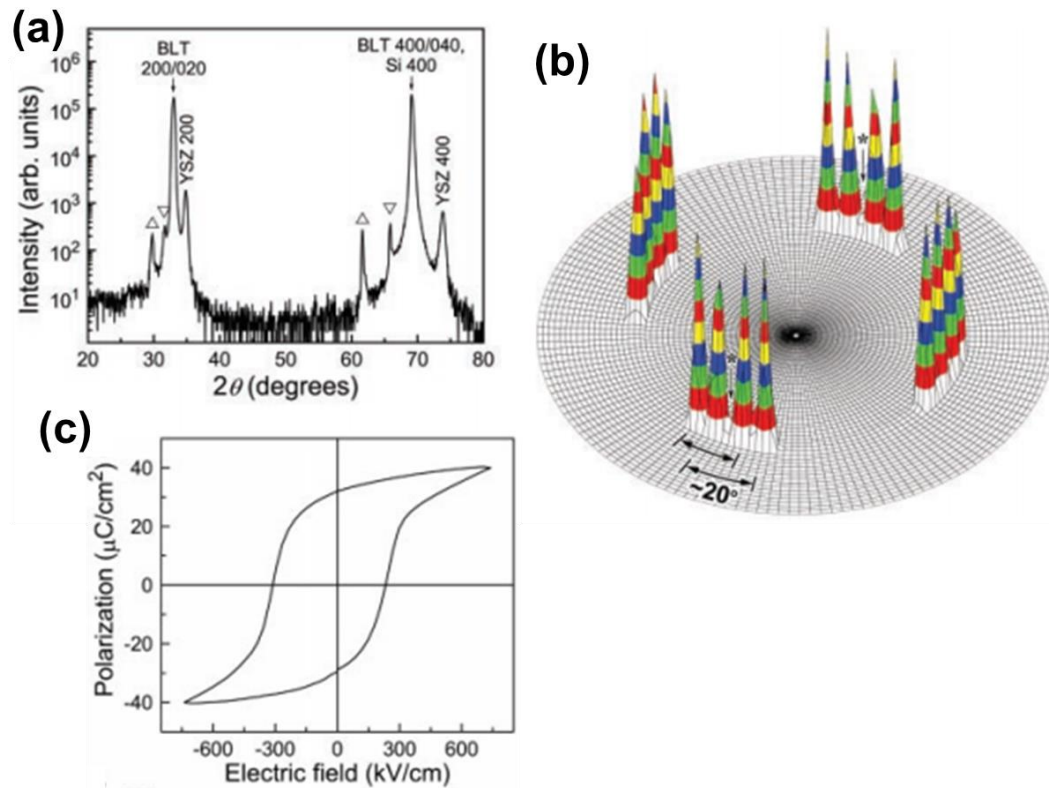
Figure 1.34 (a) XRD θ-2θ scan and (b) pole figure of an almost purely a axis-oriented BLT thin film. (c) Polarization-electric field hysteresis loop of a Pt/BLT (100)-SrRuO$_3$ (110) capacitor.[181]

Multiferroics have been created based on the Aurivillius phases either by incorporating magnetic cations or by integrating with a magnetic material to form a composite. One example is the epitaxial m = 6 Aurivillius phase Bi$_7$Mn$_{3.75}$Ti$_{2.25}$O$_{21}$ fabricated via pulsed laser deposition by incorporating the magnetically active manganese into the perovskite structure of the ferroelectric Bi$_4$Ti$_3$O$_{12}$.[182] Imai et al. created a multiferroic composite consisting of ferroelectric Bi$_5$Ti$_3$FeO$_{15}$ (BTFO) and ferrimagnetic CoFe$_2$O$_4$ (CFO) as shown by Figure 1.35(a) and (b). The multiferroic composite shows much stronger magnetic response than that of pure BTFO. With the CFO pillars

incorporated into the BTFO matrix, the in-plane piezoelectric force microscopy response is also enhanced which saturated at 35% composition Figure 1.35(d)-(g).[183]
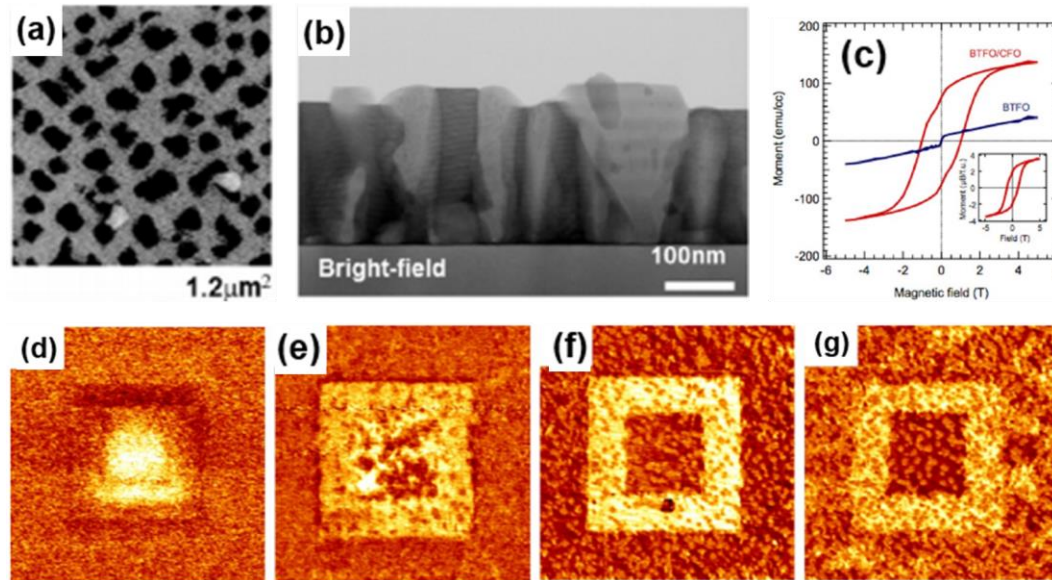
Figure 1.35 (a) Scanning electron microscopy image showing that CFO is well dispersed in the BTFO matrix throughout the entire sample. (b) TEM images showing that the nanopillars grow vertically to the bottom of the matrix. (c) In-plane magnetic hysteresis loops measured at 10 K for BTFO and BTFO/CFO nanocomposite (30 vol.% CFO). (d)-(g) In-plane piezoelectric force microscopy (PFM) images for four compositions where the volume fraction of the CFO is systematically increased (d, 5%; e, 20%; f, 35%; and g, 45%).[183]

1.4.3.2 Novel bismuth-based layered supercell structures

Very recently, Chen et al. reported a novel self-assembled Bi-based 2D layered supercell structure $Bi_3Fe_2Mn_2O_{10-\delta}$ (BFMO322 SC), from the double perovskite Bi_2FeMnO_6. The layered structure was deposited on single crystal $LaAlO_3$ and exhibits a magnetization of 110 emu/cc and 6 $\mu C/cm^2$ at room temperature (Figure 1.36).[184] The BFMO322 SC is composed of alternating stacking of Bi_2O_2 layers and FeO_6/MnO_6

octahedra along the out-of-plane direction epitaxially. The multiferroic property of this Bi-based layered structure is much stronger than that of the conventional pseudocubic phase of BFMO grown on $SrTiO_3$ (001) substrate (34 emu/cc). The layered structure can also be grown on CeO_2 buffered $LaAlO_3$ or $SrTiO_3$ (001) substrates.[185] Geometric phase analysis (GPA) study on the pseudocubic BFMO phase and the layered BFMO322 SC phase indicates that strain plays a critical role in the formation of the layered structure.[186] The strain between the pseudocubic phase of BFMO and STO is -0.6% leading to the cube-on-cube growth of BFMO while a strain as large as -2.0% exists between the BFMO322 SC and LAO substrate. This large strain leads to the highly strained growth of a tetragonal phase (c/a = 1.15) on which the layered BFMO322 SC phase was formed.
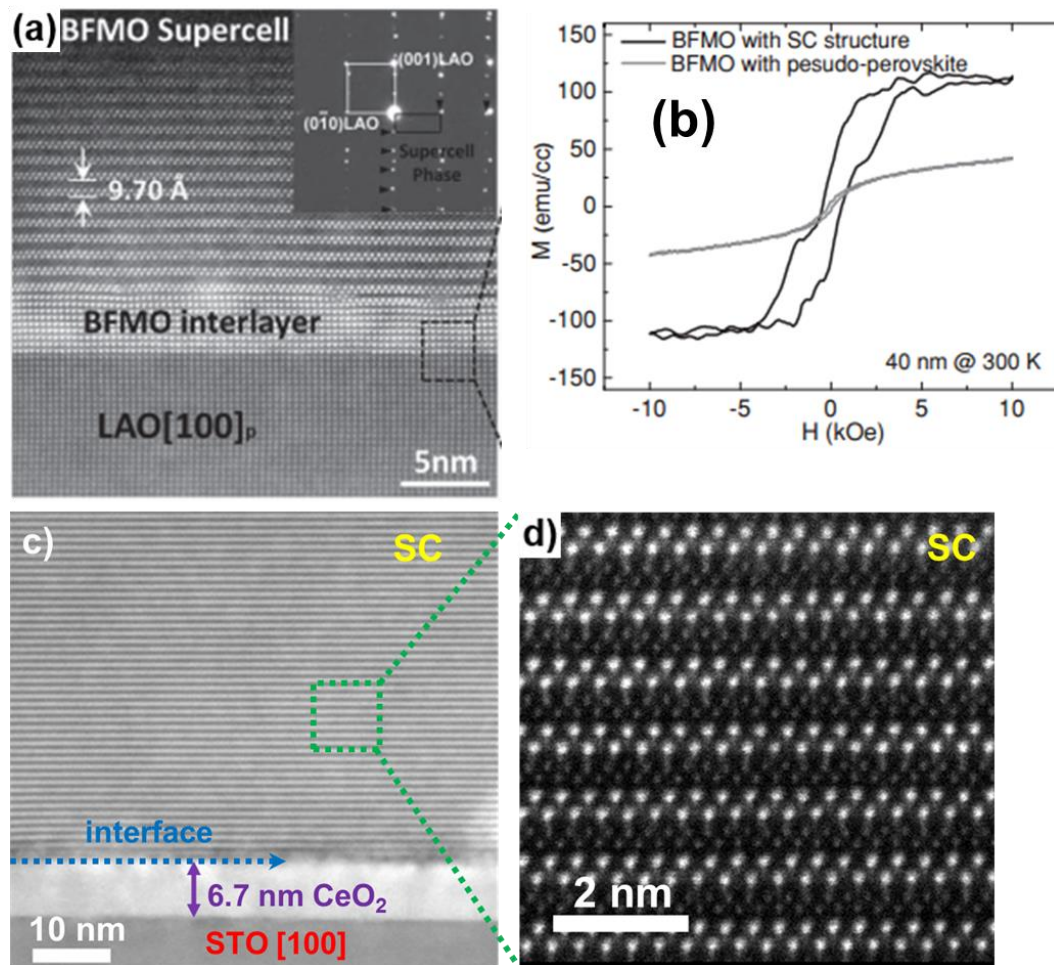
Figure 1.36 Cross-sectional scanning transmission electron microscopy (STEM) images of the BFMO322 SC structure grown on (a) LaAlO$_3$ (001) and (c) CeO$_2$ buffered STO substrate. (b) Magnetization hysteresis loops of the BFMO322 SC structure and the pseudocubic Bi$_2$FeMnO$_6$ phase. (d) Magnified STEM image of the BFMO322 SC structure.[184, 185]

1.5 Research motivation

The newly fabricated Bi-based layered BFMO322 SC shows stronger room temperature multiferroic response compared to the pseudocubic phase. Strain analysis shows that strain may play a critical role in the formation of the new layered structure and it can also be grown on CeO$_2$ buffer layer. However, several questions still remain

unsolved including the growth mechanism of BFMO322 SC and several related aspects as described below.

(1) What is the growth mechanism of the Bi-based BFMO322 SC?

(2) What is the influence of CeO_2 thickness to the growth and physical properties of BFMO322 SC? As with the increase of CeO_2 thickness the growth mode of CeO_2 transforms from 2D layer-by-layer growth to 3D island growth.

(3) What is the role of Fe and Mn in the formation of the Bi-based layered supercell structure? Which cation is more important during the growth of the layered supercell structure?

(4) Is there possibility that the Bi-based layered supercell structure can be fabricated in other Bi-based double-perovskites besides Bi_2FeMnO_6.

With these questions in mind, the influence of CeO_2 thickness to the growth and physical property of BFMO322 SC, the role of Fe and Mn in the formation of BFMO322 SC, and the possibility of growing other new Bi-based layered supercell structures for multiferroism are investigated in this dissertation. It is expected that with these exploration to the above questions we can have more understanding to the growth mechanism of the Bi-based layered structures which can help the design and creation of new Bi-based layered supercell structures with more interesting structural and physical phenomena discovered.

CHAPTER II

EXPERIMENTAL TECHNIQUES

2.1 Pulsed laser deposition

All the thin film samples in this dissertation were fabricated by pulsed laser deposition (PLD, Lambda Physik Compex Pro 205, KrF excimer laser, $\lambda = 248$ nm). Laser is an acronym for "Light Amplification by Stimulated Emission of Radiation". Laser is a very collimated, monochromatic and coherent beam and in pulsed laser modem the output of a laser beam varies with time in the form of alternated "on" and "off" periods.

Laser has wide applications and PLD is an outstanding representative which has achieved significant development in the past several decades. PLD is one of the physical vapor deposition (PVD) techniques with simple system setup. Figure 2.1 shows the schematic diagram of a typical PLD system. It mainly includes a vacuum chamber and a pulsed laser source. Inside the vacuum chamber, there is a multiple target holder and a substrate holder. A molecular turbo pump is used to achieve a high vacuum of at least 1.0 $\times$ 10^{-6} mbar before the deposition. The high-energy laser beam is focused on the target surface to vaporize the target material to deposit the thin films. The angle between the laser beam and target surface is 45°. The distance between the target surface and the substrates is between 3 cm and 5 cm. The substrate temperature varies between room temperature and 750 $^{\circ}$C. A laser beam with an energy of 400 mJ and a frequency of 2 Hz is used in this study. The quality and phases of the fabricated thin films depend on various

PLD parameters, including substrate temperature, oxygen pressure, laser energy density, laser frequency, and substrate-target geometry.
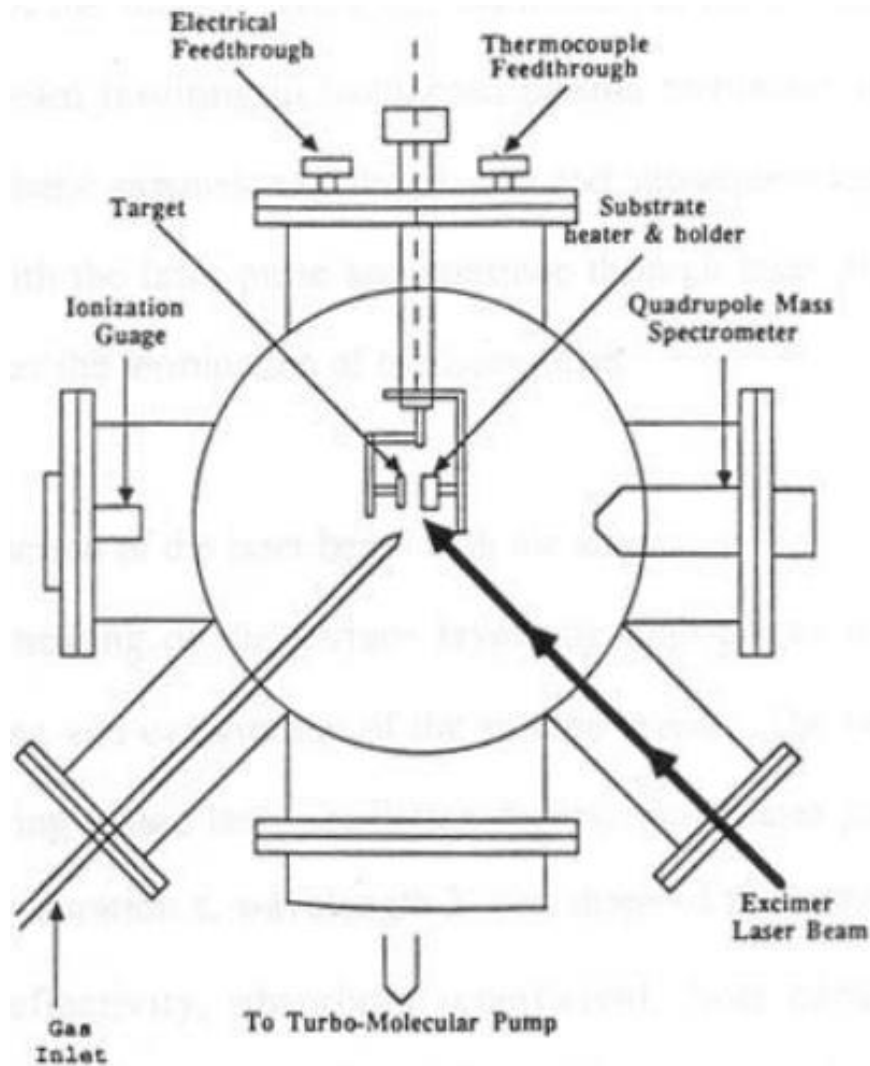
Figure 2.1 Schematic diagram showing the pulsed laser deposition system.[187]

PLD takes the advantages of all the characteristics of laser beam. The high energy density and directionality of laser beam allow localized heat treatment of materials with high spatial resolution. The monochromaticity of the laser could allow for the control of

77

depth of heat treatment by simply changing the laser wavelength. The advantages of PLD also include reproduction of the target stoichiometry, low contamination level and in-situ control of thin film quality.

Despite the simplicity of PLD, the laser-target interaction is a very complicated process. In 1990, R. K. Singh and J. Narayan described the basic PLD physical principles,[187] which include the laser-target interaction, the interaction of laser beam with evaporated materials, and adiabatic plasma expansion as shown in Figure 2.2. PLD combines both equilibrium and non-equilibrium processes. After the laser beam is absorbed on the target surface, the electromagnetic energy of the incident laser beam will be first converted into electronic excitation and lastly into thermal, chemical, and mechanical energy. These series of energy transfer will lead to the target material evaporation, ablation, excitation, plasma formation and exfoliation. A plume consisting of a mixture of energetic species of small particles, molted globules, clusters, molecules, atoms, ions, and even electrons will be formed. The collisional mean free path inside the plume is very short and the plume will rapidly expand into the vacuum and reach the substrates for the thin film growth. With the appropriate laser and gas inside the chamber, versatile thin films can be grown by PLD.
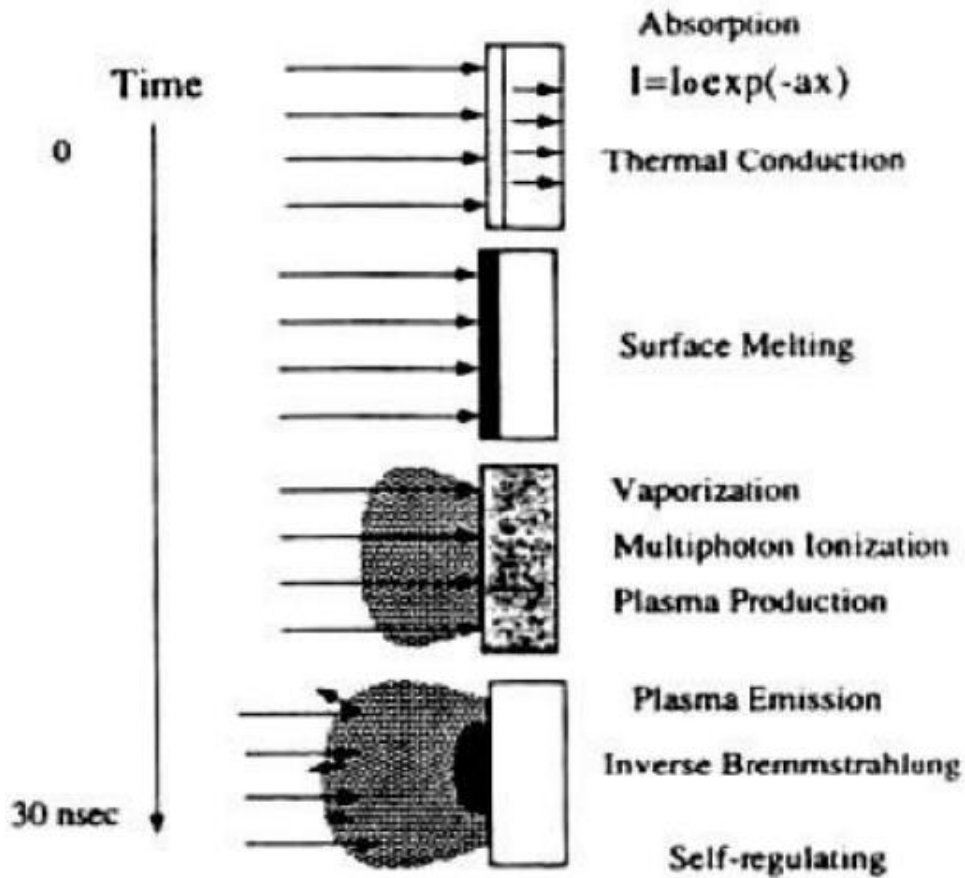
Figure 2.2 Schematic diagram showing the laser-target interaction stages during the short pulsed laser process.[187]

The laser-target interaction can be divided into three stages for each nanosecond laser pulse, as shown in Figure 2.2. (1) the evaporation of target surface layers resulted from the interaction of the laser beam and the target; (2) the isothermal plasma formation and expansion resulted from the interaction of the evaporated materials with the incident laser beam; (3) the anisotropic adiabatic expansion of the plume which subsequently leads to the deposition process. The first two regimes happen at the beginning of the laser radiation and continue through the laser pulse duration. The third stage starts right after the laser pulse termination.

High-power laser irradiation of the surface layers of the target materials will cause the melting and evaporation of the surface materials. The heating rate, melting and evaporation depend both on the laser beam (e.g. pulse energy density, pulse duration time, wavelength, and shape of the laser) and material properties of the target (e.g. reflectivity, absorption coefficient, heat capacity, density, thermal conductivity). During a nanosecond pulsed laser processing, the thermal diffusion distances are short and the dimension of the laser beam large compared to the melting depth. The thermal gradients perpendicular to the interface is much larger than the thermal gradients parallel to the interface. Hence, the three-dimensional heat flow problem can be reduced to a one-dimensional heat flow problem which can be expressed by the following equation,

$$\rho_{i(T)} C_{p(T)} \frac{\partial T(x,t)}{\partial t} = \frac{\partial}{\partial t} \left[K_i(T) \frac{\partial T(x,t)}{\partial x} \right] + I_0(t)[1 - R(T)]e^{-a(T)x} \quad (2\text{-}1)$$

where x is the distance perpendicular to the surface of the sample and t is the time. $\rho_i(T)$ is temperature-dependent density, $C_p(T)$ is the thermal heat capacity per unit mass of the target material, $R(T)$ is the temperature-dependent reflectivity, $a(T)$ is the absorption coefficient, $I_0(t)$ is the time-dependent incident laser intensity and $K_i(T)$ is for the thermal conductivity of the solid and liquid phases at the interface. The subscript $i = 1$ and 2 refers to solid and liquid phases, respectively.

Emission of positive ions and electrons from the target surface will happen due to the interaction of high-power laser beam with the bulk materials. The emission of positive ions and electrons shows an exponential increase with temperature which can be calculated by Langmuir-Sha equation,

$$\frac{i_+}{i_0} = \frac{g_+}{g_0} e^{[(\phi - I)KT]} \quad (2\text{-}2)$$

where i_+ and i_0 refers to fluxes of positive and neutral ions emitted from the surface at a certain temperature T. g_+ and g_0 are the weights of the ions which are in the ionic and neutral states, ϕ is the work function of the electron and I is the material ionization potential. Despite that the surface temperature of the target is close to the boiling point, higher temperature can be achieved in the plasma due to the interaction of the laser beam with the plasma. The penetration and absorption of the laser beam by the plasma is related to the electron-ion density, temperature, and the laser wavelength. And the penetration or reflection of the incident laser beam depends on the plasma frequency and the plasma frequency should be lower than that of the laser for the laser energy to be transmitted or absorbed. The plasma is further heated by absorption of laser radiation. The primary absorption mechanism for plasma is based on the electron-ion collisions and the absorption involves absorption of a photon by free electrons.

After the plasma formation and the initial isothermal expansion, the adiabatic expansion of the plasma will occur which gives rise to the laser-deposition process. With the thermal energy converted to kinetic energy, the velocity of the plasma will increase. At the meantime, the temperature drop of the plasma is slow because the cooling is balanced by the energy regain from the ions recombination processes and the plasma will only expand in one direction. The initial dimensions of the plasma are much larger in the transverse direction.

2.2 Microstructure characterization

2.2.1 X-ray diffraction

X-ray diffraction (XRD) is one of the most popular methods to study the structure and composition of crystalline materials. It is also used for determining crystalline orientation, crystalline size and stress in thin films. It is an interaction between X-rays and the periodic electronic potential geometry of crystals. Diffraction occurs when the wavelength of the X-ray is the same order as a structure's repeat distance. The XRD equipment used in this dissertation is the high-resolution XRD from PANalytical Empyrean. The diffraction process is shown in Figure 2.3 and the diffraction is governed by the Bragg's equation,

$$n\lambda = 2d\ sin\ \theta \quad (2\text{-}3)$$

where n is an integer, λ the wavelength (1.5406 Å for Cu K$_\alpha$), d the lattice spacing, and θ the diffraction. XRD is a non-destructive method for studying the microstructure of the materials. The θ-2θ is used to study the out-of-plane crystalline orientations. The φ scan is used to study the in-plane orientation of the thin films. Reciprocal space mapping (RSM) can be used to study the strain of the thin films.
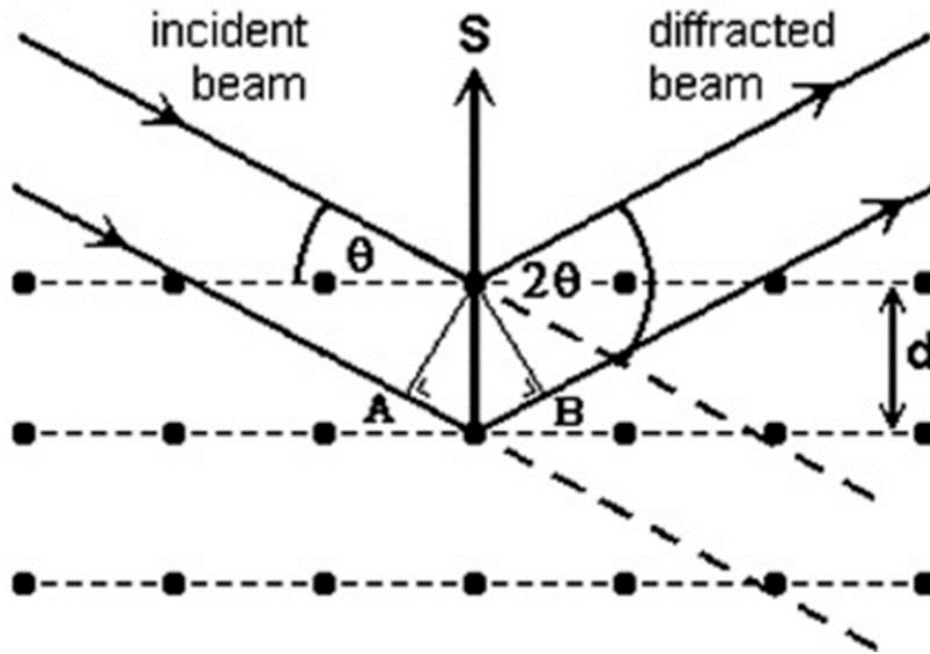
Figure 2.3 Schematic showing the Bragg diffraction for a set of crystal planes.[188]

2.2.2 Transmission electron microscopy

Transmission electron microscopy (TEM) was widely used in this dissertation to obtain the structural and morphological information for the layered structures. TEM uses the electron as the beam source which can transmit through an electronic transparent sample to study the microstructure of the samples. The TEM tool used in this study is FEI Tecnai F20 analytical microscope (200 kV, ZrO_2/W Schottky field emitter with 0.27 nm point resolution).

The resolving power or spatial resolution of an imaging device can be estimated by the classical Raleigh criterion without any aberration of lenses,

$$\delta = \frac{0.61\lambda}{\mu \sin\beta} \quad (2\text{-}4)$$

where λ is the wavelength of the radiation, μ is the refractive index of the viewing medium, and β is the semi-angle of collection of the magnifying lens. Because of the coherency of electron beam and short wavelength of the accelerated electrons, the resolution limit can go to several Å. The TEM uses the electron beam with much shorter wavelength as the illuminating source can reach much higher resolution than the optical microscope which uses the photons as the beam source.

The wavelength of an electron beam in nm at an accelerating voltage V is given by

$$\lambda = \frac{1.22}{\sqrt{V}} \quad (2\text{-}5)$$

With an accelerating voltage of 200 kV, the wavelength of the resulted electron beam is 0.0027 nm. However, the practical resolution of a microscope can not reach the ideal value of the resolution power of an imaging device using the accelerated electrons as the beam source. Spherical aberration, chromatic aberration and stigmatism are the main electromagnetic lens defects that limit the resolution power of an electron microscope as shown in Figure 2.4.

Spherical aberration is a lens defect coming from the non-paraxiality of the electron beam. The electrons that leave from point P with different angles with respect to the optical axis of the microscope will focus before the image plane or on the image plane. Instead of a point, a disk with a radius r_s is formed, where $r_s = C_s\beta^2$, β is the angular aperture of the lens. Chromatic aberration arises from the non-chromaticity of the electron beam with slightly different energies. The electrons with higher energy will be less strongly refracted from the objective lens than the electrons with lower energy. Thus the electrons with higher energy will be brought into focus beyond the image plane. The

astigmatism comes from the asymmetric magnetic field which occurs when the lens exhibits different focal lengths. As shown in Figure 2.4(c), the rays traveling through plane A will be focused at point P_A while those traveling through plane B will be focused at point P_B. In this situation, a point on the object will be imaged at a disk with a radius $r_A = \beta f_A$, where f_A is the maximum difference in focal length arising from astigmatism.

The spherical aberration will limit the resolution of the microscope if all the astigmatism are corrected, the sample is thin enough, and chromatic aberration is negligible. The resolution of a microscope is given by the combination of Rayleigh criterion and the aberration error,

$$r_{min} = 0.91(C_s\lambda^3)^{1/4} \quad (2\text{-}6)$$

where r is the aberration error, C_s is the spherical aberration, and λ is the wavelength of the electrons.
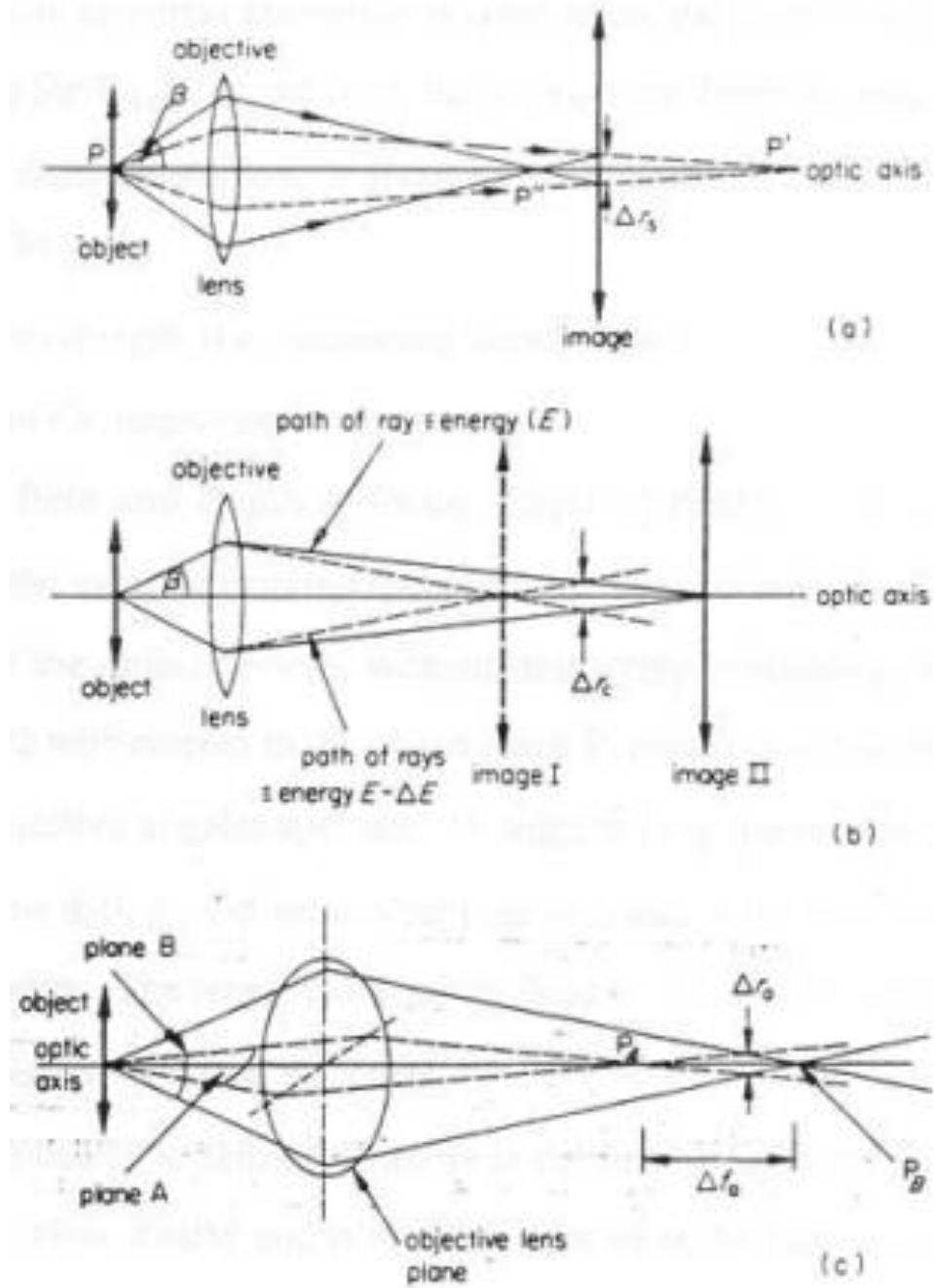
Figure 2.4 Objective aberration: spherical (a), chromatic (b), astigmatism (c).[189]

There are two basic operation modes for TEM: diffraction mode and image mode as shown in Figure 2.5. The working mode of the TEM can be controlled by changing the

focal length of the intermediate lens. For diffraction mode, the image plane coincides with

the back focal plane of the objective lens while the image plane coincides with the image

plane of the objective lens for the image mode.
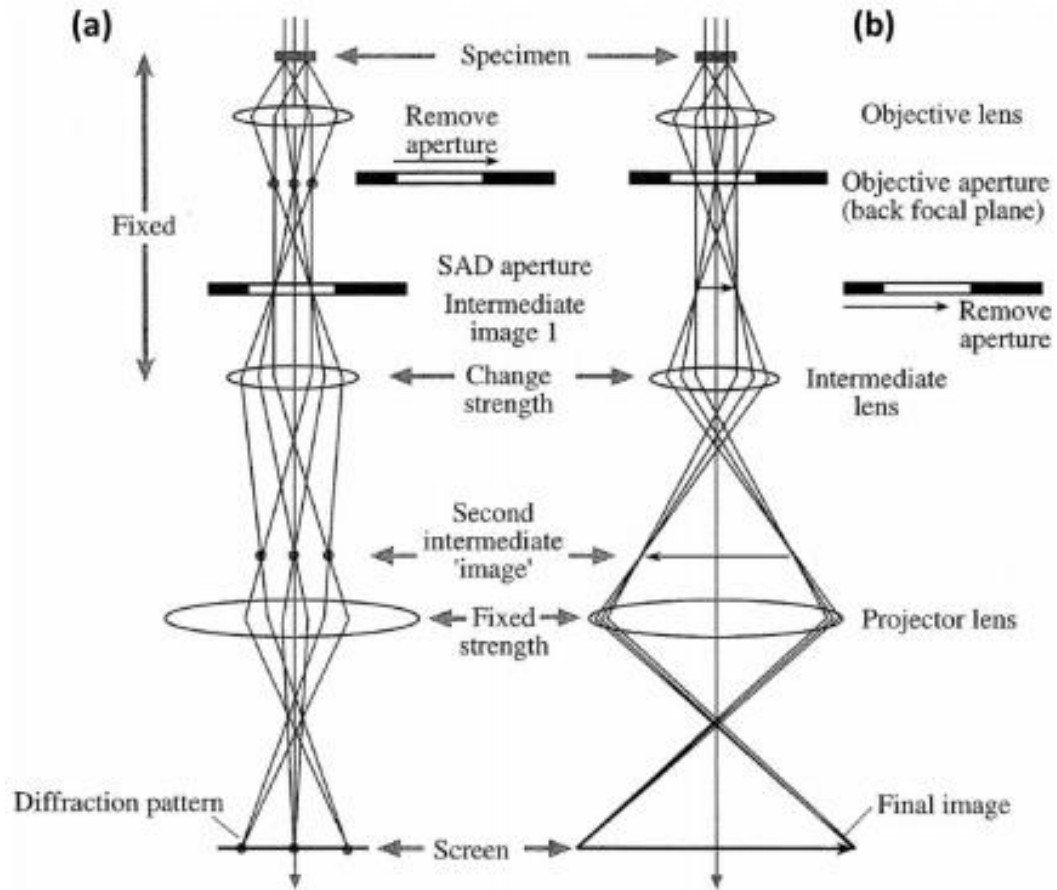
Figure 2.5 The two basic operation modes of the TEM system: (a) diffraction mode and (b) image mode. In each case the intermediate lens selects either the back focal plane or the image plane of the objective lens as its objects.[190]

To improve the contrast of imaging, appropriate objective apertures can be inserted

at the back focal plane of the objective lens. Two imaging modes can be obtained

depending on the objective aperture configuration and the beam diffraction. If only

transmitted electrons are allowed to pass, a bright-field (BF) image is formed as shown in

Figure 2.6(a). A dark-field (DF) image is obtained when only certain diffracted electrons

are allowed to pass as shown in Figure 2.6(b).
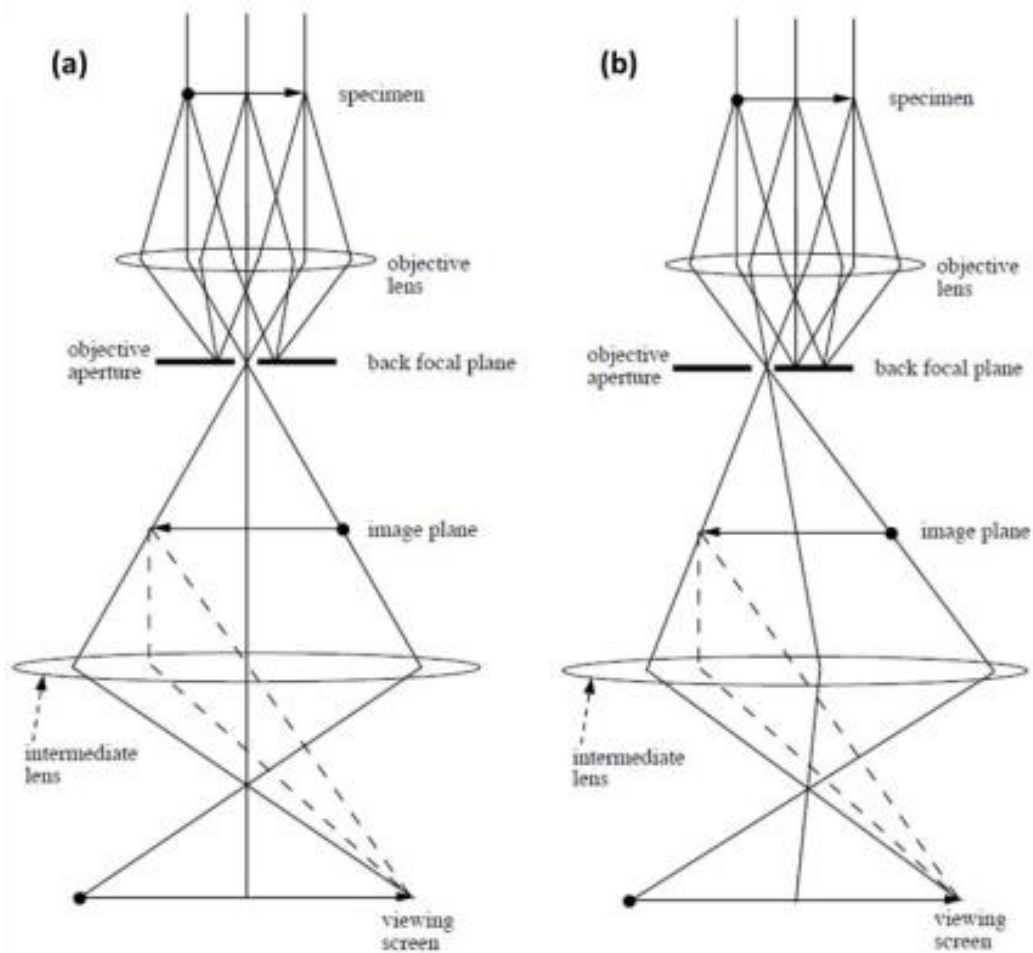
Figure 2.6 Schematic diagram showing the (a) bright-field and (b) dark-field imaging modes.[191]

2.2.3 Scanning transmission electron microscopy

Scanning transmission electron microscopy (STEM) is a Z-contrast technique

which can provide high-resolution images at atomic level with strong compositional

sensitivity. A key feature with STEM is that the scanning beam must not change direction as the beam is scanning. An advantage with STEM is that no lens is used in an STEM. The resolution of the STEM is controlled by beam only and is not affected by the defects in imaging lenses. A fundamental difference between the scanning STEM and static TEM is that the magnification of STEM is controlled by the scan dimensions on the specimen while the magnification of TEM is controlled by the lenses. For example, if the scanned dimension on the specimen is 10 nm and the resultant image is displayed with an area of 10 cm $\times$ 10 cm, then the magnification is 10^7 times. Similar to TEM, STEM also has two working modes: bright-field and dark-field STEM.

Different from the TEM using an objective aperture to select the direct or scattered electrons, in STEM detectors are used to select the direct or scattered electrons to form BF or DF images as shown by the comparison between TEM and STEM in Figure 2.7. As we can see in Figure 2.7, a BF on-axis detector or an annular DF (ADF) detector is inserted in a conjugate plane to the back focal plane. The electrons are controlled to fall on which detector and thus contribute to the image by adjusting the post-specimen (imaging) lenses to change the camera length. The ADF detector gathers more electrons than the objective aperture for DF imaging, which is good for imaging some specimens. More information regarding the BF and DF imaging can be found in some other references (Transmission electron microscopy: a textbook for materials science / David B. Williams and C. Barry Carter). In this dissertation, the HR-STEM images in high-angle annular dark-field (HAADF) mode were obtained using a FEI Titan G2 80-200 STEM with a Cs probe

corrector operated at 200 kV and a modified FEI Titan STEM TEAM 0.5 with a convergence semi-angle of 17 mrad operating at 200 kV, respectively.
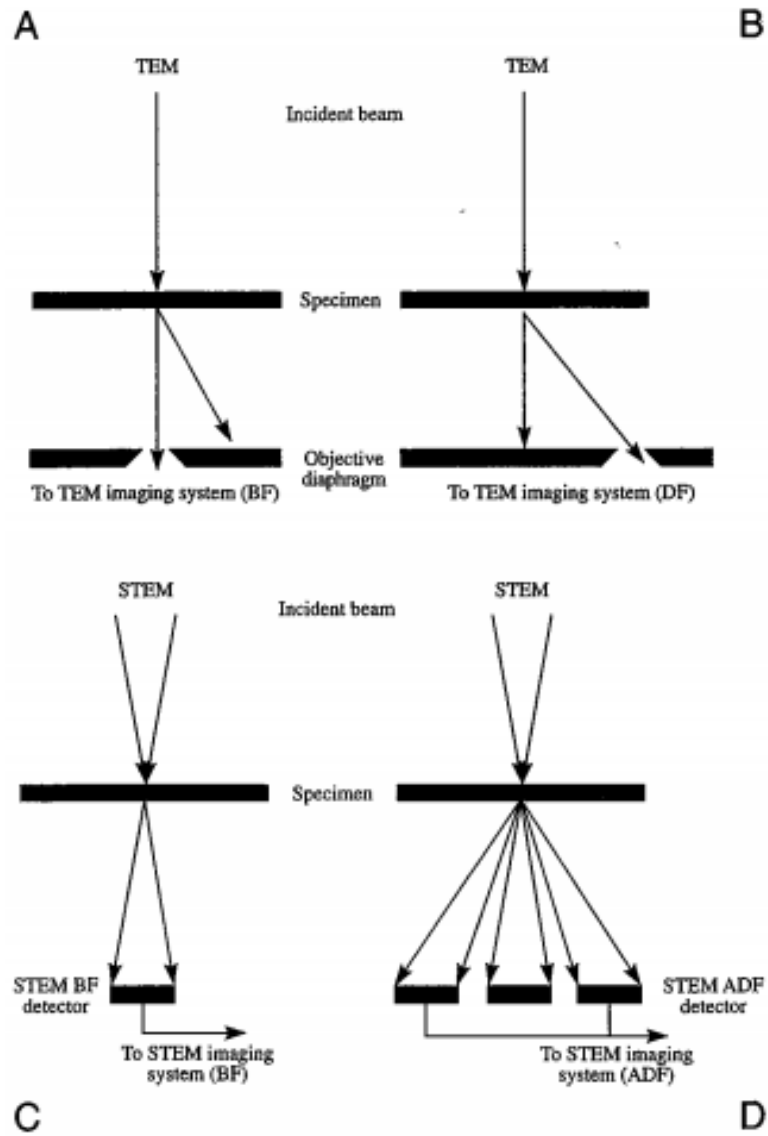
Figure 2.7 Comparison of the use of an objective aperture in TEM to select (A) the direct of (B) the scattered electrons form BF and DF images, respectively. In STEM an on-axis detector (C) or an annular detector is used to form BF or DF images.[191]

2.2.4 Energy-dispersive X-ray spectroscopy

Energy-dispersive X-ray spectroscopy (EDS) is used for elemental analysis or chemical characterization. With the help of an energy dispersive spectrometer, the number and energy of the X-rays emitted from the specimen will be measured quantitatively. The energies of the X-rays are characteristic of the energy difference of electrons from different shells and of the atomic structures of the element, the EDS has the capabilities of determining the chemical compositions of the specimen. For the high-resolution energy-dispersive X-ray spectroscopy (EDS) mapping in this dissertation, a FEI Titan^{TM} G2 80-200 STEM with a Cs probe corrector and ChemiSTEM^{TM} technology (X-FEG^{TM} and SuperX^{TM} EDS with four windowless Si drift detectors) operated at 200 kV was used.

2.2.5 TEM sample preparation

TEM sample preparation plays an important role in the microstructural characterization of the thin film samples. The main steps of preparing a TEM sample include: (1) cut small pieces of sample with the size of ~ 2 × 2 mm; (2) glue the two pieces of sample face-to-face and heat the sample; (3) thinning of the glued sample from the cross-section direction to 40-70 μm; (4) final grinding and polishing; (5) ion mill the sample to get a hole with thin area. A tripod polisher is used for the pre-thinning of the sample to 40-70 μm with the help of diamond lapping films and diamond polishing paste. After that, the sample is grinded to 20-25 μm and polished by a leather grinder. Finally, the sample is ion milled to get electron-transparent thin area in a Gatan Precision Ion Polishing System (Gatan).

2.3 Physical property measurement

2.3.1 Magnetic property measurement

The magnetic properties including magnetizations and resistance were measured in a Physical Properties Measurement System (PPMS 6000, Quantum Design) equipped with a vibrating sample magnetometer (VSM) option. The PPMS can achieve magnetic field up to 9 T and a temperature range of 1.9-400 K. The noise for VSM measurement is less than 5×10^{-7} emu. Figure 2.8(a) shows the basic components of the PPMS. The black container is the EverCool dewar system and the blue box on the right side is the electronic control part for VSM option. The sample drive motor and detection coil set of the VSM option is shown in Figure 2.8(b). The induced voltage is detected by oscillating the sample near a detection coil after the sample is loaded at the center of the magnet. Two magnetic measurements were conducted in this study. The first is the magnetization *vs.* magnetic field (*M-H*) measurement. The magnetizations were recorded at different temperatures after applying a magnetic field which is either perpendicular (out-of-plane) or parallel (in-plane) to the film plane. The second magnetic measurement is the magnetization *vs.* temperature (*M-T*). For *M-T* measurement, it includes zero-field cooling (ZFC) and field cooling (FC) measurement. For ZFC and FC measurements, the samples were first cooled down from a high temperature to a low temperature without or with a magnetic field applied to the samples, respectively, and the magnetizations were recorded when the samples were heated to a high temperature.

Figure 2.8 (a) The Quantum Design PPMS equipment in the laboratory. (b) The sample motor drive and detection coil set for VSM option.

2.3.2 Electrical property measurement

The piezoelectric properties were measured at ambient conditions with a conductive Pt-Ir coated Si tip (model: SCM-PIT) via a Bruker Dimension Icon atomic force microscopy (AFM) with high resolution (Z < 0.1 nm, XY < 1 nm). The schematic in Figure 2.9 shows how the AFM works for piezoelectric property measurement. During the piezoelectric measurement, an external voltage with a certain frequency was applied to the sample through the conductive tip. Due to the converse piezoelectric effect, the sample under the electric field will vibrate at the same frequency. The vibration of the sample will force the tip to oscillate and the modulated deflection signal is detected by the lock-in amplifier. In order to avoid the mechanical resonance of the cantilever, the frequency of the applied voltage is much lower than that of the cantilever. The ferroelectric property of the samples is referenced to the piezoelectric response in the forms of amplitude change and phase change.
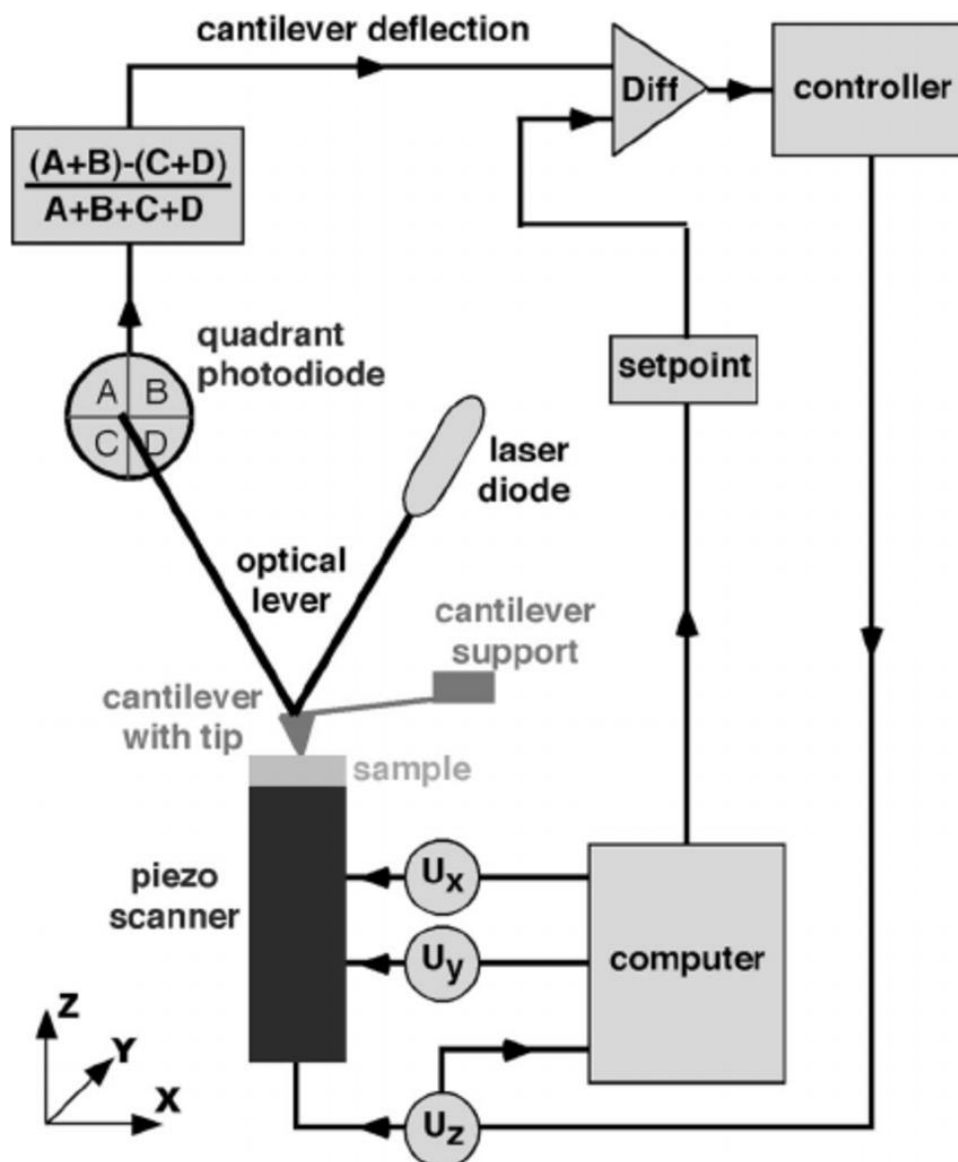
Figure 2.9 Schematic of piezoelectric response measurement in contact mode AFM.[192]

2.4 Precision electron diffraction tomography

Precession electron diffraction (PED) patterns were obtained using a JEOL 2010 (200 kV) transmission electron microscope (TEM) equipped with a side-mounted Gatan Orius CCD camera and a Nanomegas Digistar PED unit. The data collection was performed on a cross-sectional sample prepared from a film using the tomography

approach.[193] In such a case, the rotation axis is mostly limited to the out-of-plane direction to avoid shadowing the film by the substrate. PED patterns were recorded in the tilt range from -44.5 to +34.8 degrees with a precession angle of 1.2 degree. The data were processed using the programs PETS[194] and Jana2006[195].

CHAPTER III

STRAIN AND INTERFACE EFFECTS IN A NOVEL BISMUTH-BASED SELF-ASSEMBLED SUPERCELL STRUCTURE[*]

3.1 Overview

BFMO thin films with both conventional pseudocubic structure and novel supercell structure have been grown on $SrTiO_3$ (001) substrates with different thicknesses of CeO_2 buffer layers (ranging from 6.7 nm to 50.0 nm) using pulsed laser deposition. The correlation between the thickness of the CeO_2 buffer layer and the structure of the BFMO films shows that the CeO_2 buffer layer, as thin as 6.7 nm, is sufficient in triggering the novel BFMO supercell structure. This may be ascribed to the interfacial strain between the BFMO supercell structure and the CeO_2 buffer layer which also serves as a seed layer. The buffer layer thickness is found to be critical to control the microstructure and magnetism of the formed BFMO supercell structures. Thin seed layers can produce a smoother interface between the BFMO film and the CeO_2 buffer layer, and therefore better ferrimagnetic properties. Our results have demonstrated that strain and interface could be utilized to generate novel thin film structures and to tune the functionalities of the thin films.

3.2 Introduction

Complex transition metal oxides, including perovskite, double-perovskite, spinel, rocksalt, rutile, etc., have been extensively studied in the past decades.[7, 56, 196, 197, 198, 199, 200, 201] The development of state-of-the-art thin film growth techniques and the growing needs for oxide-based functional devices have further stimulated the progress in this field.[44, 202, 203] Diversified unique physical properties have been reported, such as magnetoresistance,[40, 41, 43] multiferroism,[7, 200, 204, 205, 206, 207] magnetoelectricity,[208, 209] and high-temperature superconductivity[210]. These physical properties are strongly correlated to the lattice structures of complex oxides. Among all the factors controlling complex oxide lattice structures, strain has been reported to play a critical role in tailoring the lattice structures and therefore the functionalities of transition metal oxide thin films.[184, 196] For example, strain engineering provides an easy and effective way to control the overall film structure and thus tune the physical properties, such as the giant magnetocaloric effect in $La_{0.7}Ca_{0.3}MnO_3$,[211] the enhanced perpendicular magnetic anisotropy in $BiFeO_3:CoFe_2O_4$,[25] and the tunable low-field magnetoresistance in $(La_{0.7}Sr_{0.3}MnO_3)_{0.5}:(ZnO)_{0.5}$.[40, 42]

More attractively, strain engineering could trigger new structures, for example, the intermediate pseudomorphic structures Ti_2O_3 and V_2O_3 have been previously reported in $TiO_2/Ti_2O_3/Al_2O_3$ and $VO_2/V_2O_3/Al_2O_3$ heterostructures,[11, 184, 212] respectively. Another exciting example is the formation of the novel self-assembled $Bi_3Fe_2Mn_2O_x$ supercell (BFMO322 SC), which was enabled by the careful selection of substrates and deposition parameters.[184, 186] It is a novel layered oxide structure which is formed on $LaAlO_3$ (LAO)

substrates, and exhibits superior multiferroic properties at room temperature with the saturation magnetization value of 110 emu/cc. Strain was found to play a critical role in the formation of the new BFMO322 SC structure.[184, 186] Comparing the lattice mismatch between the SrTiO$_3$ (STO) substrate and the BFMO pseudocubic structure (–0.6%) with that between LAO and BFMO322 SC (–2.0%), the later exhibits a much larger lattice mismatch which could be the primary reason triggering the formation of a thin strained transition layer (~5 nm) before the formation of the supercell phase. This reassembles the characteristics of a typical pseudomorphic growth in thin film epitaxy, i.e., a thin layer of highly strained layer was formed within a critical thickness and beyond that, the film is relaxed with misfit dislocations nucleated at the transition interface.[11, 212] However the BFMO322 SC case is much more complicated with a new phase formation and the strain relaxation mechanism is thus quite different from the simple nucleation of misfit dislocations.

To explore the formation mechanism of the BFMO322 SC structure, a unique approach could be used to grow the critical transition layer with various film thicknesses, and explore the corresponding phase transformation. Here we select a CeO$_2$ buffer layer as the critical transition layer. We have demonstrated that a thin layer of CeO$_2$ could also serve as an excellent buffer layer enabling the growth of BFMO322 SC. This is because a 45° in-plane rotated CeO$_2$ (a = 5.411 Å, a/$\sqrt{2}$ = 3.826 Å) provides a perfect lattice match for the growth of the BFMO322 SC phase on SrTiO$_3$ substrates (a = 3.905 Å). In this study, the effects of the strain and the interface structure of the CeO$_2$ buffer layer on the microstructure and ferrimagnetic property of BFMO films were investigated by

systematically controlling the CeO_2 buffer layer thickness. The results could shed light on the supercell growth mechanisms that can be generalized to other supercell systems for new functionalities.

3.3 Experimental

The composite BFMO and the CeO_2 targets were prepared by a conventional solid state sintering method. For the BFMO target, the powders of Bi_2O_3, Fe_2O_3 and MnO_2 were mixed in stoichiometric ratio, pressed into a pellet, and then sintered at 800 ^{o}C for 3 hours. For CeO_2 target, the powder of CeO_2 was pressed into a pellet and annealed at 1200 ^{o}C for 6 hours. The growth of BFMO films and CeO_2 buffer layers was conducted using pulsed laser deposition (PLD) under an optimized substrate temperature of 700 ^{o}C and an oxygen pressure of 200 mTorr. After deposition, the films were *in-situ* annealed at 400 ^{o}C for 1 hour with an oxygen pressure of 500 Torr and then cooled down to room temperature with a cooling rate of 5 ^{o}C/min.

The microstructures of the films were investigated by high resolution X-ray diffraction (HRXRD, PANalytical Empyrean) and transmission electron microscopy (TEM, FEI Tecnai G2 F20). The high resolution scanning transmission electron microscopy (HRSTEM) images in high angle annular dark-field (HAADF) mode (also called Z-contrast imaging) were obtained using a FEI Titan G2 80–200 STEM with a Cs probe corrector operated at 200 kV and a modified FEI Titan STEM TEAM 0.5 with a convergence semi-angle of 17 mrad operating at 300 kV. The magnetic properties of the films were investigated using the vibrating sample magnetometer (VSM) option in a

commercial Physical Properties Measurement System (PPMS 6000, Quantum Design). During measurements, the out-of-plane and in-plane magnetization were recorded by applying a magnetic field of 1 T perpendicular and parallel to the film plane, respectively.

3.4 Results and discussion

Figure 3.1 shows the θ-2θ XRD patterns of the BFMO films directly on STO and on CeO_2 buffered STO substrates. Figure 3.1(a) indicates the high quality textured growth of BFMO pseudocubic structure along the (00l) direction of STO as evidenced by the dominant BFMO (00l) diffractions. Significantly different from the pseudocubic structure directly grown on STO, however, a new set of (00l) peaks along with CeO_2 (002) and (004) peaks appear when the film was deposited on STO substrate buffered by 6.7 nm CeO_2 as shown in Figure 3.1(b). This new set of diffractions belongs to the layered BFMO322 SC structure which is composed of Bi_2O_2 sheets and distorted FeO_6/MnO_6 octahedra[184] as shown by the high resolution STEM image of the supercell structure in Figure 3.2(a) and (b).
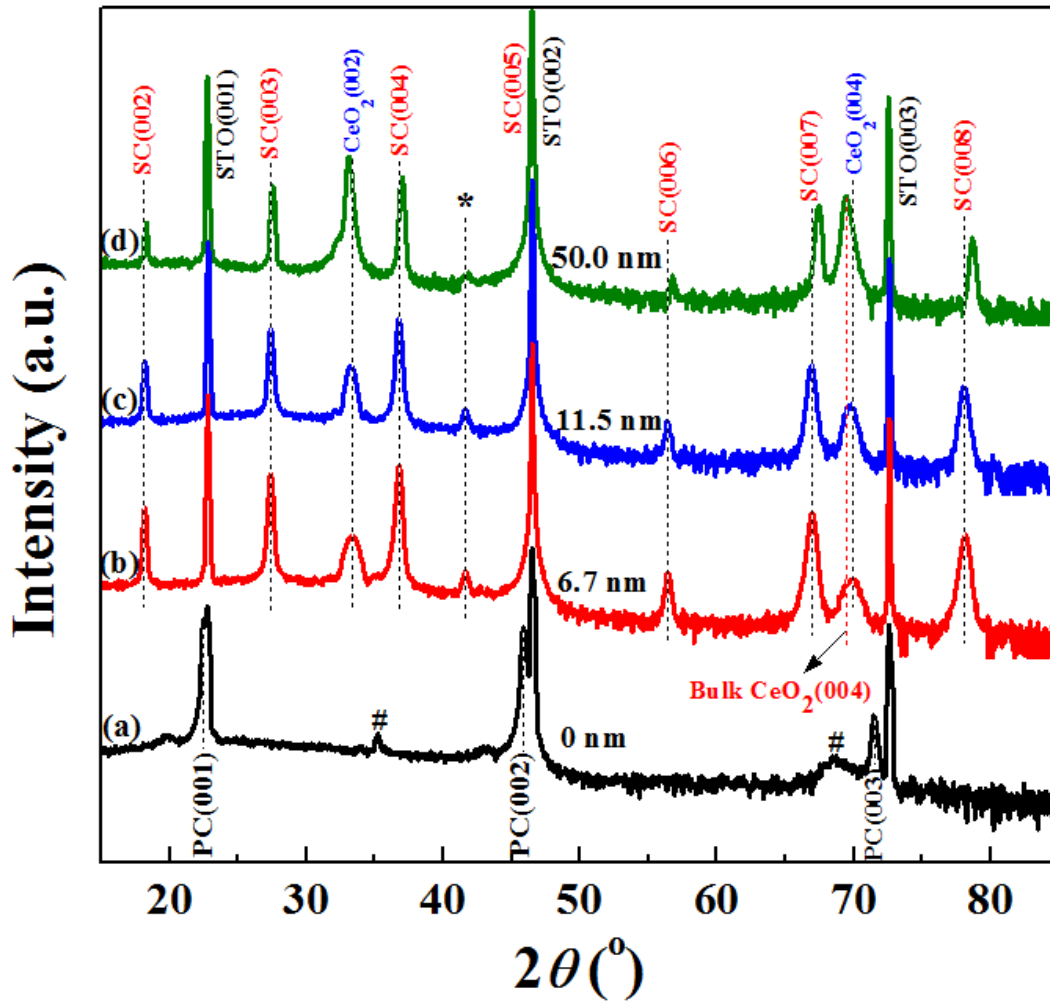
Figure 3.1 (a) XRD θ-2θ scans of BFMO film directly grown on STO substrate with a pseudocubic structure. The "#" indicates impurity phase and PC means pseudocubic phase. (b)-(d) XRD scans of the BFMO322 SC structure grown on STO substrates buffered by different thicknesses of CeO_2 ranging from 6.7 nm, 11.5 nm, to 50.0 nm, respectively. The "*" indicates a minor phase $Bi_{25}FeO_{40}$.

The bright sheets in Figure 3.2(a) are attributed to the Bi_2O_2 due to the heavier element of Bi ($Z_{Bi} = 83$) than that of Fe ($Z_{Fe} = 26$) and Mn ($Z_{Mn} = 25$). Figure 3.2(b) clearly shows the bright zigzag Bi_2O_2 sheets as well as the less bright distorted FeO_6/MnO_6 octahedra. For the composition of the BFMO thin films, dispersive x-ray spectroscopy (EDS) analysis was conducted and showed that there is about 9% bismuth loss for the

conventional pseudocubic phase while the cation ratio of the novel supercell phase is Bi:Fe:Mn = 3:2:2, with higher bismuth loss. This is also confirmed by the atomic model built for the supercell structure based on the previous report.[184] As the CeO_2 thickness increases to 11.5 nm and 50.0 nm, similar XRD results to that of Figure 3.1(b) have been obtained as shown in Figure 3.1(c) and (d), respectively. It is interesting to note that the peaks of the CeO_2 buffer layer shift to the left while the new supercell structure shifts to the right with increasing the CeO_2 thickness. For example, the CeO_2 (004) peak shifts from 69.80° to 69.40° and SC (008) peak shifts from 78.10° to 78.65° when the CeO_2 thickness increases from 6.7 nm to 50.0 nm. For the left shift of the CeO_2 peaks, it could be attributed to that, with the increase of the CeO_2 thickness from 6.7 nm to 50.0 nm, the strain generated from the substrate is relaxed as shown by the red dashed line for bulk CeO_2 (004) peak in Figure 3.1. For the right shift of the supercell peaks buffered by 50.0 nm CeO_2, it is to be discussed in the later part.
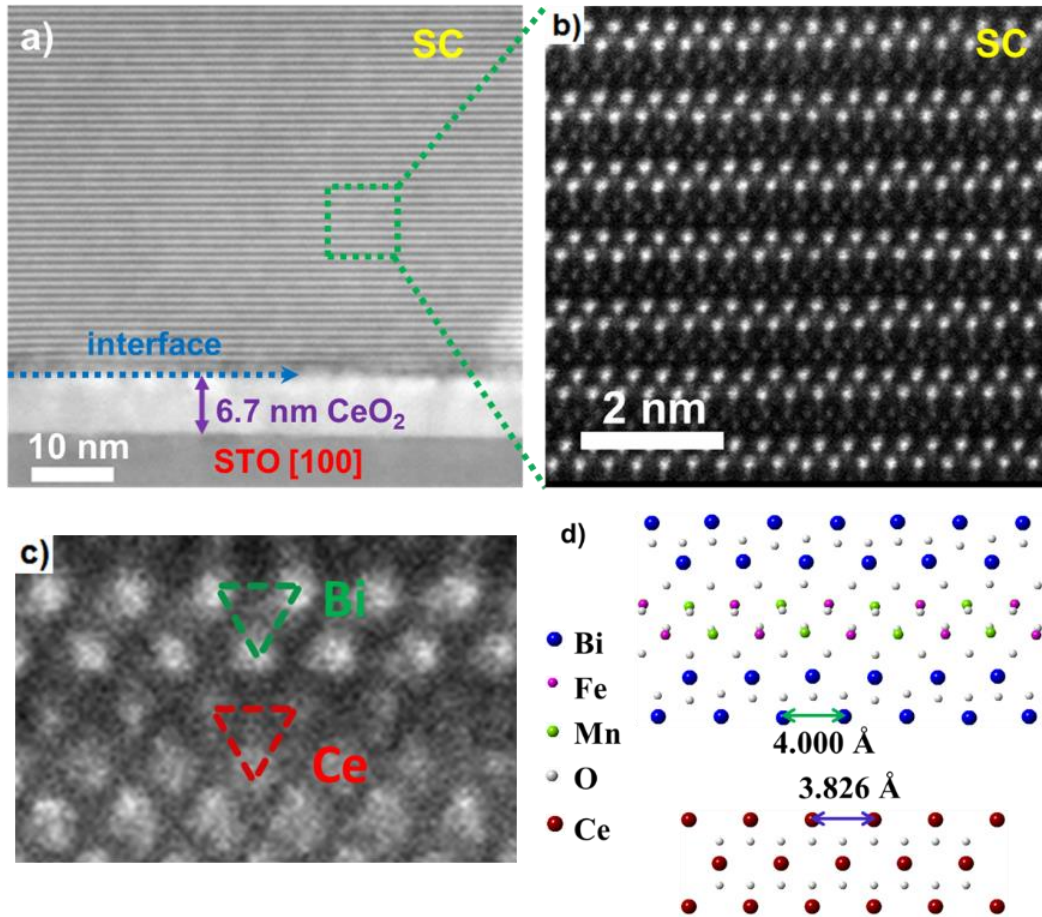
Figure 3.2 Cross-sectional STEM image of the 6.7 nm CeO$_2$ buffered BFMO322 SC with low magnification (a) and high magnification (b), STEM image of the interface between BFMO322 SC and CeO$_2$ (c), schematic model showing the interface lattice matching between BFMO322 SC and CeO$_2$ (c), schematic model showing the interface lattice matching between BFMO322 SC and CeO$_2$ (d).

To better understand the microstructure evolution as a function of the CeO$_2$ buffer layer thickness, cross-sectional TEM was conducted for both the BFMO films grown on STO only and CeO$_2$-buffered STO substrates, as shown in Figure 3.3. Figure 3.3(a) shows the cross-sectional TEM image of the BFMO film directly grown STO substrate with the pseudocubic structure. The corresponding selected area diffraction (SAED) pattern shown as the inset in Figure 3.3(a) clearly illustrates the pseudocubic structure and high-quality

epitaxy of the film with clear cubic lattice fringes. Completely different from the pseudocubic BFMO structure directly grown on STO substrate, however, a distinctively new layered structure (BFMO322 SC) is formed on the 6.7 nm CeO_2 buffered STO substrates, as shown in Figure 3.2(b) and Figure 3.3(b). The distinguished diffraction dots in the inset of Figure 3.3(b) indicate the highly epitaxial growth of the BFMO322 SC structure. For the two distinctively different BFMO structures, the strain mapping analysis of these two structures has shown that strain may play an indispensable role in triggering the formation of the supercell structure.[186] As discussed above, the strain between the BFMO film and the STO substrate is only -0.6% while it is -2.0% for the BFMO film and the LAO substrate. The relatively small lattice mismatch between the BFMO film and the STO substrate has enabled the cube-on-cube growth. The much larger lattice mismatch between BFMO film and LAO substrate, however, leads to the growth of highly distorted pseudocubic structure, forming a thin transition layer. With the increase of film thickness, the large strain in the transition layers gets relaxed followed by the formation of the novel layered structure. For the CeO_2 buffered BFMO samples in this work, the 45º-rotated CeO_2 provides an optimal lattice match between CeO_2 and BFMO322 SC and the strain is calculated to be about -4.4% between CeO_2 and BFMO322 SC (Figure 3.2(c) and (d)). Furthermore, the zigzagged Ce-Ce layer has served as an ideal template for the following Bi-Bi layer. Overall, both the large strain between CeO_2 and BFMO322 SC and the zigzagged Ce-Ce bonding structure have triggered the formation of the BFMO322 SC.
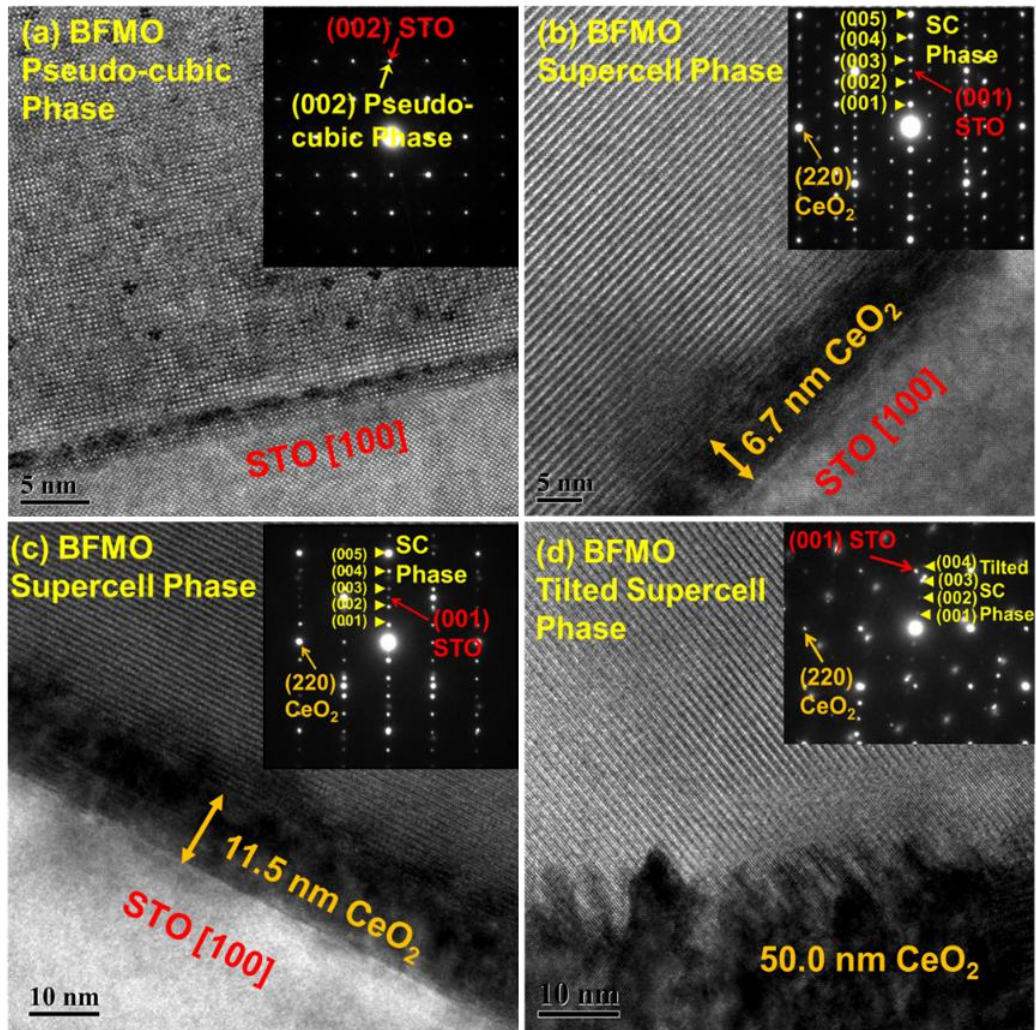
Figure 3.3 Cross-sectional TEM images and diffraction patterns of the BFMO samples (along (100) zone axis). (a) BFMO with pseudocubic structure. (b)-(d) BFMO322 SC structure with the CeO_2 thickness of 6.7 nm, 11.5 nm, and 50.0 nm, respectively.

For the 11.5 nm CeO_2 buffered case, a similar quality of BFMO films with distinctive diffraction patterns was obtained (Figure 3.3(c)), except a small amount of tilted supercell growth observed in few areas (Figure 3.4). When the thickness of the CeO_2 buffer layer was increased to 50.0 nm, the film quality of both the CeO_2 buffer layer and the BFMO film is distinctively lower than those of the thinner buffer layer cases, as shown

by Figure 3.3(d). The interface between the BFMO film and the CeO_2 buffer layer is no longer smooth as that in Figure 3.3(b) and (c) and the Bi_2O_2 lattices of the supercell are not parallel to the surface of the STO substrate. Instead, the Bi_2O_2 lattices form a certain angle with the lattice of the STO substrate. This tilted supercell structure is quite different from the 6.7 nm and 11.5 nm CeO_2 buffered samples and thus results in different peak positions in XRD results (Figure 3.1). The microstructure evolution of BFMO films with the increase of the CeO_2 buffer layer thickness could be correlated to the strain state of the CeO_2 buffer layer and the interface morphology between the BFMO film and the CeO_2 buffer layer. The interface between the BFMO film and the CeO_2 buffer layer of the 6.7 nm CeO_2 buffered sample is sharp and smooth (Figure 3.2(a) and Figure 3.3(b)) owing to the layer-by-layer growth of the strained CeO_2 buffer layer with the in-plane 45° rotation on STO. This smooth interface has served as an optimal surface seed layer to trigger the growth of the highly epitaxial supercell structure with the Bi_2O_2 sheets parallel to the surface of the STO substrate. The film structure and the interface of the 11.5 nm CeO_2 buffered sample resembles that of the 6.7 nm CeO_2 buffered sample except that tilted supercell phase has been observed in some areas (Figure 3.4) due to the island growth of the CeO_2 buffer layer initiated around this CeO_2 thickness. The growth of the tilted supercell become dominant for the 50.0 nm CeO_2 buffered sample (Figure 3.3(d) and Figure 3.5). This could be ascribed to the rough interface due to the dominant island growth of the CeO_2 buffer layer. Owing to the island morphology of the CeO_2 buffer layer, the BFMO322 SC lattice has coupled to island lattice facets which could trigger the tilted

growth of the supercell. Overall the above findings suggest the CeO$_2$ buffer layer thickness

plays a critical role in the film strain, surface morphology and the resulted film structures.
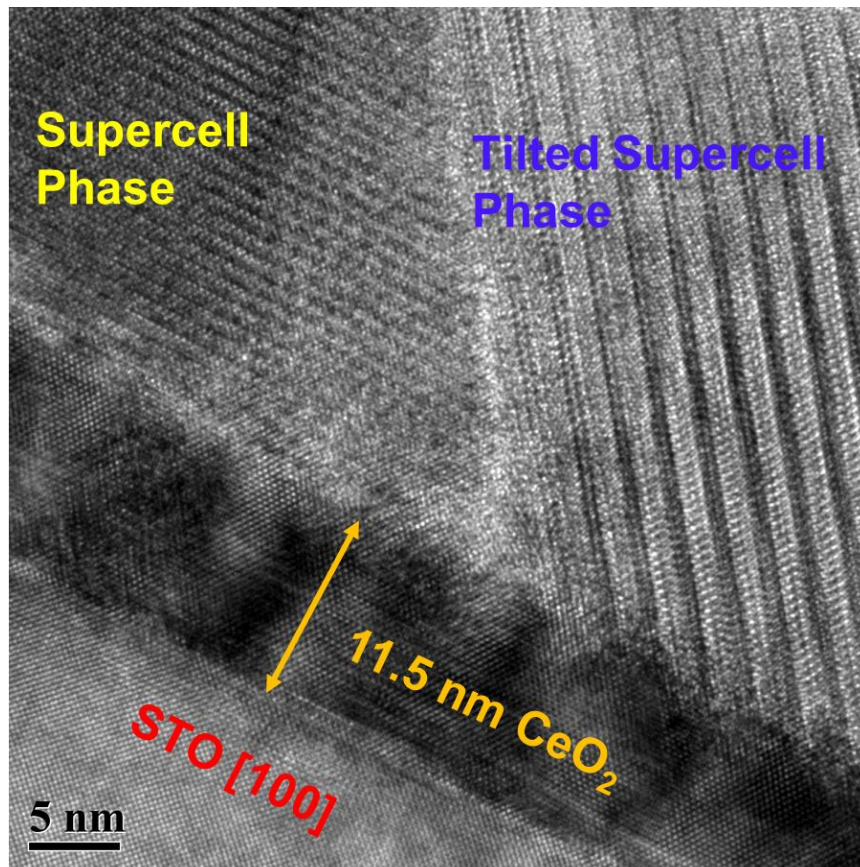
Figure 3.4 Cross-sectional TEM image of 11.5 nm CeO$_2$ buffered BFMO sample.
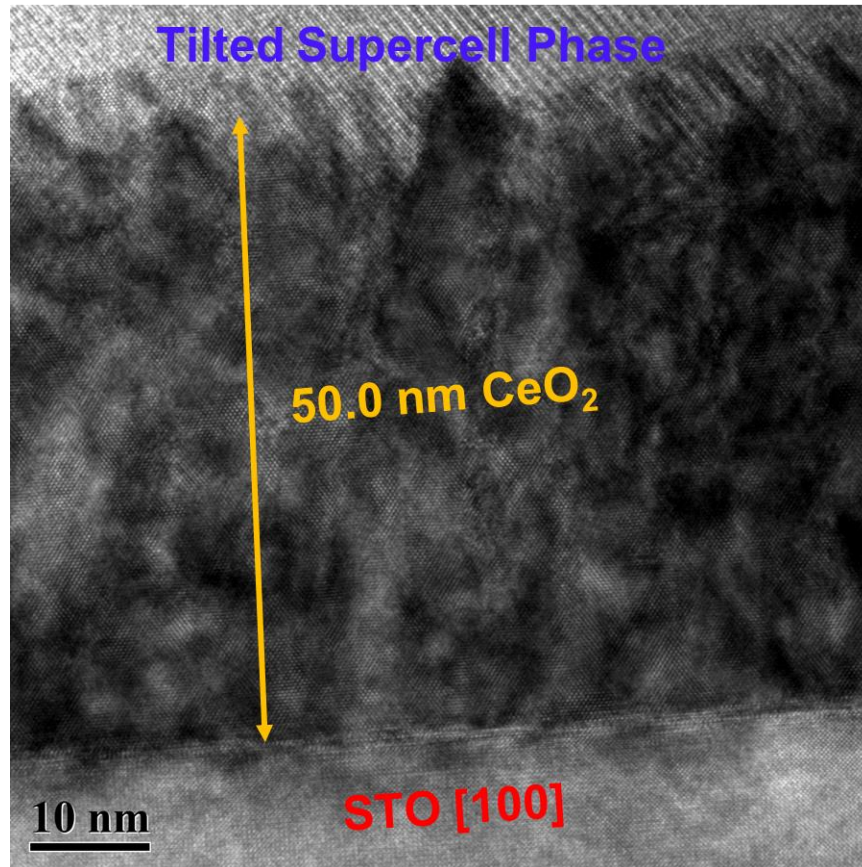
Figure 3.5 Cross-sectional TEM image of 50.0 nm CeO_2 buffered BFMO sample.

To reveal the structure-property correlation of the BFMO films, room temperature (300 K) magnetic hysteresis loops were obtained by applying magnetic field perpendicular (out-of-plane, OP) and parallel (in-plane, IP) to the film surface as shown in Figure 3.6. By comparing the out-of-plane magnetic hysteresis of the BFMO films directly deposited on STO with that on CeO_2 buffered STO, it is obvious that the supercell structure grown on the CeO_2 buffer layer is superior to the conventional pseudocubic structure. From Figure 3.6(b), it is clearly shown that the BFMO film with a 6.7 nm CeO_2 buffer layer has a higher out-of-plane saturation magnetization value of about 226 emu/cc than that of the

BFMO sample with the pseudocubic structure (126 emu/cc in Figure 3.6(a)) in this work. This result clearly suggests the superior magnetic properties of the novel self-assembled supercell structure. Furthermore, the 6.7 nm CeO_2 buffered sample shows a strong magnetic anisotropy, which benefits the high-density magnetic memory device applications. The much stronger magnetization and distinguished magnetic anisotropy of the supercell structure could be attributed to the strong anisotropic layered structure and the resulted highly anisotropic properties. Coupled with the ferroelectric properties from the previous report,[184] the remnant polarization value P_r is 6.0 $\mu C/cm^2$ for the novel BFMO supercell phase while the conventional BFMO phase showed a P_r of 2.7 $\mu C/cm^2$. Although its P_r value is lower than that of other ferroelectric materials, such as $BiFeO_3$ with P_r of 60-80 $\mu C/cm^2$, the supercell structure with CeO_2 buffer showed a much stronger room temperature magnetization of 226 emu/cc compared to $BiFeO_3$ (< 40 emu/cc).

It is noted that with the increase of the CeO_2 buffer layer thickness, the saturation magnetization values decrease. For example, when the CeO_2 thickness increases to 11.5 nm, the supercell structure exhibits a relatively lower out-of-plane saturation magnetization value of 161.9 emu/cc (Figure 3.6(c)). This lowered saturation magnetization value could be related to the tilted supercell structure in certain areas of the film (Figure 3.4). For the sample with 50.0 nm CeO_2 buffer layer, it shows the lowest saturation magnetization value and magnetic hysteresis anisotropy among all the supercell structures (Figure 3.6(d)). In this case, the interface between the film and the CeO_2 buffer layer is no longer as smooth as that in the other samples and a large amount of tilted supercell phase exists (Figure 3.3(d) and Figure 3.5). This results in a much lower

saturation value and magnetic anisotropy. There is a concern on the possible magnetic properties introduced by the CeO_2 layer, since CeO_2 with high density Ce and/or oxygen vacancies has been reported to be ferromagnetic by previous reports.[213, 214] However, in this case the magnetism contribution from CeO_2 is minimal as the CeO_2 layer is thin and the films have minimum amount of oxygen vacancies due to the post-deposition annealing procedure.

The variation of the magnetic property as a function of the CeO_2 buffer thickness is also consistent with the above TEM, STEM, and XRD results. These results indicate that a critical thickness range for the CeO_2 buffer layer is required for the formation of the smooth interface and thus the high phase purity and high epitaxial quality of the BFMO322 SC structure. The 6.7 nm CeO_2 buffer layer is the optimal condition with a smooth interface between the supercell structure and the CeO_2 buffer layer and the optimal seed layer pattern for the formation of highly epitaxial BFMO322 SC structure with the highest saturation magnetization value and magnetic anisotropy. This clearly suggests the advantage of the CeO_2 buffer layer in enabling the formation of novel supercell structure with enhanced magnetic properties. The correlation between the magnetic properties and the structures of the BFMO films has demonstrated the important role of the interface and strain in tailoring the microstructure of the film as well as tuning the physical properties.
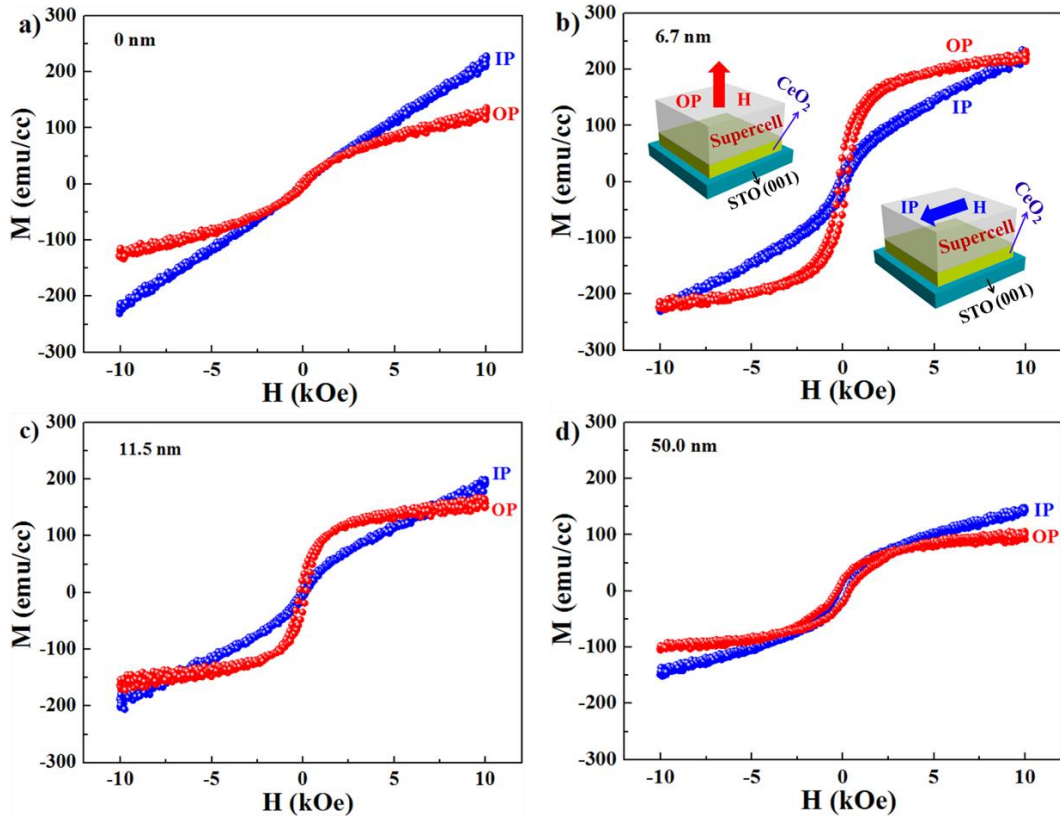
Figure 3.6 Room-temperature magnetic properties of the BFMO films. (a) Out-of-plane (OP) and in-plane (IP) magnetic hysteresis loops of the BFMO film with pseudocubic structure. (b)-(d) OP and IP magnetic hysteresis loops of the BFMO322 SC structure grown on STO substrates buffered by different thicknesses of CeO$_2$ ranging from 6.7 nm, 11.5 nm, to 50.0 nm, respectively.

3.5 Conclusion

In summary, the thickness dependence effects of the CeO$_2$ buffer layer on the microstructure and magnetic properties of the BFMO films have been studied. Without the CeO$_2$ buffer layer, a conventional pseudocubic structure has been obtained on STO substrate with a minimum saturation magnetization value. When buffered by CeO$_2$, a novel layered supercell structure forms because of the strain and surface structure induced by the CeO$_2$ buffer layer. The magnetic property measurement shows that the novel

supercell structure with the optimal CeO_2 buffer layer thickness of 6.7 nm exhibits significantly enhanced magnetic properties compared to the conventional pseudocubic structure without the CeO_2 buffer. Moreover, it has been demonstrated that the interface morphology between the BFMO and CeO_2 layers plays a crucial role in the formation of the supercell structure with superior magnetic property. This study demonstrates that both strain and interface can be used to tune the structural and physical properties of the transition metal oxide thin films for novel structures and new functionalities.

CHAPTER IV

TUNABLE PHYSICAL PROPERTIES IN TWO-DIMENSIONAL BI-BASED LAYERED SUPERCELL STRUCTURES VIA COMPOSITION VARIATION

4.1 Overview

$Bi_2Fe_{1-x}Mn_xO_6$ systems with layered supercell structure have been grown on CeO_2 buffered $SrTiO_3$ (STO) (001) substrates by pulsed laser deposition. The Fe/Mn molar ratio has been varied to explore the fundamental growth mechanism of the layered structures and their corresponding magnetic property. It is found that Mn element plays a critical role in the formation of the bismuth-based layered supercell structures. With Mn-rich composition ($x \geq 0.5$), the Bi-based layered structures can be easily fabricated on CeO_2 buffer layer, while Fe-rich ($x < 0.5$) results in regular psuedocubic phase. More interestingly, the layered supercell structure can be fabricated from $BiMnO_3$ on both CeO_2-buffered STO and STO substrates, respectively, under well controlled growth conditions. This study sheds light on the growth mechanism of the Bi-based layered supercell structures and the mechanism for its ferromagnetic properties, and thus is of great significance to the design of new Bi-based layered structures.

4.2 Introduction

Multiferroics with more than one ferroic order coexisting in a single phase have attracted significant research interests because of their rich physics behind and enormous potential for device applications.[26, 44, 63, 98, 114] Among the several groups of multiferroic

materials, Bi-based lone-pair multiferroics with the perovskite ABO_3 structure, have attracted renewed interest. For Bi-based ABO_3 perovskites, the ferroelectricity comes from the high stereochemical activity of the lone-pair electrons on the A-site cation while the smaller B-site cation provides the magnetism. $BiFeO_3$[7, 215, 216, 217] and $BiMnO_3$,[85, 88, 91, 98, 218] are two of the most important lone-pair multiferroic materials and have been extensively studied due to their multiferroic properties and magnetoelectric effect. Besides the above mentioned single-perovskites, Bi-based double-perovskites, BiBB'O$_6$ (B and B' are transition metal cations), have also triggered special attention arising from their long-range ferro/ferri-magnetically ordered B and B' cations as well as desirable ferroelectricity from the Bi $6s^2$ lone pairs. For example, Bi_2NiMnO_6, the most extensively studied double-perovskite in pseudocubic structure, has been proven to possess long-range ordered ferromagnetism with a Curie temperature of about 105 K.[127, 129, 130, 131]

Bi_2FeMnO_6 (i.e., $BiFeO_3$:$BiMnO_3$ = 1:1, BF_1M_1O), another well-known Bi-based double-perovskite, has also been widely studied.[113, 114, 184] Bi_2FeMnO_6 in pseudocubic phase has been reported with room-temperature ferroelectricity and ferrimagnetism, in either bulk form prepared under extreme conditions or thin film form deposited by pulsed laser deposition (PLD) on single-crystal substrate $SrTiO_3$ (STO) (001).[102, 108, 110, 111, 113, 114] When deposited on $LaAlO_3$ (LAO) (001) substrate, however, a novel layered $Bi_3Fe_2Mn_2O_{10-\delta}$ supercell (called BFMO322 SC) structure was obtained with enhanced multiferroic property.[184, 185, 186, 219] For the novel BFMO322 SC structure, it can be grown on LAO substrates or CeO_2 buffered STO (as thin as 6.7 nm).[185, 219] STEM images combined with geometric phase analysis (STEM-GPA) suggested that the interfacial strain

plays a special role in the formation of the BFMO322 SC.[186] However, the fundamental

formation mechanisms of the BFMO322 SC structure is still unclear. One of the key

parameters yet to be explored is the role of Mn composition, i.e., the molar ratio of Fe/Mn,

on the overall formation of such layered supercell structure and the impacts on their

magnetic property.

In this work, $Bi_2Fe_{1-x}Mn_xO_6$ (BFMO) thin films with different Fe/Mn molar ratios

were designed and deposited on ~6.7 nm CeO_2 buffered STO substrates to investigate the

fundamental formation mechanisms and to achieve tunable physical properties, such as

multiferroic properties. Composite $BiFeO_3$-$BiMnO_3$ targets with molar ratios of 1:0 (pure

$BiFeO_3$), 4:1, 2:1, 1:1, 1:2, 1:4, and 0:1 (pure $BiMnO_3$) were prepared (denoted as $F_{all}M_0$,

F_4M_1, F_2M_1, F_1M_1, F_1M_2, F_1M_4, and F_0M_{all}, respectively). This study could serve two roles,

one is to shed light on the growth mechanism of the Bi-based layered supercell structures

which may further help the design and fabrication of other new Bi-based layered structures

for multiferroism; another is to explore the tunability of physical properties in these novel

layered supercell structures by fine tuning of the compositions.

4.3 Experimental details and first-principle calculation

To prepare the composite $Bi_2Fe_{1-x}Mn_xO_6$ targets with different Fe/Mn molar ratios

(1:0, 4:1, 2:1, 1:1, 1:2, 1:4, and 0:1), Bi_2O_3, Fe_2O_3, and MnO_2 powders in specific ratios

were mixed, pressed into pellets, and annealed at 800 °C for 3 hours. For the CeO_2 target,

CeO_2 powder was pressed into a pellet and annealed at 1200 °C for 6 hours. Pulsed laser

deposition (PLD, Lambda Physik, KrF, $\lambda = 248$ nm) was employed to deposit the CeO_2

buffer layers and BFMO films at an optimized substrate temperature of 700 $^{\circ}$C. An oxygen pressure of 200 mTorr was maintained during deposition. After deposition, the films were *in-situ* annealed at 400 $^{\circ}$C for 1 hour with an oxygen pressure of 500 Torr and then cooled down to room temperature with a cooling rate of 5 $^{\circ}$C/min. High resolution X-ray diffraction (HR-XRD, PANalytical Empyrean), transmission electron microscopy (TEM, FEI Tecnai G2 F20), and high resolution scanning transmission electron microscopy (HR-STEM) were used to characterize the microstructures of the as-deposited films. The HR-STEM images in high angle annular dark-field (HAADF) mode were obtained using a FEI Titan G2 80-200 STEM with a Cs-probe corrector operated at 200 kV and a modified FEI Titan STEM TEAM 0.5, respectively. The magnetic properties of the films were measured by the vibrating sample magnetometer (VSM) option in a commercial Physical Properties Measurement System (PPMS 6000, Quantum Design). During the measurement, the out-of-plane and in-plane magnetizations were recorded by applying a magnetic field of 1 T perpendicular and parallel to the film plane, respectively.

The elastic constants are calculated using plane-wave pseudopotential method within the generalized gradient approximation (GGA)[220] as implemented in the density-function theory based Vienna Ab initio Simulation Package (VASP).[221] The cut-off for plane-wave basis set of 400 eV and Monkhorst-Pack[222] k-point sampling grid of 12×4×2 are used, with a convergence criteria of 10^{-6} eV for electronic relaxation.

4.4 Results and discussion

The θ-2θ scans of BFMO thin films grown from composite BFMO targets with different Fe/Mn molar ratios are shown in Figure 4.1 and 4.2. The dominant (00l)-type diffraction peaks in Figure 4.1 demonstrate the highly textured growth of both CeO$_2$ buffer layers and BFMO films along (00l).
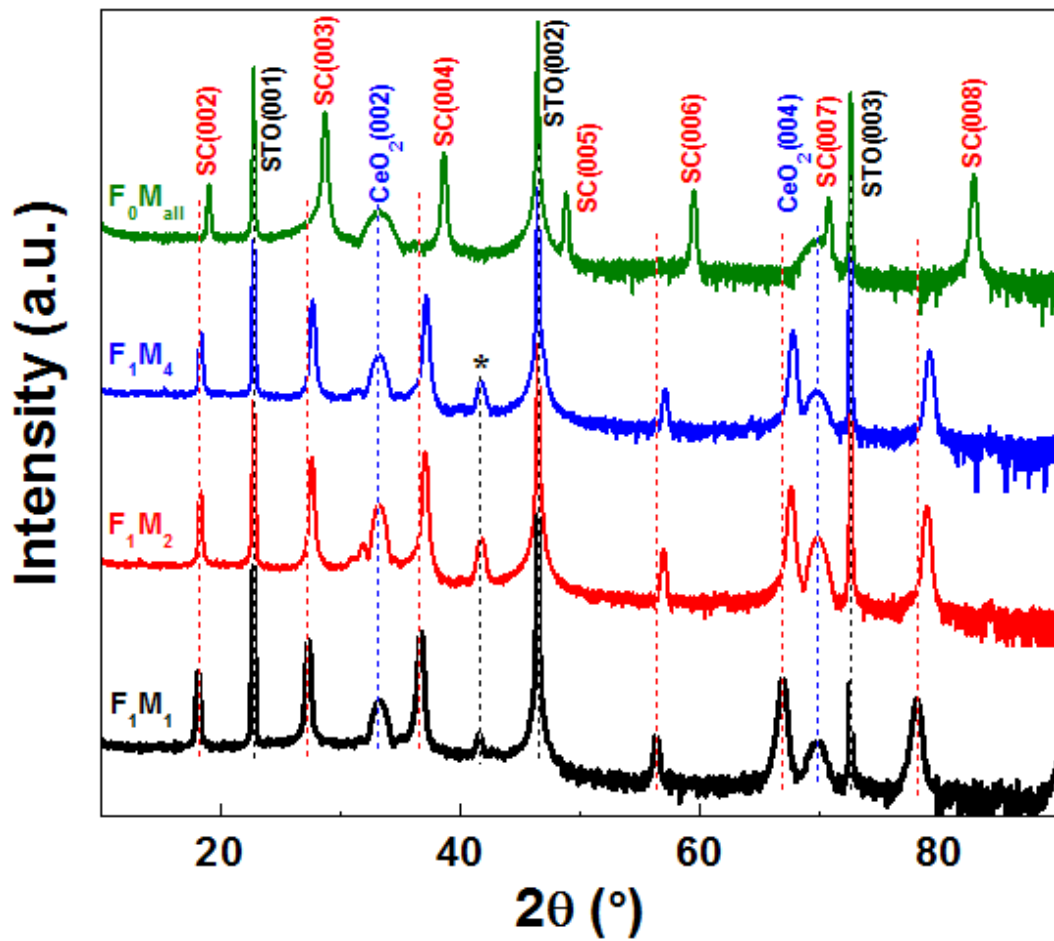
Figure 4.1 XRD θ-2θ scans of BFMO thin films with different Fe/Mn molar ratios, 1:1 (F$_1$M$_1$), 1:2 (F$_1$M$_2$), 1:4 (F$_1$M$_4$), and 0:1 (F$_0$M$_{all}$). The "$*$" indicates a minor phase Bi$_{25}$FeO$_{40}$.

As shown in Figure 4.1, the layered supercell structure can still be obtained with the increase of Mn amount (Fe:Mn < 1:1) while with the increase of Fe molar ratio, the layered supercell structure is not formed (Figure 4.2). The XRD diffraction results suggest that Mn-rich cases facilitate the formation of the layered supercell structures while Fe-rich ones are difficult to achieve such supercell structure. In addition, Figure 4.1 shows an obvious and gradual right shift of the supercell peaks with the increase of the Mn amount, indicating a decreased d-spacing of the layered supercell structures. For example, a right peak shift of 4.76^o is found from the F_0M_{all} (008) peak to the F_1M_1 (008) peak. The out-of-plane d-spacing is determined to be 9.76, 9.68, 9.64, and 9.30 Å for F_1M_1, F_1M_2, F_1M_4, and F_0M_{all} layered thin films, respectively.
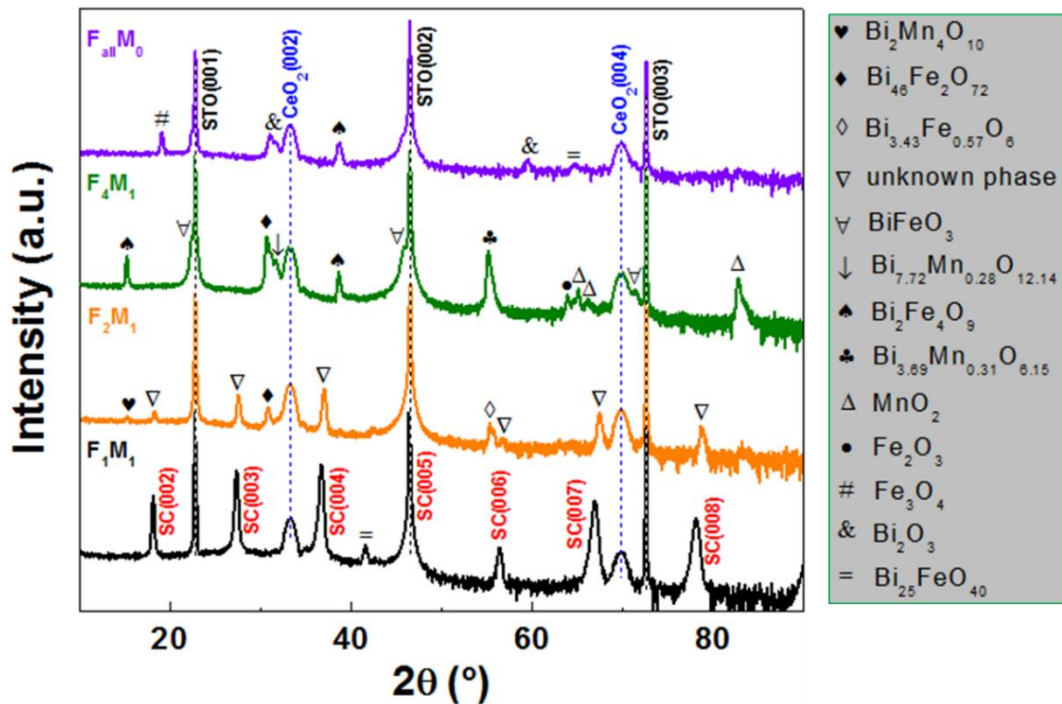
Figure 4.2 XRD θ-2θ scans of BFMO thin films with different BFO and BMO molar ratios, 1:1 (F_1M_1), 2:1 (F_2M_1), 4:1 (F_4M_1), and 1:0 ($F_{all}M_0$).

TEM/STEM studies were employed to investigate the microstructure of these BFMO thin films (Figure 4.3). The low-magnification STEM images of F_1M_1, F_1M_4, and F_0M_{all} thin films in Figure 4.3(a), (d) and (g) clearly show the layered structures grown on CeO_2 buffered STO substrates. The corresponding high-resolution STEM images in Figure 4.3(b), (e) and (h) demonstrate the layered structure where the brighter layers are attributed to the Bi_2O_2 sheets due to the higher atomic number ($Z_{Bi} = 83$) while the darker layers are identified as distorted Fe/Mn octahedra ($Z_{Fe} = 26$, $Z_{Mn} = 25$). Both Bi_2O_2 and Fe-Mn-O slabs indicate a highly epitaxial layered stacking manner with zig-zag shaped arrangements along the out-of-plane direction. An interesting phenomenon to note here is the different Bi_2O_2 layer and Fe-Mn-O layer matching relationship for F_1M_1 and F_1M_4. From the high-resolution STEM image of F_1M_1 in Figure 4.3(b), a 1:1 matching relationship is observed for Bi_2O_2 and Fe-Mn-O layers and the neighboring Bi_2O_2 layers are at the same location along the horizontal [010] direction as indicated by the labeled triangles along the same direction. For F_1M_4, however, the Bi_2O_2 sheets are shifted by half period along the horizontal [100] direction (Figure 4.3(e)). In addition, the Bi_2O_2 and Fe-Mn-O layers have a 3:4 matching relationship along the [010] direction as marked in 2e. The Bi_2O_2 and Fe-Mn-O layer matching relationship for F_1M_1 along [100] direction (Figure 4.3(b)) and for F_1M_4 along [010] direction (Figure 4.3(e)) is consistent with the previously reported Bi_2O_2 and Fe-Mn-O layer matching relationship for F_1M_1 along [100] and [010] directions, respectively.[184] More interestingly, for F_0M_{all} case (Figure 4.3(g) and (h)), it is noteworthy that there is only one layer of Mn atoms between the two Bi_2O_2 layers which is very different from the other BFMO layered samples with two atomic layers of

Fe-Mn-O. The distinctive selected area electron diffraction dots (SAED) in Figure 4.3(c), (f) and (i) also prove the highly epitaxial growth of F_1M_1, F_1M_4, and F_0M_{all} layered structures.
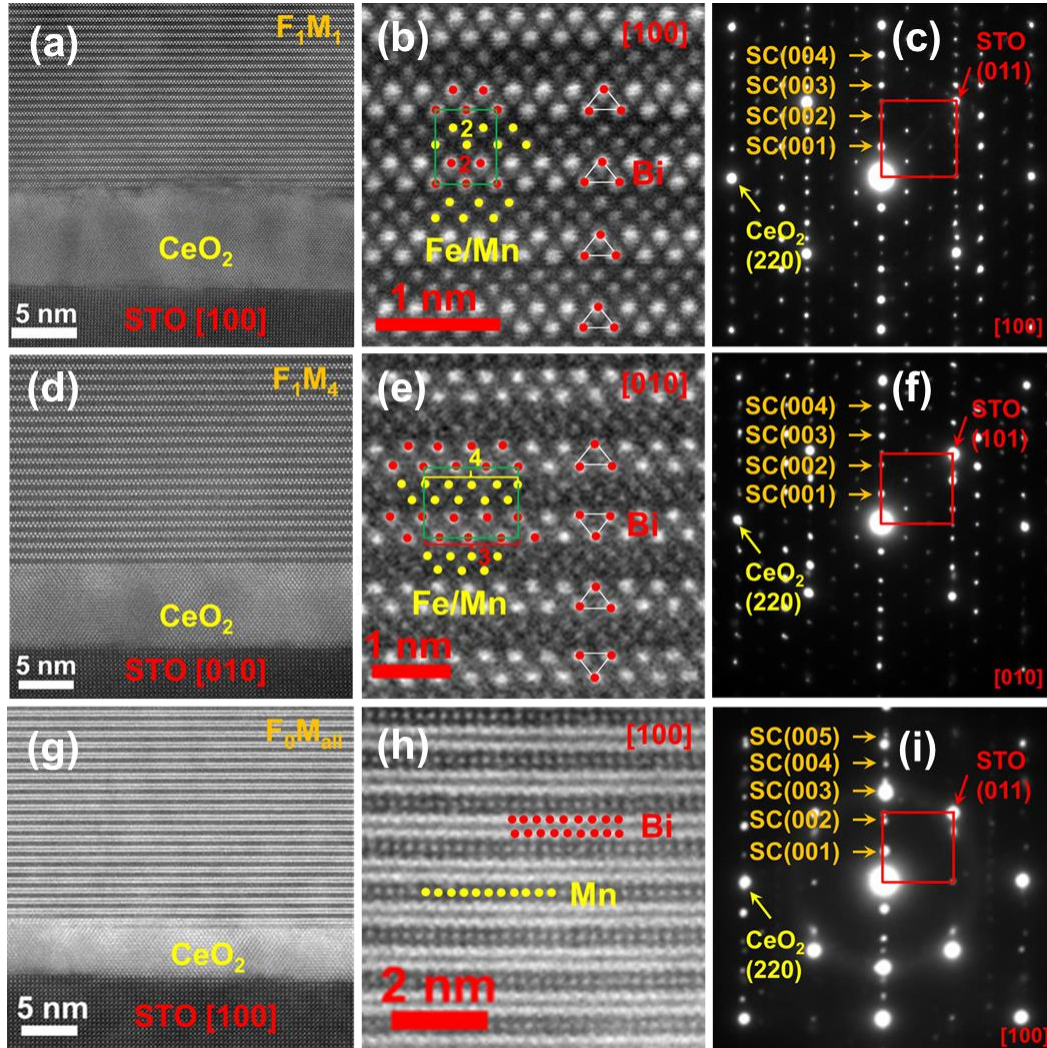
Figure 4.3 Cross-sectional low-magnification STEM images of (a) F_1M_1, (d) F_1M_4, and (g) F_0M_{all}. High-magnification STEM images of (b) F_1M_1, (e) F_1M_4, and (h) F_0M_{all}. The corresponding selected area electron diffraction patterns of (c) F_1M_1, (f) F_1M_4, and (i) F_0M_{all} grown on CeO_2 buffered STO substrates.

An interesting phenomenon noteworthy here is the unique layered supercell structure formed in the case of F_0M_{all} (BiFeO$_3$:BiMnO$_3$ = 0:1, i.e. BiMnO$_3$). BiMnO$_3$ (BMO), possessing ferromagnetism and ferroelectricity simultaneously, is famous as a rare multiferroic material which has been studied in both bulk and thin film forms.[82, 97] On the other hand, BMO is not stable at atmosphere pressure and thus strain coming from the single crystal substrates, e.g. SrTiO$_3$ (001) and LaAlO$_3$ (001), is often used to stabilize the BMO phase at ambient conditions.[82] And the BMO phase obtained on these single crystal substrates usually has a typical pseudocubic structure.[82, 85] In this work, however, novel layered supercell structure has grown on CeO$_2$ buffered STO substrate (Figure 4.1 and Figure 4.3), which is quite different from the previously reported pseudocubic structure of BMO grown on STO (001) and LAO (001). Furthermore, the novel layered supercell structure of BMO can also be obtained directly on STO (001) without the CeO$_2$ buffer layer by finely controlling the growth conditions (Figure 4.4(a) and (c)). As indicated by the dominant (00l)-type diffraction peaks ($2\theta = 19.06°, 28.72°, 38.70°, 48.83°,…$) in Figure 4.4(a), a new phase which is not pseudocubic phase formed from BMO (F_0M_{all}) on STO (001) substrate in this work. Figure 4.4(c) confirms that this new phase is the layered supercell structure mentioned above. For F_1M_1, however, a pseudocubic phase is formed on STO (001) substrate under similar growth conditions (Figure 4.4(b) and (d)).

The growth of the BMO layered supercell structure on STO (001) substrate is very different from previous reports where a pseudocubic phase BMO has grown on STO (001) or other similar cubic substrates. For example, previous reported BMO was not stable at ambient conditions and its growth was sensitive to the growth conditions as well as other

factors such as strain, which all play an important role in controlling or stabilizing its crystal structure or phases obtained in thin film form. In comparison, the new layered supercell structure is a metastable phase and temperature plays a critical role in the formation of this unique layered supercell structure. The structural origin of the Bi-based layered supercell structures in this work is related to the Aurivillius phases, a Bi-based layered compounds composed of alternative stacking of $[Bi_2O_2]^{2+}$ layers. Typical examples include Aurivillius phases (e.g. Bi_2WO_6 and $Bi_4Ti_3O_{12}$),[166] Sillen phases (e.g. $Pb_{0.6}Bi_{1.4}Rb_{0.6}O_2Z_2$, Z = Cl, Br, and I),[223] bismuth subcarbonate ($Bi_2O_2CO_3$),[224] bismuth hydroxyl borates ($Bi_2O_2[B_3O_5(OH)]$ and $Bi_2O_2[BO_2(OH)]$),[225] etc. The closest Bi-Bi distance of the layered supercell structure is measured to be around 4.00 Å which is comparable to the lattice parameter of STO (001) (a = 3.905 Å). In these compounds, the Bi-O bonds shows covalent nature which is weaker than that of pure ionic bonds exhibiting structural flexibility. During the diffusion and nucleation of the adatoms on the single-crystal substrates, $[Bi_2O_2]^{2+}$ layers are possible to form under proper growth thermodynamic and kinetics which can be controlled by the deposition parameters. Considering all the factors affecting the growth of BMO films, the close lattice parameters of STO (001) and Bi-Bi distance in the layered supercell structure, and the wide existence of $[Bi_2O_2]^{2+}$ layers, it is reasonable that novel layered supercell structure consisting $[Bi_2O_2]^{2+}$ layers and Fe/Mn octahedra has grown on STO (001) substrate under well-controlled growth conditions. For the case of F_1M_1, the growth of pseudocubic phase instead of the layered supercell structure on STO (001) substrate might be due to the better lattice match between the F_1M_1 pseudocubic phase and STO (001) substrate. The

formation of BMO layered supercell structure and BF_1M_1O pseudocubic phase on STO substrate further confirms the more important role of Mn in the growth of the 2D layered supercell structure.
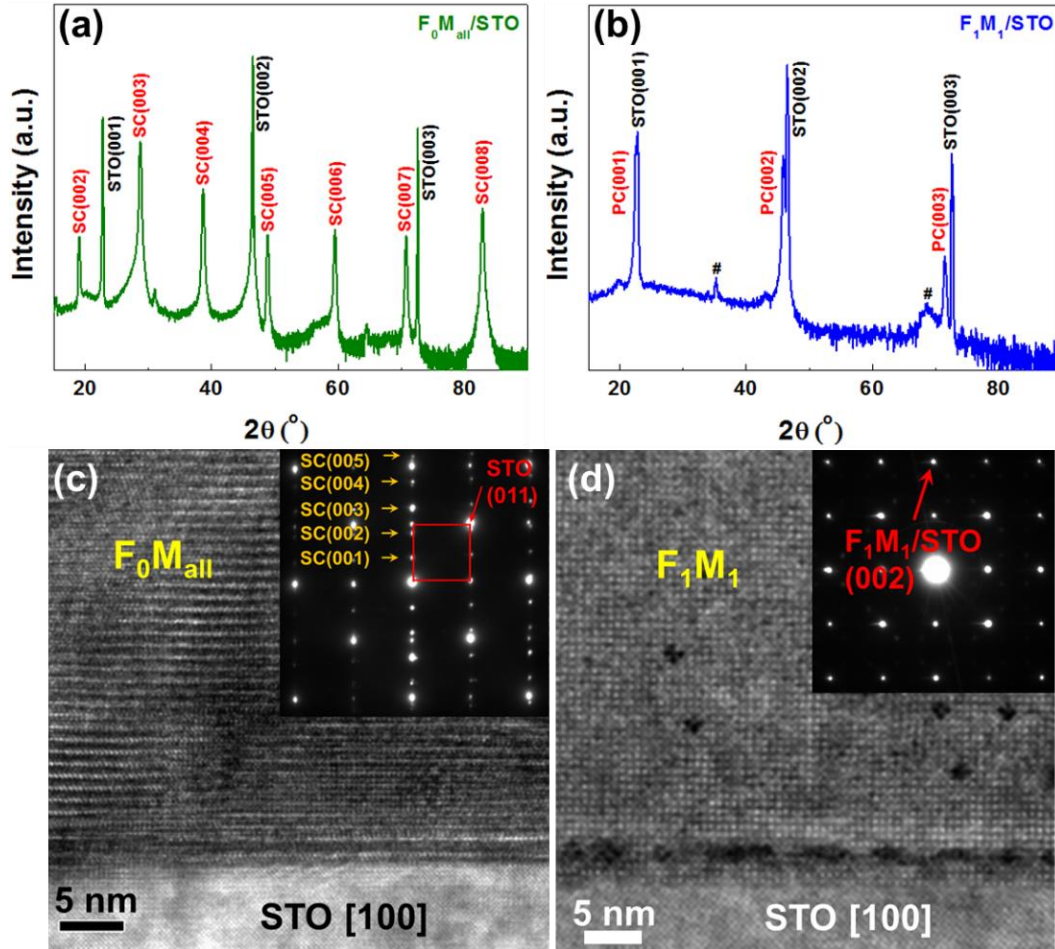
Figure 4.4 XRD θ-2θ scans of F_0M_{all} (a) and F_1M_1 (b) grown on STO substrate directly. The symbol "#" indicates minor unknown phases. TEM images of F_0M_{all} (c) and F_1M_1 (d) directly grown on STO. The insets are the corresponding diffraction patterns of layered F_0M_{all} (c) and pseudocubic F_1M_1 (d).

To systematically investigate the layered supercell's growth mechanism, i.e. the role of Fe and Mn in the formation of the BFMO based layered supercell structures, first-

principles calculations were performed to evaluate the mechanical properties of the layered supercell structures. The anisotropic mechanical properties, for example, Young's modulus, shear modulus and Poisson ratio of materials, can be described by the second-order elastic constants which can be obtained from first-principles calculations. For a mechanically stable material system, the fourth order stiffness tensor relates to the second order stress and strain tensor:

$$\sigma_{ij} = C_{ijkl}\varepsilon_{kl}$$

Einstein's summation rule is adopted in this work. The fourth order tensor can be rewritten to a second order tensor using Voigt notation due to translational and rotational symmetries. Using first-principles calculations, we can obtain the second order stiffness tensor. The tensor rotation can be described by Euler angles (θ, φ). The Young's modulus defined as the ratio of normal stress to linear normal strain (both in the direction of applied load) results in[226]

$$Y(\theta, \varphi) = \frac{1}{a_i a_j a_k a_l S_{ijkl}}$$

Here S_{ijkl} is the fourth order compliance tensor, satisfying the inversion relation

$$\varepsilon_{ij} = S_{ijkl}\sigma_{kl}$$

a_i is the ith element of vector $\mathbf{a} = \begin{pmatrix} sin\theta cos\varphi \\ sin\theta sin\varphi \\ cos\theta \end{pmatrix}$. Thus, we can visualize the Young's modulus in three-dimensional space. The mechanical stability requires the elastic stiffness matrix must be definite positive and all eigenvalues of the matrix are positive, first noted by Max Born,[227] which is originated from the convexity of the energy. Thus, the criteria

can be obtained by expanding the internal energy in terms of strain and substituting to the energy condition. The second-order elastic constants E_{ij} of F_1M_1 and $F_{all}M_0$ are calculated as shown below.

F_1M_1:

$$[E_{ij}] = \begin{bmatrix} 3706.4053 & 1185.3376 & 1258.9211 & 0.0000 & 0.0000 & 0.0000 \\ 1121.8942 & 2350.5048 & 1114.6980 & 0.0000 & 0.0000 & 0.0000 \\ 1258.9211 & 1114.6980 & 2192.2310 & 0.0000 & 0.0000 & 0.0000 \\ 0.0000 & 0.0000 & 0.0000 & 242.1905 & 0.0000 & 0.0000 \\ 0.0000 & 0.0000 & 0.0000 & 0.0000 & 620.1631 & 0.0000 \\ 0.0000 & 0.0000 & 0.0000 & 0.0000 & 0.0000 & 681.2253 \end{bmatrix} \text{KBar}$$

$F_{all}M_0$ (BFO):

$$[E_{ij}] = \begin{bmatrix} 3283.5640 & 1131.9091 & 1037.8040 & 0.0000 & 0.0000 & 0.0000 \\ 1131.9091 & 2558.3034 & 1114.2511 & 0.0000 & 0.0000 & 0.0000 \\ 1313.5854 & 1037.8040 & 1868.5841 & 0.0000 & 0.0000 & 0.0000 \\ 0.0000 & 0.0000 & 0.0000 & 190.0046 & 0.0000 & 0.0000 \\ 0.0000 & 0.0000 & 0.0000 & 0.0000 & -267.3361 & 0.0000 \\ 0.0000 & 0.0000 & 0.0000 & 0.0000 & 0.0000 & 709.1486 \end{bmatrix} \text{KBar}$$

$E_{55} = C_{1313} = C_{3131} = \frac{\partial \sigma_{31}}{\partial \varepsilon_{31}} < 0$, which means the assumed $F_{all}M_0$ (BFO) structure cannot bear the in-plane shear along the x direction. The Young's modulus of the F_1M_1 layered supercell structure is calculated and shown in Figure 4.5. The large anisotropy of the Young's modulus matches well with the 2D anisotropic layered structure and the result proves the structural stability of the F_1M_1 layered supercell structure theoretically. For the case of $F_{all}M_0$, i.e. with all the Mn substituted by Fe, however, the 2D layered structure becomes mechanically unstable, as proved by the negative E_{55} in the elastic stiffness

matrix which provides theoretical foundation that Fe does not facilitate the growth of Bi-based layered supercell structure.
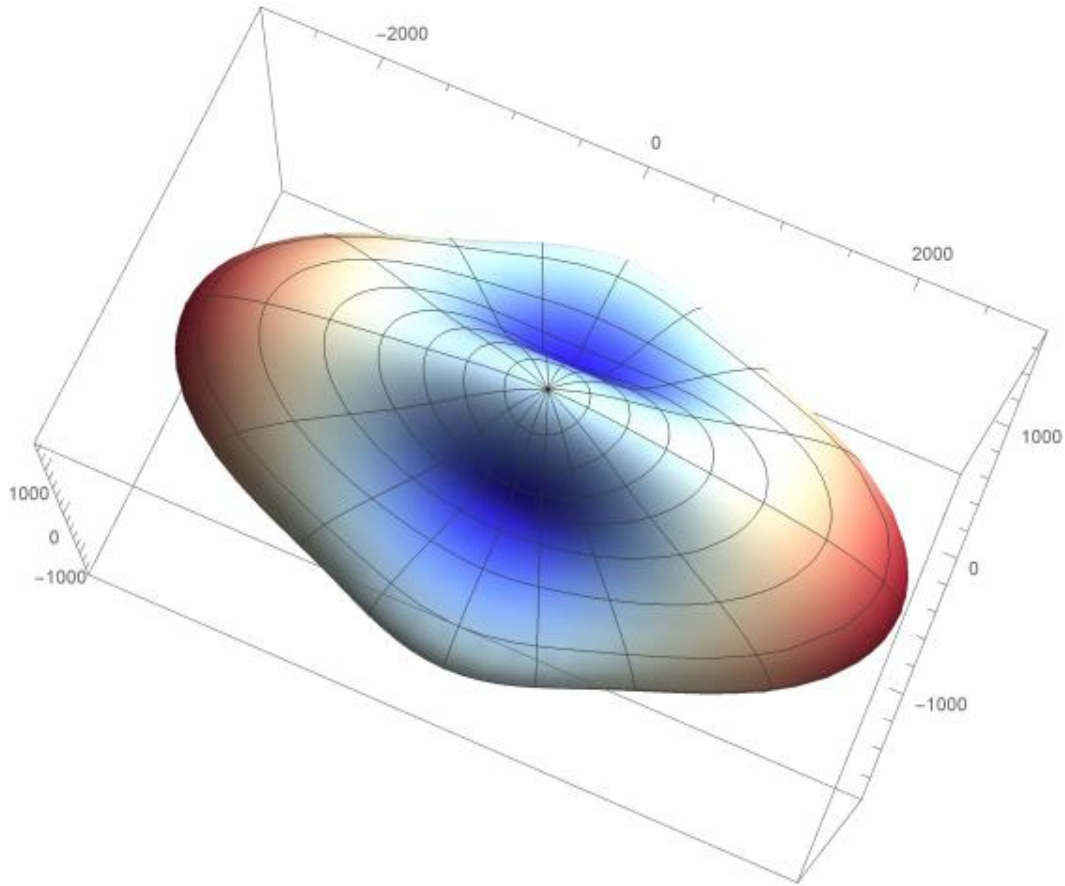
Figure 4.5 Visualization of Young's modulus of F_1M_1 layered supercell structure in unit KBar.

To explore the tunability of the magnetic properties of the BFMO layered supercell structures, the magnetic response of the samples was measured by the vibrating sample magnetometer (VSM) option in a commercial Physical Properties Measurement System as shown in Figure 4.6. The saturation magnetization of F_1M_1, F_1M_2, F_1M_4, and F_0M_{all} is ~166 emu/cc, ~90 emu/cc, ~60 emu/cc, and ~112 emu/cc at 300 K and 10 kOe along the

out-of-plane direction (Figure 4.6(a)), respectively, indicating tunable magnetic properties

of the samples with different Fe/Mn molar ratios (Figure 4.6(b)). It is noteworthy here that

the magnetic property of the BFMO supercell structures is much better than that of the

BFMO and $BiMnO_3$ thin films with conventional pseudocubic structures. For example,

the pseudocubic Bi_2FeMnO_6 thin films exhibit a magnetization value ranging from 0.8

emu/cc to 90 emu/cc depending on the growth conditions, strain states, annealing

procedures, etc.[86, 108, 111, 113, 184] Although the magnetizations of some of the pseudocubic

Bi_2FeMnO_6 thin films are comparable and even higher than the BFMO supercell structures,

the high magnetization of 90 emu/cc in the pseudocubic Bi_2FeMnO_6 thin films only exists

in very thin films which are highly strained.[111, 113] With the increase of the thickness of the

pseudocubic Bi_2FeMnO_6 thin films, the magnetization value is as low as 0.8 emu/cc.[86]

Regarding the single-phase multiferroic $BiMnO_3$, a problem is the low ferromagnetic

transition temperature which limits its practical applications at room temperature. The

bulk $BiMnO_3$ shows a ferromagnetic transition temperature of as low as 105 K and a

ferromagnetic Curie temperature of 50 K was reported for the pseudocubic $BiMnO_3$ thin

film grown on LAO (001) substrate.[86] It was proposed in the previous work that the

magnetization of the BFMO322 SC may stem from a net magnetization of Fe and Mn

cations, which form zigzag-shaped rows favoring the spin canting effect.[184] From the

current results, it is not sufficient to understand the magnetic structure. The magnetization

of the BFMO layered supercell structures might be a result of several magnetic coupling

mechanisms such as orbital hybridization and spin compensation between the cations. For

the case of BMO layered supercell with only one layer of Mn cations between the

$[Bi_2O_2]^{2+}$ sheets, the magnetization may be related to the superexchange coupling of the neighboring Mn cations through the oxygen. Figure 4.6(c) shows the tunable transmittance of the BFMO thin films with different compositions and structures and a direct band gap of ~2.50, ~2.59, ~2.63, ~2.64 and ~2.66 eV was obtained for pseudocubic BFMO, F_1M_1, F_1M_2, F_1M_4, and F_0M_{all}, respectively, by the Tauc method Figure 4.6(d).
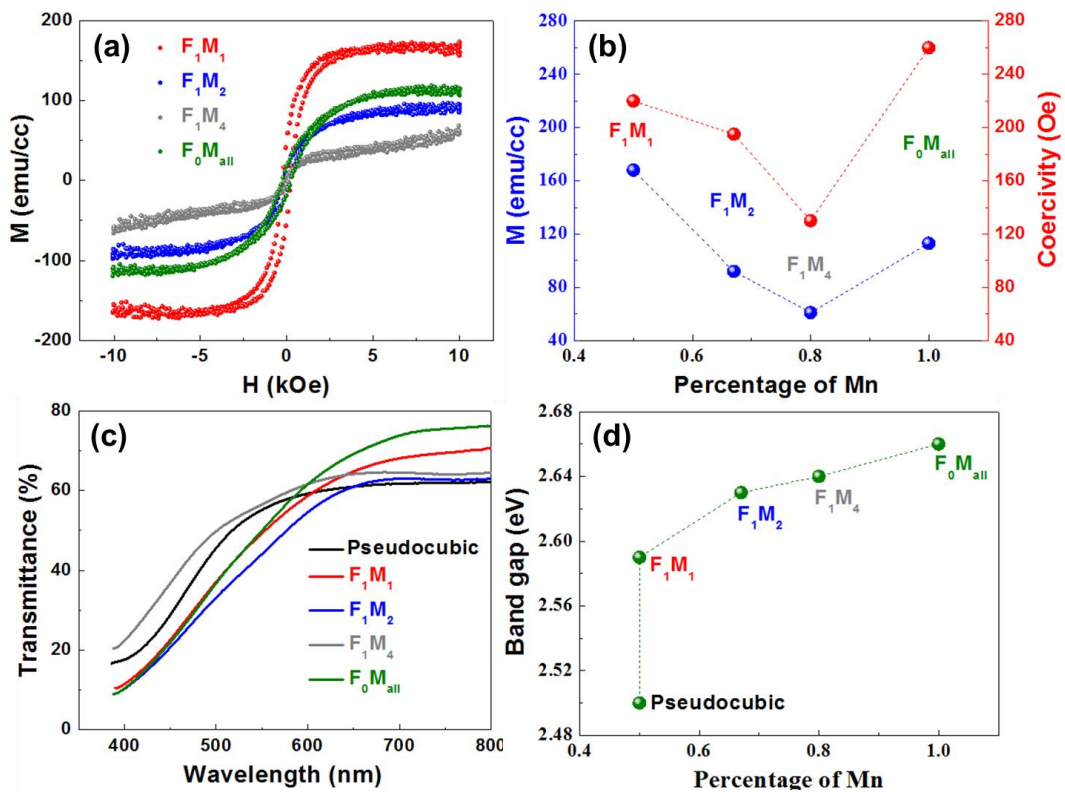
Figure 4.6 Tunable physical properties of the BFMO thin films with different compositions and structures. (a) Magnetic hysteresis (M-H) loops of F_1M_1, F_1M_2, F_1M_4 and F_0M_{all} at 300 K along the out-of-plane direction. (b) Variation of saturation magnetization and coercivity of F_1M_1, F_1M_2, F_1M_4 and F_0M_{all} with different Mn contents. (c) and (d) Tunable transmittance and band gaps of pseudocubic BFMO, F_1M_1, F_1M_2, F_1M_4 and F_0M_{all}.

4.5 Conclusion

In conclusion, the influence of Fe/Mn ratio in $Bi_2Fe_{1-x}Mn_xO_6$ on the formation of the layered supercell structure and its magnetic property has been investigated. Both XRD and STEM results indicate that Mn concentration plays a dominant role in the formation of the novel layered supercell structures grown on CeO_2 buffered STO (001) substrates. The net magnetization of the BFMO layered supercell structures might be the interplay of several magnetic coupling mechanisms including orbital hybridization and spin compensation between the Mn and Fe cations. This study reveals the key factors for the 2D layered supercell formation and demonstrates the possibilities in microstructural and physical property tuning in these novel 2D systems.

CHAPTER V

TWO-DIMENSIONAL LAYERED SUPERCELLS FROM BIMNO$_3$ AND BI$_2$NIMNO$_6$: SELF-ASSEMBLED GROWTH, STRUCTURE MODULATION, AND TUNABLE PHYSICAL PROPERTIES

5.1 Overview

With the rise of graphene and transition metal dichalcogenides (TMDC), two-dimensional (2D) materials holding great promises in nanoscale device applications has become an extensively studied topic in fundamental research areas including physics, chemistry and materials science. In parallel with the non-oxide 2D graphene and TMDC, layered oxides (e.g. Aurivillius and Ruddlesden-Popper phases) are also intriguing both because of the variety of rich physics behind and the potential device applications. Here, by one-step self-assembled growth we designed and fabricated four novel Bi-based layered supercell structures from the metastable single-perovskite BiMnO$_3$ (BMO) and double-perovskite Bi$_2$NiMnO$_6$ (BNMO). The four layered supercell structures consist of alternative layered stacking of Bi$_2$O$_x$/Bi$_3$O$_x$ slabs and Mn-O/Ni-Mn-O octahedral layers, respectively. Robust room-temperature multiferroic properties with tunable magnetic response have been demonstrated for the four anisotropic layered supercell structures. The realization of these four new layered supercell structures has paved an avenue towards exploring and designing new single-phase materials with desired room-temperature multiferroic properties.

130

5.2 Introduction

Two-dimensional (2D) layered materials, no longer possessing the same behavior as their three-dimensional forms, has sparked special research interest because of their unique anisotropic structures and rich physical phenomena as well as the enormous potentials of fabricating nanoscale devices.[228, 229, 230] Graphene[135, 231] and transition metal chalcogenides (e.g., GeS, SnSe, WS_2 and MoS_2)[232, 233] represent two kinds of extensively studied 2D materials nowadays with varieties of physical phenomena predicted or discovered such as quantum spin Hall effects,[147, 234] topological insulating transitions,[235] and ferromagnetism,[236, 237, 238, 239] which paves an avenue towards 2D devices. Besides the non-oxide 2D materials, oxide-based 2D materials have also attracted wide attention and have been the focus of condensed matter physics and material science with the underlying rich physics. For example, perovskite-related 2D materials like Aurivillius[165, 182, 240] and Ruddlesden-Popper[241, 242, 243] phases exhibit remarkable structural variability because of their unique ionic structural framework. And intriguing physical properties such as piezoelectricity and ionic conductivity have been reported for these kinds of perovskite-related 2D layered materials.

In parallel, Bi-based perovskites, including Bi-based single-perovskites (e.g., $BiFeO_3$ and $BiMnO_3$)[7, 82] and double-perovskites (e.g., Bi_2FeMnO_6, Bi_2FeCrO_6, and Bi_2NiMnO_6),[127, 184, 185] have drawn a tremendous amount of attention owing to their multiferroism and magnetoelectric effect. For example, $BiMnO_3$ (BMO) is a well-known single-perovskite and one of the most promising single-phase multiferroic materials with ferromagnetic ordering at about 105 K. Bi_2NiMnO_6 (BNMO), a Bi-based double-

131

perovskite multiferroic material, possesses long-range ordered Ni^{2+} and Mn^{4+} cations with a ferromagnetic transition temperature of 140 K.[127] At the meantime, both BMO and BNMO are metastable phases at ambient conditions and the bulk synthesis requires high temperature (~1100 K) and high pressure (~6 GPa).[82, 127, 129, 131] The thin film growth of BMO and BNMO on single-crystal substrates is sensitive to the deposition parameters such as temperature and oxygen pressure. The development of high-quality thin film growth techniques and the accompanying strain engineering have provided people much more freedom to explore and design new materials in thin film form with new structures and functionalities.[184] For example, the high-pressure requirement for the stabilization of metastable BMO and BNMO phase can be replaced by strain exposed by the substrate.

Considering the metastable nature of BMO and BNMO and their sensitive thin film growth conditions, novel phases from BMO and BNMO may be achieved by appropriately controlling the growth parameters. Here, in this work we designed and created four novel 2D layered supercell structures from BMO and BNMO systems via pulsed laser deposition by finely controlling the deposition parameters. More interestingly, the BMO and BNMO structures can be easily modulated between layered supercell structures consisting of two-layer-thick and three-layer-thick Bi-based slabs by adjusting the deposition parameters. The BMO and BNMO high-temperature layered supercell (HLSC) structure consists of alternated Bi_2O_x slabs and Mn-O/Ni-Mn-O octahedra layers while the BMO and BNMO low-temperature layered supercell (LLSC) structure is formed by intergrowth of Bi_3O_x slabs and Mn-O/Ni-Mn-O octahedra layers both along the film out-of-plane direction. Both BMO and BNMO HLSC and LLSC can be fabricated on both

LaAlO$_3$ (LAO) (001) and SrTiO$_3$ (STO) (001) substrates, respectively, and exhibit robust room-temperature multiferroic properties. The demonstration of the self-assembled multiferroic 2D layered supercell structures in this study paves an avenue towards designing new single-phase materials with unique anisotropic structures and multiferroic response.

5.3 Experimental

Sample preparation. Epitaxial BiMnO$_3$ and Bi$_2$NiMnO$_6$ thin films were deposited on single crystal LaAlO$_3$ (001) and SrTiO$_3$ (001) substrates by pulsed laser deposition (PLD, Lambda Physik, KrF, $\lambda = 248$ nm) from stoichiometric BiMnO$_3$ and Bi$_2$NiMnO$_6$ target, respectively. To prepare the BiMnO$_3$ and Bi$_2$NiMnO$_6$ target, well-mixed pellets from stoichiometric ratio of Bi$_2$O$_3$, MnO$_2$ and Bi$_2$O$_3$, NiO, MnO$_2$ powders were sintered at 800 ^{o}C and 750 ^{o}C for 3 hours in air, respectively. The substrate temperature ranged from 400 to 700 ^{o}C and a dynamic oxygen pressure of 20~200 mTorr was maintained during depositions. After deposition, the films were *in-situ* annealed at 400 ^{o}C for 1 hour in 500 Torr of oxygen and then cooled down to room temperature.

XRD, STEM HAADF imaging, EDS, and AFM imaging. High-resolution X-ray diffraction (HR-XRD, PANalytical Empyrean), transmission electron microscopy (TEM, FEI Tecnai G2 F20), and high-resolution scanning transmission electron microscopy (HR-STEM) were used to characterize the microstructures of the prepared BMO and BNMO thin films. The HR-STEM images in high-angle annular dark-field (HAADF) mode were obtained using a FEI Titan G2 80-200 STEM with a Cs probe

corrector operated at 200 kV and a modified FEI Titan STEM TEAM 0.5 with a convergence semi-angle of 17 mrad operating at 200 kV, respectively. For the high-resolution energy-dispersive X-ray spectroscopy (EDS) mapping, a FEI Titan[TM] G2 80-200 STEM with a Cs probe corrector and ChemiSTEM[TM] technology (X-FEG[TM] and SuperX[TM] EDS with four windowless Si drift detectors) operated at 200 kV was used. The film composition was analyzed by EDS of both transmission electron microscopy and scanning electron microscopy. A Bruker Dimension Icon atomic force microscope (AFM) with high resolution (Z < 0.1 nm, XY < 1 nm) was used to get the surface topography image.

PED tomography. Precession electron diffraction (PED) patterns were obtained using a JEOL 2010 (200 kV) transmission electron microscope (TEM) equipped with a side-mounted Gatan Orius CCD camera and a Nanomegas Digistar PED unit. The data collection was performed on a cross-sectional sample prepared from a ~80 nm film using the tomography approach.[193] In such a case, the rotation axis is mostly limited to the out-of-plane direction to avoid shadowing the film by the substrate. PED patterns were recorded in a tilted range with a precession angle. The data were processed using the programs PETS[194] and Jana2006[195].

Physical property measurement. The magnetic properties of the fabricated samples were measured in a commercial Physical Properties Measurement System (PPMS 6000, Quantum Design) via the vibrating sample magnetometer (VSM) option. The in-plane and out-of-plane magnetizations were recorded by applying a magnetic field of 1 T parallel and perpendicular to the film plane, respectively. For the zero-field cooling (ZFC)

and field cooling (FC) measurements, the samples were cooled down without and with a magnetic field applied, respectively, from 380 K to 10 K and the magnetizations were recorded during the heating cycle from 10 K to 380 K. For the electrical property measurements, the conductive $La_{0.7}Sr_{0.3}MnO_3$ (LSMO) was firstly deposited on STO substrate as the bottom electrode. The piezoelectric properties were measured at ambient conditions with a conductive Pt-Ir coated Si tip (model: SCM-PIT) via the Bruker Dimension Icon atomic force microscope (AFM).

5.4 Results and discussion

The microstructure of the two BMO layered supercell (LSC) structures was first investigated by X-ray diffraction (XRD) as presented in Figure 5.1. Figure 5.1(a) and (c) shows the XRD θ-2θ pattern of BMO HLSC which exhibits a series of periodic (00l)-type diffraction peaks besides the LAO (001) and STO (001) substrate peaks. The out-of-plane d-spacing of BMO HLSC was determined to be ~9.31 Å with the diffraction peaks centered at $2\theta = 9.49°$, 19.06°, 28.76°, 38.68°, 48.89°,… for the HLSC film grown on both LAO (001) and STO (001) substrates. With the decrease of the deposition temperature, another set of (00l)-type diffraction peaks are observed for the film BMO LLSC grown both on LAO (001) and STO (001) substrates as shown in Figure 5.1(b) and (d). With the diffraction peaks centered at $2\theta = 6.80$, 13.45, 20.16, 27.01, 33.97, 41.03,… the d-spacing for BMO LLSC was calculated to be ~12.99 Å. The dominant (00l)-type diffraction peaks of both BMO HLSC and LLSC indicate that both films have epitaxially grown along the film out-of-plane direction on both LAO (001) and STO (001) substrates. In addition, the

large *d*-spacing as well as the unique periodic diffraction features of BMO HLSC and LLSC do not fit any of the reported $BiMnO_3$ phases with pseudocubic structure, which implies that two new BMO phases have been fabricated. More interestingly, the BMO HLSC and LLSC can be both fabricated on CeO_2 buffer layers (Figure 5.1(e) and (f)).
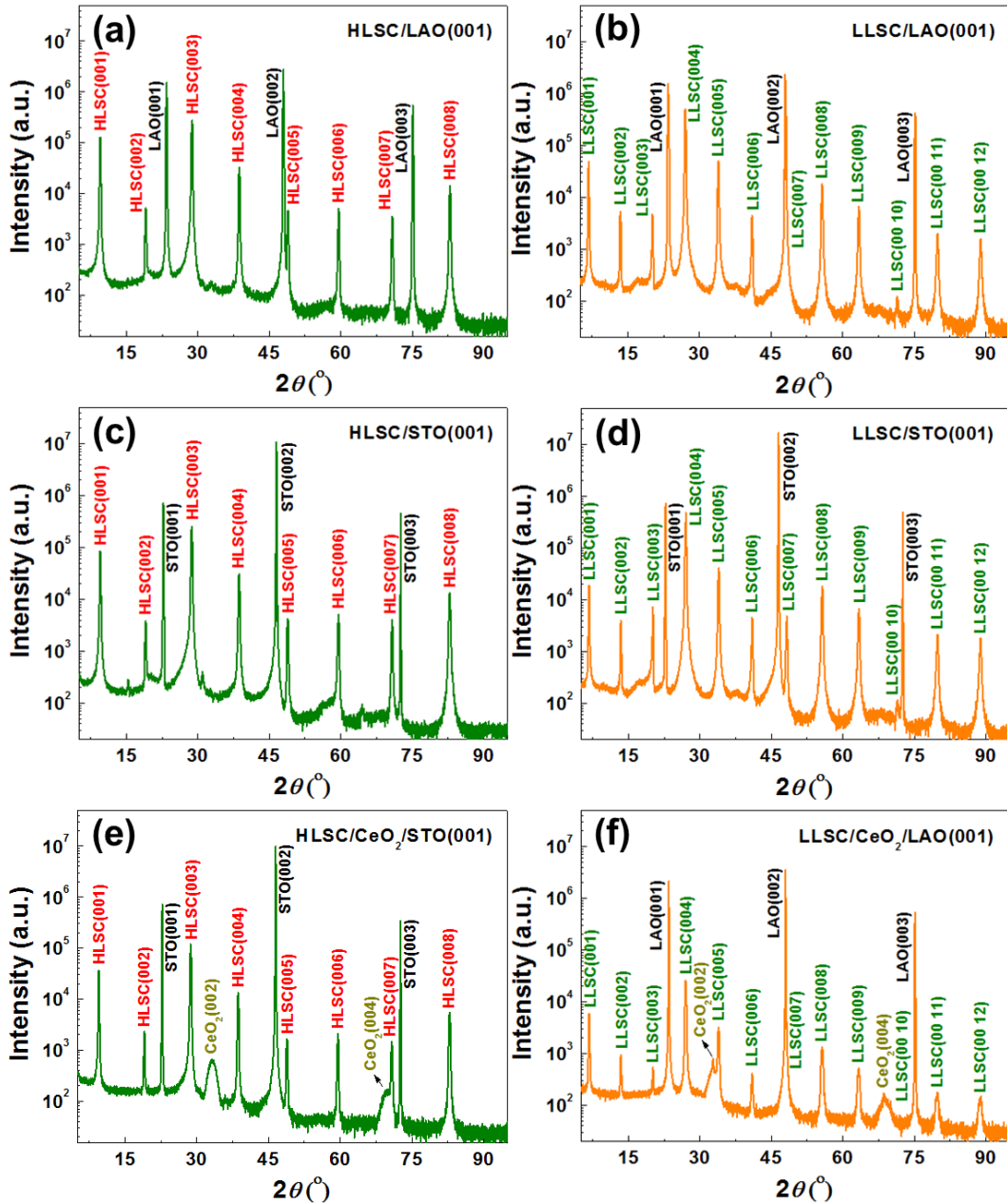
Figure 5.1 XRD patterns of the self-assembled BMO layered supercell structures. θ-2θ scans of BMO HLSC grown on (a) LAO (001), (c) STO (001), and (e) CeO_2-buffered STO (001) substrates, respectively. θ-2θ scans of BMO LLSC grown on (b) LAO (001), (d) STO (001), and (f) CeO_2-buffered LAO (001) substrates, respectively.

The epitaxial growth of the novel layered supercell structures and conventional pseudocubic phase of BNMO was also examined by XRD. As shown by the diffraction patterns of BNMO HLSC grown on LAO (001) in Figure 5.2(a), a series of periodic (00l)-type diffraction peaks ($2\theta = 9.54^o$, 19.21^o, 28.85^o, 38.81^o,… corresponding to out-of-plane lattice distances of 9.25 Å, 4.62 Å, 3.09 Å, 2.32 Å,… respectively.) are observed besides the substrate peaks. For the sample grown on STO (001), a conventional pseudocubic phase was obtained. When decreasing the deposition temperature, however, another set of sharp (00l)-type diffraction peaks ($2\theta = 6.81^o$, 13.56^o, 20.35^o, 27.31^o, 34.32^o, 41.47^o,… corresponding to out-of-plane lattice distances of 12.97 Å, 6.52 Å, 4.36 Å, 3.26 Å, 2.61 Å, 2.18 Å,… respectively.) are exhibited for BNMO LLSC grown on both LAO (001) and STO (001) substrates, demonstrating that the films deposited at low temperatures have also grown in a highly epitaxial manner along the out-of-plane direction (Figure 5.2(b)). The large out-of-plane d-spacing as well as the unique periodic diffraction features of the two new BNMO thin films in this work do not fit any of the reported Bi_2NiMnO_6 phases,[127] indicating that two new BNMO phases (called BNMO HLSC and BNMO LLSC hereafter) have been fabricated from the Bi-based double-perovskite Bi_2NiMnO_6 under well-controlled growth conditions.
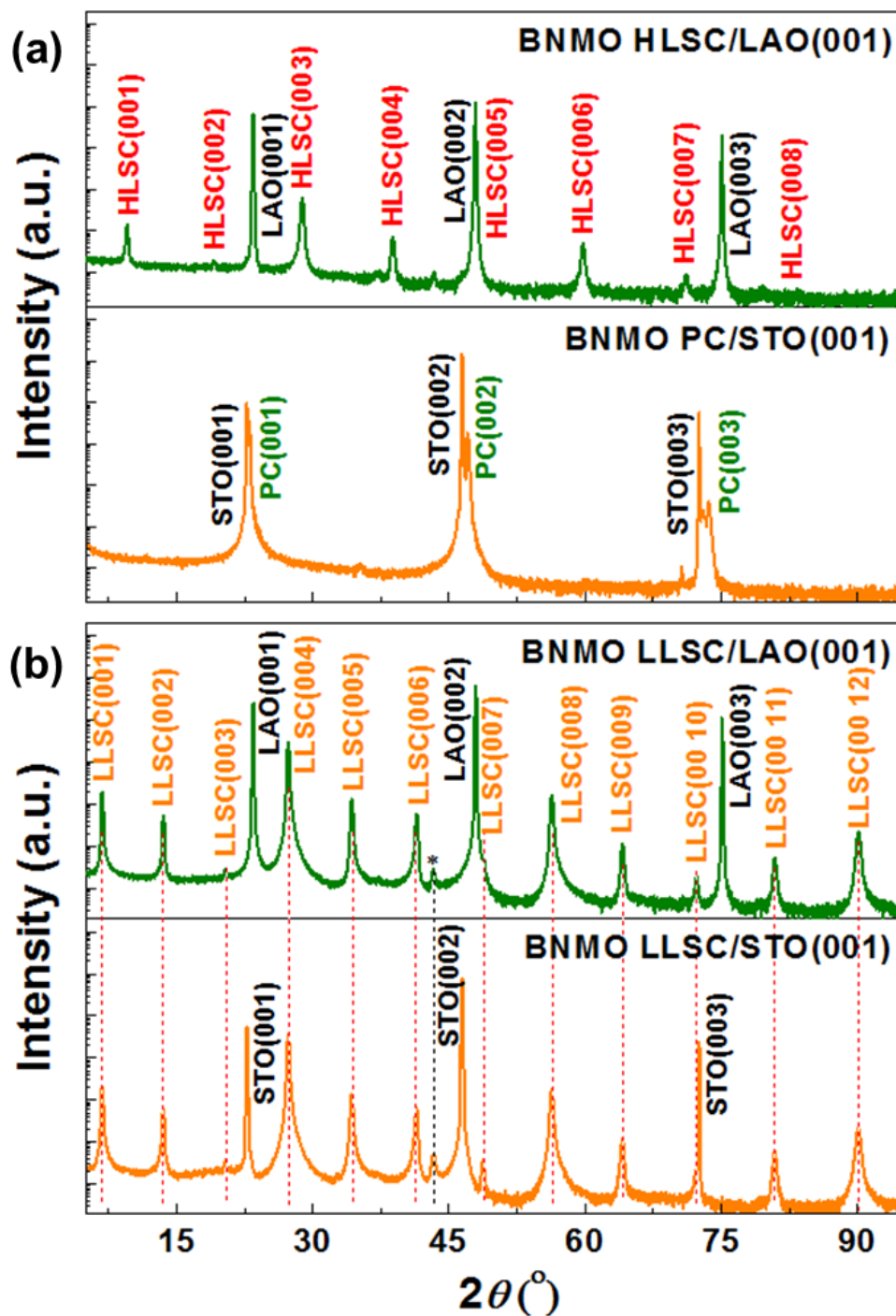
Figure 5.2 XRD θ-2θ patterns of the BNMO thin films with novel layered supercell structures and conventional pseudocubic structure. Typical θ-2θ scans of the BNMO thin films deposited on LAO (001) and STO (001) substrates at (a) high temperature and (b) low temperature, respectively. HLSC and LLSC mean high-temperature and low-

temperature layered supercell, respectively, while PC indicates the pseudocubic structure. The "*" indicates a minor phase $Bi_{12}MnO_{20}$.

To further characterize the microstructure of both BMO and BNMO HLSC and LLSC, aberration-corrected scanning transmission electron microscopy (STEM) equipped with energy-dispersive X-ray spectroscopy (EDS) analysis was performed on both BMO and BNMO grown on LAO (001) (Figure 5.3 and 5.4). Figure 5.3(a) presents the STEM image of BMO HLSC in high angle annular dark-field (HAADF) mode taken from LAO [100] zone axis. The STEM image of BMO HLSC shows clear epitaxial layered stacking growth manner of BMO HLSC along the LAO (001) *c*-axis which consists of two sublattices. The bright sheets are composed of Bi-O (Z_{Bi} = 83) while the dark slabs are attributed to Mn-O (Z_{Mn} = 25) as the contrast of STEM HAADF image is proportional to Z^n (Z is the atomic number.). High-resolution STEM image of BMO HLSC on atomic scale taken from LAO [100] and [110] zone axis in Figure 5.3(b) and (c) clearly shows the intergrowth of bright Bi-based slabs and dark Mn-based monolayers along the film out-of-plane direction. Figure 5.3(b) shows the zig-zag atom arrangement of two-layer-thick Bi atoms and Figure 5.3(c) demonstrates the monolayer of Mn atoms which are aligned in a straight line. The STEM HAADF image of BMO LLSC is shown in Figure 5.3(d) which also exhibits layered stacking of bright and dark layers alternatively along the out-of-plane direction. Similar to BMO HLSC, the bright layers are also attributed to Bi-based slabs and the dark layers are composed of Mn-O. The cation ratio for BMO HLSC and LLSC is estimated to be Bi/Mn = 1.76:1 and 2.44:1, respectively. Contrary to the two-layer-thick of Bi-O slabs of BMO HLSC, each bright slab of BMO LLSC contains

three layers of Bi atoms (Figure 5.3(e)), which is quite different from the well-known Aurivillius phases consisting of two-layer-thick of Bi-based slabs. Between the three-layer-thick Bi-based slabs of LLSC are also one-layer-thick Mn atoms (Figure 5.3(f)).
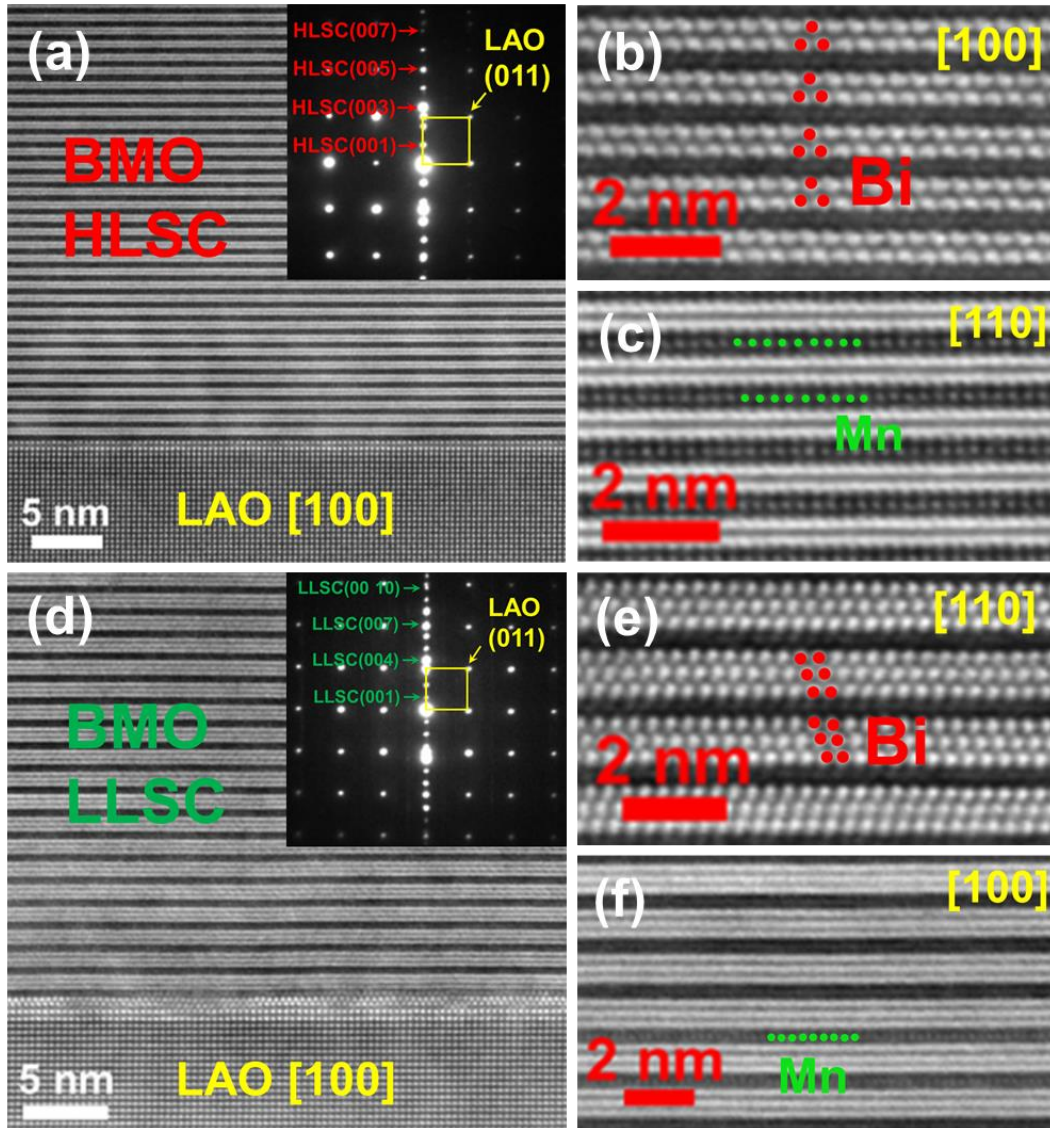
Figure 5.3 Microstructural characterization of the BMO layered supercell structures. (a) and (d) STEM HAADF images of BMO HLSC and LLSC along LAO [100] zone axis, respectively. The inset shows the corresponding selected area electron diffraction patterns of BMO HLSC and LLSC, respectively. (b) and (f) High-resolution STEM images of

BMO HLSC and LLSC taken from the LAO [100] and [110] zone axis, respectively, showing the Bi atoms at atomic resolution. (c) and (e) High-resolution STEM images of BMO HLSC and LLSC taken from the LAO [110] and [100] zone axis, respectively, showing the Mn atoms at atomic resolution.

High-resolution STEM images in high-angle annular dark-field (HAADF) mode (along the substrate LAO [100] zone axis) in Figure 5.4(a) and (b) clearly demonstrate that both BNMO HLSC and LLSC grows in a layered stacking manner along the film out-of-plane direction. Due to the in-plane film rotation of both BNMO HLSC and LLSC, only stripes with bright and dark contrast are observed in the HAADF STEM images from the substrate LAO [100] zone axis. It is believed that the in-plane film rotation is related to the strain relaxation which is caused by the high misfit of the two sublattices. Since the contrast of HAADF STEM images is proportional to Z^n (Z is the atomic number.), the bright sheets of both BNMO HLSC and LLSC are ascribed to the Bi-O layers ($Z_{Bi} = 83$) while the dark layers between the bright slabs arise from Ni-Mn-O atoms ($Z_{Ni} = 28$, $Z_{Mn} = 25$). The Bi-based slabs for BNMO HLSC and LLSC consist of two-layer-thick and three-layer-thick Bi atoms which are later identified as Bi_2O_x and Bi_3O_x, respectively, while the Ni-Mn-O layers consist of one-layer-thick Ni and Mn atoms. The STEM HAADF image in Figure 5.4(a) and (b) reveals a periodicity of ~8.42 Å and ~6.97 Å along the out-of-plane direction for BNMO HLSC and LLSC, respectively. The inset high-resolution HAADF STEM images obtained after tilting the film on the bottom right corner of Figure 5.4(a) and (b) clearly demonstrate the Bi atoms at atomic scale with zig-zag atom arrangement. The periodic selected area electron diffraction (SAED) pattern of both

BNMO HLSC and LLSC (the inset on the top right corner of Figure 5.4(a) and (b)) also proves the highly epitaxial growth of the BNMO LSC along the film out-of-plane direction.

To better understand the microstructure of the two new BNMO LSC, high-resolution energy-dispersive X-ray spectroscopy (EDS) elemental mapping was also performed on both BNMO HLSC and LLSC. The EDS composite color mapping and/or mapping for each element as well as the corresponding X-ray intensity profiles acquired from a local area along the horizontal axis for HLSC (Figure 5.4(c), (e) and (g)) and LLSC (Figure 5.4(d), (f) and (h)) confirms that the bright slabs consist of Bi atoms and the dark layers are composed of Ni and Mn for both layered structures. Ni and Mn cations cannot be well distinguished from each other by EDS because of their quite similar atomic numbers (($Z_{Ni} = 28$, $Z_{Mn} = 25$)). Both the elemental EDS mapping results as well as the X-ray profiles have provided the elemental distribution for the BNMO LSC directly. The cation ratio for BNMO HLSC and LLSC is estimated to be Bi/(Ni+Mn) = 1.01:1 and 1.81:1, respectively. The atomic resolution STEM images in Figure 5.4(c) and (d) demonstrate the Ni/Mn atoms on atomic scale which are densely arranged in the same line. The high-resolution STEM images in Figure 5.4(c) and (d) and X-ray profiles in Figure 5.4(g) and (h) have also provided a clear picture of the interface microstructure where a thin transition layer is observed between the LAO substrate and the BNMO LSC thin film. The thin transition layer can be divided into two interlayers: interlayer 1 and interlayer 2. For interlayer 1, it is a perovskite-type structure with one or two unit cells while interlayer 2 consists of a single layer of Bi atoms. An interesting phenomenon is that the Bi atoms

of interlayer 2 are densely stacked on the Bi atoms of interlayer 1 for both HLSC and

LLSC.
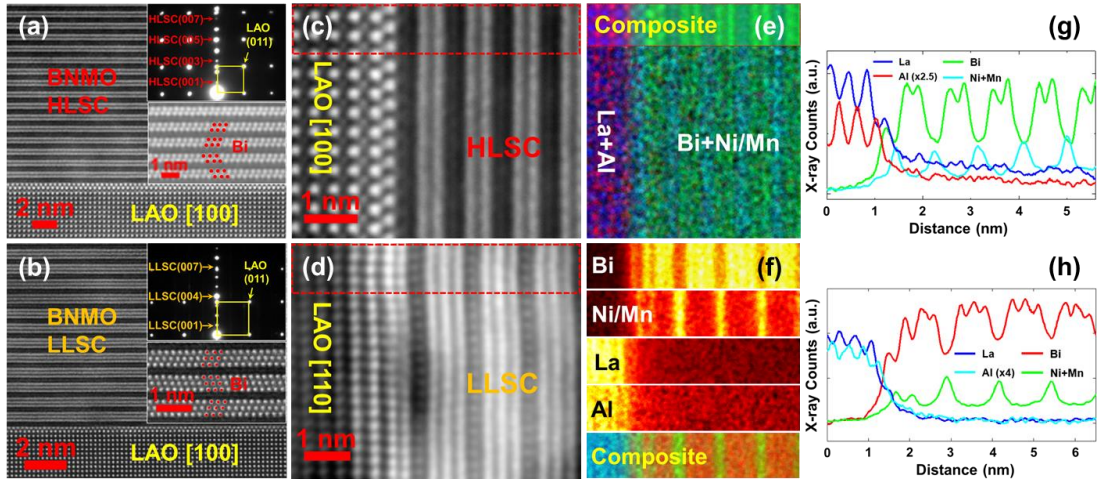
Figure 5.4 Microstructural characterization of the two new BNMO LSC. (a) and (b) HAADF STEM images of BNMO HLSC and LLSC along LAO [100] zone axis, respectively. The insets on the top right corner and bottom right corner in both (a) and (b) are the SAED pattern and high-resolution HAADF STEM image on atomic scale, respectively. (c) and (d) High-resolution HAADF STEM images of BNMO HLSC and LLSC along [100] and [110] zone axis, respectively. (e) and (g) EDS composite color mapping and X-ray profiles for Bi, Ni/Mn, La and Al along the horizontal axis for BNMO HLSC. (f) EDS mapping of Bi (L+M), Ni/Mn (K_α), La (K_α), Al (K_α), and composite color mapping for BNMO LLSC. (h) X-ray profiles for Bi, Ni/Mn, La and Al along the horizontal axis for BNMO LLSC.

A phenomenon observed for both BMO and BNMO HLSC and LLSC is that the

film atoms cannot be resolved from the substrate LAO [100] zone axis because of the in-

plane atom rotation. The in-plane atom rotation is believed to result from the

incommensurate matching between the Bi-based slabs and Mn-O/Ni-Mn-O layers. The

large misfit between the two sublayers causes high strain energy which is released by in-

plane atom rotation in order to achieve stable layered stacking of the two sublayers.

Despite the in-plane atom rotation, the BMO and BNMO layered supercell structures are highly epitaxial along the film out-of-plane direction as proved by the dominant selected area electron diffraction pattern (SAED). The BMO and BMO HLSC and LLSC can be viewed as epitaxial layered stacking of two sublattices, i.e. lattice 1 of octahedra layer and sublattice 2 of Bi-based layer. Here, the BNMO LLSC was taken as an example for a detailed structural analysis of the misfit layered supercell structure as shown in Figure 5.5 and 5.6. In order to obtain crystallographic information of BNMO LLSC, selected area electron diffraction tomography (EDT) analysis has been performed on BNMO LLSC. Figure 5.5 (a) and (b) shows the selected EDS patterns of sublattice 1 (encircled in green) and sublattice 2 (encircled in red). The sublattice 1 exhibits sharp reflections while the sublattice 2 is disordered with the presence of diffuse scattering lines along $[001]^*$. Figure 5(c) presents the reciprocal space of BNMO LLSC which shows the characteristic of the so-called misfit layered structure with two sublattices stacked along the c-axis but having a lattice mismatch in both in-plane directions. Sublattice 1 can be indexed a hexagonal cell with R-centering (hkl: h-k+l=3n) leading to the lattice parameters: $a_1 = b_1 \approx 2.51$ Å and $c_1 \approx 39.0$ Å in agreement with the out-of-plane lattice distance measured by XRD (the first diffraction peak at $2\theta = 6.81°$ being then indexed *003*). Sublattice 2 is only made of diffuse scattering lines running along $[001]^*$ indicating the presence of stacking faults. Sublattice 2 can also be indexed in a hexagonal cell with in-plane lattice parameters of $a_2 = b_2 \approx 3.42$ Å. To express the relation linking sublattice 1 and sublattice 2, a modulation vector in the form $\mathbf{q_1}=\sigma_1.\mathbf{a_2}^*+\beta\sigma_2.\mathbf{b_2}^*$ with $\sigma_1 = 0.72$ and $\sigma_2 = 0.85$ should be considered.
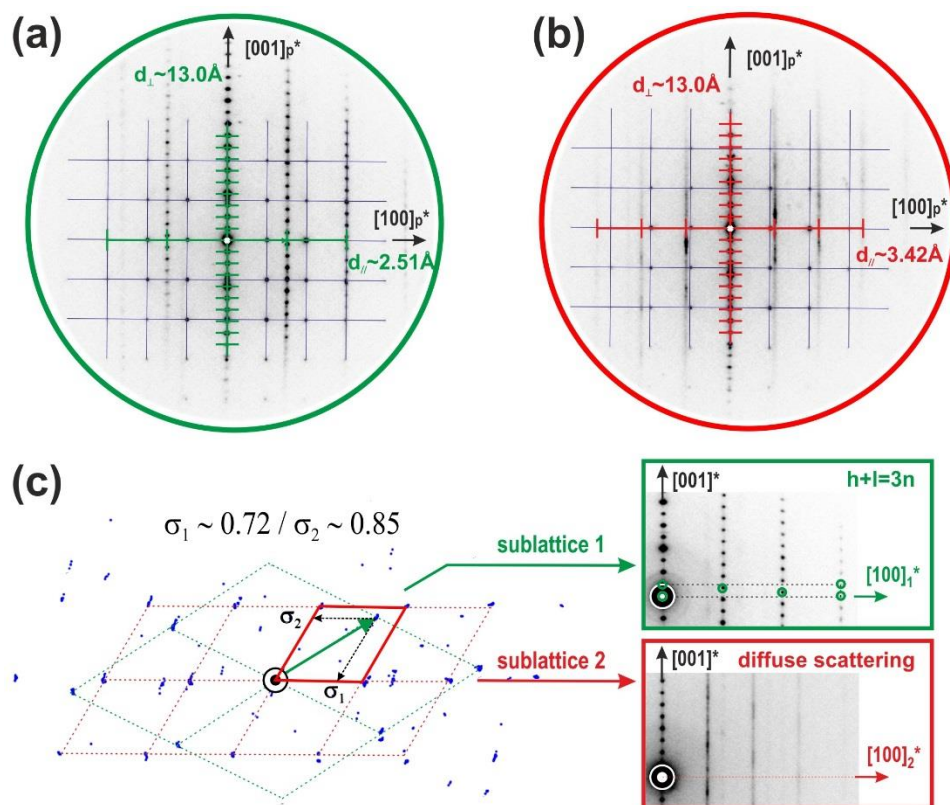
Figure 5.5 Reciprocal space electron diffraction tomography (EDT) investigation of the BNMO LLSC. (a) and (b) Selected EDT patterns showing the sublattice 1 (in green) and sublattice 2 (in red). The sublattice 1 exhibits sharp reflections while the sublattice 2 is disordered with the presence of diffuse scattering lines along [001]*. (c) (hk0)* plane reconstructed from the EDT experiment performed by collecting patterns in zone with [001]*. Modulation vector $\mathbf{q_1}=\sigma_1.\mathbf{a_2^*}+\sigma_2.\mathbf{b_2^*}$ relating the sublattice 1 to the sublattice 2.

The structure construction could not be performed because of the diffuse scattering as presented in the EDT pattern. But the structure of the two sublattices constituting BNMO LLSC can be reasonably guessed. For sublattice 1, it is mostly likely that it consists of MO_6 edge-sharing octahedral layers, $[MO_2]_\infty$ with M = Ni/Mn, separated by 13.0 Å based on the previous work.[184, 185, 186, 219] For sublattice 2, from the STEM-HAADF images (Figure 5.6(a) and (b)), the sublattice 2 contains blocks of three-layer-thick Bi-O, i.e. would have as a first guess a composition in the form $[Bi_3O_n]$ assuming this sublattice

is only occupied by Bi cations. The misfit layered supercell structure can be written as [Bi$_3$O$_n$][MO$_2$]$_x$ because of the in-plane mismatch between the two sublattices, where x represents the in-plane area difference between the two sublattices expressed as x=(a$_2$/a$_1$)^2~1.86. Regarding the cations' content, from EDS analyses the Bi/(Ni+Mn) ratio is about 1.81. Regarding oxygen's content, it is hard to estimate from the existing information. If sublattice 2 is only constituted by three Bi-O layers, the chemical formula for sublattice can be written as [Bi$_3$O$_{3+\delta}$] if oxygen vacancy/extra oxygen is considered. The above analysis then leads to the chemical formula [Bi$_3$O$_{3+\delta}$][MO$_2$]$_{1.86}$ for BNMO LLSC, where M = Ni and Mn.

The above structural analysis by EDT, although not leading to a strict crystal structure of BNMO LLSC, has provided people a reasonable view of this kind of misfit layered structures. For the BMO and BNMO HLSC, they are composed of [Bi$_2$O$_{2+\delta}$] slabs and Mn-O/Ni-Mn-O octahedra layers while BMO LLSC consists of [Bi$_3$O$_{3+\delta}$] and Mn-O octahedra slabs.
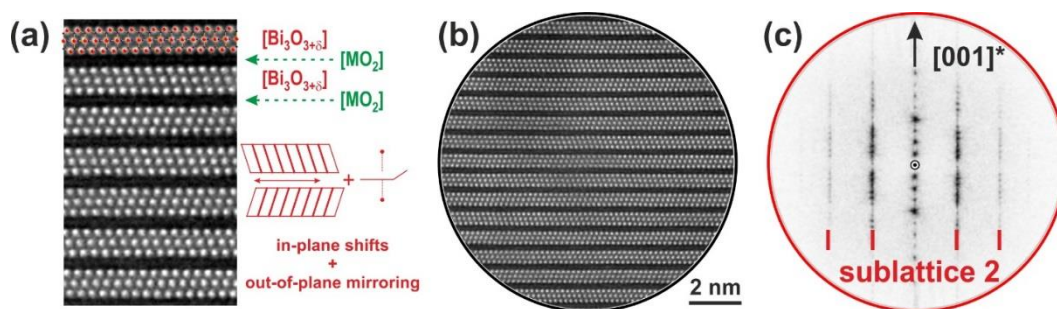
Figure 5.6 Structural analysis for BNMO LLSC. (a) High-resolution HAADF-STEM image of BNMO LLSC showing the in-plane shifts and out-of-plane mirroring of Bi-based slabs. The BNMO LLSC is composed of layered stacking of [Bi$_3$O$_{3+\delta}$] and [MO$_2$] along

the out-of-plane direction. (c) Fourier transform of the larger area STEM-HAADF image (b) showing the disorder related to the Bi-based stacking (sublattice 2).

To explore the physical properties of the BMO and BNMO layered sueprcell structures, a physical properties measurement system with a vibrating sample magnetometer (VSM) option was used to measure the magnetic properties. Figure 5.7(a) shows that the in-plane (IP) and out-of-plane (OP) saturation magnetization of BMO HLSC at 300 and 1 T is 204 emu/cc and 178 emu/cc, respectively, with a similar coercive field of ~230 Oe along both IP and OP directions. For BMO LLSC, the magnetization behaviors are quite similar to each other with a saturation magnetization of ~190 emu/cc at 300 K and 1 T, and a coercivity of ~210 Oe (Figure 5.7(b)).
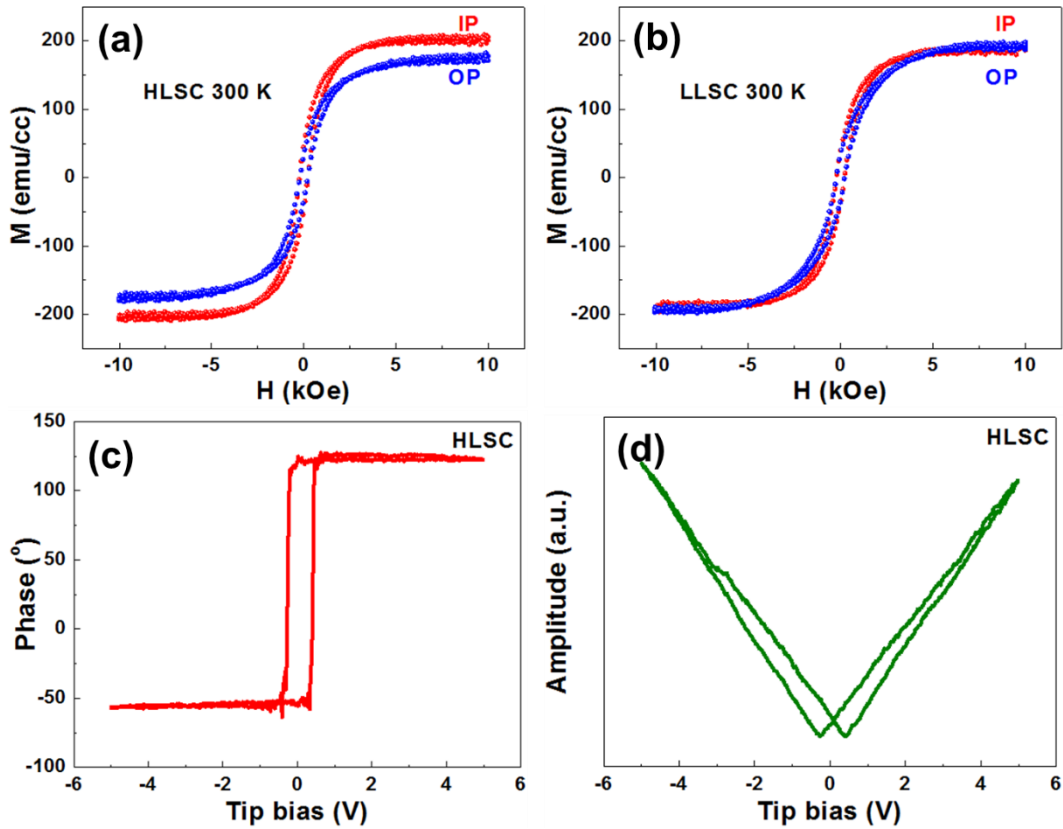
Figure 5.7 Room-temperature multiferroic properties of the 2D BMO layered supercell structures. In-plane (IP) and out-of-plane (OP) magnetization hysteresis (M-H) loops of the BMO (a) HLSC and (b) LLSC at 300 K. (c) Phase and (d) amplitude switching curves of the BMO HLSC as a function of the tip bias at room temperature.

The temperature-dependent measurement (M-T curves, Figure 5.8) of BMO HLSC and LLSC both exhibit strong magnetizations even at 380 K revealing a ferromagnetic Curie transition temperature (T_C) of at least 380 K. Based on the Kanamori-Goodenough rules, the strong magnetizations of both BMO HLSC and LLSC at 300 K may come from the superexchange coupling between the Mn^{3+} cations which form distorted MnO_6 octahedra (see XPS spectrum in Figure 5.9) which align between the Bi-O slabs in a straight line. Compared to the previously reported $BiMnO_3$ both in bulk and thin film

forms, the magnetic properties of both BMO HLSC and LLSC are much better. The ferromagnetic transition temperature for bulk $BiMnO_3$ with monoclinic structure is 105 K and for thin film $BiMnO_3$ with pseudocubic structure, it is even lower depending on the substrate and growth conditions. The pseudocubic $BiMnO_3$ thin film grown on LAO (001) substrate exhibits a low ferromagnetic Curie temperature of 50 K.[86] The BMO novel layered supercell structures with strong magnetizations at room temperature and much higher ferromagnetic transition temperature prevail over the BMO conventional pseudocubic phase. With the presence of $6s^2$ *lone pair* electrons from the Bi^{3+} cations, ferroelectric ordering is expected to occur in the BMO layered supercell structures. To demonstrate the ferroelectric properties, piezoelectric force microscopy (PFM) analysis was performed on the BMO HLSC as shown in Figure 5.7(c) and (d). As proved by the sharp 180° phase change and amplitude change, obvious ferroelectric domain switch has occurred in the BMO HLSC at room temperature.
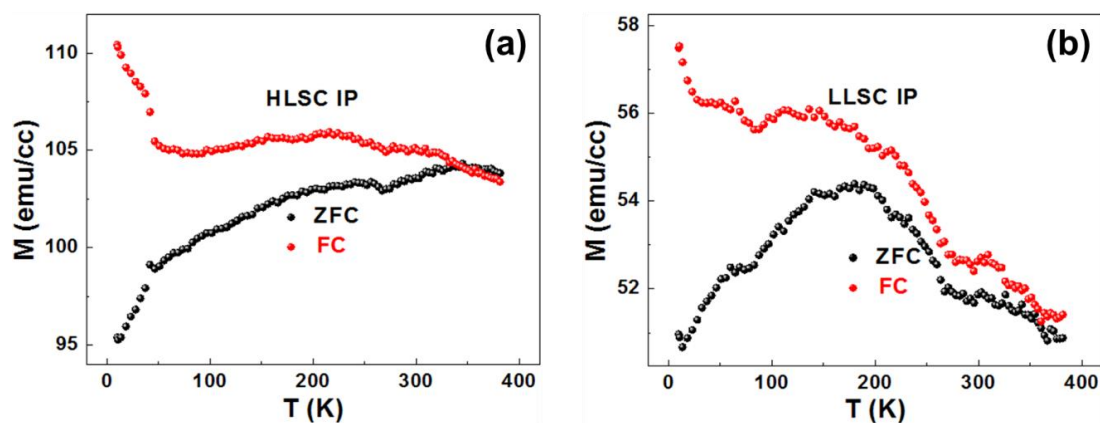
Figure 5.8 Magnetizations of BMO (a) HLSC and (b) LLSC as a function of temperature cooled under zero magnetic field (ZFC) and an in-plane magnetic field of 1000 Oe (FC), respectively.
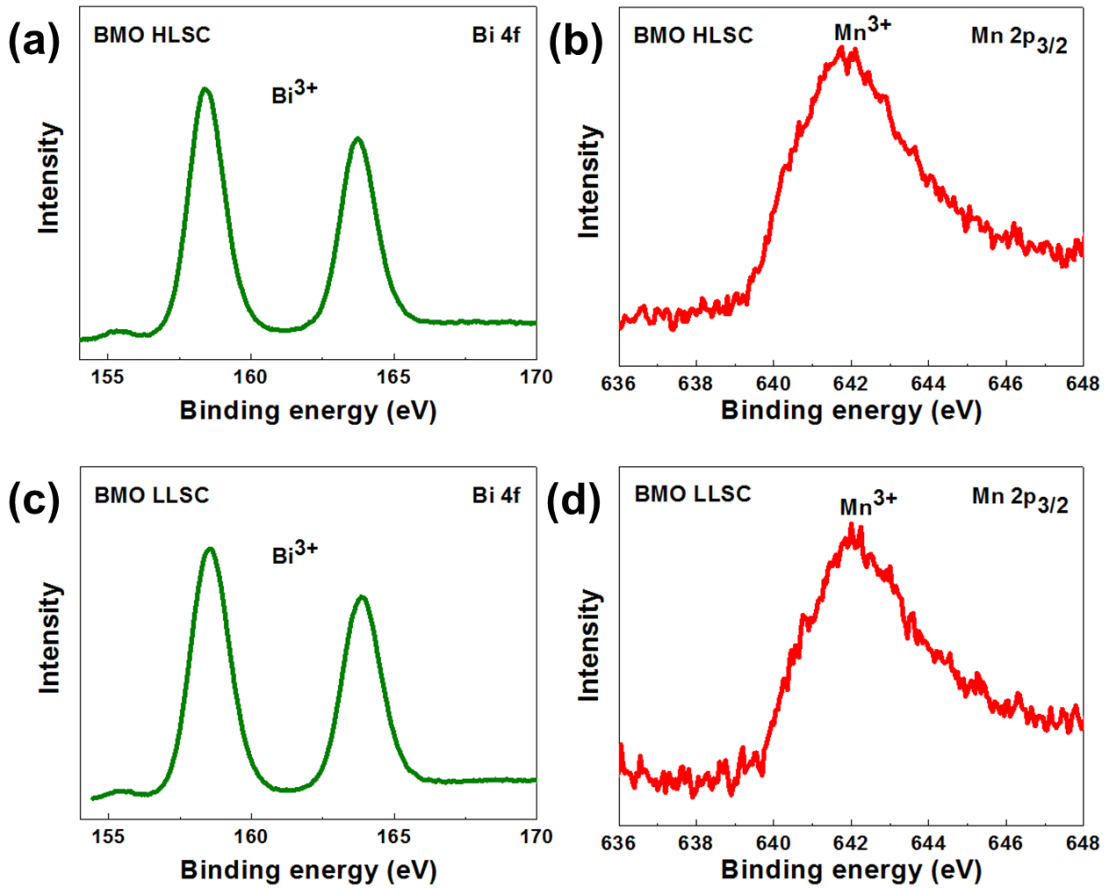
Figure 5.9 The XPS spectra of (a) and (c) Bi 4f; (b) and (d) Mn $2p_{3/2}$ for BMO HLSC and LLSC, respectively.

Figure 5.10(a) and (b) shows the magnetization hysteresis loops of the BNMO LSC measured at 300 K by applying a magnetic field of 1 T parallel (in-plane, IP) and perpendicular (out-of-plane, OP) to the film plane, respectively. Figure 5.10(a) shows that the IP and OP magnetizations of BNMO HLSC at 300 K and 1 T are 817 emu/cc and 685 emu/cc, respectively, with a coercive field of ~253 Oe for both IP and OP directions. The magnetizations of BNMO LLSC at 300 K and 1 T are 147 and 80 emu/cc, respectively, with a coercivity of ~243 Oe, along the IP and OP directions (Figure 5.10(b)). The ferroelectric response of the BNMO LSC is characterized by piezoelectric force

151

microscope (PFM) taking the BNMO LLSC as an example. As shown in Figure 5.10(c) and (d), BNMO LLSC also exhibits sharp 180º phase change as well as amplitude change indicating obvious ferroelectric domain switching in BNMO LLSC. The BNMO layered supercell structures showing both strong ferromagnetic and ferroelectric responses are proved to be desired multiferroic materials with unique 2D layered structures at room temperature.
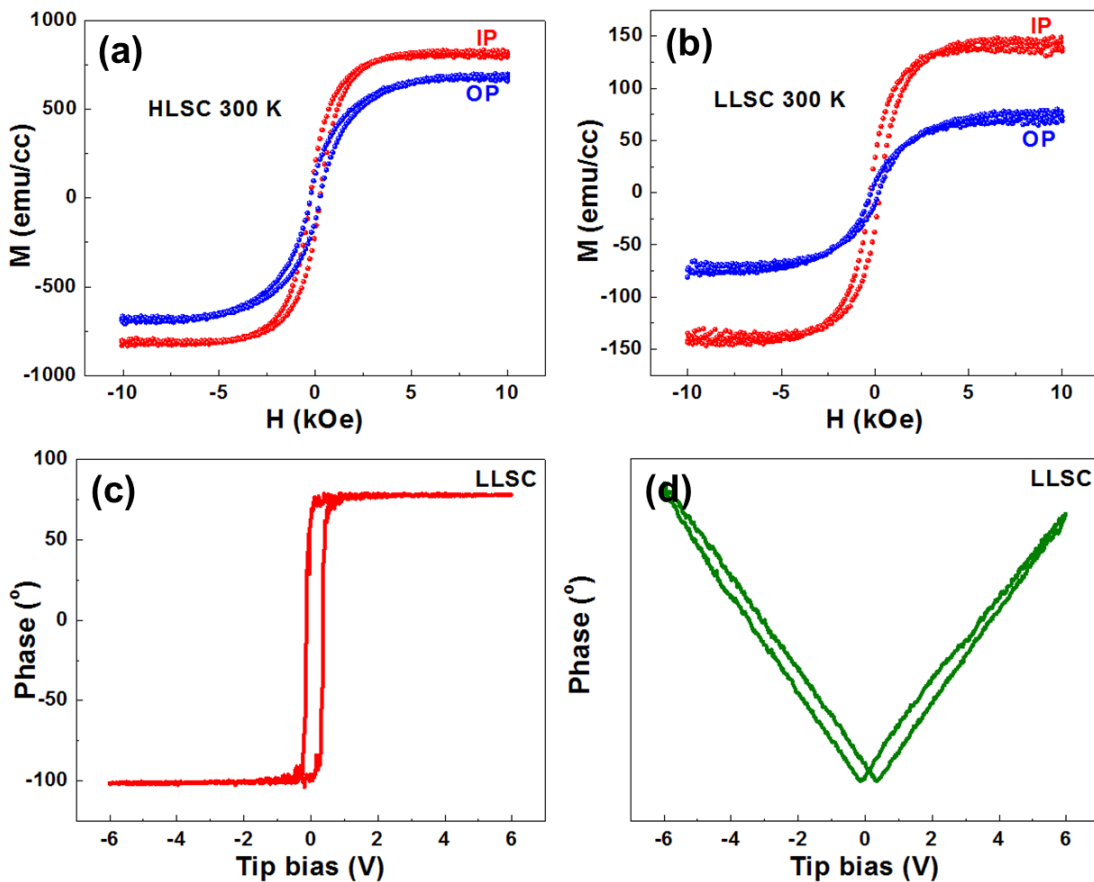
Figure 5.10 Room-temperature multiferroic properties of the 2D BNMO LSC. Magnetization hysteresis (M-H) loops of the BNMO (a) HLSC and (b) LLSC at 300 K along both in-plane (IP) and out-of-plane (OP) directions. (c) Phase and (d) amplitude switching curves of the BNMO LLSC as a function of the tip bias at room temperature showing the ferroelectric domain switching behavior.

The magnetization behaviors of both BNMO HLSC and LLSC at different temperatures (300 K, 100 K and 10 K) are quite similar with nearly the same magnetization value and coercivity (Figure 5.11 (a) and (c)). The temperature-dependent magnetizations of BNMO HLSC and LLSC measured with and without an in-plane magnetic field of 1000 Oe applied parallel to the film plane both show high magnetization value even at 380 K, indicating that the magnetic transition temperature (T_C) of both BNMO HLSC and LLSC is above 380 K (Figure 5.11 (b) and (d)). In addition, the BNMO LLSC exhibits a sharp magnetization increase at around 100 K, indicating that another ferromagnetic ordering has occurred due to the mixed valence states of Ni and Mn cations in the BNMO LLSC (see XPS in Figure 5.12(c) and (d)).
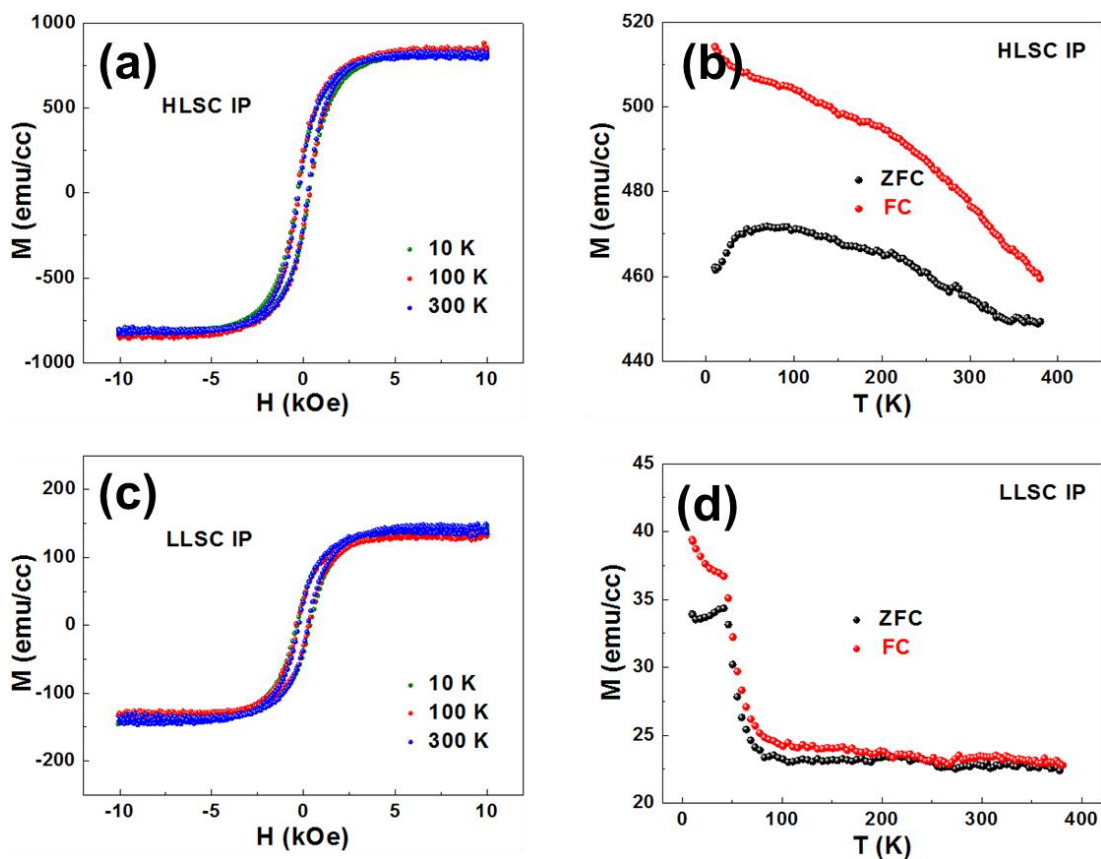
Figure 5.11 (a) and (c) Temperature-dependent magnetizations of BNMO HLSC and LLSC at 10 K, 100 K and 300 K along the in-plane direction, respectively. (b) and (d) Magnetizations of BNMO HLSC and LLSC as a function of temperature cooled under zero magnetic field (ZFC) and an out-of-plane magnetic field of 1000 Oe (FC), respectively.

Both BNMO HLSC and LLSC exhibit highly anisotropic characteristics in the magnetic response with strong magnetizations. And in particular, the BNMO HLSC shows extraordinarily high magnetizations along both IP (817 emu/cc) and OP (685 emu/cc) directions at room temperature. The XPS spectra of BNMO HLSC indicate that the valence state for Ni and Mn may be +2 and +4, respectively (Figure 5.12(a) and (b)). The extraordinarily strong magnetizations of BNMO HLSC may be a result of ferromagnetically coupled Ni^{2+} (t_{2g}^6, e_g^2) having half-filled e_g orbitals and Mn^{4+} (t_{2g}^3, e_g^0)

having empty e_g orbitals based on the Goodenough-Kanamori rules for 180° superexchange couplings. Moreover, the Ni^{2+} and Mn^{4+} cations might have been alternatively ordered between the Bi-based layers along the horizontal direction forming Ni^{2+}-O-Mn^{4+}-O-Ni^{2+}-O-Mn^{4+}-O-Ni^{2+}-O-... chains in order to enable the ferromagnetic superexchange interactions. The large space between the neighboring Bi-based layers (~2.94 Å) may have weakened the structural influence of the Bi $6s^2$ *lone pairs* to the NiO_6/MnO_6 octahedra and may have enhanced the ferromagnetic coupling between Ni^{2+} and Mn^{4+} cations. Compared to the HLSC, the LLSC sample exhibits much lower magnetizations despite that it also has a 2D anisotropic layered structure. The reason may lie in that both Ni and Mn cations between the Bi-based slabs show mixed valence states (Figure 5.12(c) and (d)). From the XPS spectra of BNMO LLSC, the Ni cations may have mixed valence states of +2 and +3 while the Mn cations are +3 and +4 mixed. By the Goodenough-Kanamori rules, several possible antiferromagnetic routes may exist in BNMO LLSC besides the ferromagnetic coupling of Ni^{2+} (t_{2g}^6, e_g^2) and Mn^{4+} (t_{2g}^3, e_g^0) such as: (1) Ni^{2+}(t_{2g}^6, e_g^2)-Ni^{2+}(t_{2g}^6, e_g^2); (2) Ni^{2+}(t_{2g}^6, e_g^2)-Mn^{3+}(t_{2g}^3, e_g^1); (3) Ni^{3+}(t_{2g}^5, e_g^2)-Mn^{3+}(t_{2g}^3, e_g^1); and (4) Mn^{3+}(t_{2g}^3, e_g^1)-Mn^{3+}(t_{2g}^3, e_g^1).
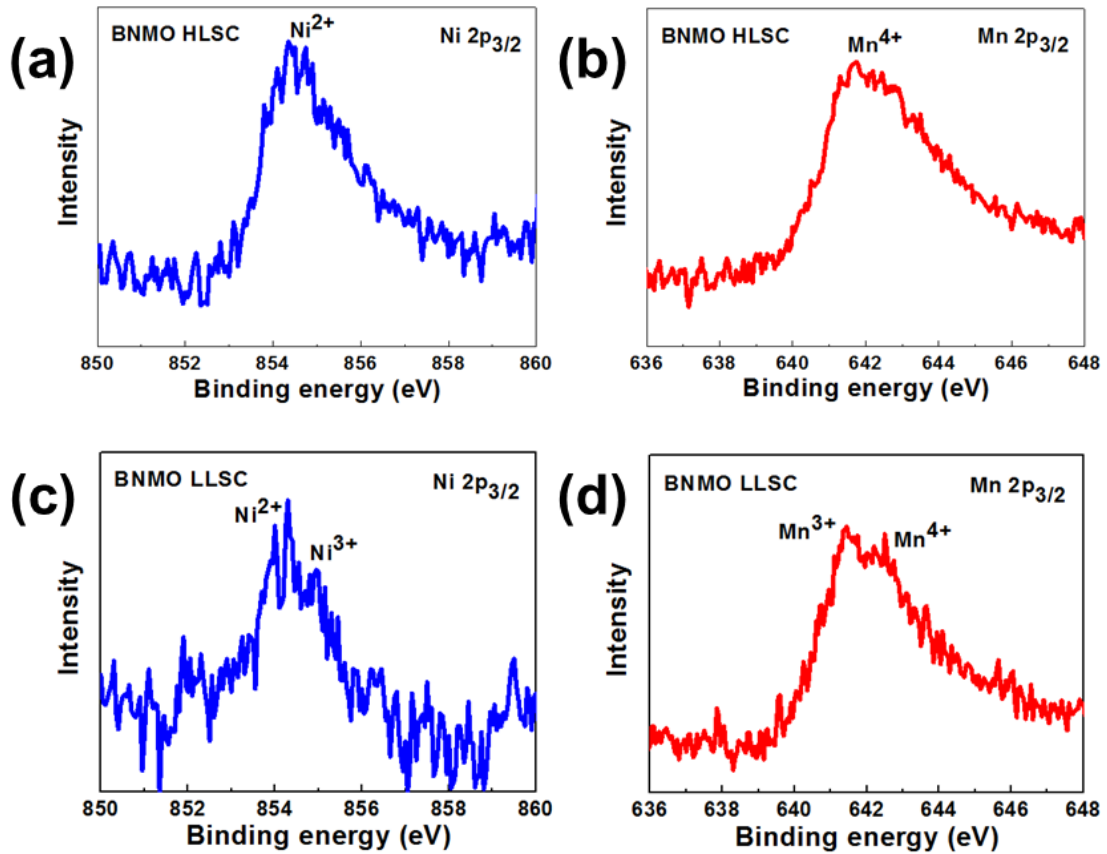
Figure 5.12 The XPS spectra of (a) and (c) Ni $2p_{3/2}$; (b) and (d) Mn $2p_{3/2}$ for BNMO HLSC and LLSC, respectively.

With different compositions and structures, different physical properties, i.e. magnetic response, are expected. Figure 5.13 (a) and (b) summarizes the varied saturation magnetizations and coercive fields of the BMO and BNMO layered supercell structures, indicating tunable magnetic response by tuning the film composition and structure. In particular, a saturation magnetization value of 817 emu/cc for BNMO HLSC along the in-plane direction shows that the magnetic response can be highly enhanced by incorporating Ni cations into the BMO HLSC, substituting part of the Mn cations, forming strong ferromagnetic Ni^{2+}-O-Mn^{4+} ordering. Furthermore, the optical response of the BMO and

BNMO films is measured to characterize the tunability of physical properties by varying the compositions and structures. Figure 5.13(c) and (d) shows the tunable optical transmittance and band of the BMO and BNMO thin films with either layered or pseudocubic structures.
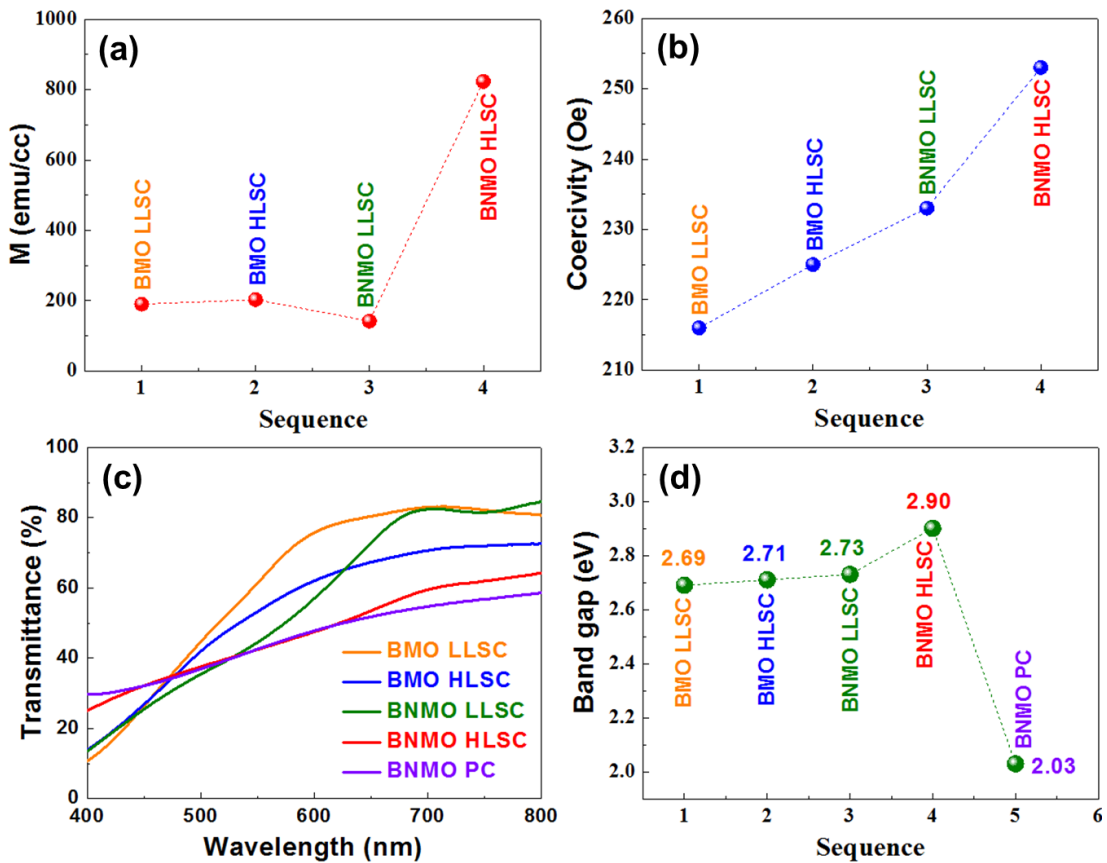
Figure 5.13 Tunable physical properties of the BMO and BNMO thin films with different structures. (a) Saturation magnetization, (b) Coercivity, (c) Transmittance, and (d) Band gaps.

The growth of BMO and BNMO HLSC and LLSC can be viewed as the alternated stacking of two sublattices of Bi_2O_x/Bi_3O_x slabs and MnO_6/NiO_6 and MnO_6 octahedra layers epitaxially along the out-of-plane direction. Because of the difference in lattice

parameters, the two sublattices are misfit (incommensurate) along the in-plane direction. It is proposed here that the in-plane lattice mismatch between the two sublattices leads to high strain energy and in-plane atom rotation of the films occurs to alleviate the high energy state to achieve the stable 2D layered structures. To demonstrate the growth process of the BMO and BNMO layered structures formed by layer stacking, BNMO HLSC is taken as an example here to illustrate the growth mechanism. First, lattice match may play an important role in facilitating the growth of Bi-based layered structures. As shown by the high-resolution STEM image, the in-plane Bi-Bi distance (~3.96 Å) in the first initial unit cell with $Bi(Ni/Mn)O_x$ perovskite structure (interlayer 1) can well match with that of La-La distance (3.79 Å) of the $LaAlO_3$ substrate which is indispensable for epitaxial thin film growth. Following the growth of interlayer 1, interlayer 2 with one layer of Bi atoms is stacked on interlayer 1. Notably, the Bi atoms of interlayer 2 directly stack onto the Bi atom interstitial of interlayer 1 with tight Bi-Bi bonding and Bi atoms' zig-zag arrangement formed. By comparing the structural difference of the BNMO layered structures and pseudocubic phase, it is believed that the formation of the zig-zagged Bi-Bi arrays with tight Bi-Bi bonding in the BNMO layered structures is critical in achieving the following alternated stacking of Bi-based slabs and Ni-Mn-O octahedra layers. The interlayer 2 with zig-zagged Bi arrangement might have served as both "interruption layer" (interrupt the cube-on-cube growth of the pseudocubic phase) and "seed layer" (a template for the growth of the layered structure). The formation of interlayer 2 might be achieved only under appropriate growth thermodynamics and kinetics which is controlled by the deposition parameters such as substrate temperature and partial oxygen pressure. From the

158

comparison study of BNMO HLSC and LLSC, it is found that the growth of the Bi-based layered structures is very sensitive to the substrate temperature which significantly influences the diffusion kinetics of the adatoms and structures of the films. The Bi atoms have faster diffusion kinetics at higher temperature and only Bi-based slabs with two-layer-thick of Bi atoms can be structurally stable under the certain thermodynamics at higher temperature. At low temperatures, the Bi atoms have lower diffusion rate and Bi-based slabs with three-layer-thick Bi atoms can be thermodynamically stable. Thirdly, to create Bi-based layered structures the ionic radius of the two cations lying between the Bi-based slabs should be close to each other in order to enable the formation of octahedron layers. The approach for creating BNMO layered structures and the design rules proposed above are likely to be extendable to a wide range of Bi-based double-perovskite systems with significant composition flexibility allowing the realization of other novel 2D layered structures with potential applications as multiferroic memory, thermoelectric materials, etc.

5.5 Conclusion

To conclude, novel Bi-based layered supercell structures of BMO and BNMO HLSC and LLSC have been fabricated by one-step self-assembled growth from single-perovskite $BiMnO_3$ and double-perovskite Bi_2NiMnO_6, respectively. Microstructural characterizations show that the layered supercell structures grow epitaxially along the out-of-plane direction by alternative layered stacking of Bi_2O_x/Bi_3O_x slabs and Mn-O/Ni-Mn-O octahedra layers. Robust multiferroic properties have been demonstrated for the novel

layered supercell structures at room temperature. The creation of the new BMO and BNMO layered supercell structures has provided people very important clues of designing new 2D layered structures and will stimulate further exploration of new single-phase multiferroic materials.

CHAPTER VI

SELF-ASSEMBLED LAYERED SUPERCELL STRUCTURE OF BI$_2$ALMNO$_6$

WITH STRONG ROOM-TEMPERATURE MULTIFERROIC PROPERTIES

6.1 Overview

Room-temperature (RT) multiferroics, possessing ferroelectricity and ferromagnetism simultaneously at RT, hold great promise in miniaturized devices including sensors, actuators, transducers, and multi-state memories. In this work, we report a novel 2D layered RT multiferroic system with self-assembled layered supercell structure consisting of two mismatch-layered sub-lattices of [Bi$_3$O$_{3+\delta}$] and [MO$_2$]$_{1.84}$ (M=Al/Mn, simply named as BAMO), i.e., alternative layered stacking of two mutually incommensurate sublattices made of a three-layer-thick Bi-O slab and a one-layer-thick Al/Mn-O octahedra slab along the out-of-plane direction. Strong room-temperature multiferroic responses, e.g., ferromagnetic and ferroelectric properties, have been demonstrated and attributed to the highly anisotropic 2D nature of the non-ferromagnetic and ferromagnetic sublattices which are highly mismatched. The work demonstrates an alternative design approach for new 2D layered oxide materials that hold promises as single-phase multiferroics, 2D oxides with tunable bandgaps, and beyond.

6.2 Introduction

Complex oxides have drawn extensive research interest motivated by their fascinating physical properties as well as their enormous potentials for technological

applications. Up to date, ferroelectricity,[244] piezoelectricity,[245] single-phase multiferroicity,[7, 74] magnetoresistance,[40, 246, 247] high-temperature superconductivity,[248, 249, 250] and many other intriguing phenomena have been discovered in complex oxides. Multiferroics, in particular, room-temperature (RT) multiferroics, possessing ferroelectric and ferromagnetic ordering simultaneously in a single phase, have received significant attention owing to their potential applications in data storage, spin valves, and tunnel magnetoresistance sensors. However, single-phase multiferroics are scarce because of the drastically different orbital requirements for ferroelectricity (requiring empty d-orbital) and ferromagnetism (coming from partially filled d-orbitals).[44]

Combining two cations possessing ferroelectric and ferromagnetic ordering respectively into one phase is one of the effective routes towards creating single-phase multiferroic materials. $BiFeO_3$, a well-known Bi-based room-temperature multiferroic material with perovskite structure, is one such multiferroic material with its ferroelectricity coming from the Bi^{3+} $6s^2$ lone-pair electrons and (anti)ferromagnetism from the Fe^{3+} cation.[7, 47] Bi-based double-perovskites ($Bi_2BB'O_6$, B and B' are transition metal cations), e.g., Bi_2FeMnO_6 and Bi_2NiMnO_6,[184, 185, 219] are also widely studied in the exploration of single-phase multiferroic materials because of their long-range ferro/ferri-magnetically ordered B and B' cations as well as the desired ferroelectricity from the lone-pair electrons. Despite the prior success of Bi-based multiferroic materials which all have conventional pseudocubic phases, the antiferromagnetic nature and/or relatively weak room-temperature magnetism have limited their practical applications. Based on these findings, Bi-based perovskites with the Bi $6s^2$ lone-pair electrons giving rise to ferroelectricity and

magnetic cations in one phase provide a very important clue for designing new multiferroic materials.

Layered complex oxides with commensurate or incommensurate sublayered structures present new functionalities such as thermoelectric properties, multiferroics, and ionic conductors.[165, 251] Taking advantages of recent advances in high-quality thin film growth techniques, new oxide layered structures have been demonstrated by artificially controlling the stacking sequence of layers precisely via molecular beam epitaxy.[252] In parallel, self-assembled layered oxide growth represents another powerful approach for creating new layered material structures with desired physical properties.[184] For example, starting from a target with the composition of Bi_2FeMnO_6 using pulsed laser deposition (PLD), one can selectively grow either a conventional double perovskite structure with poor multiferroic properties or a self-assembled layered supercell structure $Bi_3Fe_2Mn_2O_{10+\delta}$ (BFMO) with room-temperature multiferroic properties.[184, 185, 219] In this work, we demonstrate a new class of self-assembled layered supercell (LSC) oxide structures with a non-magnetic B site cation. Such LSC structures were deposited from a Bi_2AlMnO_6 (BAMO) target via PLD with well controlled deposition parameters. The BAMO LSC can be fabricated on various substrates and buffer layers (e.g., $SrTiO_3$ (001), $LaAlO_3$ (001), CeO_2 (001) buffer, and $La_{0.7}Sr_{0.3}MnO_3$ (001) buffer). With a non-magnetic B site cation (in this case, Al), the new LSC system exhibits robust ferromagnetic and piezoelectric response at room temperature. This demonstrates the potential of fabricating new Bi-based LSC oxides with room-temperature multiferroicity beyond the limited

ferro/ferri-magnetic B or B' cations and may provide a facile route to the fabrication of many other new layered structures.

6.3 Experimental

Sample preparation. Pulsed laser deposition (PLD, Lambda Physik, KrF, $\lambda = 248$ nm) was employed to fabricate the high-quality epitaxial BAMO layered thin films on both single-crystal $LaAlO_3$ (001) and $SrTiO_3$ (001) substrates from the Bi_2AlMnO_6 target. To prepare the Bi_2AlMnO_6 target, stoichiometric ratio of Bi_2O_3, Al_2O_3, and MnO_2 powders were mixed, pressed into a pellet, and sintered at 750 ^{o}C for 3 hours in air. The substrate temperature ranged from 400 to 700 ^{o}C and a dynamic oxygen pressure of 20~200 mTorr was maintained during depositions. The buffer layer $La_{0.7}Sr_{0.3}MnO_3$ (LSMO) and CeO_2 was deposited at 750 ^{o}C and 700 ^{o}C, respectively, in 200 mTorr of oxygen. After deposition, the films were *in-situ* annealed at 400 ^{o}C for 1 hour in 500 Torr of oxygen before cooling down to room temperature.

XRD, TEM, STEM HAADF and ABF imaging, AFM imaging, EDS, and XPS. The microstructures of the fabricated BAMO samples were characterized by high-resolution X-ray diffraction (HRXRD, PANalytical Empyrean), transmission electron microscopy (TEM, FEI Tecnai G2 F20), high resolution scanning transmission electron microscopy (HRSTEM), and atomic force microscopy (AFM). The HRSTEM images both in high angle annular dark-field (HAADF) mode and annular bright-field (ABF) mode were obtained using a FEI Titan G2 80-200 STEM with a Cs probe corrector operated at 200 kV and a modified FEI Titan STEM TEAM 0.5 with a convergence semi-

angle of 17 mrad operating at 200 kV, respectively. For high-resolution energy-dispersive X-ray spectroscopy (EDS) profiling, a FEI Titan[TM] G2 80-200 STEM with a Cs probe corrector and ChemiSTEM[TM] technology (X-FEG[TM] and SuperX[TM] EDS with four windowless Si drift detectors) operated at 200 kV was used. To obtain the surface topography image, a Bruker Dimension Icon AFM with high resolution ($Z < 0.1$ nm, XY < 1 nm) was used to scan the surface of the sample with an area of 5 μm $\times$ 5 μm. The film composition was analyzed by EDS in a JEOL JSM-7500F scanning electron microscope. X-ray photoelectron spectroscopy (XPS) measurement was done by an Omicron XPS system with Argus detector using Omicron's DAR 400 X-ray source.

Precession electron diffraction tomography (PEDT). Precession electron diffraction (PED) patterns were obtained using a JEOL 2010 (200 kV) transmission electron microscope (TEM) equipped with a side-mounted Gatan Orius CCD camera and a Nanomegas Digistar PED unit. The data collection was performed on a cross-sectional sample prepared from a ~100 nm film using the tomography approach.[193] In such a case, the rotation axis is mostly limited to the out-of-plane direction to avoid shadowing the film by the substrate. 88 PED patterns were recorded in the tilt range from -44.5 to +34.8 degrees with a precession angle of 1.2 degree. The data were processed using the programs PETS[194] and Jana2006[195].

Magnetic and electrical property measurement. To measure the magnetic properties, a commercial Physical Properties Measurement System (Quantum Design, PPMS 6000) with vibrating sample magnetometer (VSM) option was employed. The out-of-plane and in-plane magnetizations were measured by applying a magnetic field of 1 T

perpendicular and parallel to the film plane, respectively. For the field-cooling (FC)/zero-field cooling (ZFC) measurements, the samples were cooled down from 380 K to 10 K with/without a magnetic field, respectively, and the magnetizations were recorded during the heating cycle from 10 K to 380 K. For electrical property measurements, 30 nm thick $La_{0.7}Sr_{0.3}MnO_3$ (LSMO) was firstly deposited on STO substrate at 750 ^{o}C under 200 mTorr of oxygen before depositing the BAMO thin film. The piezoelectric properties were measured at ambient conditions with a conductive Pt-Ir coated Si tip (model: SCM-PIT) via a Bruker Dimension Icon AFM with high resolution (Z < 0.1 nm, XY < 1 nm).

6.4 Results and discussion

X-ray diffraction (XRD) was first conducted to investigate the BAMO thin films grown on both STO (001) and LAO (001) substrates. As shown in Figure 6.1(a) and (b), a set of dominant (00l)-type diffractions exist besides the peaks from the substrates in the θ-2θ scans, indicating that the new BAMO thin film grows along the out-of-plane direction in a highly textured manner on both STO (001) and LAO (001) substrates. This single set of thin film diffraction peaks (2θ = 6.73^o, 13.40^o, 20.10^o, 27.00^o, 33.90^o, 40.93^o,…, corresponding to the out-of-plane d-spacing of 13.13 Å, 6.60 Å, 4.41 Å, 3.30 Å, 2.64 Å, 2.20 Å,…, respectively) with a large out-of-plane d-spacing do not fit the diffraction patterns of any known crystalline materials in the database, suggesting the formation of a new crystalline structure. More interestingly, this new BAMO thin film can also grow on $La_{0.7}Sr_{0.3}MnO_3$ (LSMO) and CeO_2 buffered STO (001) substrates, respectively, as shown

in Figure 6.1(c) and (d), indicating that the new BAMO thin film could be integrated on other substrates with proper buffer layers.
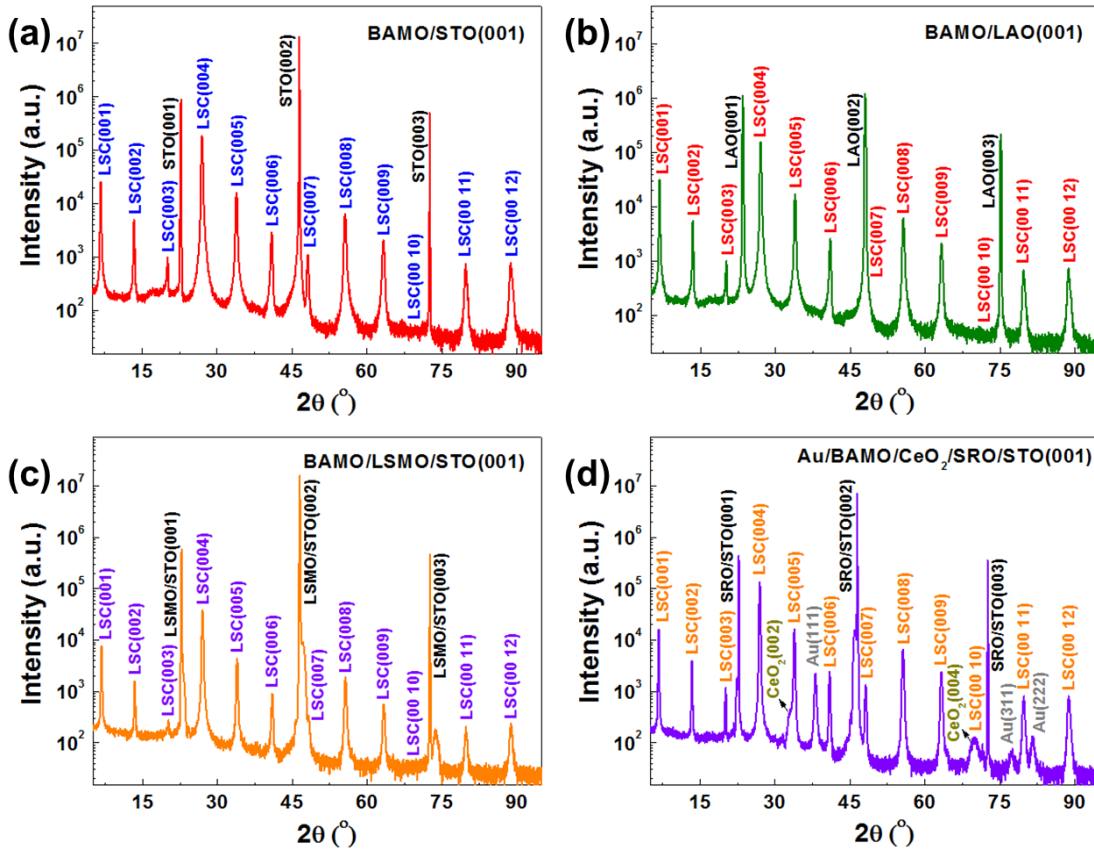
Figure 6.1 XRD patterns of the self-assembled BAMO layered supercell structure. θ-2θ scans of BAMO layered thin films fabricated on LAO (a), STO (b), LSMO-buffered STO (c), and CeO_2-buffered STO (d) substrates, respectively.

Aberration-corrected scanning transmission electron microscopy (STEM) coupled with energy-dispersive X-ray spectroscopy (EDS) and high-resolution atomic force microscopy (AFM) were adopted to further investigate the microstructure of the BAMO LSC as shown in Figure 2. High-resolution STEM images taken in high-angle annular dark-field (HAADF) mode along the substrate [100] zone axis in Figures 6.2(a) and Figure

6.3 clearly demonstrate the layered stacking growth of BAMO LSC along the out-of-plane direction both on STO (001) and LAO (001) substrates.
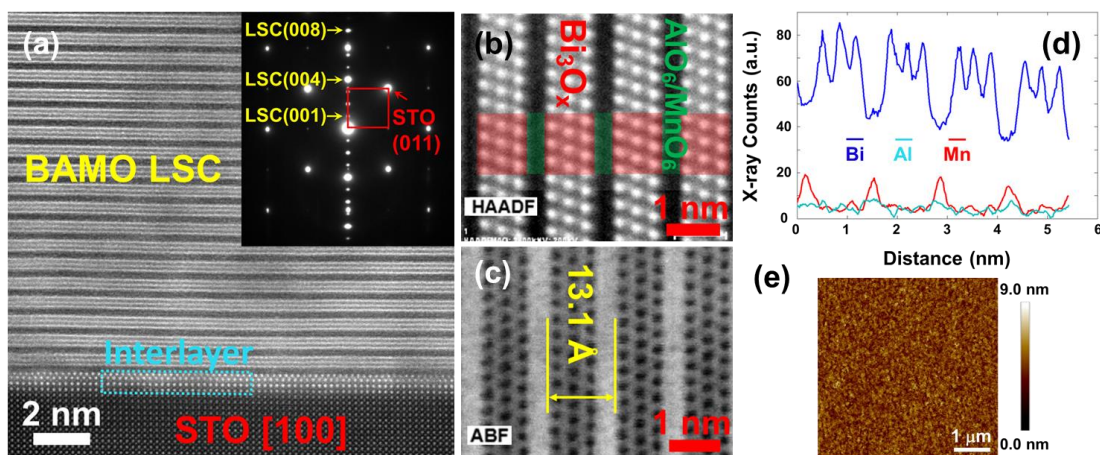
Figure 6.2 Microstructural charaterization of the BAMO layered supercell structure. (a) STEM HAADF image of BAMO LSC along the STO [100] zone axis. The inset shows the SAED pattern. (b-c) High-resolution STEM HAADF (b) and ABF (c) images showing the layered oxide supercell with a three-atom-thick Bi-based slab and one single Al/Mn based layer. (d) EDS profile showing Bi, Al and Mn along the [001] direction. (e) AFM surface topography image indicating the high surface quality of the BAMO LSC.

The satellite diffraction dots in the selected area electron diffraction (SAED) pattern taken along the [100] zone axis (the inset at the top right corner of Figure 6.2(a)) again confirm the large out-of-plane d-spacing and the highly epitaxial nature of BAMO LSC on both substrates. In the STEM HAADF mode, the image intensity is proportional to the Z^n (Z is the atomic number and $1.5 \leq n \leq 2$). The bright layers of the BAMO LSC are ascribed as Bi-based slabs ($Z_{Bi} = 83$) while the dark layers in-between contains Al and Mn ($Z_{Al} = 13$, $Z_{Mn} = 25$). Because of the minor in-plane rotation between the film and the substrate, and, the limited probe resolution, only the layers of Bi-based slabs can be resolved along the STO [100] zone axis. By tilting the BAMO LSC film slightly off from

168

the substrate [100] zone axis under both HAADF and ABF modes, atomic columns of Bi can be resolved where each bright/dark sheet consists of three layers of Bi columns(and also oxygen columns but oxygen columns are not resolvable in the STEM images). The composition of BAMO LSC is also identified by high-resolution EDS profile along the film out-of-plane direction (Figure 6.2(d)) which shows the presence of Al and Mn between the Bi-based slabs. The EDS composition analysis reveals that the cation atomic ratio in the BAMO LSC is Bi/Al+Mn = 1.64:1 (see Table 6.1). Both the STEM HAADF and ABF images reveal a periodicity of ~13.2 Å along the film out-of-plane direction (Figure 6.2(b) and (c)) in agreement with the d-spacing measured by XRD. The AFM topography image acquired from an area of 5 μm × 5 μm reveals a surface roughness of 0.76 nm showing high surface quality of the BAMO LSC (Figure 6.2(e)).
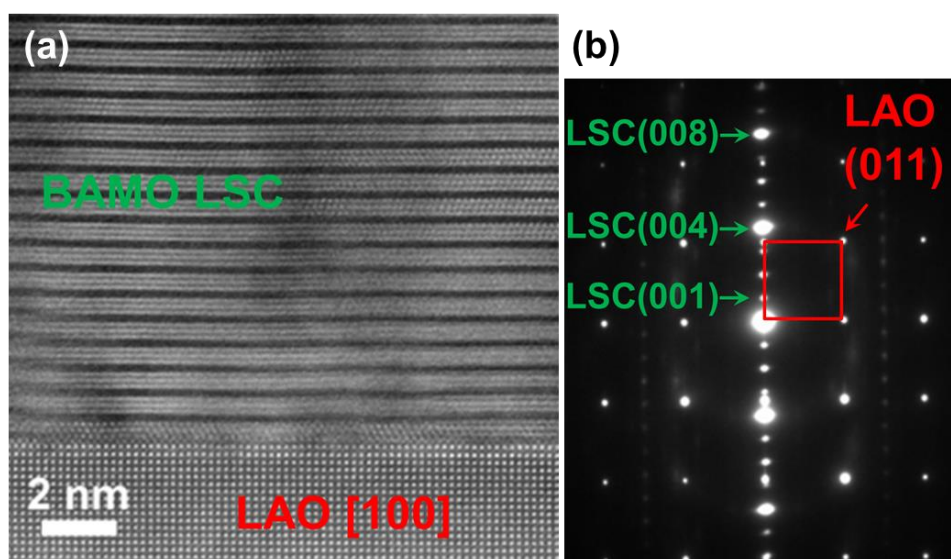
Figure 6.3 (a) STEM HAADF image of BAMO LSC along the LAO [100] zone axis. (b) Selected area electron diffraction pattern of the BAMO LSC grown on LAO (100) substrate.

Table 6.1 Cation ratio in the BAMO LSC with the STO substrate ratio as a reference.

| Spectrum | Bi-Al-Mn-O Film | | | | | | SrTiO₃ Substrate | | |
	Bi	Al	Mn	Bi/Al (atom %)	Bi/Mn (atom %)	Bi/Al+Mn (atom %)	Sr	Ti	Sr/Ti (atom %)
1	2.93	0.99	0.85	2.9596	3.44706	1.59239	15.46	15.61	0.99039
2	2.97	0.97	0.86	3.06186	3.45349	1.62295	15.53	15.77	0.98478
3	3.05	1.06	0.88	2.87736	3.46591	1.57216	15.9	15.9	1
4	2.95	0.96	0.84	3.07292	3.5119	1.63889	15.68	15.77	0.99429
5	2.96	0.99	0.77	2.9899	3.84416	1.68182	15.54	15.61	0.99552
6	2.99	1.07	0.85	2.79439	3.51765	1.55729	16	16.07	0.99564
7	2.95	1.02	0.82	2.89216	3.59756	1.60326	15.71	15.8	0.9943
8	2.97	0.9	0.88	3.3	3.375	1.66854	15.77	16.1	0.9795
9	2.98	0.95	0.82	3.13684	3.63415	1.68362	15.71	15.94	0.98557
10	2.9	0.95	0.8	3.05263	3.625	1.65714	15.57	15.67	0.99362
11	2.97	0.93	0.87	3.19355	3.41379	1.65	15.91	16.17	0.98392
12	2.77	0.98	0.84	2.82653	3.29762	1.52198	14.79	14.97	0.98798
13	2.89	0.97	0.79	2.97938	3.65823	1.64205	15.6	15.7	0.99363
14	2.94	0.88	0.83	3.34091	3.54217	1.7193	15.83	15.96	0.99185
15	2.98	1.01	0.79	2.9505	3.77215	1.65556	15.73	15.87	0.99118
16	2.96	0.98	0.88	3.02041	3.36364	1.5914	15.94	16.19	0.98456
17	2.95	1.01	0.84	2.92079	3.5119	1.59459	15.72	15.88	0.98992
18	2.98	0.92	0.82	3.23913	3.63415	1.71264	15.95	16.01	0.99625
18	2.93	0.92	0.76	3.18478	3.85526	1.74405	15.69	15.87	0.98866
20	3.01	0.97	0.74	3.10309	4.06757	1.76023	15.92	16.2	0.98272
Average	Film			3.0448365	3.579418	1.643493	Substrate		0.990214

170

The crystal structure of the new BAMO LSC has been investigated further by precession electron diffraction tomography (PEDT) in order to obtain crystallographic information from an area corresponding to the entire film thickness. From PEDT (Figure 6.4(a)) the reciprocal space of BAMO LSC presents the characteristic of a so-called misfit layered structure with two sublattices stacked along a common direction (c-axis) but having a lattice mismatch in both in-plane directions. One sublattice (further denoted 1) exhibits sharp reflections as can be evidenced in the PEDT patterns presented in Figure 6.4(c) (encircled in green) and in the (h0l)* section of the reciprocal space reconstructed from PEDT data (Figure 6.4(d)). Sublattice 1 can be indexed considering a hexagonal cell with a R-centering (hkl: h-k+l=3n) leading to the lattice parameters: $a_1 = b_1 \approx 2.92$ Å and $c_1 \approx 39.4$ Å in agreement with the out-of-plane lattice distance measured by XRD (the first diffraction peak at $2\theta = 6.73^o$ being then indexed *003*). The second sublattice (further sublattice 2) is only made of diffuse scattering lines running along [001]* (see PEDT patterns encircled in red in Figure 6.4(c)) indicating the presence of stacking faults. Sublattice 2 (in red in Figure 6.4) can also be indexed in a hexagonal cell with in-plane lattice parameters: $a_2 = b_2 \approx 3.96$ Å. The out-of-plane lattice parameter and the possible conditions limiting the reflections cannot be obtained due to the presence of diffuse scattering. Notice that the [100]* direction of sublattice 2 is almost aligned with the [110]* direction of the sublattice 1 (Figure 6.4(a)). The misfit layered supercell structure adopted by BAMO is further attested by the presence of rows of satellites reflections originating from the interactions between the two sublattices. They are clearly visible in the (h0l)* section of Figure 6.4(d).
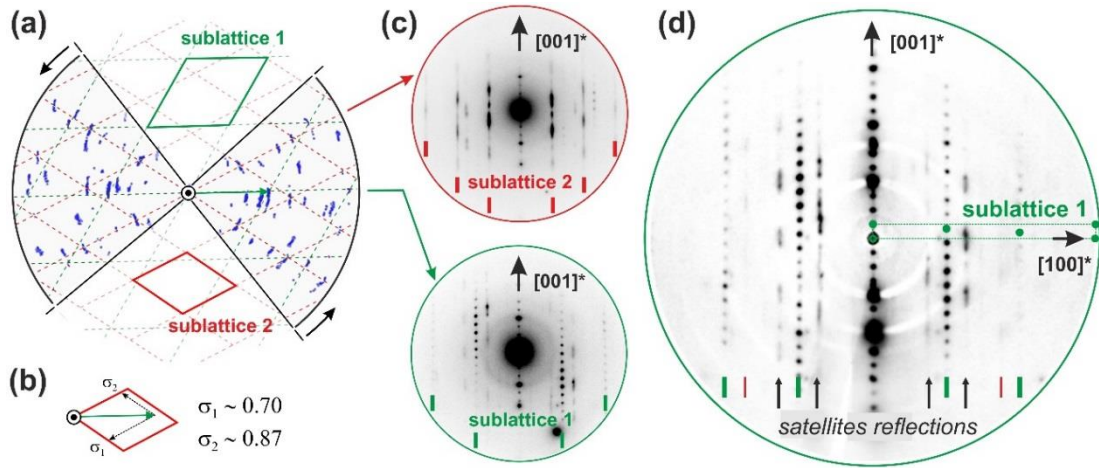
Figure 6.4 Reciprocal space PEDT investigation of the BAMO layered supercell structure. (a) (hk0)* plane reconstructed from the PEDT experiment performed by collecting patterns in zone with [001]*. (b) Modulation vector $\mathbf{q_1}=\sigma_1.\mathbf{a_2^*}+\sigma_2.\mathbf{b_2^*}$ relating the sublattice 1 to the sublattice 2. (c) Selected PEDT patterns showing the sublattices 1 (in green) and 2 (in red). The sublattice 1 exhibits sharp reflections while the sublattice 2 is disordered with the presence of diffuse scattering lines along [001]*. (d) (h0l)* reciprocal space section reconstructed for the sublattice 1 where the R-centering is evidenced. In this section, the sublattice 2 (in red) is almost not visible but the satellites reflections/diffuse lines (black arrows) are strong.

Despite the fact that the perfect structure solution could not be achieved due to the diffuse scattering present in the PEDT patterns, the information obtained from PEDT on the two sublattices' parameters provides precious hints on the overall crystal structure. First, the PEDT results clearly suggest the incommensurate nature between two sublattices, i.e., the Bi-O slabs and the Al/Mn-O slabs. More specifically, to express the relation linking the sublattice 1 to the sublattice 2 (Figure 6.4(b)), one shall consider a modulation vector in the form $\mathbf{q_1}=\sigma_1.\mathbf{a_2^*}+\beta\sigma_2.\mathbf{b_2^*}$ with $\sigma_1\neq\sigma_2$. Assuming a R lattice centering for both sublattices, this actually leads to a limited number of possible super-space groups (SSG) with the necessity to consider a (3+2)-d incommensurately modulated structure. Hence, after examination of the Stokes tables,[253] the selected SSG is R3($\alpha,\beta,0$)($-\alpha-\beta,\alpha,0$)0 with a

second modulation vector in the form $\mathbf{q_2}=(-\sigma_1-\sigma_2).\mathbf{a_2^*}+\sigma_1.\mathbf{b_2^*}$. Second, based on the PEDT and high-resolution STEM analysis above, the specific structure of the two sublattices constituting the BAMO LSC can be reasonably deduced. For sublattice 1, it is most likely that the in-plane parameter of 2.92 Å signs the presence of MO_2 layers similar to that observed in $LiCoO_2$ (R-3m, a ~ 2.82 Å and c ~ 14.05 Å).[254] This structure can be used as a starting point to build a model for sublattice 1 (Figure 5) that would consist of MO_6 edge-sharing octahedral layers, $[MO_2]_\infty$ with M = Al/Mn, separated by 13.1 Å. For sublattice 2, with in-plane parameters of 3.96 Å, it could be related to the Bi-Bi distances found in many Bi-based layered oxides such as Aurivillius phases. From the STEM-HAADF images (Figure 6.2), sublattice 2 contains blocks of three-layer-thick Bi-O, i.e. would have a composition in the form $[Bi_3O_n]$ assuming this sublattice is only occupied by Bi cations. In Figure 6.5(a), using the R3(σ_1,σ_2,0)(-σ_1-σ_2,σ_1,0)0 SSG with $c_2 = c_1 =$ 39.4 Å (see Table 6.2 in supplementary information), the bismuth stacking is modeled so that bismuth atoms face each other in two consecutive three-layer-thick Bi-based slabs. In Figure 6.5(b), using the same SSG with $c_1 = 39.4$ Å and $c_2 = 78.8$ Å (see Table 6.3 in supplementary information), it is possible to construct another stacking type where bismuth atoms do not face each other in two consecutive three-layer-thick Bi-based slabs. These two models are equivalent for the $[MO_2]_\infty$ layers (sublattice 1) but differ for the three-layer-thick Bi-based slabs. Locally both configurations are found explaining the presence of diffuse lines affecting only sublattice 2 (Figure 6.5(c)).
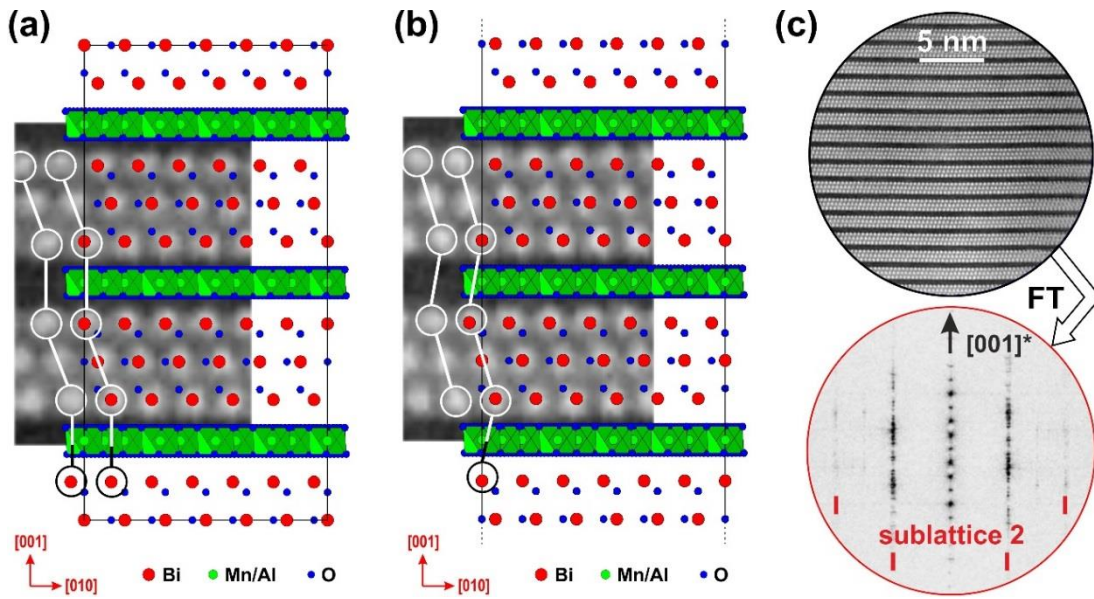
Figure 6.5 Structural models for the BAMO layered system. Details of a STEM-HAADF $[100]_{STO}/[100]_{sublattice2}$ image showing two consecutive blocks of the three-layer-thick Bi-based subsystem. In (a) Bi atoms face each other from one block to the other. This situation is well reproduced with our first model ($c_2 = 39.4$ Å). In (b) Bi atoms are shifted by 1/3 along b. This situation is well reproduced with our second model ($c_2 = 78.8$ Å). Along this $[100]_{STO}$ direction, the $[MO_2]$ layers (sublattice 1), represented in green, does not project along a direction permitting to resolve the M-M distances. (c) Fourier transform of the larger area STEM-HAADF image showing the disorder related to the Bi-based stacking (sublattice 2).

Table 6.2 Positional parameters of the misfit layered BAMO structure (model 1).

Sublattice 2: [Bi₃O₃]				
Cell parameters: $a_2=b_2=3.96$ Å, $c_2=39.4$ Å $\alpha=\beta=90°$, $\gamma=120°$				
Wave vectors: $q_1=0.7a^*+0.87b^*$ $q_2=-1.57a^*+0.7b^*$				
SSG: $R3(\sigma_1,\sigma_2,0)0(-\sigma_1-\sigma_2, \sigma_1,0)0$				
atom	occupancy	x	y	z
Bi1	1	0	0	0
Bi2	1	0.6667	0.3333	-0.08

174

Table 6.2 Continued.

atom	occupancy	x	y	z
Bi3	1	0.3333	0.6667	0.08
O1	1	0.6667	0.3333	0
O2	1	0	0	0.0586
O3	1	0	0	-0.0586

Sublattice 1: [(Mn/Al)O$_2$]				
Cell parameters: $a_1=b_1=2.907$ Å, $c_1=39.4$ Å $\alpha=\beta=90°$, $\gamma=120°$				
Wave vectors: $q_1=-0.377a*-0.469b*$ $\quad$ $q_2=-0.846a*+0.377b*$				
SSG: $X3(\sigma_1,\sigma_2,0)0(\sigma_1+\sigma_2, -\sigma_1,0)0$ with $X=(0;0;1/3;2/3;1/3)$ $(0;0;2/3;1/3;2/3)$				
atom	occupancy	x	y	z
(Mn/Al)1	1	0	0	0.1667
O4	1	0.6667	0.3333	0.1944
O5	1	0.3333	0.6667	0.1389

W_2 is a permutation matrix[255] which interchanges in five-dimensional space the coordinate axes (x_1 and x_2) and (x_4 and x_5) and then leads to the relationship between the cell parameters of the sublattice 2 and sublattice 1:

$$W_2 = \begin{pmatrix} 0 & 0 & 0 & \bar{1} & 0 \\ 0 & 0 & 0 & 0 & 1 \\ 0 & 0 & 1 & 0 & 0 \\ 1 & 0 & 0 & 0 & 0 \\ 0 & 1 & 0 & 0 & 0 \end{pmatrix}$$

Table 6.3 Positional parameters of the misfit layered BAMO structure (model 2).

Sublattice 2: [Bi$_3$O$_3$]				
Cell parameters: $a_2=b_2=3.96$ Å, $c_2=78.8$ Å $\alpha=\beta=90°$, $\gamma=120°$				
Wave vectors: $q_1=0.7a^*+0.87b^*$ $q_2=-1.57a^*+0.7b^*$				
SSG: R3($\sigma_1,\sigma_2,0$)0($-\sigma_1-\sigma_2$, $\sigma_1,0$)0				
atom	occupancy	x	y	z
Bi1_1	1	0	0	0
Bi1_2	1	0	0	0.5
Bi2_1	1	0.6667	0.3333	-0.04
Bi2_2	1	0.6667	0.3333	0.46
Bi3_1	1	0.3333	0.6667	0.04
Bi3_2	1	0.3333	0.6667	0.54
O1_1	1	0.6667	0.3333	0
O1_2	1	0.6667	0.3333	0.5
O2_1	1	0	0	0.0293
O2_2	1	0	0	0.5293
O3_1	1	0	0	-0.0293
O3_2	1	0	0	0.4707

Table 6.3 Continued.

Sublattice 1: [(Mn/Al)O$_2$]				
Cell parameters: a$_1$=b$_1$=2.907 Å, c$_1$=39.4 Å α=β=90°, γ=120°				
Wave vectors: q$_1$=-0.377a*-0.469b* q$_2$=-0.846a*+0.377b*				
SSG: X3(σ$_1$,σ$_2$,0)0(σ$_1$+σ$_2$, -σ$_1$,0)0 with X=(0;0;2/3;2/3;1/3) (0;0;1/3;1/3;2/3)				
atom	occupancy	x	y	z
(Mn/Al)1	1	0	0	0.1667
O4	1	0.6667	0.3333	0.1944
O5	1	0.3333	0.6667	0.1389

$$W_2 = \begin{pmatrix} 0 & 0 & 0 & \bar{1} & 0 \\ 0 & 0 & 0 & 0 & 1 \\ 0 & 0 & 2 & 0 & 0 \\ 1 & 0 & 0 & 0 & 0 \\ 0 & 1 & 0 & 0 & 0 \end{pmatrix}$$

Figure 6.6 and 6.7 presents the crystal structure model 1 and model 2, respectively, which provide a base structure of the BAMO layered structure with the two sublattices stacked alternatively along the *c* axis.
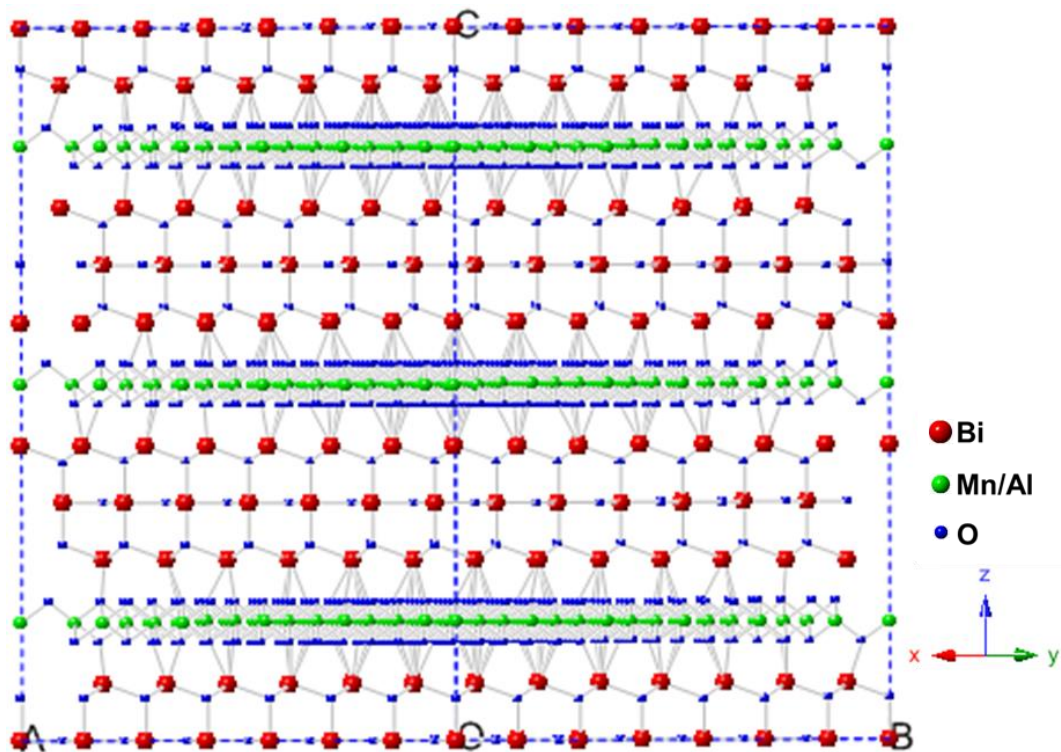
Figure 6.6 Crystal structure model 1 for BAMO misfit layered structure. In this model, Bi atoms face each other from one block to the other.
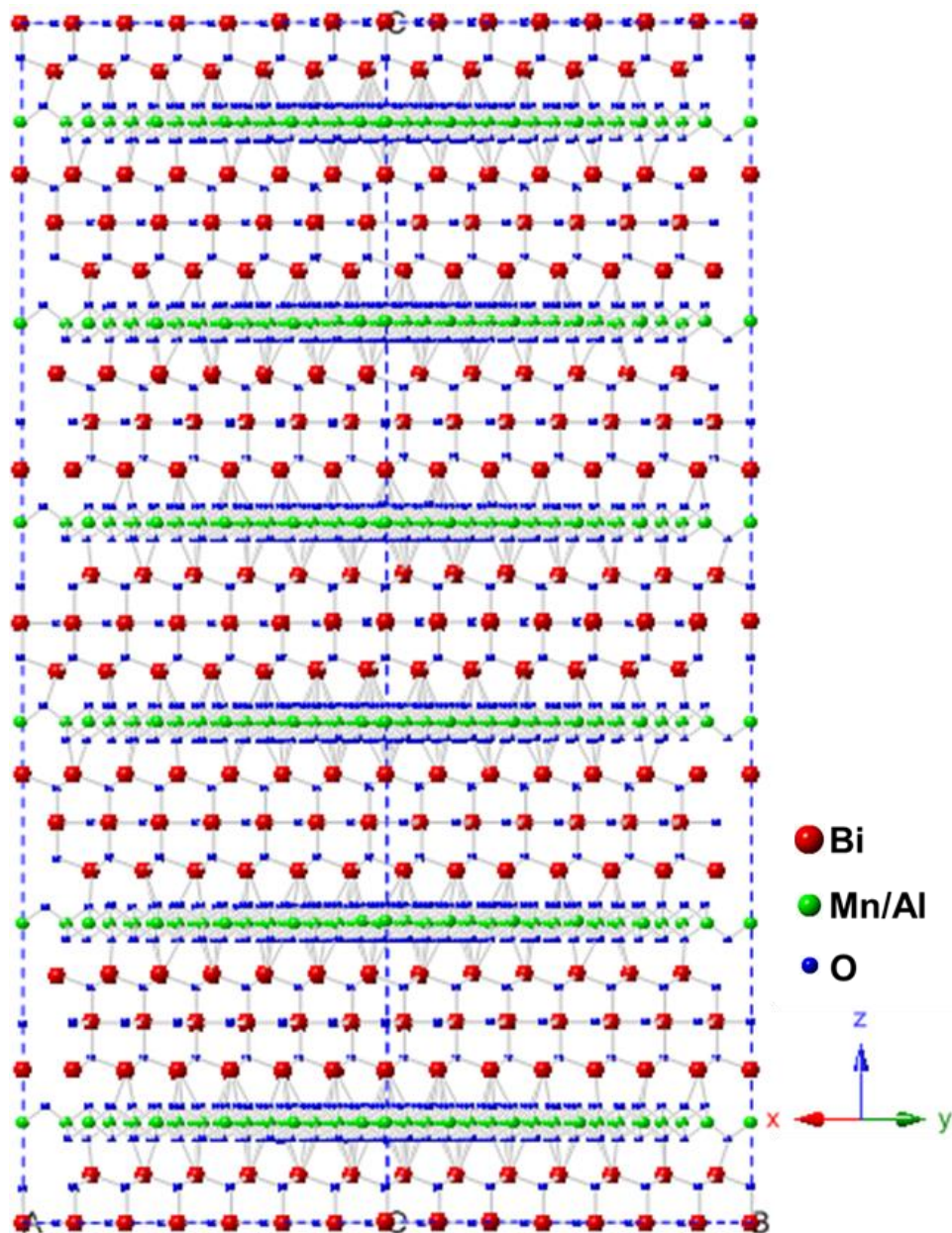
Figure 6.7 Crystal structure model 2 for BAMO misfit layered structure. Bi atoms are shifted by 1/3 along b from one block to the other.

Because of the in-plane mismatch (i.e., incommensurate nature) between the two sublattices, the misfit layered supercell structure can be written as $[Bi_3O_n][MO_2]_x$, where x represents the in-plane area difference between the two sublattices expressed as

$x=(a_2/a_1)^2 \sim 1.84$. Regarding the cations' content, from EDS analyses the Bi/(Al+Mn) ratio is about 1.64 (see Table 6.1) in agreement with the Bi/M ratio of 1.63 expected from our models. Regarding oxygen content, considering formal valences of +3 for all cations (see XPS spectra in Figure 6.8), one can estimate that the oxygen content of sublattice 2 is close to $O_{3.58}$, i.e. sublattice 2 cannot only be constituted by three Bi-O layers but extra oxygen atoms need to be incorporated leading to the proposed chemical formula $[Bi_3O_{3+\delta}][MO_2]_{1.84}$.
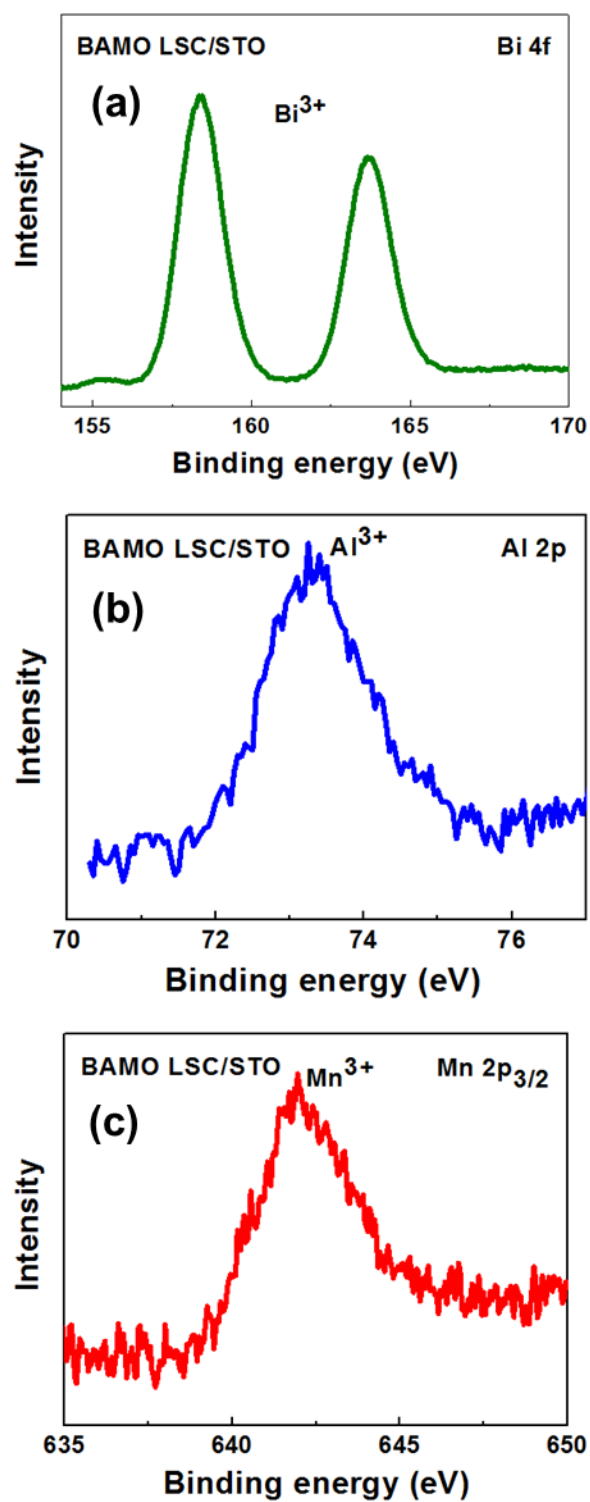
Figure 6.8 The XPS spectra of (a) Bi 4f, (b) Al 2p, and (c) Mn $2p_{3/2}$ for the BAMO LSC.

The growth mechanism for the new Bi-based 2D layered supercell structure created from BAMO, though still under investigation, leads to the stabilization of a 2D composite structure[256] resembling the misfit layered cobalt oxides.[257] While possessing an equivalent [MO_2] sublattice, the second three-atom-thick Bi-based sublattice shall differ, notably, by its oxygen content. In addition the BAMO LSC is described in a trigonal crystal system with a lattice mismatch existing in both in-plane directions. With the creation of the new BAMO thin film having such an anisotropic LSC structure, one would expect highly anisotropic physical properties. The room-temperature multiferroic response of the 2D BAMO LSC was measured by the vibrating sample magnetometer (VSM) option in a physical property measurement system for ferromagnetic properties and piezoelectric force microscope (PFM) for ferroelectric response. The saturated in-plane (IP) and out-of-plane (OP) magnetizations under 1 T magnetic field were measured to be ~250 emu/cc and ~170 emu/cc at 300 K, demonstrating strong room-temperature magnetization and highly anisotropic magnetic properties (Figure 6.9(a)). The coercive field both along the IP and OP directions is determined to be ~237 Oe. The field-dependent magnetization measurement of the BAMO LSC shows quite similar magnetization behaviors at 10 K, 100 K, and 300 K, indicating a much higher Curie transition temperature than 300 K (Figure 6.9(b)).
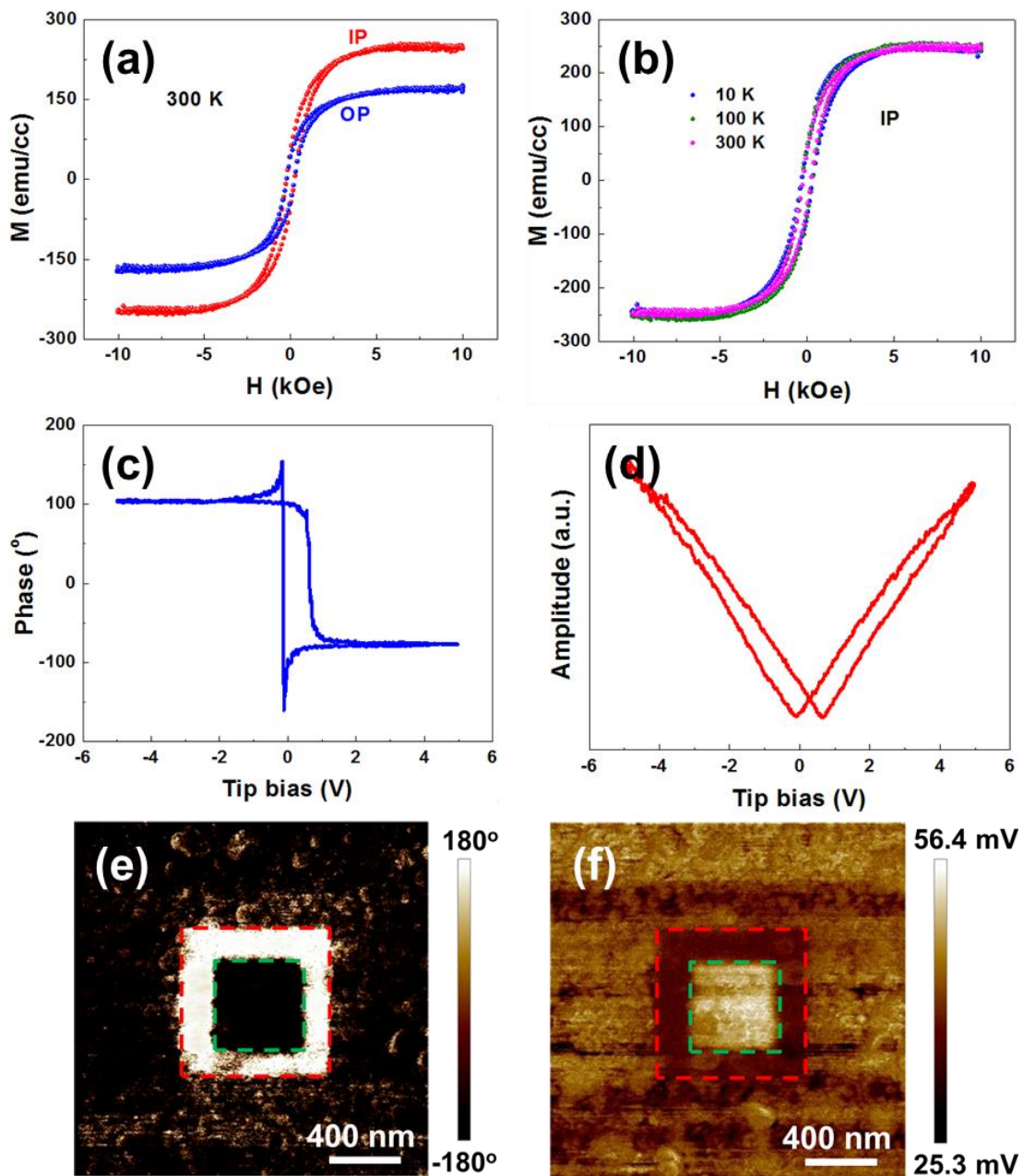
Figure 6.9 Room-temperature multiferroic properties of the 2D BAMO LSC. (a) In-plane (IP) and out-of-plane (OP) magnetization hysteresis (M-H) loops of the BAMO LSC at 300 K. (b) Temperature-dependent magnetizations of the BAMO LSC at 10 K, 100 K and 300 K along the in-plane direction. (c) Phase and (d) amplitude switching curves of the BAMO LSC as a function of the tip bias at room temperature. PFM OP (e) phase and (f) amplitude images of the BAMO LSC after +6 V writing over an area of 0.8×0.8 μm^2 followed by a 0.4×0.4 μm^2 central area rewriting with the tip biased at -6 V, respectively.

The temperature-dependent measurement (M-T curves, Figure 6.10) also shows strong magnetizations even at 380 K revealing a ferromagnetic Curie transition temperature (T_C) of at least 380 K which is consistent with the field-dependent magnetization measurement results at different temperatures. The magnetization property of the unique BAMO LSC is much better than that of the conventional pseudocubic Bi_2FeMnO_6 phase[110, 184] with the saturation magnetization value ranging from ~0.8 emu/cc to 90 emu/cc (at 300 K and H = 3 to 10 kOe) and of the pseudocubic $BiMnO_3$ phase[86, 98] with a low Curie transition temperature (105 K for bulk $BiMnO_3$ and 50 K for $BiMnO_3$ thin film grown on LAO (001)). Compared to the reported Bi_2FeMnO_6 and $BiMnO_3$ with pseudocubic structure, the much stronger magnetizations and higher Curie temperature of BAMO LSC indicate the obvious advantages of the anisotropic and unique 2D misfit layered structure of BAMO over the conventional pseudocubic ones.
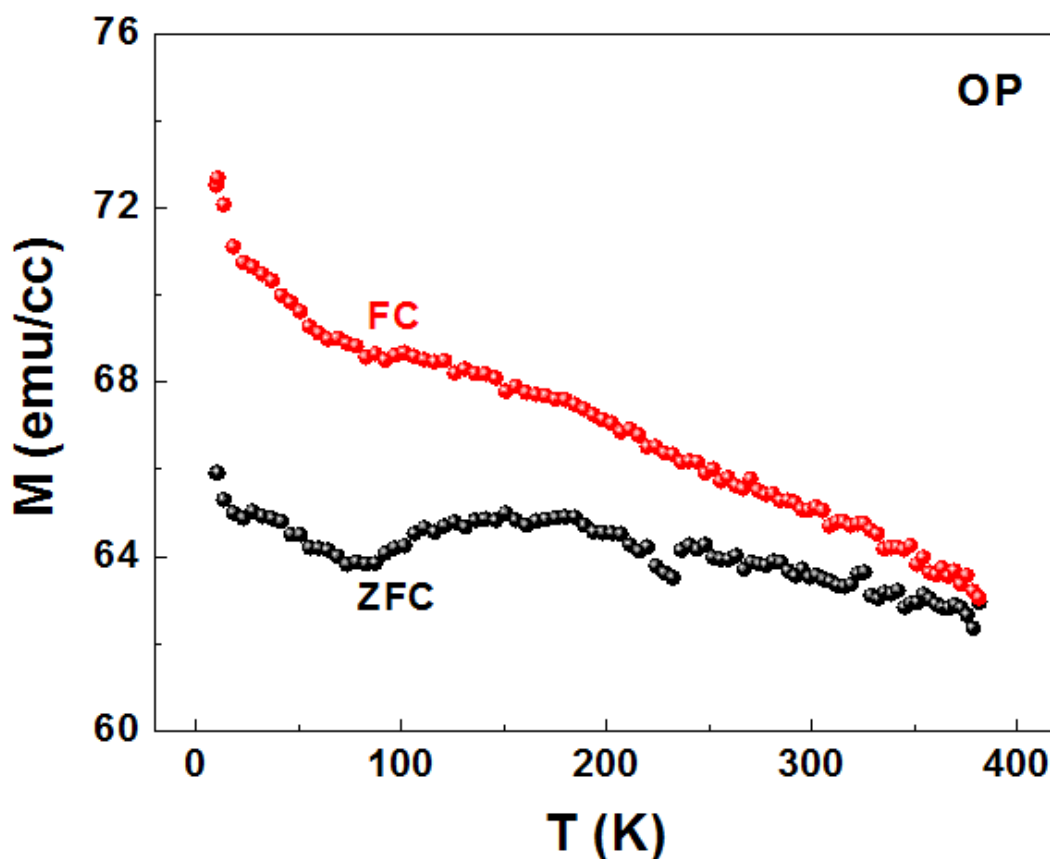
Figure 6.10 Magnetizations of BAMO LSC as a function of temperature cooled under zero magnetic field (ZFC) and an out-of-plane magnetic field of 1000 Oe (FC), respectively.

To gain more understanding of the magnetic properties of the BAMO LSC, X-ray photoelectron spectroscopy (XPS) measurement was performed on the BAMO LSC (Figure 6.8) and suggests that the main valence state of both Al and Mn cations may be +3.[219] Another fact noteworthy is that the in-plane saturation magnetization value of the BAMO LSC (~250 emu/cc) is more than twice of that of the previously reported BFMO based layered supercell structure deposited on LAO (001) substrate (~110 emu/cc).[184] The much stronger magnetization of the BAMO LSC may be due to the fact that the net magnetic moment from Mn^{3+} in BAMO LSC is not compensated by the nonmagnetic Al^{3+}

cations. For the case of BFMO based layered supercell structure, the interaction between the cations of Fe^{3+} and Mn^{3+} is complicated and the net magnetic moment came from the interplay between Fe^{3+} and Mn^{3+} in the Fe/Mn-O slab. Furthermore, for Bi-based materials, the Bi^{3+} with the electronic configuration of $[Xe]4f^{14}5d^{10}6s^{2}6p^{0}$ forms strong covalent bonds with the surrounding oxygen anion, which shifts away the $6s^{2}$ lone pairs from the centrosymmetric position because of the Coulombian electrostatic repulsion. A localized lobe-like distribution of the lone pair electrons forms an electric dipole, breaking the spatial inversion symmetry and becoming the driving force for the ferroelectric structural distortion in Bi-based multiferroic materials.[258] While requiring further investigations, the structural models presented above are non-centrosymmetric and compatible with the presence of ferroelectricity. To explore the ferroelectric properties of the BAMO LSC, PFM measurement was performed on the BAMO sample grown on $La_{0.7}Sr_{0.3}MnO_3$ (LSMO) buffer layer. Figure 6.9(c) and (d) shows the phase and amplitude switching curves of the BAMO LSC, respectively. The sharp 180º phase change and amplitude change indicate the obvious ferroelectric domain switching in BAMO LSC. Figure 6.9(e) and (f) demonstrates the out-of-plane phase and amplitude switching, respectively. The square box domain pattern was written by scanning the PFM tip with +6 V bias over an area of $0.8 \times 0.8 \ \mu m^2$ followed by a $0.4 \times 0.4 \ \mu m^2$ central area scan with the tip biased at -6 V. The distinct image contrast clearly shows the domain switching indicating the ferroelectric nature of the BAMO LSC. In addition, the transmission spectrum of BAMO LSC was also measured and a band gap value of ~2.83 eV is determined by the Tauc method (Figure 6.11). The band gap value is smaller than that of the reported BFMO

layered structure (3.27 eV)[219] and similar to that of the BFO films with pseudocubic structure (2.77 eV)[259].
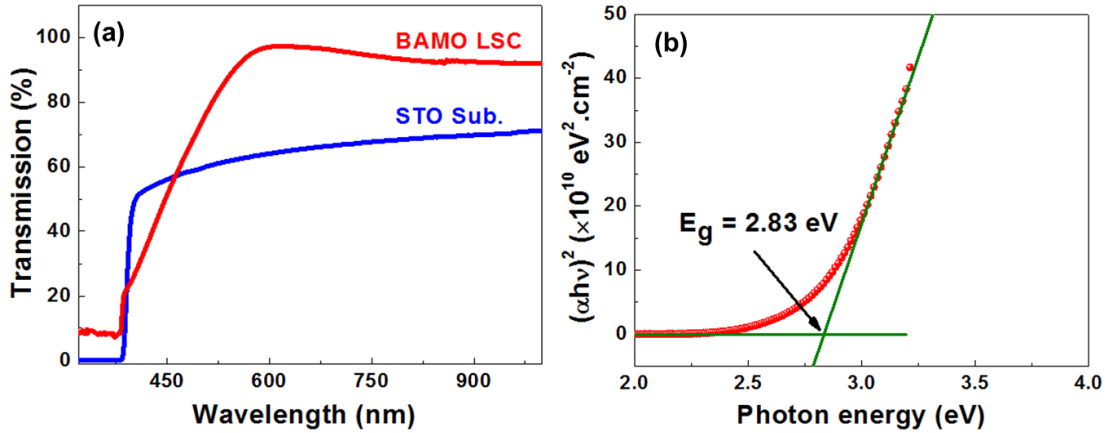
Figure 6.11 Transmission spectrum of BAMO LSC (a) and plot of $(\alpha h \nu)^2$ versus $h\nu$ for BAMO LSC (b). The optical band gap energy E_g is deduced from extrapolation of the straight line to $(\alpha h \nu)^2 = 0$.

6.5 Conclusion

In summary, a novel self-assembled 2D misfit layered structure has been designed and fabricated from a target with a Bi_2AlMnO_6 (BAMO) composition on single-crystal substrates $SrTiO_3$ (001) and $LaAlO_3$ (001), with or without CeO_2 (001) and $La_{0.7}Sr_{0.3}MnO_3$ (001) buffer layers. The epitaxial BAMO misfit layered structure is self-assembly grown by alternative layered stacking of two sublattices, i.e., sublattice 1 of one-octahedra-thick $[MO_2]_\infty$ layer (M = Al/Mn) and sublattice 2 of three-layer-thick $[Bi_3O_{3+\delta}]$ slabs as deduced from both STEM-HAADF image and PEDT analyses. Robust room-temperature multiferroic responses have been observed for this new misfit (incommensurate) layered structure with a non-magnetic B cation, which presents great potentials in terms of

composition flexibility in these new LSC systems. The study holds great significance towards many other new designs of novel single-phase materials from proper self-assembly 2D layer mixing of two perovskites $BiM'O_3$ (M'= Fe, Mn, Cr, Co, and non-magnetic cations) for various functionalities ranging from multiferroics to thermoelectrics and layered oxides with wide band gaps.

CHAPTER VII

SUMMARY AND FUTURE WORK

In this dissertation, Bi-based 2D layered supercell structures have been designed and fabricated by pulsed laser deposition. The layered supercell structures are self-assembled on single-crystal substrates of STO (001) and LAO (001) as well as buffer layer of CeO_2 (001) through the intergrowth of Bi-based slabs (Bi_2O_x, or Bi_3O_x) and octahedral layers along the film out-of-plane direction and exhibit robust room-temperature multiferroic properties.

The influence of CeO_2 thickness to the growth and magnetic properties of BFMO322 SC was investigated and an optimal CeO_2 thickness of ~6.7 nm is proved to be sufficient to trigger the growth of BFMO322 SC. The study of Fe/Mn molar ratio to the growth and physical properties of Bi-Fe-Mn-O layered supercell indicates that Mn plays a critical role in facilitating the growth of the layered supercell structures. Based on this finding, two novel Bi-based layered supercell with modulated structures have been designed and fabricated from both $BiMnO_3$ and Bi_2NiMnO_6 under well-controlled deposition conditions. In addition, another new Bi-based layered supercell structure has been also fabricated from the newly designed Bi_2AlMnO_6. All these layered supercell structures exhibit strong room-temperature multiferroic response.

The realization of the new Bi-based 2D layered supercell structures are of great significance to the design of new 2D materials with multiferroic response and other potential applications. The future research can be focused on the following aspects:

189

1. Elucidate the growth mechanism of the Bi-based layered supercell structures by both experimental and theoretical efforts;

2. Explore the magnetic interaction mechanism of the Bi-based layered supercell structures;

3. Explore new functionalities of the fabricated Bi-based layered supercell structures;

4. Design and fabricate new Bi-based layered supercell structures with new functionalities;

5. Incorporate the new Bi-based layered supercell structures in devices.

REFERENCES

1.   Yang, G.; Yue, Z.; Zhao, J.; Wen, H.; Wang, X.; Li, L. *Journal of Physics D: Applied Physics* **2006**, *39* (16), 3702.

2.   Arthur, v. H. *Reviews of Modern Physics* **1950**, *22* (3), 221-237.

3.   Wu, M. K.; Ashburn, J. R.; Torng, C. J.; Hor, P. H.; Meng, R. L.; Gao, L.; Huang, Z. J.; Wang, Y. Q.; Chu, C. W. *Physical Review Letters* **1987**, *58* (9), 908-910.

4.   Hsu, F.-C.; Luo, J.-Y.; Yeh, K.-W.; Chen, T.-K.; Huang, T.-W.; Wu, P. M.; Lee, Y.-C.; Huang, Y.-L.; Chu, Y.-Y.; Yan, D.-C.; Wu, M.-K. *Proceedings of the National Academy of Sciences* **2008**, *105* (38), 14262-14264.

5.   Cao, Q.; Zhang, H. P.; Wang, G. J.; Xia, Q.; Wu, Y. P.; Wu, H. Q. *Electrochemistry Communications* **2007**, *9* (5), 1228-1232.

6.   Wu, H. M.; Tu, J. P.; Yuan, Y. F.; Chen, X. T.; Xiang, J. Y.; Zhao, X. B.; Cao, G. S. *Journal of Power Sources* **2006**, *161* (2), 1260-1263.

7.   Wang, J.; Neaton, J. B.; Zheng, H.; Nagarajan, V.; Ogale, S. B.; Liu, B.; Viehland, D.; Vaithyanathan, V.; Schlom, D. G.; Waghmare, U. V.; Spaldin, N. A.; Rabe, K. M.; Wuttig, M.; Ramesh, R. *Science* **2003**, *299* (5613), 1719-1722.

8.   Martin, L. W.; Chu, Y. H.; Ramesh, R. *Materials Science and Engineering: R: Reports* **2010**, *68* (4–6), 89-133.

9.   Ohring, M., Chapter 8 - Epitaxy. In *Materials Science of Thin Films (Second Edition)*, Academic Press: San Diego, **2002**, pp 417-494.

10.   Wang, H.; Sharma, A.; Kvit, A.; Wei, Q.; Zhang, X.; Koch, C. C.; Narayan, J. *Journal of Materials Research* **2001**, *16* (9), 2733-2738.

11.   Narayan, J.; Larson, B. C. *Journal of Applied Physics* **2003**, *93* (1), 278-285.

12.   Wang, H.; Foltyn, S. R.; Arendt, P. N.; Jia, Q. X.; MacManus-Driscoll, J. L.; Stan, L.; Li, Y.; Zhang, X.; Dowden, P. C. *Journal of Materials Research* **2004**, *19* (6), 1869-1875.

13.   Bauer, E. *Applications of Surface Science* **1982**, *11–12*, 479-494.

14.   Ok, K. M.; Chi, E. O.; Halasyamani, P. S. *Chemical Society Reviews* **2006**, *35* (8), 710-717.

15.   Aksel, E.; Jones, J. L. *Sensors* **2010**, *10* (3), 1935.

16.   Ezhilvalavan, S.; Samper, V. D. *Applied Physics Letters* **2005**, *86* (7), 072901.

17.   Jaffe, H. *Journal of the American Ceramic Society* **1958**, *41* (11), 494-498.

18.   Haertling, G. H. *Journal of the American Ceramic Society* **1999**, *82* (4), 797-818.

19.   Kan, D.; Shimakawa, Y. *Applied Physics Letters* **2011**, *99* (8), 081907.

20.   Li, C. L.; Chen, Z. H.; Zhou, Y. L.; Cui, D. F. *Journal of Physics: Condensed Matter* **2001**, *13* (22), 5261.

21.   Chen, A. P.; Khatkhatay, F.; Zhang, W.; Jacob, C.; Jiao, L.; Wang, H. *Journal of Applied Physics* **2013**, *114* (12), -.

22.   Kolhatkar, A. G.; Jamison, A. C.; Litvinov, D.; Willson, R. C.; Lee, T. R. *International Journal of Molecular Sciences* **2013**, *14* (8), 15977-16009.

23.   Jeong, U.; Teng, X.; Wang, Y.; Yang, H.; Xia, Y. *Advanced Materials* **2007**, *19* (1), 33-60.

24.   Anderson, P. W. *Physical Review* **1950**, *79* (2), 350-356.

25.   Zhang, W.; Jian, J.; Chen, A.; Jiao, L.; Khatkhatay, F.; Li, L.; Chu, F.; Jia, Q.; MacManus-Driscoll, J. L.; Wang, H. *Applied Physics Letters* **2014**, *104* (6), 062402.

26.   Zhang, W.; Fan, M.; Li, L.; Chen, A.; Su, Q.; Jia, Q.; MacManus-Driscoll, J. L.; Wang, H. *Applied Physics Letters* **2015**, *107* (21), 212901.

27.   Pénicaud, M.; Siberchicot, B.; Sommers, C. B.; Kübler, J. *Journal of Magnetism and Magnetic Materials* **1992**, *103* (1), 212-220.

28.   Yoshida, J.; Iida, S. *Journal of the Physical Society of Japan* **1979**, *47* (5), 1627-1633.

29.   Shepherd, J. P.; Koenitzer, J. W.; Aragón, R.; Spal/ek, J.; Honig, J. M. *Physical Review B* **1991**, *43* (10), 8461-8471.

30.   Margulies, D. T.; Parker, F. T.; Spada, F. E.; Goldman, R. S.; Li, J.; Sinclair, R.; Berkowitz, A. E. *Physical Review B* **1996**, *53* (14), 9175-9187.

31.   Gong, G. Q.; Gupta, A.; Xiao, G.; Qian, W.; Dravid, V. P. *Physical Review B* **1997**, *56* (9), 5096-5099.

32.   Oliver, S. A.; Chen, M. L.; Kozulin, I.; Vittoria, C. *Journal of Magnetism and Magnetic Materials* **2000**, *213* (3), 326-334.

33.   Samarasekara, P.; Rani, R.; Cadieu, F. J.; Shaheen, S. A. *Journal of Applied Physics* **1996**, *79* (8), 5425-5427.

34.   Lüders, U.; Bibes, M.; Bobo, J.-F.; Cantoni, M.; Bertacco, R.; Fontcuberta, J. *Physical Review B* **2005**, *71* (13), 134419.

35.   Venzke, S.; van Dover, R. B.; Phillips, J. M.; Gyorgy, E. M.; Siegrist, T.; Chen, C. H.; Werder, D.; Fleming, R. M.; Felder, R. J.; Coleman, E.; Opila, R. *Journal of Materials Research* **1996**, *11* (5), 1187-1198.

36.   Dorsey, P. C.; Lubitz, P.; Chrisey, D. B.; Horwitz, J. S. *Journal of Applied Physics* **1996**, *79* (8), 6338-6340.

37.   Hu, G.; Choi, J. H.; Eom, C. B.; Harris, V. G.; Suzuki, Y. *Physical Review B* **2000**, *62* (2), R779-R782.

38.   Jin, S.; Tiefel, T. H.; McCormack, M.; Fastnacht, R. A.; Ramesh, R.; Chen, L. H. *Science* **1994**, *264* (5157), 413-415.

39.   Aiping, C.; Zhenxing, B.; Harshad, H.; Xinghang, Z.; Qing, S.; Li, C.; Quanxi, J.; Judith, L. M.-D.; Haiyan, W. *Nanotechnology* **2011**, *22* (31), 315712.

40.   Chen, A.; Bi, Z.; Tsai, C.-F.; Lee, J.; Su, Q.; Zhang, X.; Jia, Q.; MacManus-Driscoll, J. L.; Wang, H. *Advanced Functional Materials* **2011**, *21* (13), 2423-2429.

41.   Chen, A.; Zhang, W.; Jian, J.; Wang, H.; Tsai, C.-F.; Su, Q.; Jia, Q.; MacManus-Driscoll, J. L. *Journal of Materials Research* **2013**, *28* (13), 1707-1714.

42.   Zhang, W.; Chen, A.; Khatkhatay, F.; Tsai, C.-F.; Su, Q.; Jiao, L.; Zhang, X.; Wang, H. *ACS Applied Materials & Interfaces* **2013**, *5* (10), 3995-3999.

43.   Chen, A.; Weigand, M.; Bi, Z.; Zhang, W.; Lu, X.; Dowden, P.; MacManus-Driscoll, J. L.; Wang, H.; Jia, Q. *Scientific Reports* **2014**, *4*, 5426.

44.   Ramesh, R.; Spaldin, N. A. *Nature Materials* **2007**, *6* (1), 21-29.

45.   Zhao, T.; Scholl, A.; Zavaliche, F.; Lee, K.; Barry, M.; Doran, A.; Cruz, M. P.; Chu, Y. H.; Ederer, C.; Spaldin, N. A.; Das, R. R.; Kim, D. M.; Baek, S. H.; Eom, C. B.; Ramesh, R. *Nature Materials* **2006**, *5* (10), 823-829.

46.   Ma, J.; Hu, J.; Li, Z.; Nan, C.-W. *Advanced Materials* **2011**, *23* (9), 1062-1087.

47.   Chu, Y.-H.; Martin, L. W.; Holcomb, M. B.; Gajek, M.; Han, S.-J.; He, Q.; Balke, N.; Yang, C.-H.; Lee, D.; Hu, W.; Zhan, Q.; Yang, P.-L.; Fraile-Rodriguez, A.; Scholl, A.; Wang, S. X.; Ramesh, R. *Nature Materials* **2008**, *7* (6), 478-482.

48.   Folen, V. J.; Rado, G. T.; Stalder, E. W. *Physical Review Letters* **1961**, *6* (11), 607-608.

49.   Velev, J. P.; Jaswal, S. S.; Tsymbal, E. Y. *Philosophical Transactions of the Royal Society A: Mathematical, Physical and Engineering Sciences* **2011**, *369* (1948), 3069-3097.

50.   Ascher, E.; Rieder, H.; Schmid, H.; Stössel, H. *Journal of Applied Physics* **1966**, *37* (3), 1404-1405.

51.   Sai, N.; Meyer, B.; Vanderbilt, D. *Physical Review Letters* **2000**, *84* (24), 5636-5639.

52.   Duan, C.-G.; Jaswal, S. S.; Tsymbal, E. Y. *Physical Review Letters* **2006**, *97* (4), 047201.

53.   Tanaka, H.; Zhang, J.; Kawai, T. *Physical Review Letters* **2001**, *88* (2), 027204.

54.   Zheng, H.; Wang, J.; Lofland, S. E.; Ma, Z.; Mohaddes-Ardabili, L.; Zhao, T.; Salamanca-Riba, L.; Shinde, S. R.; Ogale, S. B.; Bai, F.; Viehland, D.; Jia, Y.; Schlom, D. G.; Wuttig, M.; Roytburd, A.; Ramesh, R. *Science* **2004**, *303* (5658), 661-663.

55.   Zheng, H.; Straub, F.; Zhan, Q.; Yang, P. L.; Hsieh, W. K.; Zavaliche, F.; Chu, Y. H.; Dahmen, U.; Ramesh, R. *Advanced Materials* **2006**, *18* (20), 2747-2752.

56.   Luo, H.; Yang, H.; Baily, S. A.; Ugurlu, O.; Jain, M.; Hawley, M. E.; McCleskey, T. M.; Burrell, A. K.; Bauer, E.; Civale, L.; Holesinger, T. G.; Jia, Q. *Journal of the American Chemical Society* **2007**, *129* (46), 14132-14133.

57.   Chi, Z. H.; Yang, H.; Feng, S. M.; Li, F. Y.; Yu, R. C.; Jin, C. Q. *Journal of Magnetism and Magnetic Materials* **2007**, *310* (2, Part 2), e358-e360.

58.   Oka, K.; Yamada, I.; Azuma, M.; Takeshita, S.; Satoh, K. H.; Koda, A.; Kadono, R.; Takano, M.; Shimakawa, Y. *Inorganic Chemistry* **2008**, *47* (16), 7355-7359.

59.		Salvador, P. A.; Doan, T.-D.; Mercey, B.; Raveau, B. *Chemistry of Materials* **1998**, *10* (10), 2592-2595.

60.		Choi, T.; Horibe, Y.; Yi, H. T.; Choi, Y. J.; Wu, W.; Cheong, S. W. *Nature Materials* **2010**, *9* (3), 253-258.

61.		Scott, J. F. *NPG Asia Materials* **2013**, *5*, e72.

62.		Ederer, C.; Spaldin, N. A. *Physical Review B* **2006**, *74* (2), 020401.

63.		Fujimura, N.; Ishida, T.; Yoshimura, T.; Ito, T. *Applied Physics Letters* **1996**, *69* (7), 1011-1013.

64.		Ito, D.; Fujimura, N.; Yoshimura, T.; Ito, T. *Journal of Applied Physics* **2003**, *93* (9), 5563-5567.

65.		Subramanian, M. A.; He, T.; Chen, J.; Rogado, N. S.; Calvarese, T. G.; Sleight, A. W. *Advanced Materials* **2006**, *18* (13), 1737-1739.

66.		Ikeda, N.; Ohsumi, H.; Ohwada, K.; Ishii, K.; Inami, T.; Kakurai, K.; Murakami, Y.; Yoshii, K.; Mori, S.; Horibe, Y.; Kito, H. *Nature* **2005**, *436* (7054), 1136-1138.

67.		Kimura, T.; Goto, T.; Shintani, H.; Ishizaka, K.; Arima, T.; Tokura, Y. *Nature* **2003**, *426* (6962), 55-58.

68.		Hur, N.; Park, S.; Sharma, P. A.; Ahn, J. S.; Guha, S.; Cheong, S. W. *Nature* **2004**, *429* (6990), 392-395.

69.		Pérez, E. L. Growth and Characterisation of Bi-Based Multiferroic Thin Films. Doctoral thesis, Universitat de Barcelona, Facultat de Física, **2013**.

70.		Martin, L. W.; Crane, S. P.; Chu, Y. H.; Holcomb, M. B.; Gajek, M.; Huijben, M.; Yang, C. H.; Balke, N.; Ramesh, R. *Journal of Physics: Condensed Matter* **2008**, *20* (43), 434220.

71.		Teague, J. R.; Gerson, R.; James, W. J. *Solid State Communications* **1970**, *8* (13), 1073-1074.

72.		Tabares-Muñoz, C.; Rivera, J. P.; Bezinges, A.; Monnier, A.; Schmid, H. *Japanese Journal of Applied Physics* **1985**, *24* (S2), 1051.

73.		Zhang, J. X.; Li, Y. L.; Choudhury, S.; Chen, L. Q.; Chu, Y. H.; Zavaliche, F.; Cruz, M. P.; Ramesh, R.; Jia, Q. X. *Journal of Applied Physics* **2008**, *103* (9), 094111.

74.   Chu, Y. H.; Zhan, Q.; Martin, L. W.; Cruz, M. P.; Yang, P. L.; Pabst, G. W.; Zavaliche, F.; Yang, S. Y.; Zhang, J. X.; Chen, L. Q.; Schlom, D. G.; Lin, I. N.; Wu, T. B.; Ramesh, R. *Advanced Materials* **2006**, *18* (17), 2307-2311.

75.   Pabst, G. W.; Martin, L. W.; Chu, Y.-H.; Ramesh, R. *Applied Physics Letters* **2007**, *90* (7), 072902.

76.   Chu, Y. H.; Cruz, M. P.; Yang, C. H.; Martin, L. W.; Yang, P. L.; Zhang, J. X.; Lee, K.; Yu, P.; Chen, L. Q.; Ramesh, R. *Advanced Materials* **2007**, *19* (18), 2662-2666.

77.   Qi, X.; Dho, J.; Tomov, R.; Blamire, M. G.; MacManus-Driscoll, J. L. *Applied Physics Letters* **2005**, *86* (6), 062903.

78.   Yang, C. H.; Seidel, J.; Kim, S. Y.; Rossen, P. B.; Yu, P.; Gajek, M.; Chu, Y. H.; Martin, L. W.; Holcomb, M. B.; He, Q.; Maksymovych, P.; Balke, N.; Kalinin, S. V.; Baddorf, A. P.; Basu, S. R.; Scullin, M. L.; Ramesh, R. *Nature Materials* **2009**, *8* (6), 485-493.

79.   Ederer, C.; Spaldin, N. A. *Physical Review B* **2005**, *71* (6), 060401.

80.   Naganuma, H.; Kovacs, A.; Harima, T.; Shima, H.; Okamura, S.; Hirotsu, Y. *Journal of Applied Physics* **2009**, *105* (7), 07D915.

81.   Kimura, T.; Kawamoto, S.; Yamada, I.; Azuma, M.; Takano, M.; Tokura, Y. *Physical Review B* **2003**, *67* (18), 180401.

82.   Moreira dos Santos, A. F.; Cheetham, A. K.; Tian, W.; Pan, X.; Jia, Y.; Murphy, N. J.; Lettieri, J.; Schlom, D. G. *Applied Physics Letters* **2004**, *84* (1), 91-93.

83.   Gajek, M.; Bibes, M.; Barthélémy, A.; Bouzehouane, K.; Fusil, S.; Varela, M.; Fontcuberta, J.; Fert, A. *Physical Review B* **2005**, *72* (2), 020406.

84.   Eerenstein, W.; Morrison, F. D.; Scott, J. F.; Mathur, N. D. *Applied Physics Letters* **2005**, *87* (10), 101906.

85.   Fujino, S.; Murakami, M.; Lim, S.-H.; Salamanca-Riba, L. G.; Wuttig, M.; Takeuchi, I. *Journal of Applied Physics* **2007**, *101* (1), 013903.

86.   Son, J. Y.; Kim, B. G.; Kim, C. H.; Cho, J. H. *Applied Physics Letters* **2004**, *84* (24), 4971-4973.

87.   Atou, T.; Chiba, H.; Ohoyama, K.; Yamaguchi, Y.; Syono, Y. *Journal of Solid State Chemistry* **1999**, *145* (2), 639-642.

88.   Gajek, M.; Bibes, M.; Wyczisk, F.; Varela, M.; Fontcuberta, J.; Barthélémy, A. *Physical Review B* **2007**, *75* (17), 174417.

89.   Havelia, S.; Wang, S.; Skowronski, M.; Salvador, P. A. *Journal of Applied Physics* **2009**, *106* (12), 123509.

90.   Langenberg, E.; Varela, M.; García-Cuenca, M. V.; Ferrater, C.; Sánchez, F.; Fontcuberta, J. *Materials Science and Engineering: B* **2007**, *144* (1–3), 138-142.

91.   Gajek, M.; Bibes, M.; Fusil, S.; Bouzehouane, K.; Fontcuberta, J.; Barthelemy, A.; Fert, A. *Nature Materials* **2007**, *6* (4), 296-302.

92.   Lee, B. W.; Yoo, P. S.; Nam, V. B.; Toreh, K. R. N.; Jung, C. U. *Nanoscale Research Letters* **2015**, *10* (1), 47.

93.   Yang, C. H.; Koo, T. Y.; Lee, S. H.; Song, C.; Lee, K. B.; Jeong, Y. H. *Europhysics Letters* **2006**, *74* (2), 348.

94.   Troyanchuk, I. O.; Mantytskaja, O. S.; Szymczak, H.; Shvedun, M. Y. *Low Temperature Physics* **2002**, *28* (7), 569-573.

95.   Kimura, T.; Kawamoto, S.; Yamada, I.; Azuma, M.; Takano, M.; Tokura, Y. *Physical Review B: Condensed Matter* **2003**, *67*.

96.   Sugawara, F.; Iiida, S.; Syono, Y.; Akimoto, S.-i. *Journal of the Physical Society of Japan* **1968**, *25* (6), 1553-1558.

97.   De Luca, G. M.; Preziosi, D.; Chiarella, F.; Di Capua, R.; Gariglio, S.; Lettieri, S.; Salluzzo, M. *Applied Physics Letters* **2013**, *103* (6), 062902.

98.   Choi, E.-M.; Kursumovic, A.; Lee, O. J.; Kleibeuker, J. E.; Chen, A.; Zhang, W.; Wang, H.; MacManus-Driscoll, J. L. *ACS Applied Materials & Interfaces* **2014**, *6* (17), 14836-14843.

99.   Yoshitaka, U.; Tatsuya, S.; Fumiyuki, I.; Tamio, O. *Japanese Journal of Applied Physics* **2005**, *44* (9S), 7130.

100.   Son, J. Y.; Park, C. S.; Shin, Y.-H. *Applied Physics Letters* **2008**, *92* (22), 222911.

101.   Pálová, L.; Chandra, P.; Rabe, K. M. *Physical Review B* **2010**, *82* (7), 075432.

102.   Azuma, M.; Kanda, H.; Belik, A. A.; Shimakawa, Y.; Takano, M. *Journal of Magnetism and Magnetic Materials* **2007**, *310* (2, Part 2), 1177-1179.

103.   Rana, D. S.; Kawayama, I.; Takahashi, K.; Mavani, K. R.; Murakami, H.; Tonouchi, M.; Yanagida, T.; Tanaka, H.; Kawai, T. *Europhysics Letters* **2008**, *84* (6), 67016.

104.   Huang, J.-Z.; Shen, Y.; Li, M.; Nan, C.-W. *Journal of Applied Physics* **2011**, *110* (9), 094106.

105.   Huang, J.-Z.; Wang, Y.; Lin, Y.; Li, M.; Nan, C. W. *Journal of Applied Physics* **2009**, *106* (6), 063911.

106.   Naganuma, H.; Miura, J.; Okamura, S. *Applied Physics Letters* **2008**, *93* (5), 052901.

107.   Pálová, L.; Chandra, P.; Rabe, K. M. *Physical Review Letters* **2010**, *104* (3), 037202.

108.   Bi, L.; Taussig, A. R.; Kim, H.-S.; Wang, L.; Dionne, G. F.; Bono, D.; Persson, K.; Ceder, G.; Ross, C. A. *Physical Review B* **2008**, *78* (10), 104106.

109.   Mandal, P.; Sundaresan, A.; Rao, C. N. R.; Iyo, A.; Shirage, P. M.; Tanaka, Y.; Simon, C.; Pralong, V.; Lebedev, O. I.; Caignaert, V.; Raveau, B. *Physical Review B* **2010**, *82* (10), 100416.

110.   Miao, J.; Zhang, X.; Zhan, Q.; Jiang, Y.; Chew, K.-H. *Applied Physics Letters* **2011**, *99* (6), 062905.

111.   Choi, E.-M.; Patnaik, S.; Weal, E.; Sahonta, S.-L.; Wang, H.; Bi, Z.; Xiong, J.; Blamire, M. G.; Jia, Q. X.; MacManus-Driscoll, J. L. *Applied Physics Letters* **2011**, *98* (1), 012509.

112.   Delmonte, D.; Mezzadri, F.; Pernechele, C.; Calestani, G.; Spina, G.; Lantieri, M.; Solzi, M.; Cabassi, R.; Bolzoni, F.; Migliori, A.; Ritter, C.; Gilioli, E. *Physical Review B* **2013**, *88* (1), 014431.

113.   Choi, E.-M.; Fix, T.; Kursumovic, A.; Kinane, C. J.; Arena, D.; Sahonta, S.-L.; Bi, Z.; Xiong, J.; Yan, L.; Lee, J.-S.; Wang, H.; Langridge, S.; Kim, Y.-M.; Borisevich, A. Y.;

MacLaren, I.; Ramasse, Q. M.; Blamire, M. G.; Jia, Q.; MacManus-Driscoll, J. L. *Advanced Functional Materials* **2014**, *24* (47), 7478-7487.

114.   Xu, Q.; Sheng, Y.; He, M.; Qiu, X.; Du, J. *Journal of Applied Physics* **2015**, *117* (17), 17D911.

115.   Singh, M. P.; Truong, K. D.; Fournier, P.; Rauwel, P.; Rauwel, E.; Carignan, L. P.; Ménard, D. *Applied Physics Letters* **2008**, *92* (11), 112505.

116.   Dass, R. I.; Goodenough, J. B. *Physical Review B* **2003**, *67* (1), 014401.

117.   Chen, C. T.; Idzerda, Y. U.; Lin, H. J.; Smith, N. V.; Meigs, G.; Chaban, E.; Ho, G. H.; Pellegrin, E.; Sette, F. *Physical Review Letters* **1995**, *75* (1), 152-155.

118.   Ciucivara, A.; Sahu, B.; Kleinman, L. *Physical Review B* **2007**, *76* (6), 064412.

119.   Yuichi, S.; Daisuke, K.; Masanori, K.; Maiko, S.; Satoru, I.; Masaki, A.; Shigeru, K.; Osami, S. *Japanese Journal of Applied Physics* **2007**, *46* (9L), L845.

120.   Sakai, M.; Masuno, A.; Kan, D.; Hashisaka, M.; Takata, K.; Azuma, M.; Takano, M.; Shimakawa, Y. *Applied Physics Letters* **2007**, *90* (7), 072903.

121.   Padhan, P.; LeClair, P.; Gupta, A.; Srinivasan, G. *Journal of Physics: Condensed Matter* **2008**, *20* (35), 355003.

122.   Du, Y.; Cheng, Z. X.; Wang, X. L.; Liu, P.; Dou, S. X. *Journal of Applied Physics* **2011**, *109* (7), 07B507.

123.   Iliev, M. N.; Padhan, P.; Gupta, A. *Physical Review B* **2008**, *77* (17), 172303.

124.   Zhang, T. F.; Tang, X. G.; Liu, Q. X.; Jiang, Y. P.; Lai, J. L. *Superlattices and Microstructures* **2015**, *85*, 653-657.

125.   Lai, J. L.; Tang, X. G.; Ma, C. B.; Li, R.; Liu, Q. X.; Jiang, Y. P. *Integrated Ferroelectrics* **2012**, *139* (1), 26-31.

126.   Shimakawa, Y.; Azuma, M.; Ichikawa, N. *Materials* **2011**, *4* (1), 153.

127.   Azuma, M.; Takata, K.; Saito, T.; Ishiwata, S.; Shimakawa, Y.; Takano, M. *Journal of the American Chemical Society* **2005**, *127* (24), 8889-8892.

128.   Barón-González, A. J.; Frontera, C.; García-Muñoz, J. L.; Blasco, J.; Ritter, C. *Journal of Physics: Conference Series* **2011**, *325* (1), 012007.

129.   Langenberg, E.; Varela, M.; García-Cuenca, M. V.; Ferrater, C.; Polo, M. C.; Fina, I.; Fàbrega, L.; Sánchez, F.; Fontcuberta, J. *Journal of Magnetism and Magnetic Materials* **2009**, *321* (11), 1748-1753.

130.   Langenberg, E.; Rebled, J.; Estradé, S.; Daumont, C. J. M.; Ventura, J.; Coy, L. E.; Polo, M. C.; García-Cuenca, M. V.; Ferrater, C.; Noheda, B.; Peiró, F.; Varela, M.; Fontcuberta, J. *Journal of Applied Physics* **2010**, *108* (12), 123907.

131.   Langenberg, E.; Fina, I.; Gemeiner, P.; Dkhil, B.; Fàbrega, L.; Varela, M.; Fontcuberta, J. *Applied Physics Letters* **2012**, *100* (2), 022902.

132.   Nechache, R.; Harnagea, C.; Carignan, L.-P.; Gautreau, O.; Pintilie, L.; Singh, M. P.; Ménard, D.; Fournier, P.; Alexe, M.; Pignolet, A. *Journal of Applied Physics* **2009**, *105* (6), 061621.

133.   Kim, D. H.; Lee, H. N.; Biegalski, M. D.; Christen, H. M. *Applied Physics Letters* **2007**, *91* (4), 042906.

134.   Nechache, R.; Harnagea, C.; Pignolet, A.; Normandin, F.; Veres, T.; Carignan, L.-P.; Ménard, D. *Applied Physics Letters* **2006**, *89* (10), 102902.

135.   Geim, A. K.; Novoselov, K. S. *Nature Materials* **2007**, *6* (3), 183-191.

136.   Lee, C.; Wei, X.; Kysar, J. W.; Hone, J. *Science* **2008**, *321* (5887), 385-388.

137.   Tombros, N.; Jozsa, C.; Popinciuc, M.; Jonkman, H. T.; van Wees, B. J. *Nature* **2007**, *448* (7153), 571-574.

138.   Tehrani, Z.; Burwell, G.; Azmi, M. A. M.; Castaing, A.; Rickman, R.; Almarashi, J.; Dunstan, P.; Beigi, A. M.; Doak, S. H.; Guy, O. J. *2D Materials* **2014**, *1* (2), 025004.

139.   Xu, Y.; He, K. T.; Schmucker, S. W.; Guo, Z.; Koepke, J. C.; Wood, J. D.; Lyding, J. W.; Aluru, N. R. *Nano Letters* **2011**, *11* (7), 2735-2742.

140.   Carlsson, J. M. *Nature Materials* **2007**, *6* (11), 801-802.

141.   Fasolino, A.; Los, J. H.; Katsnelson, M. I. *Nature Materials* **2007**, *6* (11), 858-861.

142.   Eftekhari, A.; Jafarkhani, P. *The Journal of Physical Chemistry C* **2013**, *117* (48), 25845-25851.

143.   Castro Neto, A. H.; Guinea, F.; Peres, N. M. R.; Novoselov, K. S.; Geim, A. K. *Reviews of Modern Physics* **2009**, *81* (1), 109-162.

144.   Morozov, S. V.; Novoselov, K. S.; Katsnelson, M. I.; Schedin, F.; Elias, D. C.; Jaszczak, J. A.; Geim, A. K. *Physical Review Letters* **2008**, *100* (1), 016602.

145.   Jariwala, D.; Sangwan, V. K.; Lauhon, L. J.; Marks, T. J.; Hersam, M. C. *ACS Nano* **2014**, *8* (2), 1102-1120.

146.   Pumera, M.; Loo, A. H. *TRAC Trends in Analytical Chemistry* **2014**, *61*, 49-53.

147.   Qian, X.; Liu, J.; Fu, L.; Li, J. *Science* **2014**, *346* (6215), 1344-1347.

148.   Qi, Y.; Naumov, P. G.; Ali, M. N.; Rajamathi, C. R.; Schnelle, W.; Barkalov, O.; Hanfland, M.; Wu, S.-C.; Shekhar, C.; Sun, Y.; Süß, V.; Schmidt, M.; Schwarz, U.; Pippel, E.; Werner, P.; Hillebrand, R.; Förster, T.; Kampert, E.; Parkin, S.; Cava, R. J.; Felser, C.; Yan, B.; Medvedev, S. A. *Nature Communications* **2016**, *7*, 11038.

149.   Ma, Y.; Kou, L.; Li, X.; Dai, Y.; Heine, T. *Physical Review B* **2016**, *93* (3), 035442.

150.   Nourbakhsh, A.; Zubair, A.; Dresselhaus, M. S.; Palacios, T. *Nano Letters* **2016**, *16* (2), 1359-1366.

151.   Pan, Z.; Sun, H.; Zhang, Y.; Chen, C. *Physical Review Letters* **2009**, *102* (5), 055503.

152.   Watanabe, K.; Taniguchi, T.; Kanda, H. *Nature Materials* **2004**, *3* (6), 404-409.

153.   Tao, O.; Yuanping, C.; Yuee, X.; Kaike, Y.; Zhigang, B.; Jianxin, Z. *Nanotechnology* **2010**, *21* (24), 245701.

154.   Nagamatsu, J.; Nakagawa, N.; Muranaka, T.; Zenitani, Y.; Akimitsu, J. *Nature* **2001**, *410* (6824), 63-64.

155.   Paton, K. R.; Varrla, E.; Backes, C.; Smith, R. J.; Khan, U.; O'Neill, A.; Boland, C.; Lotya, M.; Istrate, O. M.; King, P.; Higgins, T.; Barwich, S.; May, P.; Puczkarski, P.; Ahmed, I.; Moebius, M.; Pettersson, H.; Long, E.; Coelho, J.; O'Brien, S. E.; McGuire, E. K.; Sanchez, B. M.; Duesberg, G. S.; McEvoy, N.; Pennycook, T. J.; Downing, C.; Crossley, A.; Nicolosi, V.; Coleman, J. N. *Nature Materials* **2014**, *13* (6), 624-630.

156.   Molina-Sánchez, A.; Wirtz, L. *Physical Review B* **2011**, *84* (15), 155413.

157.   Mann, S.; Rani, P.; Kumar, R.; Dubey, G. S.; Jindal, V. K. *RSC Advances* **2016**, *6* (15), 12158-12168.

158.   Taha-Tijerina, J.; Peña-Parás, L.; Maldonado-Cortés, D., *2D-Based Nanofluids: Materials Evaluation and Performance*. **2016**.

159.   Antolini, E. *Solid State Ionics* **2004**, *170* (3–4), 159-171.

160.   Chen, A.; Bi, Z.; Zhang, W.; Jian, J.; Jia, Q.; Wang, H. *Applied Physics Letters* **2014**, *104* (7), -.

161.   Shao-Horn, Y.; Croguennec, L.; Delmas, C.; Nelson, E. C.; O'Keefe, M. A. *Nature Materials* **2003**, *2* (7), 464-467.

162.   Huang, H.; Wang, S.; Tian, N.; Zhang, Y. *RSC Advances* **2014**, *4* (11), 5561-5567.

163.   Ganguli, A. K.; Prakash, J.; Thakur, G. S. *Chemical Society Reviews* **2013**, *42* (2), 569-598.

164.   Chernova, N. A.; Roppolo, M.; Dillon, A. C.; Whittingham, M. S. *Journal of Materials Chemistry* **2009**, *19* (17), 2526-2552.

165.   Kendall, K. R.; Navas, C.; Thomas, J. K.; zur Loye, H.-C. *Chemistry of Materials* **1996**, *8* (3), 642-649.

166.   Frit, B.; Mercurio, J. P. *Journal of Alloys and Compounds* **1992**, *188*, 27-35.

167.   Yanovskii, V. K.; Voronkova, V. I. *Physica Status Solidi (A)* **1986**, *93* (1), 57-66.

168.   McDowell, N. A.; Knight, K. S.; Lightfoot, P. *Chemistry – A European Journal* **2006**, *12* (5), 1493-1499.

169.   Thompson, J. G.; Schmid, S.; Withers, R. L.; Rae, A. D.; Gerald, J. D. F. *Journal of Solid State Chemistry* **1992**, *101* (2), 309-321.

170.   McCabe, E. E.; Jones, I. P.; Zhang, D.; Hyatt, N. C.; Greaves, C. *Journal of Materials Chemistry* **2007**, *17* (12), 1193-1200.

171.   Zhou, Z.; Dong, X.; Huang, S.; Yan, H. *Journal of the American Ceramic Society* **2006**, *89* (9), 2939-2942.

172.   Peng, Z.; Yan, D.; Chen, Q.; Xin, D.; Liu, D.; Xiao, D.; Zhu, J. *Current Applied Physics* **2014**, *14* (12), 1861-1866.

173.   Gritzner, G.; Pissenberger, A. *Applied Physics A* **2007**, *87* (4), 807-811.

174. Krzhizhanovskaya, M.; Filatov, S.; Gusarov, V.; Paufler, P.; Bubnova, R.; Morozov, M.; Meyer, D. C. *Zeitschrift fur Anorganische und Allgemeine Chemie* **2005**, *631* (9), 1603-1608.

175. Deepak, N.; Carolan, P.; Keeney, L.; Pemble, M. E.; Whatmore, R. W. *Journal of Materials Chemistry C* **2015**, *3* (22), 5727-5732.

176. Snedden, A.; Lightfoot, P.; Dinges, T.; Islam, M. S. *Journal of Solid State Chemistry* **2004**, *177* (10), 3660-3665.

177. Chu, M.-W.; Caldes, M.-T.; Brohan, L.; Ganne, M.; Marie; Joubert, O.; Piffard, Y. *Chemistry of Materials* **2004**, *16* (1), 31-42.

178. Kikuchi, T. *Materials Research Bulletin* **1979**, *14* (12), 1561-1569.

179. Mazurek, M.; Jartych, E.; Lisińska-Czekaj, A.; Czekaj, D.; Oleszak, D. *Journal of Non-Crystalline Solids* **2010**, *356* (37–40), 1994-1997.

180. Armstrong, R. A.; Newnham, R. E. *Materials Research Bulletin* **1972**, *7* (10), 1025-1034.

181. Lee, H. N.; Hesse, D.; Zakharov, N.; Gösele, U. *Science* **2002**, *296* (5575), 2006-2009.

182. Zurbuchen, M. A.; Freitas, R. S.; Wilson, M. J.; Schiffer, P.; Roeckerath, M.; Schubert, J.; Biegalski, M. D.; Mehta, G. H.; Comstock, D. J.; Lee, J. H.; Jia, Y.; Schlom, D. G. *Applied Physics Letters* **2007**, *91* (3), 033113.

183. Imai, A.; Cheng, X.; Xin, H. L.; Eliseev, E. A.; Morozovska, A. N.; Kalinin, S. V.; Takahashi, R.; Lippmaa, M.; Matsumoto, Y.; Nagarajan, V. *ACS Nano* **2013**, *7* (12), 11079-11086.

184. Chen, A.; Zhou, H.; Bi, Z.; Zhu, Y.; Luo, Z.; Bayraktaroglu, A.; Phillips, J.; Choi, E.-M.; MacManus-Driscoll, J. L.; Pennycook, S. J.; Narayan, J.; Jia, Q.; Zhang, X.; Wang, H. *Advanced Materials* **2013**, *25* (7), 1028-1032.

185. Li, L.; Zhang, W.; Khatkhatay, F.; Jian, J.; Fan, M.; Su, Q.; Zhu, Y.; Chen, A.; Lu, P.; Zhang, X.; Wang, H. *ACS Applied Materials & Interfaces* **2015**, *7* (21), 11631-11636.

186. Zhu, Y.; Chen, A.; Zhou, H.; Zhang, W.; Narayan, J.; MacManus-Driscoll, J. L.; Jia, Q.; Wang, H. *APL Materials* **2013**, *1* (5), 050702.

187.   Singh, R. K.; Holland, O. W.; Narayan, J. *Journal of Applied Physics* **1990**, *68* (1), 233-247.

188.   Moram, M. A.; Vickers, M. E. *Reports on Progress in Physics* **2009**, *72* (3), 036502.

189.   Williams, D. B., *Practical Analytical Electron Microscopy in Materials Science*. Philips Electronic Instruments: **1984**.

190.   David B. Williams, B. C. C., *Transmission Electron Microscopy*. Plenum Press: New York, **1996**.

191.   David B. Williams, B. C. C., *Transmission Electron Microscopy*. Springer: London, **2009**.

192.   Schitter, G.; Menold, P.; Knapp, H. F.; Allgöwer, F.; Stemmer, A. *Review of Scientific Instruments* **2001**, *72* (8), 3320-3327.

193.   Kolb, U.; Gorelik, T.; Kübel, C.; Otten, M. T.; Hubert, D. *Ultramicroscopy* **2007**, *107* (6-7), 507-513.

194.   Palatinus, L. *Prague: Institute of Physics of the AS CR* **2011**.

195.   Petříček, V.; Dušek, M.; Palatinus, L., Crystallographic Computing System Jana2006: General Features. In *Zeitschrift für Kristallographie - Crystalline Materials*, **2014**; Vol. 229, p 345.

196.   MacManus-Driscoll, J. L.; Zerrer, P.; Wang, H.; Yang, H.; Yoon, J.; Fouchet, A.; Yu, R.; Blamire, M. G.; Jia, Q. *Nature Materials* **2008**, *7* (4), 314-320.

197.   Khatkhatay, F.; Chen, A.; Lee, J. H.; Zhang, W.; Abdel-Raziq, H.; Wang, H. *ACS Applied Materials & Interfaces* **2013**, *5* (23), 12541-12547.

198.   Du, Y.; Cheng, Z. X.; Dou, S. X.; Wang, X. L.; Zhao, H. Y.; Kimura, H. *Applied Physics Letters* **2010**, *97* (12), 122502.

199.   Bi, Z.; Lee, J. H.; Yang, H.; Jia, Q.; MacManus-Driscoll, J. L.; Wang, H. *Journal of Applied Physics* **2009**, *106* (9), 094309.

200.   Zheng, H.; Wang, J.; Lofland, S. E.; Ma, Z.; Mohaddes-Ardabili, L.; Zhao, T.; Salamanca-Riba, L.; Shinde, S. R.; Ogale, S. B.; Bai, F.; Viehland, D.; Jia, Y.; Schlom, D. G.; Wuttig, M.; Roytburd, A.; Ramesh, R. *Science* **2004**, *303* (5658), 661-663.

201.   Jian, J.; Chen, A.; Zhang, W.; Wang, H. *Journal of Applied Physics* **2013**, *114* (24), 244301.

202.   Chen, A.; Bi, Z.; Jia, Q.; MacManus-Driscoll, J. L.; Wang, H. *Acta Materialia* **2013**, *61* (8), 2783-2792.

203.   Zhang, W.; Chen, A.; Bi, Z.; Jia, Q.; MacManus-Driscoll, J. L.; Wang, H. *Current Opinion in Solid State and Materials Science* **2014**, *18* (1), 6-18.

204.   Yang, H.; Wang, H.; Yoon, J.; Wang, Y.; Jain, M.; Feldmann, D. M.; Dowden, P. C.; MacManus-Driscoll, J. L.; Jia, Q. *Advanced Materials* **2009**, *21* (37), 3794-3798.

205.   Wu, J.; Wang, J.; Xiao, D.; Zhu, J. *ACS Applied Materials & Interfaces* **2011**, *3* (7), 2504-2511.

206.   Wu, J.; Wang, J.; Xiao, D.; Zhu, J. *ACS Applied Materials & Interfaces* **2011**, *3* (9), 3261-3263.

207.   Wu, J.; Wang, J.; Xiao, D.; Zhu, J. *ACS Applied Materials & Interfaces* **2012**, *4* (3), 1182-1185.

208.   Eerenstein, W.; Mathur, N. D.; Scott, J. F. *Nature* **2006**, *442* (7104), 759-765.

209.   Spaldin, N. A.; Fiebig, M. *Science* **2005**, *309* (5733), 391-392.

210.   Logvenov, G.; Gozar, A.; Bozovic, I. *Science* **2009**, *326* (5953), 699-702.

211.   Moya, X.; Hueso, L. E.; Maccherozzi, F.; Tovstolytkin, A. I.; Podyalovskii, D. I.; Ducati, C.; Phillips, L. C.; Ghidini, M.; Hovorka, O.; Berger, A.; Vickers, M. E.; Defay, E.; Dhesi, S. S.; Mathur, N. D. *Nature Materials* **2013**, *12* (1), 52-58.

212.   Bayati, M. R.; Molaei, R.; Narayan, R. J.; Narayan, J.; Zhou, H.; Pennycook, S. J. *Applied Physics Letters* **2012**, *100* (25), 251606.

213.   Chen, S.-Y.; Tsai, C.-H.; Huang, M.-Z.; Yan, D.-C.; Huang, T.-W.; Gloter, A.; Chen, C.-L.; Lin, H.-J.; Chen, C.-T.; Dong, C.-L. *The Journal of Physical Chemistry C* **2012**, *116* (15), 8707-8713.

214.   Fernandes, V.; Mossanek, R. J. O.; Schio, P.; Klein, J. J.; de Oliveira, A. J. A.; Ortiz, W. A.; Mattoso, N.; Varalda, J.; Schreiner, W. H.; Abbate, M.; Mosca, D. H. *Physical Review B* **2009**, *80* (3), 035202.

215.   Yang, H.; Wang, Y. Q.; Wang, H.; Jia, Q. X. *Applied Physics Letters* **2010**, *96* (1), 012909.

216.   Kumar, M. M.; Palkar, V. R.; Srinivas, K.; Suryanarayana, S. V. *Applied Physics Letters* **2000**, *76* (19), 2764-2766.

217.   Qi, X.; Wei, M.; Lin, Y.; Jia, Q.; Zhi, D.; Dho, J.; Blamire, M. G.; MacManus-Driscoll, J. L. *Applied Physics Letters* **2005**, *86* (7), 071913.

218.   Belik, A. A.; Kodama, K.; Igawa, N.; Shamoto, S.-i.; Kosuda, K.; Takayama-Muromachi, E. *Journal of the American Chemical Society* **2010**, *132* (23), 8137-8144.

219.   Zhang, W.; Li, M.; Chen, A.; Li, L.; Zhu, Y.; Xia, Z.; Lu, P.; Boullay, P.; Wu, L.; Zhu, Y.; MacManus-Driscoll, J. L.; Jia, Q.; Zhou, H.; Narayan, J.; Zhang, X.; Wang, H. *ACS Applied Materials & Interfaces* **2016**, *8* (26), 16845-16851.

220.   Perdew, J. P.; Burke, K.; Ernzerhof, M. *Physical Review Letters* **1996**, *77* (18), 3865-3868.

221.   Kresse, G.; Furthmüller, J. *Computational Materials Science* **1996**, *6* (1), 15-50.

222.   Monkhorst, H. J.; Pack, J. D. *Physical review B* **1976**, *13* (12), 5188.

223.   Charkin, D. O.; Dytyatiev, O. A.; Dolgikh, V. A.; Lightfoot, P. *Journal of Solid State Chemistry* **2003**, *173* (1), 83-90.

224.   Greaves, C.; Blower, S. K. *Materials Research Bulletin* **1988**, *23* (7), 1001-1008.

225.   Cong, R.; Sun, J.; Yang, T.; Li, M.; Liao, F.; Wang, Y.; Lin, J. *Inorganic Chemistry* **2011**, *50* (11), 5098-5104.

226.   Marmier, A.; Lethbridge, Z. A. D.; Walton, R. I.; Smith, C. W.; Parker, S. C.; Evans, K. E. *Computer Physics Communications* **2010**, *181* (12), 2102-2115.

227.   Born, M. In *On the Stability of Crystal Lattices. I*, Mathematical Proceedings of the Cambridge Philosophical Society, Cambridge Univ Press: **1940**; pp 160-172.

228.   Jena, D.; Banerjee, K.; Xing, G. H. *Nature Materials* **2014**, *13* (12), 1076-1078.

229.   Schwierz, F. *Nature Nanotechnology* **2010**, *5* (7), 487-496.

230.   Wang, Q. H.; Kalantar-Zadeh, K.; Kis, A.; Coleman, J. N.; Strano, M. S. *Nature Nanotechnology* **2012**, *7* (11), 699-712.

231. Novoselov, K. S.; Falko, V. I.; Colombo, L.; Gellert, P. R.; Schwab, M. G.; Kim, K. *Nature* **2012**, *490* (7419), 192-200.

232. *Nature Materials* **2014**, *13* (12), 1073-1073.

233. Chhowalla, M.; Shin, H. S.; Eda, G.; Li, L.-J.; Loh, K. P.; Zhang, H. *Nature Chemistry* **2013**, *5* (4), 263-275.

234. Cazalilla, M. A.; Ochoa, H.; Guinea, F. *Physical Review Letters* **2014**, *113* (7), 077201.

235. Nukala, P.; Agarwal, R.; Qian, X.; Jang, M. H.; Dhara, S.; Kumar, K.; Johnson, A. T. C.; Li, J.; Agarwal, R. *Nano Letters* **2014**, *14* (4), 2201-2209.

236. Sachs, B.; Wehling, T. O.; Novoselov, K. S.; Lichtenstein, A. I.; Katsnelson, M. I. *Physical Review B* **2013**, *88* (20), 201402.

237. Tongay, S.; Varnoosfaderani, S. S.; Appleton, B. R.; Wu, J.; Hebard, A. F. *Applied Physics Letters* **2012**, *101* (12), 123105.

238. Zhang, S.; Li, Y.; Zhao, T.; Wang, Q. *Scientific Reports* **2014**, *4*, 5241.

239. Wu, F.; Huang, C.; Wu, H.; Lee, C.; Deng, K.; Kan, E.; Jena, P. *Nano Letters* **2015**, *15* (12), 8277-8281.

240. Birenbaum, A. Y.; Ederer, C. *Physical Review B* **2014**, *90* (21), 214109.

241. Battle, P. D.; Green, M. A.; Laskey, N. S.; Millburn, J. E.; Murphy, L.; Rosseinsky, M. J.; Sullivan, S. P.; Vente, J. F. *Chemistry of Materials* **1997**, *9* (2), 552-559.

242. Fawcett, I. D.; Sunstrom; Greenblatt, M.; Croft, M.; Ramanujachary, K. V. *Chemistry of Materials* **1998**, *10* (11), 3643-3651.

243. Tahara, S.; Ichikawa, T.; Kajiwara, G.; Sugahara, Y. *Chemistry of Materials* **2007**, *19* (9), 2352-2358.

244. Haeni, J. H.; Irvin, P.; Chang, W.; Uecker, R.; Reiche, P.; Li, Y. L.; Choudhury, S.; Tian, W.; Hawley, M. E.; Craigo, B.; Tagantsev, A. K.; Pan, X. Q.; Streiffer, S. K.; Chen, L. Q.; Kirchoefer, S. W.; Levy, J.; Schlom, D. G. *Nature* **2004**, *430* (7001), 758-761.

245. Baek, S. H.; Park, J.; Kim, D. M.; Aksyuk, V. A.; Das, R. R.; Bu, S. D.; Felker, D. A.; Lettieri, J.; Vaithyanathan, V.; Bharadwaja, S. S. N.; Bassiri-Gharb, N.; Chen, Y. B.;

231. Novoselov, K. S.; Falko, V. I.; Colombo, L.; Gellert, P. R.; Schwab, M. G.; Kim, K. *Nature* **2012**, *490* (7419), 192-200.

232. *Nature Materials* **2014**, *13* (12), 1073-1073.

233. Chhowalla, M.; Shin, H. S.; Eda, G.; Li, L.-J.; Loh, K. P.; Zhang, H. *Nature Chemistry* **2013**, *5* (4), 263-275.

234. Cazalilla, M. A.; Ochoa, H.; Guinea, F. *Physical Review Letters* **2014**, *113* (7), 077201.

235. Nukala, P.; Agarwal, R.; Qian, X.; Jang, M. H.; Dhara, S.; Kumar, K.; Johnson, A. T. C.; Li, J.; Agarwal, R. *Nano Letters* **2014**, *14* (4), 2201-2209.

236. Sachs, B.; Wehling, T. O.; Novoselov, K. S.; Lichtenstein, A. I.; Katsnelson, M. I. *Physical Review B* **2013**, *88* (20), 201402.

237. Tongay, S.; Varnoosfaderani, S. S.; Appleton, B. R.; Wu, J.; Hebard, A. F. *Applied Physics Letters* **2012**, *101* (12), 123105.

238. Zhang, S.; Li, Y.; Zhao, T.; Wang, Q. *Scientific Reports* **2014**, *4*, 5241.

239. Wu, F.; Huang, C.; Wu, H.; Lee, C.; Deng, K.; Kan, E.; Jena, P. *Nano Letters* **2015**, *15* (12), 8277-8281.

240. Birenbaum, A. Y.; Ederer, C. *Physical Review B* **2014**, *90* (21), 214109.

241. Battle, P. D.; Green, M. A.; Laskey, N. S.; Millburn, J. E.; Murphy, L.; Rosseinsky, M. J.; Sullivan, S. P.; Vente, J. F. *Chemistry of Materials* **1997**, *9* (2), 552-559.

242. Fawcett, I. D.; Sunstrom; Greenblatt, M.; Croft, M.; Ramanujachary, K. V. *Chemistry of Materials* **1998**, *10* (11), 3643-3651.

243. Tahara, S.; Ichikawa, T.; Kajiwara, G.; Sugahara, Y. *Chemistry of Materials* **2007**, *19* (9), 2352-2358.

244. Haeni, J. H.; Irvin, P.; Chang, W.; Uecker, R.; Reiche, P.; Li, Y. L.; Choudhury, S.; Tian, W.; Hawley, M. E.; Craigo, B.; Tagantsev, A. K.; Pan, X. Q.; Streiffer, S. K.; Chen, L. Q.; Kirchoefer, S. W.; Levy, J.; Schlom, D. G. *Nature* **2004**, *430* (7001), 758-761.

245. Baek, S. H.; Park, J.; Kim, D. M.; Aksyuk, V. A.; Das, R. R.; Bu, S. D.; Felker, D. A.; Lettieri, J.; Vaithyanathan, V.; Bharadwaja, S. S. N.; Bassiri-Gharb, N.; Chen, Y. B.;

Sun, H. P.; Folkman, C. M.; Jang, H. W.; Kreft, D. J.; Streiffer, S. K.; Ramesh, R.; Pan, X. Q.; Trolier-McKinstry, S.; Schlom, D. G.; Rzchowski, M. S.; Blick, R. H.; Eom, C. B. *Science* **2011**, *334* (6058), 958-961.

246.   Fan, M.; Zhang, W.; Khatkhatay, F.; Li, L.; Wang, H. *Journal of Applied Physics* **2015**, *118* (6), 065302.

247.   Chen, A.; Hu, J.-M.; Lu, P.; Yang, T.; Zhang, W.; Li, L.; Ahmed, T.; Enriquez, E.; Weigand, M.; Su, Q.; Wang, H.; Zhu, J.-X.; MacManus-Driscoll, J. L.; Chen, L.-Q.; Yarotski, D.; Jia, Q. *Science Advances* **2016**, *2* (6).

248.   MacManus-Driscoll, J. L.; Foltyn, S. R.; Jia, Q. X.; Wang, H.; Serquis, A.; Civale, L.; Maiorov, B.; Hawley, M. E.; Maley, M. P.; Peterson, D. E. *Nat Mater* **2004**, *3* (7), 439-443.

249.   Jijie, H.; Li, C.; Jie, J.; Kevin, T.; Leigang, L.; Han, W.; Haiyan, W. *Journal of Physics: Condensed Matter* **2016**, *28* (2), 025702.

250.   Huang, J.; Fan, M.; Wang, H.; Chen, L.; Tsai, C.-F.; Li, L.; Wang, H. *Ceramics International* **2016**, *42* (10), 12202-12209.

251.   Yamauchi, H.; Sakai, K.; Nagai, T.; Matsui, Y.; Karppinen, M. *Chemistry of Materials* **2006**, *18* (1), 155-158.

252.   Lee, C.-H.; Orloff, N. D.; Birol, T.; Zhu, Y.; Goian, V.; Rocas, E.; Haislmaier, R.; Vlahos, E.; Mundy, J. A.; Kourkoutis, L. F.; Nie, Y.; Biegalski, M. D.; Zhang, J.; Bernhagen, M.; Benedek, N. A.; Kim, Y.; Brock, J. D.; Uecker, R.; Xi, X. X.; Gopalan, V.; Nuzhnyy, D.; Kamba, S.; Muller, D. A.; Takeuchi, I.; Booth, J. C.; Fennie, C. J.; Schlom, D. G. *Nature* **2013**, *502* (7472), 532-536.

253.   Stokes, H. T.; Campbell, B. J.; van Smaalen, S. *Acta Crystallographica Section A* **2011**, *67* (1), 45-55.

254.   Akimoto, J.; Gotoh, Y.; Oosawa, Y. *Journal of Solid State Chemistry* **1998**, *141* (1), 298-302.

255.   Yamamoto, A. *Acta Crystallographica Section A* **1992**, *48* (4), 476-483.

256.   Makovicky, E.; Hyde, B. G., Non-Commensurate (Misfit) Layer Structures. In *Inorganic Chemistry*, Springer Berlin Heidelberg: Berlin, Heidelberg, **1981**, pp 101-170.

257.   Boullay, P.; Domengès, B.; Hervieu, M.; Groult, D.; Raveau, B. *Chemistry of Materials* **1996**, *8* (7), 1482-1489.

258.   Seshadri, R.; Hill, N. A. *Chemistry of Materials* **2001**, *13* (9), 2892-2899.

259.   Ihlefeld, J. F.; Podraza, N. J.; Liu, Z. K.; Rai, R. C.; Xu, X.; Heeg, T.; Chen, Y. B.; Li, J.; Collins, R. W.; Musfeldt, J. L.; Pan, X. Q.; Schubert, J.; Ramesh, R.; Schlom, D. G. *Applied Physics Letters* **2008**, *92* (14), 142908.